Author:
Bullock, Steve

Title:
Cooperative Control for Automated Air-to-Air Refuelling

Cooperative Control for Automated Air-to-Air Refuelling

Steve Bullock

Department of Aerospace Engineering

A dissertation submitted to the University of Bristol in accordance with the requirements of the degree of Doctor of Philosophy in the Faculty of Engineering.

2017

Approx 50,000 words

Abstract

The proliferation of Unmanned Aircraft Systems has led to demand for Air-to-Air Refuelling capabilities similar to those available to manned aircraft, and there also exist fuel and cost savings which can be realised. Autonomous Air-to-Air Refuelling presents interesting challenges in the areas of control, sensing, and decision making. This thesis focuses primarily on probe-drogue refuelling.

Work exists on automating Air-to-Air Refuelling using conventional leader-follower architectures. In these schemes, the refuelling drogue is aerodynamically stabilised but subject to disturbances such as gusts, tanker wake, and receiver bow wave, and the receiver is controlled in such a way as to capture the drogue.

This method does not effectively utilise all available degrees of freedom – the tanker is usually much larger and less manoeuvrable than the receiver, but there is potential to control and harness the drogue's motion, for example by adding aerodynamic control surfaces. This thesis investigates the feasibility of this approach and compares control architectures by which these degrees of freedom may be harnessed.

A drogue control model is developed, and two candidate architectures are investigated: Common-target-point Control uses a shared target point approach, which is found to improve capture rate under turbulence, and is extended using a novel scheduled-gain method. Intimate Control optimises the whole drogue-receiver system using Multiple-Input Multiple-Output techniques. Verification of the control schemes is conducted via the University of Bristol's Relative Motion Robotic hybrid testing facility. A well-characterised F-16 aircraft model is used as a surrogate for future mid-sized Unmanned Aircraft System.

This thesis presents evidence that harnessing the additional degrees of freedom available via drogue control is likely to improve capture performance in Autonomous Air-to-Air Refuelling, and has been tested at a higher Technology Readiness Level than is usual in academic fields.

The work presented here forms part of the Autonomous Systems Technology Related Airborne Evaluation & Assessment (ASTRAEA) programme in the UK, and was funded by Cobham plc.

To my family, for their support and encouragement.

Acknowledgements

I would like to express my sincere gratitude to my supervisor, Dr. Thomas Richardson, for his support, guidance and patience throughout this project, and in the wider work that I have undertaken alongside it... we got there in the end. Many thanks also to colleagues and friends in the Faculty of Engineering and around the University – you've made my time here most excellent, and I look forward to working alongside you or keeping in touch in the future. Finally, this work was funded as part of the ASTRAEA project by Cobham plc. Thank you to all of the Cobham team for the opportunity, resources and direction.

Declaration

I declare that the work in this dissertation was carried out in accordance with the requirements of the University's Regulations and Code of Practice for Research Degree Programmes and that it has not been submitted for any other academic award. Except where indicated by specific reference in the text, the work is the candidate's own work. Work done in collaboration with, or with the assistance of, others, is indicated as such. Any views expressed in the dissertation are those of the author.

Signed:

Date:

Contents

List of Figures

The appearance of U.S. Department of Defense (DoD) visual information does not imply or constitute DoD endorsement.

List of Tables

Notation

Acronyms

AAR	Air-to-Air Refuelling
AAAR	Autonomous Air-to-Air Refuelling
AARD	Autonomous Airborne Refueling Demonstration
ACARE	Advisory Council for Aviation Research and Innovation in Europe
ACCIS	Advanced Composites Centre for Innovation in Science
AHS	Automated Highway System
ARS	Aerial Refuelling Store
ASTRAEA	Autonomous Systems Technology Related Airborne Evaluation & Assessment
BANTAM	Barron Associates Nonlinear Tailless Aircraft Model
CC	Common-target-point Control
CCD	Charge-Coupled Device
CG	Centre of Gravity
CFD	Computational Fluid Dynamics
COTS	Commercial Off-The-Shelf
DATCOM	USAF Stability and Control Data Compendium
DARPA	Defense Advanced Research Projects Agency

DDVP	Dimensionless Drogue Vertical Position
DFRC	Dryden Flight Research Centre
DGPS	Differential GPS
DoD	Department of Defense
DoF	Degrees of Freedom
EA	Eigenstructure Assignment
ECEF	Earth-Centered, Earth-Fixed
EOGRS	Electro-Optical Grid Reference System
ESDU	Engineering Sciences Data Unit
FAA	Federal Aviation Administration
FCS	Flight Control System
FEM	Finite Element Method
FRL	Flight Refuelling Limited
GPS	Global Positioning System
HAL	Hindustan Aeronautics Limited
HALE	High Altitude, Long Endurance
HDU	Hose Drum Unit
HIL	Hardware-in-the-Loop
IC	Intimate Control
ICE	Innovative Control Effector
INS	Intertial Navigation System
IMU	Inertial Measurement Unit
IR	Infra-Red
ISA	International Standard Atmosphere

KIAS	Knots Indicated Air Speed
LED	Light Emitting Diode
L/F	Leader/Follower
LQ	Linear Quadratic
LQE	Linear Quadratic Estimator
LQG	Linear Quadratic Gaussian
LQR	Linear Quadratic Regulator
LTP	Local Tangent Plane
MAC	Mean Aerodynamic Chord
MIMO	Multiple-Input Multiple-Output
MSI	Multiple Spacecraft Interferometry
NATO	North Atlantic Treaty Organisation
NASA	National Aeronautics and Space Administration
NED	North, East, Down
PD	Probe-and-Drogue
PID	Proportional, Integral, Derivative
PIO	Pilot-Induced Oscillation
PSD	Power Spectral Density
RAF	Royal Air Force
RG	Rendezvous Guidance
RMR	Relative Motion Robotic
RMS	Root Mean Square
SE	Simulation Environment
SISO	Single-Input Single-Output

SQP	Sequential Quadratic Programming
SUSAN	Smallest Univalue Segment Assimilating Nucleus
TRL	Technology Readiness Level
UAS	Unmanned Aircraft System
UAV	Unmanned Air Vehicle
UCAV	Unmanned Combat Air Vehicle
UGV	Unmanned Ground Vehicle
UK	United Kingdom
UoB	University of Bristol
US	United States (of America)
USA	United States of America
USAF	United States Air Force
VLM	Vortex Lattice Method
VS	Virtual Structure

Symbols

This thesis integrates work from several fields. Notation varies between areas therefore, in order to maintain parity with referenced works, symbols are defined as they are used.

Chapter 1

Introduction

Air-to-Air Refuelling (AAR) is used to increase the endurance, range, and/or payload of an aircraft by supplying additional fuel whilst airborne. Conceived in 1917 and first performed in 1923, the past hundred years have seen the development and evolution of a number of techniques by which AAR can be achieved.

Work exists on automating AAR using conventional leader-follower architectures, however this approach does not effectively utilise all available degrees of freedom – the tanker is usually much larger and less manoeuvrable than the receiver, but there is potential to control and harness the drogue's motion, for example by adding aerodynamic control surfaces. This thesis investigates the feasibility of this approach and compares control architectures by which these degrees of freedom may be harnessed.

This introductory chapter gives a brief history of the field, outlines the demand for Autonomous Air-to-Air Refuelling (AAAR)[1] and the challenges it presents, and describes the context in which the work presented in this thesis has been undertaken.

1.1 A brief history of Air-to-Air Refuelling

AAR was first proposed in 1917 by Russian naval pilot Alexander P. Seversky, and patented by him in 1921 [1]. Apart from a stunt in 1921 where wing walker Wesley May climbed between aircraft with a jerry can strapped

[1] Throughout this thesis, the initialisms AAR and AAAR are used distinctly from one another, for manned and autonomous aerial refuelling respectively.

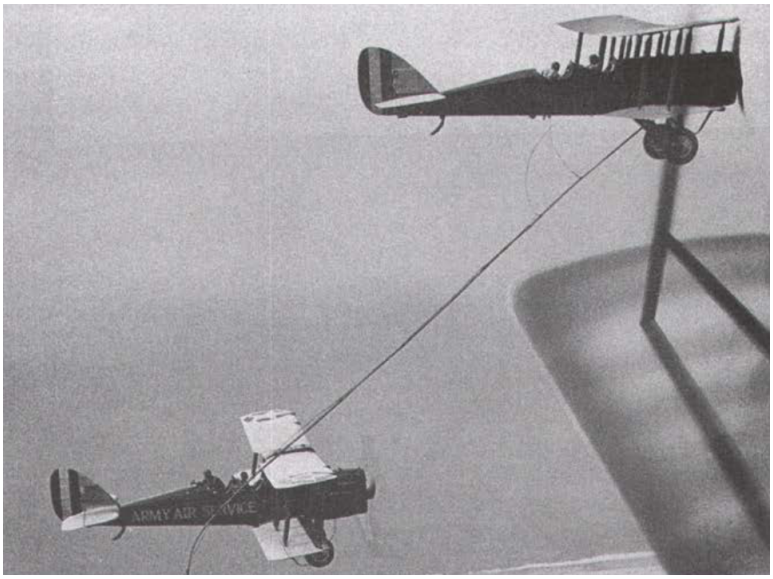

Figure 1.1: 'Dangle-and-grab' refuelling [2].

to his back, the first practical demonstration of AAR took place a mere twenty years after the Wright brothers' first powered flight. In July 1923, seventy-five gallons of fuel was transferred between two US Army de Havilland DH-4B biplanes. The procedure used a fifteen-metre rubber hose and was fraught with risk and difficulty—the six-and-a-half hour process has been described as "dangle-and-grab" [2] (figure 1.1). Two months later the same team set a world record for aircraft endurance, refuelling fourteen times over more than a day and a half. Shortly after that they flew non-stop from the northern to southern borders of the United States of America (USA), extending their aircraft's range by over a factor of four.

The 'dangle-and-grab' method was dismissed as a stunt, particularly after a fatality in November of that year, and although the feat was repeated and surpassed in various military and civilian attempts, culminating in 1935 with an as-yet unbeaten twenty-seven day flight[2], the challenge and risk of the method prevented wider adoption.

The first AAR system that was robust enough for routine use was devised by RAF squadron leader Richard L.R. Atcherly in the mid 1930s. His 'looped hose' system (figure 1.2) provided additional connectors and fittings to streamline the hookup process, enabling small freight aircraft to reduce

[2]For air-to-air transfer. Longer flights have been achieved using ground-to-air transfer methods, with the record standing since 1959 at just under 65 days.

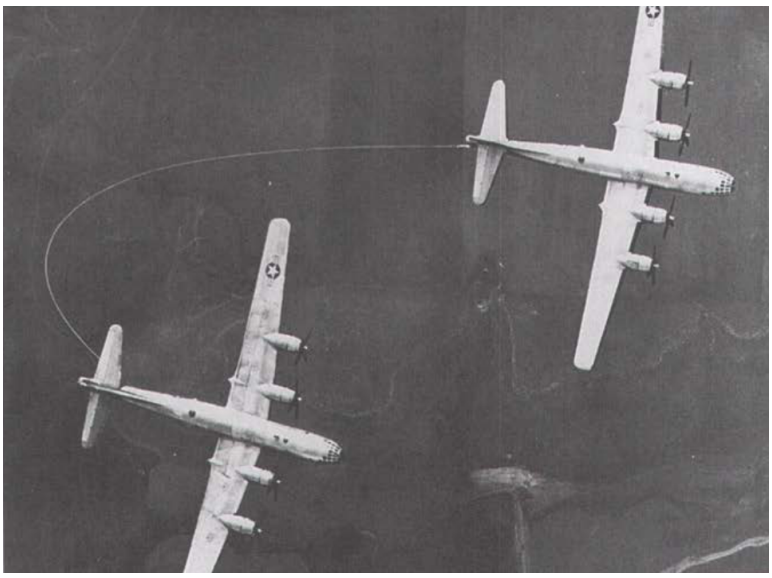

Figure 1.2: Looped-hose refuelling [2].

fuel usage during take-off by replenishing them at altitude. Its use lasted only briefly due to the onset of World War II.

Sir Alan Cobham was a prominent figure in long-distance flying throughout the 1920s, piloting noteworthy flights that took advantage of the ability to take off with a low fuel load, then refuel in-air to beyond maximum take-off weight. Realising the limitations of the 'dangle-and-grab' method he founded Flight Refuelling Limited (FRL) on October 29th 1934, and in 1938 FRL purchased the patent to Atcherly's 'looped hose' cable and grapnel system.

Cobham continued development and demonstration work after the Second World War, with flights between Dover and Land's End, followed by Heathrow to Bermuda, and London to Montreal. With the advent of the Cold War the U.S. Air Force gained interest in range extension, adopting FRL's system in 1948 and using it to conduct the first non-stop flight around the world in 1949.

The looped-hose method was unsuitable for fighter aircraft as it required a crew to connect the refuelling hose. In 1949 FRL performed its first trials of a new probe-and-drogue system, which was used in a variety of scenarios in the following years. The United States (of America) (US) Strategic Air Command preferred Boeing's flying-boom approach, first tested in 1948, for

(a) Probe-and-drogue. **(b)** Flying-boom.

Figure 1.3: Current AAR systems.

its larger, less manoeuvrable bombers, whereas their Tactical Air Command, and subsequently the Navy, Marines, RAF and NATO, adopted the probe-and-drogue system due to its simplicity, lower cost and lower weight.

An alternative method developed by the Soviet Union in the 1950s used a grapnel device trailed from the receiver's port wing to capture a flexible hose, released from a tanker's wing tip. This 'wing-to-wing' method was only used on a small number of Soviet fighters and Tu-16 bombers due to its complexity, and replaced with the probe-and-drogue system in later aircraft.

The flying-boom and probe-and-drogue systems eliminated the requirement for crew members to be available on the receiving aircraft: the former migrated the workload to the tanker's boom controller, and the latter to the receiver pilot. Since then, both systems have been widely used, and are presently the only two methods used in regular AAR operations.

1.2 Modern AAR

The two AAR methods in current use are Cobham's probe-and-drogue system and Boeing's flying-boom, both depicted in figure 1.3. The flying-boom system is used by the United States Air Force (USAF), Netherlands, Israel, Turkey and Iran, and the probe-and-drogue system by the United Kingdom (UK) Royal Air Force (RAF), the US military's helicopters, Navy and Marine Corps, and other North Atlantic Treaty Organisation (NATO) allies.

Probe-and-drogue systems tend to be simpler and more compact than the flying boom, and multiple hoses can be installed on a tanker in order to refuel several aircraft simultaneously. Because the drogue is passive, and

is subject to disturbance due to atmospheric turbulence, the tanker's wake, and the receiver's bow wave, the receiver pilot must expend control effort to counter these in order to capture the drogue.

In flying-boom refuelling, the receiver pilot takes up formation below and behind the tanker. The boom has 'ruddervators' with which the boom operator controls the boom to line it up with the receiver's receptacle, then extends it to make contact. The boom method can provide faster fuel transfer rates, but the boom's design adds size, weight, and complexity to the system, and only one aircraft can be refuelled at any time. Receivers equipped with probes can be refuelled from a flying-boom tanker via the use of a boom-drogue adapter, but the converse is not possible.

Principal features and differences between the two methods are summarised in table 1.1. Bolkcom and Klaus [3] detail further considerations from a USAF perspective.

Table 1.1: Comparison of AAR systems.

Probe-and-drogue	Flying-boom
Simple, light and compact	Increased size, weight and cost
Can refuel multiple receivers simultaneously	Can only refuel a single aircraft at once
Passively stabilised	Actively controlled via ruddervators
Cannot refuel receptacle-equipped receivers	Can use boom-drogue adapter to refuel probe-equipped receivers
Can refuel helicopters using low-speed drogue	Cannot refuel helicopters
Control effort largely expended by receiver pilot	Workload shared between boom operator and receiver pilot

1.3 Demand for Autonomous AAR

The proliferation of High Altitude, Long Endurance (HALE) Unmanned Aircraft System (UAS) missions in the defence sector has led to demand for AAAR capabilities similar to those available to manned aircraft, with US defence agencies initially targeting the capability for 2010-2015 [4]. AAAR would enhance UAS capabilities in surveillance, aerial search and rescue, and for applications such as airborne communication relays. It could provide fuel and cost savings via low-fuel take-off as used by Alan Cobham (described in section 1.1) and proposed elsewhere [5], and provide the ability to fly longer routes or sorties with smaller aircraft. Additionally, manual AAR is not without risk. AAAR could increase safety, limiting incidents caused by pilot fatigue, inexperience or misjudgement.

The drive for a reduction in the environmental impact of civil aviation is also a motivator for AAAR. In 2001 the Advisory Council for Aviation Research and Innovation in Europe (ACARE) presented their *Vision for 2020* [6], calling for a 50% cut in CO_2 emissions per passenger kilometre, and 2011's *Flightpath 2050* advocated for a 75% reduction [7]. Bennington and Visser [8] argue that a significant proportion of this can be achieved through civil adoption of AAR and Nangia [9–12] suggests that civil AAR can provide benefits "an order of magnitude greater than, and in addition to, those achieved by current technology evolution".

AAR has advantages beyond straightforward fuel saving, which can also be achieved via multi-stage 'hopping' flights, including potential noise reduction and engine rating benefits. A multi-strategy approach including hopping, formation flight (for drag reduction) and AAR may be an advantageous combination [9].

AAR provides a potential avenue to a step-change in civil aviation emissions, but safety is obviously of prime concern. If automated systems can provide the necessary level of safety assurance then these benefits could be realised across the civil sector, in addition to the defence applications detailed above.

Further to this, the relative positioning requirements of formation flight are similar to those of AAR, and developments in this field might enable additional fuel consumption reduction through formation flight [13–15].

1.4 Challenges

Until recently both probe-and-drogue and flying-boom AAR systems have only been employed in manned flight, and automation presents interesting challenges in the areas of control, sensing, and decision making that must be addressed. AAR involves dynamic flight in close proximity to other aircraft, and automation of this is a topic of ongoing research that, amongst other aspects, entails integration of high-bandwidth sensors with control systems that provide safety assurance against a wide range of hazards. Risks are significant, and the cost of mistakes can be catastrophic, particularly when manned aircraft are working in proximity to other manned or unmanned systems. Nalepka and Hinchman present an overview of the drivers and challenges associated with AAAR [16], summarising them as:

- the ability to "see near" in order to operate in close proximity[3];
- collision avoidance;
- command and control, including response to human operator commands;
- integration – minimising modification requirements to existing systems;
- real-world constraints including weather, day/night conditions and communication.

1.5 Novel architectures for AAAR control systems

AAAR is under current investigation in simulation and in limited flight testing by a number of research groups around the world. Current work is reviewed in more depth in chapter 2, but existing trials and proposed solutions for probe-and-drogue automation focus on a Leader/Follower (L/F) configuration, requiring the receiver aircraft to rendezvous with the tanker and track the passive, aerodynamically stabilised drogue, which is subject to atmospheric disturbances and tanker- and receiver-induced effects.

[3]Nalepka and Hinchman do not specify dimensions here, stating only that "it is critical for the UAV to know, with a high level of accuracy, where it is located relative to the tanker aircraft...to enable the UAV to safely rendezvous and maintain position with the tanker".

Whilst this class of solution is relatively straightforward to implement, and to verify in terms of stability and robustness, the full capabilities of the systems involved are underutilised [17]. The tanker is usually significantly less manoeuvrable than the receiver, but the refuelling system has its own degrees of freedom that are potentially controllable. For example the drogue can be stabilised via canopy manipulation [18] or other actuation methods – this concept is investigated, multiple approaches are reviewed, and a representative actuation envelope is developed in chapter 4.

1.5.1 Increasing capture effectiveness

Stabilisation should facilitate capture in a L/F configuration, and if an actuated drogue can be extended beyond stabilisation to permit active control, then further improvement in capture effectiveness may be achievable. A cyclic approach, with a controllable drogue's systems working alongside the receiver aircraft to facilitate capture, is more challenging to design and optimise but could improve capture time and success rate, permit operation in increasingly adverse conditions, and reduce the risk of incidents such as spokes (where the probe contacts the drogue at an offset angle or position) and hose whip (where the hose becomes slack leading to violent oscillations).

1.6 Definitions

Previous work involving the coupling of control systems on two or more vehicles has been labelled variously as 'cyclic', 'cooperative', 'collaborative' and 'intimate' control, amongst other overlapping terms. Some terms have existing usage in parallel fields, e.g. 'collaborative' often implies human-machine interaction.

There are existing fields of control research that are drawn on in chapter 2, including significant work in satellite formation keeping [19] and Automated Highway Systems (AHSs) [20].

Cyclic control denotes control methods in which two or more controlled bodies are coupled and share a common goal. In this thesis, two cyclic control methods are investigated:

- **Common-target-point Control (CC):** a cyclic control architecture using a common-target-point approach, detailed in chapter 6.

- **Intimate Control (IC):** a cyclic control architecture using a Multiple-Input Multiple-Output (MIMO) approach, detailed in chapter 7.

1.7 Thesis context

The work described in this thesis was conducted at the University of Bristol (UoB), in partnership with Cobham plc, as part of the ASTRAEA programme.

1.7.1 ASTRAEA

Autonomous Systems Technology Related Airborne Evaluation & Assessment (ASTRAEA) is:

> *"a UK industry-led consortium focusing on the technologies, systems, facilities, procedures and regulations that will allow autonomous vehicles to operate safely and routinely in civil airspace over the United Kingdom"*

which aims:

> *"to enable the routine use of UAS in all classes of airspace without the need for restrictive or specialised conditions of operation. This will be achieved through the coordinated development and demonstration of key technologies and operating procedures required to open up the airspace to UAS"* [21].

The £62 million programme was led by a consortium of seven companies: AOS, BAE Systems, Airbus Defence & Space, Cobham plc, QinetiQ, Rolls-Royce and Thales; and consists of two projects:

- **Separation Assurance & Control:** the particular technologies required to control the flying vehicle in the airspace from the ground control station; the spectrum, security and integrity of the communication system; and the vehicle's sense and avoid sensor system.
- **Autonomy & Decision Making:** providing the intelligence in the vehicle through a variable autonomy system that shares decision making for the mission and contingency management with the human operator.

The first phase, ASTRAEA I, took place from 2006 to 2008, and the second, ASTRAEA II, from 2009 to 2013. Successes of the programme include outputs from UoB and other research groups, and an autonomous flight through shared civil airspace [22, 23].

1.7.2 Cobham plc

"Cobham Mission Systems provides safety and survival systems for extreme environments, nose-to-tail refuelling systems and wing-tip to wing-tip mission systems for fast jets, transport aircraft and rotorcraft, and provides remote controlled robots and fully equipped bomb disposal vehicles for homeland security and military applications" [24].

Cobham's refuelling work focuses on probe-and-drogue systems, thus the work in this thesis is targeted at this configuration rather than boom-receptacle systems.

1.7.3 ASTRAEA at the University of Bristol

As part of the ASTRAEA programme, Cobham commissioned the University of Bristol to investigate sensing and control systems for probe-drogue AAAR. The work described in this thesis was undertaken within a research group led by Principal Investigator Dr. Tom Richardson, with two Research Assistants and two Research Postgraduates, inclusive of this author.

Objectives for the project included:

1. Development of a high-fidelity probe-drogue AAAR simulation environment;
2. Construction of a Relative Motion Robotic (RMR) facility for real-time, full-scale replication of aircraft and refuelling system motion;
3. Use of these virtual and hybrid environments to develop and evaluate control methodologies for rendezvous and capture;
4. Evaluation of real sensors in the hybrid testing environment.

Specific contributions to these by this author are detailed in section 1.9.

The integration of the real-world RMR facility to the project raises this work to a higher Technology Readiness Level (TRL) [25] than is usual in an academic environment.

Figure 1.4: Relative Motion Robotic facility.

1.7.4 Relative Motion Robotic simulation

As part of the collaboration between UoB and Cobham, analysis and verification of real-world sensing systems was desired, along with the verification of control architectures at a high TRL. A thirteen-Degrees of Freedom (DoF) relative motion facility was commissioned to support the design, testing, and validation of measurement systems and autonomous control algorithms through Hardware-in-the-Loop (HIL) simulation.

The RMR facility, shown in figure 1.4, consists of two 6-DoF robotic arms, one mounted on a linear track (which adds the thirteenth DoF. A real-time platform handles the control of the manipulators in synchronisation with streamed data generated by simulated kinematics. A 'synthetic environment' consisting of simulated aircraft, atmosphere, refuelling hardware and control systems, feeds kinematic data to the arms, and feedback is provided via position measurements from proximity and vision-based sensors. Work was conducted to develop a real-time simulation capability and implement data packaging and delay compensation to provide as high-fidelity an environment as possible [26, 27].

Further description of the RMR facility is contained in chapter 3.

1.8 Thesis aim

In performing this research as part of a five-person research group the author has contributed to each of the objectives outlined above. The primary aim for this thesis fits within the third objective.

> **This thesis aims to assess the scope for improvement in capture performance, against a baseline 'leader-follower' control architecture, in probe-drogue Autonomous Air-to-Air Refuelling, by harnessing additional degrees of freedom available in the tanker/ refuelling hardware/ receiver system.**

For this work 'capture performance' is defined as the rate of successful drogue capture in multiple simulations with randomly varying atmospheric turbulence, detailed in section 3.5.5. Work in this thesis draws upon, and is relevant to, related fields which are covered in chapter 2.

There are other challenges and areas of research associated with the wider AAAR problem, including addressing the bow-wave problem via predictive control, which was assessed by colleagues in parallel to this work [28].

1.9 Summary of contributions

Work detailed in this thesis was undertaken by the author as a member of the ASTRAEA research group at the University of Bristol. Work done in collaboration with colleagues is described as such where appropriate.

The group's work is detailed in project deliverables submitted to Cobham plc, and in a number of conference and journal papers. Elements of these works are included in this thesis.

In summary, this author's contributions to the field include:

- As part of team:
  - Development of AAAR Simulation Environment (SE)
  - Development of HIL RMR facility
- Solely author's work:

  - Development and evaluation of a Common-target-point Control approach for Probe-and-Drogue AAAR.
  - Extension of Common-target-point Control method via a scheduled gain approach
  - Development and evaluation of an Intimate Control approach for Probe-and-Drogue AAAR
  - Assessment of potential benefit achievable through harnessing additional Degrees of Freedom in Probe-and-Drogue AAAR.

1.10 Associated publications and documents

Peer-reviewed submissions (fully referenced in thesis back matter):

- As first author:
  - Steve Bullock, Peter Thomas, Ujjar Bhandari, and Thomas Richardson. Collaborative Control Methods for Automated Air-to-Air Refuelling. *AIAA Guidance, Navigation, and Control Conference*, 2012 [**Bullock2012a**]
- As co-author:
  - Thomas S Richardson, Jonathan L du Bois, Steve Bullock, and Ujjar Bhandari. Implementation of a Relative Motion Robotic Rig for Hardware in the Loop Simulation of Automated Air-to-Air Refuelling. *26th Bristol International International UAV Systems Conference*, 2011 [29]
  - Jonathan L du Bois, Peter Newell, Steve Bullock, Peter R Thomas and Thomas S Richardson. Vision Based Closed-Loop Control System for Satellite Rendezvous With Model-in-the-Loop Validation and Testing, *23rd International Symposium on Space Flight Dynamics*, 2012 [30]
  - Jonathan L du Bois, Peter R Thomas, Steve Bullock, Ujjar Bhandari and Thomas S Richardson. Control Methodologies for Relative Motion Reproduction in a Robotic Hybrid Test Simulation of Aerial Refuelling. *AIAA Guidance, Navigation, and Control Conference*, 2012 [27]

  - Ujjar Bhandari, Peter R Thomas, Steve Bullock, and Thomas S Richardson. Bow Wave Effect in Probe and Drogue Aerial Refuelling. *AIAA Guidance, Navigation, and Control Conference*, 2013 [31]
  - Peter R Thomas, Ujjar Bhandari, Steve Bullock, Thomas S. Richardson, and Jonathan Luke du Bois. Advances in air to air refuelling. *Progress in Aerospace Sciences* journal, 2014 [32]
  - Peter R. Thomas, Steve Bullock, Thomas S. Richardson, and James F. Whidborne. Collaborative Control in a Flying-Boom Aerial Refueling Simulation. *Journal of Guidance, Control, and Dynamics*, 2015 [33]

- Planned submissions:
  - Common-target control for probe-drogue AAAR: work from the first half of chapter 6, building upon the 2015 common-target control paper and detailing the application of the technique to probe-drogue refuelling.
  - common-target control with scheduled gain for probe-drogue AAAR: work from the second half of chapter 6 extending the common-target controller using a scheduled gain approach.
  - Intimate control for AAAR: work from chapter 7 applying a MIMO approach to the AAAR scenario.

Deliverables to Cobham plc (in chronological order):

- D2.3.37 part 1: *Theoretical Comparison of Intimate Control Techniques*, 2011. Initial literature review and investigation of control techniques.
- D2.3.34: *Drogue Stabilisation*, 2012. Modelling and control of hose and drogue model, integration into ASTRAEA Simulation Environment.
- D2.3.38: *Application of Intimate Control*, 2012. Cyclic control methods applied to ASTRAEA Simulation Environment.
- D2.3.34 addendum: *Drogue Stabilisation: Recommendations*, 2012. Review and tradeoff study of drogue actuation and control.

- D2.3.37 part 2: *Theoretical Comparison of Intimate Control Techniques*, 2013. Systematic comparison of selected cyclic control methods.

1.11 Thesis outline

- **Chapter 2: Literature review** - presents a summary of works related to investigation, simulation and control of AAR and AAAR.
- **Chapter 3: Simulation environment** - describes models used to investigate drogue control and AAAR control systems.
- **Chapter 4: Drogue control** - investigates the feasibility of controlling a refuelling drogue and develops a stabilisation system.
- **Chapter 5: Cooperative control methods** - reviews a range of architectures that could be employed to take advantage of the additional degrees of freedom presented by a controlled drogue.
- **Chapter 6: Cooperative control** - replicates a a common-target-point method previously applied to boom-receptacle refuelling, applies it to a probe-drogue system, and extends it using a scheduled gain approach.
- **Chapter 7: Intimate control** - uses a MIMO optimisation method to trial an alternative approach that couples receiver and drogue at a deeper level.
- **Chapter 8: Conclusions** - compares and contrasts cooperative control approaches and summarises findings and suggestions for future work.

Chapter 2

Literature review

As detailed in section 1.3 there is demand for AAAR in defence and civil applications. This chapter summarises current progress in the field, with particular attention on works relevant to the development of an AAAR simulation environment and possible novel control architectures suggested in section 1.5, and weighted towards the contributions this author made to the development of the RMR SE.

The review is structured as follows:

- **Justification for AAAR:** there are a range of arguments for the deployment of AAR in defence and civil aviation. Section 2.1 expands on the initial summary given in section 1.3.
- **Flight studies:** Section 2.2 reviews work that could be considered the 'closest to market', having been tested on flight hardware and therefore classified at a high TRL.
- **Modelling:** a summary of works modelling key components of AAR and AAAR systems – namely aircraft, atmosphere, and refuelling hardware – are reviewed in section 2.3.
- **Sensing:** awareness of relative positions of tanker, receiver and drogue are of critical importance in AAAR. Section 2.4 summarises relevant studies of sensor configurations.

A related survey was conducted by Mao and Eke in 2008 [34], and more recently by UoB's ASTRAEA group [32], to which this author contributed

significantly. Sections of the latter publication that are primarily this author's work appear in this chapter.

Simulation and multi-agent control literature is addressed in chapters 3 and 5.

2.1 Justification for AAAR

2.1.1 Defence

Unmanned vehicles are increasingly prevalent in the defence sector, expanding their initial reconnaissance-only role to strike, force protection, and signals collection. There are numerous mission scenarios that could benefit from range or endurance extension, and adding AAAR capabilities to UAS is of interest to forces around the world. In their *Unmanned Aircraft Systems Roadmap* [4], the US Department of Defense (DoD) initially set a target of 2010-2015 for in-service availability.

Any HALE mission, e.g. reconnaissance or signals collection, could benefit from increased endurance, leading to savings in the number and size of platforms required for any given mission. Many long-distance missions are currently flown by manned pilots, with aircraft taking off in home or friendly bases, and refuelling en-route to their objective. The duration of these sorties can lead to pilot fatigue and replacing them with unmanned or autonomous systems could be desirable.

Manned AAR is also a risky activity – aircraft rarely fly in such close proximity for any other reason – and requires significant pilot skill and experience, creating a large training burden. If AAAR can increase the safety and efficiency of manned or unmanned refuelling, there is a strong case for it.

2.1.2 Civil

Civil aviation has boomed in recent years, and its associated environmental impact has therefore increased. The Advisory Council for Aviation Research and Innovation in Europe (ACARE)'s *Vision for 2020* [6], calls for a 50% cut in CO_2 emissions per passenger kilometre, and *Flightpath 2050* [7] increases this to an ambitious 75% reduction. The industry is reducing emissions via countless 'conventional' approaches, including improvements in propulsion,

aerodynamics, materials, structural design and routing, however these are all incremental improvements. The ACARE goals require a step-change in fuel use.

In a series of publications, Nangia [9–12] suggests that civil AAR can provide benefits "an order of magnitude greater than, and in addition to, those achieved by current technology evolution". He suggests that "overall savings, including the fuel used during the tanker missions, would be of the order of 30-40% fuel and 35-40% financial" if smaller, greener aircraft of around 3,000 nm range are used on longer routes through the use of AAR. This is largely due to the compound effect of increased fuel load, for example a 6,000 nm flight with a 250 passenger load burns around three times the fuel of a similar 3,000 nm flight due to increased wing area, structure, landing gear etc. that are required to carry the additional fuel. More fuel requires a bigger aircraft, which requires more fuel, and so on.

In addition to the potential fuel savings, Nangia details a wide range of other advantages that civil AAR could confer, including:

- increased use of regional airports: if smaller aircraft are flying longer routes there will be more choice in destination and load on large hubs will be reduced;
- efficiencies in scheduling and maintenance: if an entire fleet can be of similarly-sized aircraft operating over a range of distances, logistical efficiencies can be found;
- reduced noise, safer takeoff, longer airframe life: with low fuel load for takeoff, engine requirements are reduced and the aircraft can operate further from the edges of its performance envelope.

Nangia sets out a roadmap to implementation, from further studies into economic gains, through safety assurance and proving exercises, to initial commercial use for cargo, culminating in passenger airline adoption and the development of a global tanker network.

Bennington and Visser [8] perform simulated missions with a 747-400 tanker for three different sized aircraft (a 747-400, a 777-300, and an A318), investigating ideas originally proposed by Alan Cobham (described in section 1.1) and reiterated elsewhere [5]. They determine that if refuelling points are at optimum distances, AAR can provide an 88-111% improvement in

payload capability. They identify additional benefits as "increased revenue to both the manufacturers and the airline operators, in the form of more product options, more revenue flight hours, increased airframe life, and the possibility for improved takeoff performance and noise reduction", following their optimisation study with a convincing analysis of the economic factors involved, and detailing a range of implementation issues including feasibility, systems and safety.

AAR provides a potential avenue to a step-change in civil aviation emissions, but safety is obviously of prime concern. If automated systems can provide the necessary level of assurance then these benefits could be realised across the civil sector.

The rendezvous, positioning, and tracking challenges that must be addressed for AAAR to be achievable are similar to those in the related field of fuel-saving through formation flight, and synergies with this evolving field may be found [13–15, 35].

2.2 Flight testing

The use of full-scale airframes and refuelling hardware in-flight is costly and presents a certain amount of risk, but it can be an effective method of research, and is certainly a necessary step in taking any AAAR solution to production.

Hansen, Murray and Campos detail 'The NASA Dryden Flight Test Approach to an Aerial Refueling System' [36], aimed at "developing a dynamic hose and drogue system model to support the development of an automated aerial refueling system". They hypothesise a parametric model of static drogue position as:

$$\Delta\text{Pos} = \Delta\text{Pos}_{\text{FltCond}} + \Delta\text{Pos}_{\text{Drogue}} + \Delta\text{Pos}_{\text{Hose}} + \Delta\text{Pos}_{\text{Tanker}} + \Delta\text{Pos}_{\text{Receiver}}$$

with variables:

- **Flight condition:** including airspeed and altitude;
- **Drogue effects:** new drogue/old drogue; high-drag/low-drag;
- **Hose effects:** empty or full of fuel;

Figure 2.1: F/A-18A towing hose and drogue. Image credit: NASA.

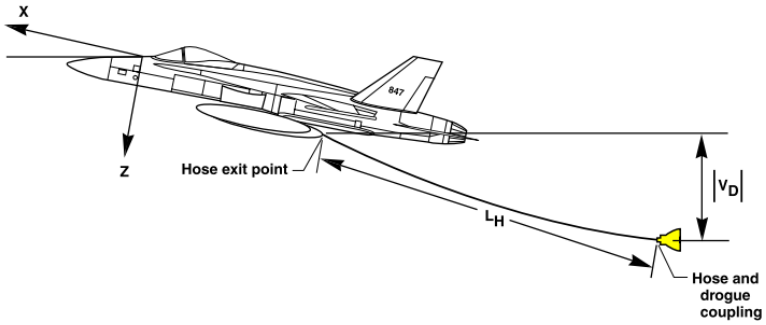

Figure 2.2: Dimensionless Drogue Vertical Position (DDVP), from [36].

- **Tanker effects:** tanker weight, configuration, downwash field (type of tanker);
- **Receiver effects:** closing direction and velocity, upwash field (type of receiver).

Hansen et al. present the results of optical measurements of a hose-and-drogue system trailed from an F/A-18A aircraft, shown in figure 2.1, including the effect of tanker flight conditions on Dimensionless Drogue Vertical Position (DDVP) (figure 2.2), and quasi-static and dynamic receiver influence on the drogue.

If this parametric superposition method provides accurate results it could

permit fast simulation and prediction of drogue position for steady flight conditions, but would be difficult to extend to dynamic scenarios, e.g. use of a controlled drogue, and capture effects. Much of their published data is obfuscated by the omission of scales from some plot axes, but this work may be useful for qualitative model validation.

More recently, flight testing has progressed to actual capture and fuel transfer. The first reported successful drogue capture was achieved in August 2006 [37, 38], in the DARPA-sponsored Autonomous Airborne Refueling Demonstration (AARD) program, also at the NASA Dryden Flight Research Centre (DFRC). Capture took place between a manned, but hands-off, F/A-18 and a Boeing 707-300 tanker (figure 2.3). Nine research flights were flown, moving from relative position keeping trials through to attempting capture on the final flight. A total of six capture attempts were made, two of which were successful and the other four resulting in safe automated recovery.

The sensing and control system included a Global Positioning System (GPS) receiver on the tanker, and GPS and vision systems on the receiver, with a data link between the two aircraft. A blended relative GPS/INS solution was used for primary guidance during approach and departure and for station keeping whilst coupled, and an optical tracker was used to enable capture. The F/A-18 receiver was equipped with a Research Flight Control System which replaced the aircraft's standard control laws. Rendezvous and initial approach were flown manually, and the AARD system was used for capture.

Issues highlighted by these tests include the effect of the receiver's bow wave on the drogue (which is addressed in ASTRAEA work in parallel to this thesis [28]), and the observation that demands from the automated controller were much smoother and smaller than manual pilot input, and would largely fall within the stick dead band for manual flight, therefore controller gains could be increased in future work. Later trials concluded with successful capture in both a refuelling turn and moderate levels of turbulence [39].

The US Air Force Institute of Technology has conducted a range of investigations via flight testing, including into sensor requirements [40] and formation flight control systems [41–43], leading up to a demonstration of autonomous station keeping of a Learjet surrogate Unmanned Air Vehicle (UAV) behind a boom-equipped KC-135R tanker. These held position

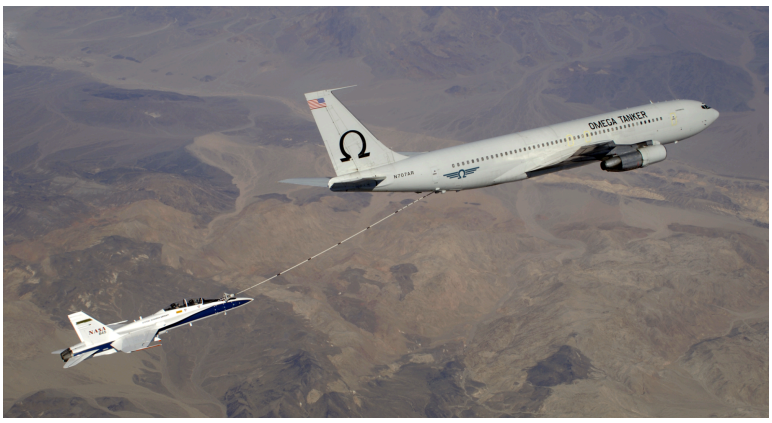

Figure 2.3: NASA Dryden Autonomous Airborne Refueling Demonstration. From [37].

for 30 min whilst the tanker flew two refuelling patterns. Final flights in 2007 demonstrated autonomous transitions between refuelling positions, from rendezvous through contact and breakaway [44]. A second phase to the project was initiated in 2009, with further simulation work and more focus on developing the precision GPS and alternative onboard navigation systems. Flight tests for these systems, again using the surrogate Learjet, were undertaken in 2011, to evaluate upgraded sensors and improved relative navigation and positioning software [45].

A US Navy-based program started in earnest in 2008 to develop and demonstrate an autonomous refuelling capability for Northrop Grumman's X-47B Unmanned Combat Air Vehicle (UCAV), via both boom and drogue refuelling systems [46]. This was part of the Navy's Unmanned Combat Air System Demonstrator (UCAS-D) for aircraft carrier-operated combat UAVs. It also shared some resources and operational aspects with the second phase of the USAFs AAAR project. In order to mature the refuelling technologies alongside the initial autonomous approach and landing tests, the autonomous refuelling systems were developed and tested on the same type of Calspan surrogate Learjet used previously with the AFRL AAR project. Flight tests began in 2008 to demonstrate autonomous closed-loop rendezvous and station keeping, around both the tanker and drogue equipment [44]. Later tests in 2011 and 2012 saw a prototype version of the X47B flight control hardware and software integrated with the surrogate platform. The Learjet, commanded remotely from a ground operator, completed mul-

Figure 2.4: Global Hawk formation flight. Image credit: Northrop Grumman.

tiple refuelling test points around an Omega K-707 tanker [44, 46]. These tests successfully demonstrated fully autonomous control from rendezvous to contact, then breakaway, with the X47B systems. The latest tests in 2013 deployed flight-qualified X-47B hardware into the Learjet, and flight tests were performed with a newly installed refuelling probe.

In 2011 Northrop Grumman demonstrated formation flight of unmanned Proteus and Global Hawk UAS under HALE conditions [47], continuing into 2012 with two Global Hawk aircraft demonstrating drogue tracking (figure 2.4) but concluding in September 2012 without capture, due to reallocation of the aircraft.

The first automated fuel transfer occurred between a K-707 tanker and an X-47B UCAV in April 2015 [48], in a US Navy programme (figure 2.5). The two aircraft communicated via a government-designed refuelling interface system. In the same week (to the excitement of industry media reporters) Daniel Wilson, a PhD student at the University of Sydney, announced that he had achieved rendezvous and capture using Commercial Off-The-Shelf (COTS) airframes and hardware [49]. Both used similar sens-

Figure 2.5: Unmanned Combat Air System fuel transfer. Image credit: US Navy.

ing approaches: the Navy effort "integrates both GPS and infrared imaging to enhance navigational precision and hedge against GPS disruption", and the PhD work uses "a combination of precise measurements from an infrared camera, with GPS and inertial sensors". Wilson's demonstration follows a series of publications detailing development of GPS-based rendezvous and IR-based drogue tracking systems [50–55].

2.2.1 Pilot experience

An investigation by Cobham plc as part of the ASTRAEA project [56] details pilots' experience and techniques in manned AAR. General techniques are described, and specifics for Harrier, Jaguar and Tornado receivers. The report describes 'drogue chasing', where pilots overcompensate for drogue motion, and states that this can be mitigated by focusing on tanker position and anticipating characteristic drogue motion.

Pilot experience is also detailed in an article in *Flying Safety* magazine [57], which outlines a wide range of risks and errors, along with their pilot-induced and physical causes, and ways to avoid them.

Small throttle increases will avoid overshooting the drogue, particularly for larger receivers with significant inertia and additionally a heavy impact between probe and drogue can also lead to 'hose whip' where the hose goes slack and the drogue can undergo violent oscillation. Counter to this, how-

Figure 2.6: COTS hardware-based drogue tracking and capture. Image credit: Daniel Wilson.

ever, a too-slow approach will increase the time that the drogue is affected by the receiver's bow wave, and will increase its movement.

A steady and continuous approach at around 3 knots relative speed is recommended, and if capture fails then the receiver should retreat to the pre-contact position and allow the drogue to settle.

2.3 Modelling

The complete AAAR system consists of a number of elements:

- **aircraft:** tanker and receiver;
- **atmosphere:** including interaction between tanker, receiver and refuelling hardware caused by wake and bow wave effects, in addition to general atmospheric turbulence;
- **refuelling hardware:** for this thesis, only probe and drogue systems are under consideration.

2.3.1 Aircraft

AAAR is likely to be first employed for manned or unmanned aircraft on long-range reconnaissance, signals collection or combat missions. There are a number of aircraft models in current use that fit these profiles.

The Innovative Control Effector (ICE) aircraft is a model of a hypothetical delta-wing tailless aircraft intended to exemplify typical future UCAV designs, which has been released for public research purposes [58–60]. Its configuration introduces control challenges including reduced yaw authority due to its lack of a vertical fin, and complex effects caused by the effects of upstream flaps and spoilers on the downstream effectors.

The Barron Associates Nonlinear Tailless Aircraft Model (BANTAM), proposed in 2005 [61], has a leading edge sweep of 50° and is statically unstable at low angles of attack. It is based on data from wind tunnel tests [62], uses data from the USAF Stability and Control Data Compendium (DATCOM), National Aeronautics and Space Administration (NASA)'s planar vortex lattice code HASC95, and spoiler effect data from the ICE model [59].

Other aircraft models use current conventional manned aircraft as base configurations, including the AV-8B Harrier, F-16, and F/A-18. The F-16 model characterised by Stevens and Lewis [63] is used in several relevant works detailed later in this section [64, 65].

Models are generally formed as 6-DoF rigid-body equations of motion. For configurations with particularly slender wings and/or high-mass additions such as external fuel tanks, aeroelastic effects would be of interest, but for the conventional models used later in this thesis, described in chapter 3, these are unnecessary.

Aerodynamic data is typically stored in lookup tables, and models are often valid over flight conditions that far exceed the moderate incidence and sideslip encountered in refuelling. Data sets can be reduced to increase simulation speed, but care should be taken that models remain applicable for higher gains or increased turbulence.

During fuel transfer, the receiver's mass, centre of mass and inertias will change, significantly more rapidly than the similar changes during standard in-flight fuel burn. Venkataramanan and Dogan [66] developed a model that includes the effect of time-varying mass and inertia properties associated with the fuel transfer, the tanker's vortex induced wind effect and atmospheric turbulence. Mao [67] presents a detailed analysis that includes fuel entry position and velocity. These changes will alter the static margin and trim conditions for level flight, and should be considered if fuel transfer is of relevance. A distributed fuel system has implications for roll control and

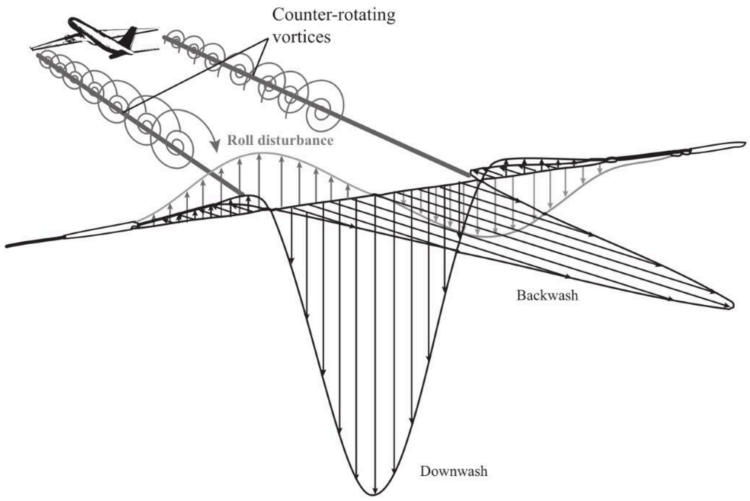

Figure 2.7: Wake effects downstream of tanker [32].

may invalidate frequently made modelling assumptions on aircraft symmetry and negligible products of inertia.

2.3.2 Aerodynamic interactions

Tanker wake and downwash

The tanker's wake influences the receiver, and has a fairly complex structure as shown in figure 2.7, consisting of backwash, downwash and roll disturbance. The receiver creates an upwash, although this influences the tanker to a lesser extent due to the relative sizes of tanker and receiver, and the fact that upwash effects extend over a smaller distance. These create pitching moments on both aircraft. Additionally, the receiver experiences a rolling moment when off-centre due to the tanker's wing vortices and differential downwash between its wings. The effects are complex and challenging to correct for, and increase in magnitude as the receiver approaches the tanker.

Contrasted against standard atmospheric turbulence, which is a stationary stochastic process with a zero mean, the tanker's wake disturbances are nonuniform and temporally invariant for a given location in the wake and a given flight condition of the tanker.

A summary of publications investigating the impact of wake on trailing aircraft is given in a 2014 paper to which this author contributed [32]. This describes early work from Jewell and Stapleford [68] focused on producing a

mathematical model of aircraft wake, Bloy et al. [69–75] and and Rossow et al. [76–82],who move from horseshoe vortex models through to Vortex Lattice Method (VLM), and then to simpler models allowing faster simulation [83]. Additional reviews can be found in works by Mao [34] and Saban [84].

Similar works have investigated effects on UAVs and in AAAR. Blake, Dickes, and Gringas [85, 86] conducted wind tunnel tests with scale models of a Boeing KC-135R tanker and the ICE model. Results indicated that lateral and vertical separation is significant, but relative longitudinal position was not.

Jackson, Tyler and Blake [87] compared VLM and Computational Fluid Dynamics (CFD) approaches with flight test data for the downwash from a KC-135R on the USAF's surrogate Learjet by comparing pitch and angle of attack. VLM predictions were found to disagree with measured results by as much as 50%. CFD calculations were, much closer, with around 10% discrepancy, and suggested that the flying boom might be a significant source of the downwash effect.

In a simulation environment, aerodynamic effects can be calculated on the fly via runtime code, or pre-calculated using lookup tables. Full VLM and CFD approaches are typically too computationally intensive for runtime simulations, however lookup tables are only valid for specific combinations of aircraft and may require large data sets to avoid inaccuracies from interpolation, and looking up total forces and moments ignores effects on aerodynamic states. Airspeed, angle of attack, and sideslip are affected by local air flow, which is not modelled when the turbulence effect is encapsulated only in force and moment increments [88]. This means that for a full physical description of the aircraft, the disturbances must be represented in aerodynamic form.

Tanker downwash induces a nose-down pitching moment on the receiver, which can influence the receiver's approach rate. This increases as tanker-receiver separation decreases. Under-running the tanker is particularly dangerous since the receiver will move out of the region of influence, resulting in a nose-up pitch. At the same time a tanker on altitude hold may instigate a nose-down pitch due to a perceived climb due to the decrease in pressure in the surrounding air [57], potentially leading to collision. These complex dynamic interactions can be mitigated by slow approaches, which introduce these effects in a steady and controlled manner and allow pilots time to react.

Receiver upwash and bow wave

If the receiver size is a significant fraction of that of the tanker, the receiver's upwash can affect the tanker. Although this effect does not usually affect the tanker's wing to a significant extent, the effective angle of attack of its tail is increased, resulting in a nose-down pitch. The receiver's forebody effects do, however, have a significant effect on the airflow over the refuelling hardware, having significant influence on drogue or refuelling boom.

This phenomenon is known as the 'bow wave effect', and is shown in figure 2.8. It has received only modest attention in the literature, with this being mainly on boom systems, but is of common knowledge to receiver pilots, and in is addressed in manned AAR via pilot experience and familiarity with the effect of each specific receiver aircraft.

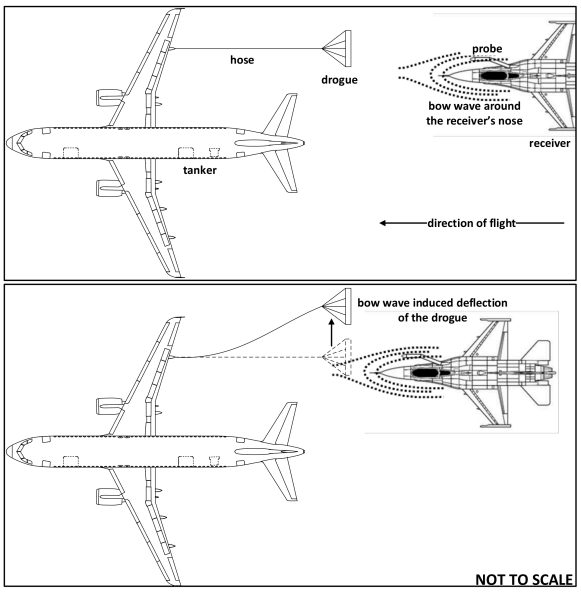

Figure 2.8: Bow wave effect [28].

Iloputaife et al. [89] investigated the effect of upwash of a C-17 receiver on the tanker, which resulted in a long-period oscillation in the relative position leading to Pilot-Induced Oscillation (PIO), caused by upwash influence on the tanker's horizontal stabiliser. This was not predicted in simulation because aerodynamic interactions were not modelled.

Dogan and Blake [90] modelled the effect of the receiver's bow wave on a tanker but obtained poor correlation with CFD results using a VLM-only approach. This led them to supplement this with a volume-induced flow

field, leading to improved reults.

Haag et al. [91] modelled interactions between tanker and large receiver (KC-135 and C-141B) with attention to the bow wave. Using HASC VLM and Euler CFD they compared results against available flight data, with good correlation, although the VLM approach under-predicted bow wave effects. It is suggested that the bow wave effect is largely due to air displacement by the volume of the receiver, rather than the previously-assumed upwash from the receiver's bound vortex.

Ro et al. [92], as part of wider work detailed in section 2.3.3, modelled bow wave effects in their finite-segment hose and drogue simulations, using a CFD approach to predict flow about a generic small-receiver forebody, along with a horseshoe-vortex model for upwash. This compared favourably with flight data.

2.3.3 Refuelling hardware

The hose and drogue system is inherently complex to model since it consists of three parts with disparate dynamics: the drogue, the hose, and the Hose Drum Unit (HDU). The infinite degrees of freedom and nonlinearities inherent in a flexible bending structure make modelling the hose particularly challenging.

A common approach to modelling the hose is to reduce its total length into a series of connected elemental linkages. Work on a 'finite-segment' approach to towed-cable modelling has been conducted since the 1970s when Huston, with various others, used developing computational methods to simulate naval towed systems [93–96]. These methods were then used, again in a naval context, by Kamman (with Huston [97, 98], and others [99]). More recently, Ro and Kamman, applied this approach to the AAR context, developing a hose-drogue model [100, 101] and extending it with a parametric model of drogue aerodynamics [102]. In a later paper they model the contact forces and reel-takeup system for a full capture cycle [103].

Zhu and Meguid [104] note that a hose or cable, and an element of such, is typically idealised as a slender body due to its large ratio of length to diameter. However situations of low cable tension, which occurs in refuelling hoses, can result in large or violent oscillations (e.g. hose whip) that classic cable theory cannot accurately deal with. Its limitations at low tension are attributed to the occurrence of a singularity when the tension disappears

anywhere along the cable, and the omission of bending stiffness. Alleviating the singularity problem can be achieved through the addition of artificial damping, higher order terms and bending stiffness. Unfortunately such a realistic and high-fidelity cable model inevitably results in a complex set of partial differential equations which must usually be solved through iterative numerical methods.

Eichler [105] attempted this in 1978 with a set of linear hyperbolic partial differential equations, however his model was restricted to small perturbations about the hose's natural catenary. Fravolini et al. [106, 107] developed a Finite Element Method (FEM) model, which was used later to formulate their flying boom models [108, 109]. Lagrangian mechanics provides the solution for the position of the linkages and their formulation included the effects of wind forces, however only three straight linkages were used, with the first being rigidly attached to the tanker.

The main difficulties with using FEMs for low-tension cable problems, as stated by Zhu and Meguid [104] are:

- the lack of a simple beam element that can handle curvature together with large displacements and rotations and
- mathematical formulation of generalised flexible beam elements is more complex than for finite difference methods.

Straight beam elements violate continuity conditions for the slope and curvature of a slack cable since the discretisation of the cable results in excessive bending stiffness or membrane locking occurring [110]. Curved elements, on the other hand, yield higher accuracy using coarser meshes but their formulation is not a simple extension of straight beams. These limitations motivated Zhu and Meguid to propose an alternative element, inspired by the concept of coupled consistency displacement fields, and extended its use to the modelling of an aerial refuelling hose [111, 112]. This implementation was verified against experimental data from the free-swinging of a steel cable, and their hose-drogue system demonstrated phenomena such as oscillation due to disturbance at the tow point, and hose whip due to failure of the reel mechanism to take in slack during the coupling process.

Bloy and Khan [113], a series of studies by Vassberg et al. [114–116], and later Ro and Kamman [100, 101] all applied a simpler lumped parameter approach based on multi-body dynamics. The hose is approximated by

straight, elemental linkages which are subject to aerodynamic, gravitational, and internal tension and torsional forces at both of their ends. Equilibrium equations can be written for each hose element, and subsequently propagated along the entirety of the elements. This permits a straightforward Newtonian solution for joint motion, with link tension derived from a constraint on the length of link elements. For the aerodynamic forces on the hose an inclined-cylinder drag method by Hoerner [117] is commonly used, although more modern approaches are available including ESDU methods [118].

The hose models developed at Boeing by Vassberg et al. [114–116] were based on a model previously created in 1993 for modelling the hose whip phenomenon, but with the addition of aerodynamic forces due to the surrounding flow (calculated using a panel method) and the distributed loads due to pressure and skin friction drag. In their first two papers the drag on the drogue was taken as point force acting in the local flow direction before being improved upon in the latter to take into account the unsteady and non-uniform flowfield about the drogue during a coupling event, by basing the drag on the airflow around the basket rim. Further to this, an implementation of the restoring hose bending moments based on simple beam theory, and a representative model for the reel take-up system in the HDU modelled with a second order linear differential equation for a rotating mass with angular acceleration.

Simulations of the hose tension in Vassberg et al.'s papers and then later by Ribbens et al. [119] demonstrated the necessity for the tension control provided by the reel take-up system in order to suppress the hose whip behaviour. Post-contact simulations by Styuart et al. [120] focused on the loads on the refuelling probe during a hose whip, showing that downward motion of the receiver into contact exacerbates hose whip by increasing the hose angle of attack, whilst upward motion into contact can be used to provide the opposite effect. This matches with pilot guidance that flying 'up the line of the hose' makes smooth contact more likely [121].

For their hose model Ro and Kamman added a parametric model of the drogue aerodynamics derived from wind tunnel experiments and CFD simulations [102]. In that study they investigated the drag characteristics of a drogue assembly as a function of its geometric parameters. CFD results were found to agree well with the wind tunnel results, except that the

simulations under-predicted the drag coefficient. This was attributed to a simplified canopy profile image and the software misrepresenting the wake from the drogue and the flow separation.

Hayashibara et al. [122] had difficulty in sizing the mesh for the canopy (an order of magnitude less than the canopy fabric thickness), which led to its exclusion from their 3D simulations, instead relying on simpler 2D flow solutions to provide qualitative results for the lift force on the canopy.

CFD analysis of a high fidelity canopy model remains a challenge. Despite Zhu and Meguid's criticism of straight-element models and the lack of inclusion of bending forces, Ro and Kamman argue for the numerical accuracy of their lumped parameter approach, stating that convergence studies demonstrate that a relatively low-fidelity 20-link model and a time step of 10 ms produce results that are close to higher-fidelity models. They verify their simulations against static and dynamic measured data, including drogue position and drag, hose tension, response to tanker manoeuvre, and atmospheric gusts, obtained from NASA Dryden flight tests [123, 124]. The lack of inclusion of bending stiffness in the model might be seen as detrimental, but Ro and Kamman's validation against flight data suggests this to be an effective and computationally efficient method.

Experimental efforts to develop a flight-validated dynamic hose and drogue model occurred between 2004 and 2005, details of which were published by Hansen et al. [36, 123, 125] on the NASA Dryden Flight Research Centre 'Automated Aerial Refueling' project. This involved a series of flight tests using two NASA F/A-18 aircraft and a conventional hose and drogue system. A quadruplex, time-synchronised video system was used: two cameras at the rear of the tanker aircraft looking towards the receiver, and a further two at the front of the receiver pointed towards the tanker, in order to provide two stereoscopic measurements of the hose and drogue dynamics. Twelve research flights were flown under multiple flight conditions to obtain flight data. In order to aid development of an accurate hose and drogue model, flight test manoeuvres exciting the dynamics of the hose and drogue system were also developed and executed. Results (of a mostly qualitative nature) are presented for the steady-state drogue position with airspeed showing that the drogue position climbs with increased tanker airspeed, following what appears to be a gentle curve. A similar though inverse relationship between drogue location and tanker angle of attack is also iden-

tified. An attempt was also made to characterise the bow wave effect by static mapping of the displacements of the drogue due to the receiver at various grid points, firstly by moving the receiver to each grid point, then via quasi-static, steady-rate sweeps through the grid points. Doing so allowed an 'area of influence' to be established at two flight conditions, which quantified the area in which the proximity of the receiver's nose had a notable influence on the drogue's position. Although the measurements were taken in static conditions they are still indicative given that the approach speeds for a successful capture are relatively low.

For such approach speeds Bloy and Khan [113] equally note that the displacement due to the bow wave of the receiver (in their case a Panavia Tornado) can be approximated to a reasonable accuracy via a static analysis of the hose and drogue's motion. Likewise Vassberg et al. [116] modelled the flowfield around the drogue by superposition of a time-marching flowfield around the receiver onto the flowfield of the tanker. In order to compensate for the induced drogue motion a vertical-plane offset in the starting position for the probe's approach was used such that the drogue would deflect into the approaching probe. Naturally these offsets are highly dependent on both the starting range and the closing speed.

Other test data and analysis from NASA flights published by Vachon et al. [124] inferred drag measurements for a high-drag configuration drogue through variations in engine thrust as the drogue was deployed, at airspeeds between 170 and 250 KIAS. Analysis of the drag polars suggested an inverse linear relationship between the drag and airspeed, and only minor dependence on altitude. Compared to wind tunnel data, the trends generally matched favourably, although the flight measured values were up to 25% lower at the higher end of the airspeed range. Both the spread and magnitude of these errors could be attributed to multiple variations in the experiments: air turbulence, stability of the drogue assembly position, shape of the drogue canopy (sometimes deformed after engagements), and the effect of changes in the airplane trim.

Lastly, it is worth noting that the dynamics of the hose will change during fuel flow. Ng and Tan [126] model a refuelling process with trailing, fuel transfer, and rewind phases, using the Flowmaster commercial CFD package to characterise the fuel-transient behaviour.

2.4 Sensing

An AAAR system must be able to sense relative position of tanker, receiver and refuelling hardware, both for rendezvous and capture, and to ensure a safe process. There are a range of current technologies that can provide this capability, including satellite navigation, machine vision, radar, and electro-optical (laser).

Hague et al. at the USAF Research Lab used simulation and flight tests to establish minimum sensor detection range and sensor field of regard (angular view) requirements for UAV AAAR in 2003 [40]. They identify that the problem is complex, and depends upon aircraft manoeuvrability and other operational criteria. They note that integration with current processes is important, so at present UAVs should approach the tanker in the same manner as manned receivers, but this requirement may be relaxed in future.

2.4.1 GPS

Differential GPS can establish relative position to sub-metre accuracy, and future systems such as the EU's Galileo will provide increased accuracy and precision [127]. Issues with these satellite systems is update frequency, and reliability considerations including selective availability and jamming. Khanafseh and Pervan [128] evaluate the sky blockage caused by the tanker body for a drogue-mounted GPS receiver, and Hansen et al. [36] also point out integration and safety issues. GPS can be augmented with Intertial Navigation System (INS) to provide higher-frequency updates, and to share signals in order to eliminate satellite-switching issues and provide precise corrections [129], but requires data transmission between tanker and receiver.

2.4.2 Machine vision

In recent years vision processing has evolved into a mainstream technology, accessible to all via open-source libraries such as OpenCV [130], and a wide range of proprietary technology is also emerging. In the field of unmanned aviation, there are numerous works that use vision-based sensing for navigation [131, 132], tracking [133], collision avoidance [134], automatic landing [135], and aerial refuelling [136, 137]. Work has been conducted on UoB's

RMR facility utilising the OpenCV library, achieving position estimation at 30 Hz [138].

These systems can be affected by atmospheric conditions such as rain, fog and cloud, and also low lighting. Many techniques also require significant processing capabilities. The task can be made more straightforward if easily-identifiable markers are used.

Non camera-based implementations also exist. Junkins et al. patented a system that uses a position-sensing diode that measures the line of sight to sequentially-illuminated beacons on the target, at up to 100 Hz with low processing requirements. This 'VisNav' system has been used in AAAR studies at Texas A&M University [139]. Pollini et al. follow a similar approach with LEDs on the drogue and an infra-red sensing CCD.

One significant barrier to active-marker approaches is that current hose and drogue systems do not carry power or signals to the drogue. This would require modification to hose and reel systems, and isolation from fuel in the hose would need to be guaranteed, particularly during failed approaches where hose and drogue can be damaged.

Markerless systems often use corner detection algorithms, commonly Harris [140] or Smallest Univalue Segment Assimilating Nucleus (SUSAN) [141]. These were compared by Fravolini et al. [108] and Vendra et al. [109], who determined that the Harris algorithm gave a lower rate of false positives, but required greater computational power. Other approaches such as pattern recognition are generally even more computationally demanding.

Vision is a promising approach due to the wide range of existing work within and outside the field of aviation and formation flight, but processing demands affect measurement frequency and must be considered.

2.4.3 Electro-optical

Laser range-finding systems such as lidar (a portmanteau of 'light' and 'radar') measure reflection times of laser light, and are more tolerant to atmospheric conditions than vision systems and are not affected by issues such as motion blur. Lidar has been used for drogue tracking by Chen and Stettner [142] and tanker detection by Curro [143].

An alternative to lidar is an Electro-Optical Grid Reference System (EOGRS), developed by General Electric for AAR applications. This measures angles between a grid transmitter and detector, and calculates range

from multiple measurements. A data link is required between tanker and receiver. In 2009, trials with an EOGRS-equipped refuelling drogue mounted on a K-707 tanker were found to provide precise motion and position data [144, 145].

2.4.4 Sensor fusion

All of the systems detailed above have advantages and disadvantages, and the strengths of multiple techniques can be combined. For example, GPS is effective at providing relatively coarse, absolute positioning at fairly low frequency, and inertial sensors can provide high frequency relative measurements but suffer from drift. Vision systems work best when provided with an initial estimation of object position and pose.

There are a variety of methods of weighting and fusing information from multiple sources. Measurements can be switched between when most accurate, for example GPS for rendezvous and initial approach, then vision for capture. Fravolini et al. used a distance-based metric for this [106, 107, 146]. Other methods fuse data in a more sophisticated manner. Mammarella et al. [147, 148] used an extended Kalman filter and achieved an order of magnitude improvement in position estimates. Williamson [149] used the same approach with GPS and electro-optical sensors augmenting an INS, achieving sub-10 cm accuracy.

Chapter 3

Simulation environment

This chapter describes the Simulation Environment (SE) developed in order to permit investigation of cyclic control systems for drogue capture later in this work. The systems developed here permit successful L/F AAAR, for which results provide a baseline against which to compare augmented methods in later chapters.

The SE integrates a number of models in order to simulate the complete AAR process, from the receiver joining in formation with the tanker, through approach, capture and fuel transfer, to breakaway and departure. This SE, and variations of it, were used for all UoB ASTRAEA simulations, but the focus of this thesis is on the approach and capture phase – the final ten metres before contact is made between the receiver's probe and the tanker's drogue.

Models and functions include:

- **Receiver:** equations of motion, aerodynamics, engine and Flight Control System (FCS) representing an F-16 fixed-wing aircraft. The F-16 was selected as it is a well-understood model already in use at UoB and will allow development of novel control architectures without the added complexity of the innovative control effectors etc. presented by the ICE and BANTAM models detailed in chapter 2.

- **Tanker:** for the purposes of this study the tanker is assumed significantly less agile than the receiver, thus represented as a moving point. This assumption should be verified or rejected for higher levels of turbulence in future work.

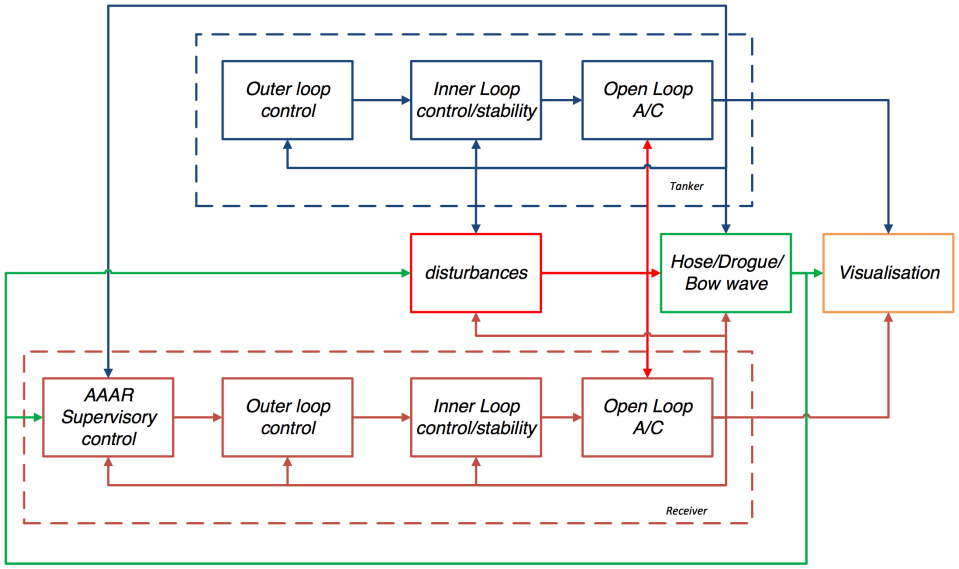

Figure 3.1: Simulation environment architecture

- **Atmosphere:** a standard International Standard Atmosphere (ISA) profile subject to variable Dryden turbulence.
- **Refuelling hardware:** hose and drogue aerodynamics and physics, using a finite-segment approach for the hose.
- **Supervisory logic:** manages the refuelling process in accordance with NATO protocol and determines drogue capture success/failure.
- **Visualisation:** FlightGear-based graphics permit visual monitoring of the process from a range of viewpoints.

This software SE can also integrate with the RMR facility (detailed in section 3.10 to enable real-time HIL replication of aircraft motion and measurement of sensor input, allowing verification of control systems and sensor configuration at a higher TRL than is usual in an academic environment. A high-level overview of the software SE architecture is shown in figure 3.1.

3.1 Software and hardware

The AAAR SE is implemented using MATLAB Simulink, with system configuration detailed in table 3.1, for fully-virtual simulation. It can also be

Table 3.1: Simulation software and hardware configuration

Component	Specification
MATLAB	R2012a 64-bit, v7.14.0.739
Simulink	R2012a v7.9
Solver	ode4 (Runge-Kutta)
Step size	0.01s fixed
Processor	Intel Core i5 650 @ 3.20 GHz
RAM	4 GB
Operating system	Windows 7 Enterprise 64-bit SP1 v6.1.7601

compiled to run on the RMR's real-time National Instruments PXIe hardware, allowing modelled sensor characteristics to be swapped out for real HIL observations. Detail of RMR systems is given in section 3.10.

3.2 AAR process and protocol

Any enhancements to current AAR capabilities will likely be implemented in an incremental fashion – they must fit within existing practices and hardware in use today. Shared practice and protocol is defined in NATO document *ATP-56(B): Air to Air Refuelling* [121].

ATP-56(B) divides the refuelling process for manned receiver and tanker aircraft into seven stages, shown in figure 3.2:

1. **Joining:** Receiver enters the refuelling area by taking a position behind the observation point, attending to the positions and movement of tanker, refuelling equipment, and any other air vehicles.

2. **Observation:** Receiver moves either ahead of the wing line of the tanker in the case of no other refuelling observers, or behind the wing line when other observers are present. Pre-refuelling checks take place.

3. **Moving astern:** Receiver descends below hose level in order to clear the tankers wing vortices, and moves astern of the drogue.

4. **Pre-contact:** Receiver moves directly behind and closer to the drogue. Relative movement between the tanker and receiver is avoided in the pre-contact position hold.

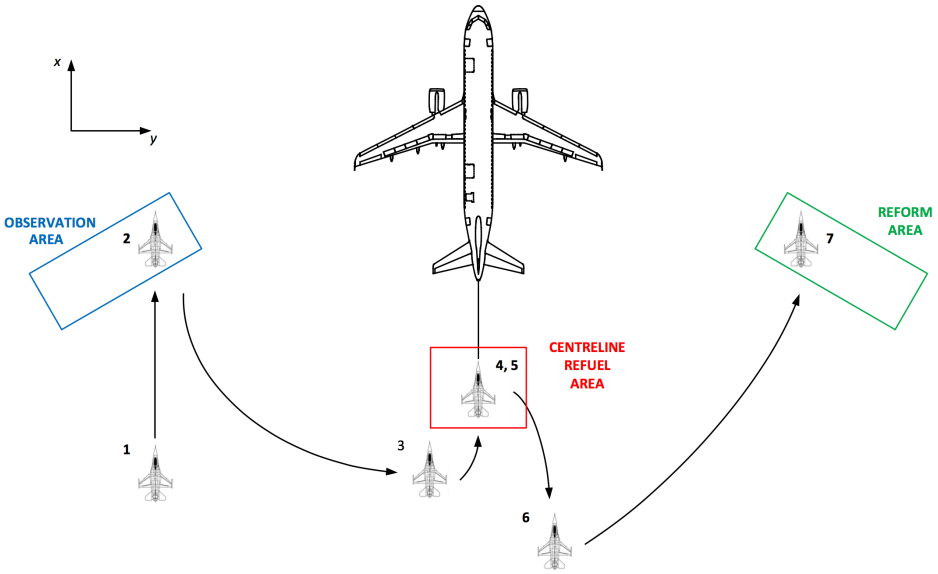

Figure 3.2: Refuelling protocol as per NATO ATP-56(B) [121]

Table 3.2: Receiver target coordinates for refuelling stages. Reference frames as in section 3.3

Stage	Coordinate system	Position /m
Observation	Receiver CG in tanker body axes o^t	(-41, 61, 0)
Moving astern	Receiver CG in tanker body axes o^t	(-33, 10, -8)
Pre-contact	Probe tip in drogue body axes o^d	(-10, 0, 0)
Contact	Probe tip in drogue body axes o^d	(0, 0, 0)

5. **Contact:** Receiver aircraft makes a steady and continuous approach up an imaginary extended line of the hose to make contact with the drogue. The drogue is pushed forwards by the receiver so the hose retracts slightly.

6. **Disconnect:** Following fuel transfer, the receiver retreats to astern position of the tanker.

7. **Reform:** Once cleared from the astern position, receiver moves to a position on the opposite side of the tanker to the observation point.

Positions and reference frames used for relevant stages of the refuelling process are given in table 3.2.

3.3 Reference axes

A number of coordinate systems are used for specific purposes. These are defined here, with some also depicted in figure 3.3. All axes are right-handed unless otherwise stated.

- **Earth-Centered, Earth-Fixed (ECEF)** $o^E(x^E, y^E, z^E)$: originates at the Earth's centre and rotates with the Earth. x^E-axis passes through Greenwich meridian, z^E-axis along Earth's rotational axis.
- **Local Tangent Plane (LTP)** $o^e(x^e, y^e, z^e)$: aligned with a plane tangent to the surface of an ellipsoid model of the Earth. z^e-axis points towards the Earth's centre, making the geodetic latitude angle with the equatorial plane. x^e-axis along tangent plane towards North Pole, thus y^e-axis points east along the plane. Equivalent to local North, East, Down (NED) system.
- **Receiver body axes** $o^r(x^r, y^r, z^r)$: originates at receiver Centre of Gravity (CG), with x^r-axis parallel to fuselage datum line, y^r-axis to receiver's starboard.
- **Probe body axes** $o^p(x^p, y^p, z^p)$: origin at probe tip, x^p along probe centreline, z^p parallel with z^r.
- **Drogue body axes** $o^d(x^d, y^d, z^d)$: origin at centre of drogue connection port.
- **Tanker body axes** $o^t(x^t, y^t, z^t)$: originates at tanker CG, with x^r-axis parallel to fuselage datum line, y^r-axis to tanker's starboard.
- **Tanker navigation axes** $o^n(x^n, y^n, z^n)$: origin at tanker CG, with $x^n y^n$ plane parallel to LTP, but free to rotate about z^n.

Additional axes are used for local derivations e.g. refuelling hose links. These are denoted in relevant sections.

3.4 Receiver model

The AAAR SE contains two aircraft: tanker and receiver, both variations on a base F-16 representation. The General Dynamics F-16 Fighting Falcon

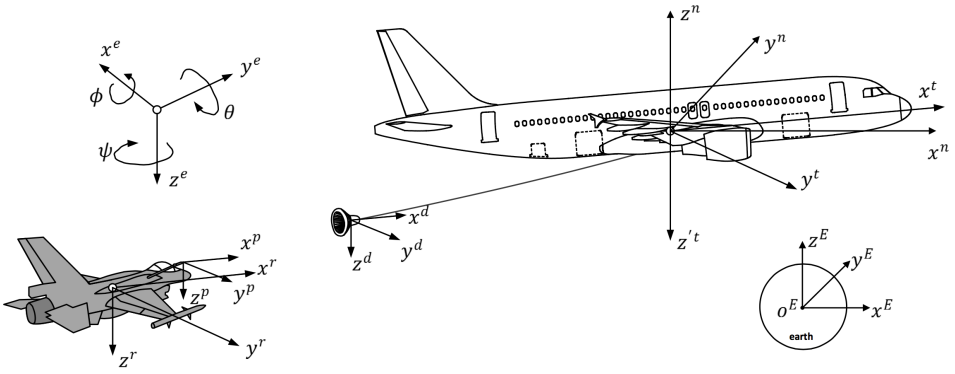

Figure 3.3: Reference axes

was selected as a model for two reasons: it is taken as representative of a typical future UAV/UCAV with an aerial refuelling capability, and there is wide availability of aerodynamic, performance and systems data [63, 150].

The F-16 Fighting Falcon multirole fighter aircraft was developed by General Dynamics (since merged with Lockheed Martin) and introduced in 1978. Originally only able to refuel via the boom-receptacle method, later variants were introduced with additional conformal fuel tanks to increase range, and Cobham, Hindustan Aeronautics Limited (HAL), and Lockheed Martin and Cobham collaborated to incorporate a telescopic probe into the conformal fuel tanks for probe-and-drogue refuelling, shown in figure 3.4.

Figure 3.4: F-16 engaged in probe-and-drogue refuelling. Image credit: USAF.

As of 2010 there were over 4,500 F-16s produced, being used by 26 air

Table 3.3: F-16 characteristics [63].

Parameter	Symbol	Value	Unit
Wing area	S	27.87	m^2
Wing mean chord	c	3.450	m
Fuselage length	l_f	15.06	m
Wing span	b	9.144	m
Mass	m	9,300	kg
Moment of inertia about x^r axis	I_{XX}	12,875	$\mathrm{kg\,m}^2$
Moment of inertia about y^r axis	I_{YY}	75,674	$\mathrm{kg\,m}^2$
Moment of inertia about z^r axis	I_{ZZ}	85,552	$\mathrm{kg\,m}^2$
Product of inertia about x^r-z^r axes	I_{XZ}	1,331	$\mathrm{kg\,m}^2$

forces across the globe. The USAF has also converted a number of older aircraft into unmanned target drones.

The flight dynamics model used in the AAAR SE is based on that from Stevens and Lewis' text *Aircraft Control and Simulation* [63]. They presented a reduced version of a full-range nonlinear model originally published by NASA in 1979 [150].

The model used here is a nonlinear, rigid body representation, valid for aerodynamic range of incidence $\alpha \in [-10°, 45°]$ and sideslip $\beta \in [-30°, 30°]$, which is presumed to be sufficient for all reasonable manoeuvres during AAR. Conditional limits are implemented in the SE to ensure that these values are not exceeded. Key characteristics of the F-16 are detailed in table 3.3.

Whilst future UAV/UCAVs will likely have differing characteristics to this model, it is used here as it is well-characterised, and its flight envelope is likely conservative compared to future vehicles.

Characteristics, equations of motion, trim and linearisation of the F-16 model can be found in appendix A.

3.5 Control system

The control system developed here enables successful L/F drogue capture. Results provide a baseline against which to compare augmented methods in later chapters.

The overall architecture of the AAAR SE is outlined in figure 3.1. The receiver's control system, shown in figure 3.5, consists of an inner-loop sta-

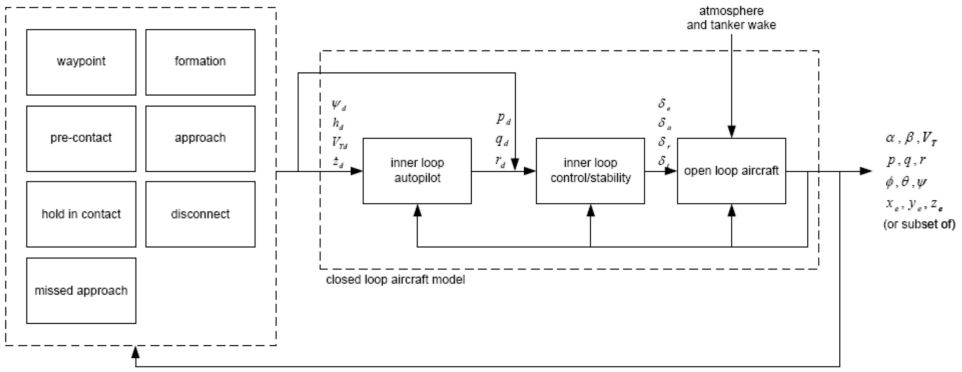

Figure 3.5: F-16 control architecture

bility augmentation and tracking system, and an autopilot. Further detail on these subsystems is given in subsequent sections.

The autopilot acts on demands given by the supervisory controller, which has a number of modes for the various stages in the refuelling process.

3.5.1 Supervisory controller

The AAAR supervisory controller measures position errors between receiver and tanker, and probe and drogue, and generates state demands $V, \dot{h}, \psi$ for the inner-loop autopilot. It also monitors success and failure of drogue capture, detailed in section 3.5.5.

3.5.2 Inner-loop control and stability

An infinite-horizon, continuous-time Linear Quadratic Regulator (LQR) approach is used to establish a state-feedback controller to be used in the inner loop. LQR is an optimal control method suitable for Single-Input Single-Output (SISO) and MIMO applications, that minimises a quadratic cost function J. The cost function contains two weighting matrices, Q and R, which are manually defined.

Alternative design approaches include manual methods such as pole-placement, which allow more direct manipulation of controller behaviour, however the wider ASTRAEA work involved evaluation of multiple aircraft platforms and the semi-automated LQR approach was beneficial in minimising time taken to design each controller, and ensuring consistency in the optimisation process.

A summary of the LQR approach is given here, based on the detailed description given by Stevens and Lewis [63].

LQR optimisation

Optimal control methods aim to generate a controller that meets given optimality criteria. Mathematically, this generally involves a cost function or performance index containing state and/or control variables that must be maximised or minimised.

For a system described by linear differential equations (such as the F-16 model detailed above), with a cost function taking the form of a quadratic equation, the resulting problem is described as Linear Quadratic (LQ), and the feedback controller, or regulator, as a LQR.

The benefits of the LQR approach (as with other H_∞ methods) are that once the cost function weightings have been selected, controller gains are algorithmically generated and closed-loop stability is usually guaranteed. Additionally, LQR achieves an infinite gain margin and guarantees phase margin $\geq 60°$, leading to robustness against sensor and controller delays. The formulation and process are described in more detail by Williams and Lawrence [151].

Problem formulation

The linearised F-16 model obtained in section 3.4 is of the form

$$\dot{\mathbf{x}} = \mathbf{A}\mathbf{x} + \mathbf{B}\mathbf{u} \tag{3.1}$$

with states $\mathbf{x} \in \mathbb{R}^n$ and control inputs $\mathbf{u} \in \mathbb{R}^m$. The state-feedback law is

$$\mathbf{u} = -\mathbf{K}\mathbf{x} \tag{3.2}$$

where $\mathbf{K} \in \mathbb{R}^{m \times n}$ is a matrix of constant feedback gains

The objective of this state regulation process is to drive non-zero state values to zero, using control inputs generated via the feedback law, with desirable time-response characteristics. To determine optimality, a cost function is used:

$$J = \frac{1}{2}\int_0^\infty (\mathbf{x}^\top \mathbf{Q}\mathbf{x} + \mathbf{u}^\top \mathbf{R}\mathbf{u})\mathrm{d}t \tag{3.3}$$

This ensures that for a minimum positive-finite value of J, the integrand becomes zero for very large t.

$\mathbf{Q} \in \mathbb{R}^{n \times n}$ and $\mathbf{R} \in \mathbb{R}^{m \times m}$, $\mathbf{R} \succ 0$, $\mathbf{Q} = \mathbf{Q}^\top \succeq 0$ are square positive weighting matrices. Values can be chosen to trade off minimal values and fast transient response of states against control effort.

By substituting the feedback control law given in equation 3.2 into the system in equation 3.1, the closed loop system is

$$\dot{\mathbf{x}} = (\mathbf{A} - \mathbf{BK})\mathbf{x} = \mathbf{A}_{cl}\mathbf{x} \tag{3.4}$$

Using equation 3.2 the cost function may also be expressed as

$$J = \frac{1}{2}\int_0^\infty \mathbf{x}^\top(\mathbf{Q} + \mathbf{K}^\top\mathbf{RK})\mathbf{x}\mathrm{d}t \tag{3.5}$$

and the task is now to select $\mathbf{K}$ such that J is minimised, subject to the constraints of equation 3.4. It can be shown that the optimal feedback matrix that minimises J is given by

$$\mathbf{K} = -\mathbf{R}^{-1}\mathbf{B}^\top\mathbf{P} \tag{3.6}$$

where the constant, symmetric, positive, definite matrix $\mathbf{P}$ is the solution to the algebraic Ricatti equation

$$\mathbf{A}^\top\mathbf{P} + \mathbf{PA} + \mathbf{Q} - \mathbf{PBR}^{-1}\mathbf{B}^\top\mathbf{P} = 0 \tag{3.7}$$

This produces a solution satisfying the Lyapunov stability criteria. The LQ method guarantees stable and optimal (against selected weighting matrices) closed-loop control, providing control gains $\mathbf{K}$ as long as:

- System $(\mathbf{A}, \mathbf{B})$ is stabilisable, i.e. there exists a state feedback gain matrix $\mathbf{K}$ for which all eigenvalues of $\mathbf{ABK}$ have strictly negative real part.
- Pair $(\mathbf{A}, \sqrt{\mathbf{Q}})$ is detectable, i.e. there exists an observer gain matrix $\mathbf{L}$ for which all eigenvalues of $\mathbf{AL}\sqrt{\mathbf{Q}}$ have strictly negative real part.
- $\mathbf{R}$ is positive definite, i.e. $\mathbf{R} \succ 0$. This means that all control inputs need to be weighted.

- $\mathbf{Q}$ is positive semi-definite and symmetric, i.e. $\mathbf{Q} = \mathbf{Q}^\top \succeq 0$. This means that all unstable states need to be weighted.

Therefore the challenge here is in selecting appropriate $\mathbf{Q}$ and $\mathbf{R}$ matrices.

Selection of weighting matrices

Values in matrices $\mathbf{Q}$ and $\mathbf{R}$ establish the costs associated with state and control input errors, however the relative magnitudes of the resulting state and input parameters are not directly related to the matrix values, as the open-loop system's dynamics are not accounted for.

Guidance on selecting $\mathbf{Q}$ and $\mathbf{R}$ to limit maximum deviations is given by Bryson and Ho [152]. They suggest (utilising their notation, at the expense of re-use of q and r):

$$\begin{aligned} \mathbf{Q}_M &= \mathrm{diag}\{q_i\}, & \mathbf{R}_M &= \mathrm{diag}\{r_i\} \\ q_i &= \frac{1}{x_{i_M}^2}, & r_i &= \frac{1}{u_{i_M}^2} \end{aligned} \tag{3.8}$$

where the maximum permissible deviation in state x_i is x_{i_M}, and similarly for u_i. Thus an increase in the maximum permissible deviation of a parameter causes a decrease in its weighting.

Selection of $\mathbf{Q}$ can also be conducted using a performance output [63]

$$\mathbf{z} = \mathbf{H}\mathbf{x} \tag{3.9}$$

which consists of states that should be minimised in the closed-loop system. Performance output matrix $\mathbf{H}$ relates performance outputs to states. The outputs are minimised using cost function:

$$J = \frac{1}{2}\int_0^\infty (\mathbf{z}^\top\mathbf{z} + \mathbf{u}^\top\mathbf{R}\mathbf{u})\mathrm{d}t = \frac{1}{2}\int_0^\infty (\mathbf{x}^\top\mathbf{H}^\top\mathbf{H}\mathbf{x} + \mathbf{u}^\top\mathbf{R}\mathbf{u})\mathrm{d}t \tag{3.10}$$

which means $\mathbf{Q} = \mathbf{H}^\top\mathbf{H}$.

The maximum-deviation method and the performance-output approach can be combined to give cost function

$$J = \frac{1}{2}\int_0^\infty (\mathbf{z}^\top\mathbf{Q}\mathbf{z} + \mathbf{u}^\top\mathbf{R}\mathbf{u})\mathrm{d}t \tag{3.11}$$

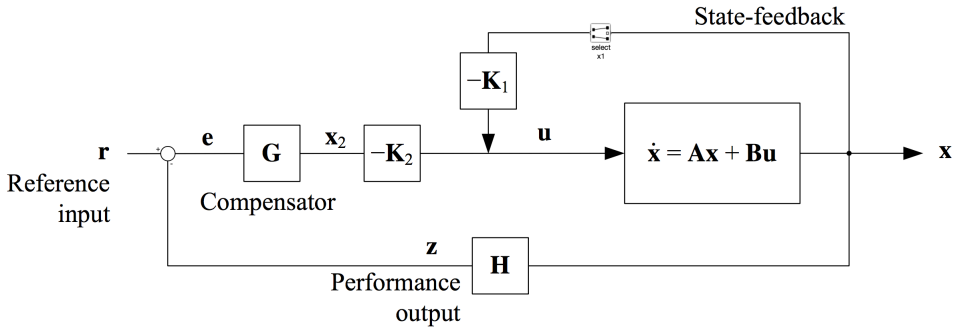

Figure 3.6: Augmented system with compensator

where $\mathbf{Q} = \mathbf{H}^\top \mathbf{Q}_M \mathbf{H}$.

Tracking formulation

Desired values of states are often non-zero, thus the tracking design problem is different to the regulator design above. The state to be tracked can be rephrased as an error to be regulated–enabling the same LQR approach to be used via definition of new states $\mathbf{x}_2$ and addition of a compensator, $\mathbf{G}$. This augmented system is shown in figure 3.6.

The compensator dynamics are

$$\mathbf{x}_2 = \mathbf{G}\mathbf{e} = \mathbf{G}\mathbf{r} - \mathbf{G}\mathbf{H}\mathbf{x} \tag{3.12}$$

where the input is tracking error $\mathbf{e} = \mathbf{r} - \mathbf{z}$. The augmented feedback law becomes

$$\mathbf{u} = -\begin{bmatrix}\mathbf{K}_1 & \mathbf{K}_2\end{bmatrix}\begin{bmatrix}\mathbf{x}_1 \\ \mathbf{x}_2\end{bmatrix} = -\mathbf{K}\mathbf{x} \tag{3.13}$$

The augmented system containing the open-loop and compensator dynamics is now

$$\begin{bmatrix}\dot{\mathbf{x}}_1 \\ \dot{\mathbf{x}}_2\end{bmatrix} = \begin{bmatrix}\mathbf{A} & \mathbf{0} \\ -\mathbf{G}\mathbf{H} & \mathbf{0}\end{bmatrix}\begin{bmatrix}\mathbf{x}_1 \\ \mathbf{x}_2\end{bmatrix} + \begin{bmatrix}\mathbf{B} \\ \mathbf{0}\end{bmatrix}\mathbf{u} + \begin{bmatrix}\mathbf{0} \\ \mathbf{G}\end{bmatrix}\mathbf{r} \tag{3.14}$$

Practical implementation

MATLAB's full-state feedback routine `lqr` is used. As this is a full-state feedback method, it requires that all states are exposed as outputs, i.e. $\mathbf{C} = \mathbf{I}$.

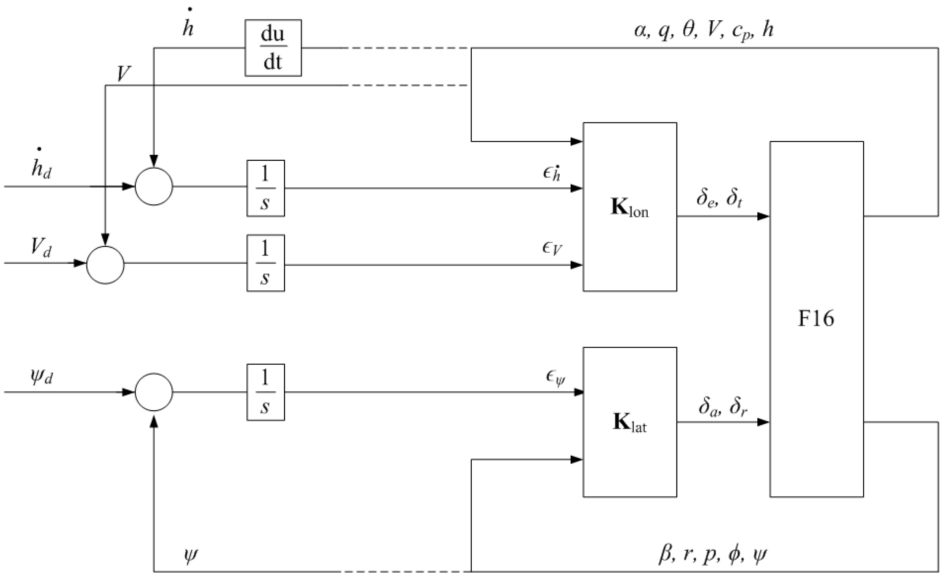

Figure 3.7: Inner-loop stability and tracking controller.

Lateral and longitudinal elements of the linearised system are decoupled, and so can be optimised separately.

The trimming, linearisation, augmentation and optimisation process is scripted as a function `f16lin`, and used across UoB ASTRAEA work. This permits consistent comparison and fast iteration of control design work.

The inner-loop stability and tracking controller is structured with separate longitudinal and lateral pathways, shown in figure 3.7. Note that compensator $\mathbf{G} = \mathbf{I}$ here and so becomes a simple set of integrators.

3.5.3 Longitudinal inner-loop

The longitudinal system detailed in equation A.26a can be simplified. Columns corresponding to x and h are null, thus there is no dependency on altitude or longitudinal position about the trim point, which is intuitively sensible. These states can be removed with no effect on local dynamic response.

To add the tracking control structure, two additional states can be used: climb rate error integral $\epsilon_{\dot{h}}$, and airspeed integral error ϵ_V.

The simplified then augmented longitudinal state vector is now

$$\mathbf{x}_{\text{lon}} = \left[\begin{array}{c} q \\ \alpha \\ V \\ \theta \\ \hline c_p \\ \hline \epsilon_{\dot{h}} \\ \epsilon_V \end{array}\right] \tag{3.15}$$

These tracking states can be added to the linear system through inclusion of their derivatives. Climb rate error (for small angles) can be given as

$$e_{\dot{h}} = \dot{h}_d - \dot{h} = \dot{h}_d - V_e\gamma = \dot{h}_d - V_e(\theta - \alpha) \tag{3.16}$$

Airspeed error is simply

$$e_V = V_d - V \tag{3.17}$$

Integrator states are therefore

$$\dot{\epsilon}_{\dot{h}} = e_{\dot{h}} = \dot{h}_d - V_e(\theta - \alpha), \qquad \dot{\epsilon}_V = e_V = V_d - V \tag{3.18}$$

Climb rate and airspeed are to be controlled, and so are used in the performance output matrix:

$$\mathbf{z}_{\text{lon}} = \begin{bmatrix} \dot{h} \\ V \end{bmatrix}, \qquad \mathbf{H}_{\text{lon}} = \begin{bmatrix} 0 & -V_e & 0 & V_e & 0 & 0 & 0 & 0 & 0 \\ 0 & 0 & 1 & 0 & 0 & 0 & 0 & 0 & 0 \end{bmatrix} \tag{3.19}$$

and compensator matrix $\mathbf{G}_{lon}$ and demand vector $\mathbf{r}_{lon}$ are

$$\mathbf{G}_{\text{lon}} = \begin{bmatrix} 1 & 0 \\ 0 & 1 \end{bmatrix}, \qquad \mathbf{r}_{\text{lon}} = \begin{bmatrix} \dot{h}_d \\ V_d \end{bmatrix} \tag{3.20}$$

The augmented system is now:

$$\begin{bmatrix} \dot{q} \\ \dot{\alpha} \\ \dot{V} \\ \dot{\theta} \\ \dot{c}_p \\ \dot{\epsilon}_{\dot{h}} \\ \dot{\epsilon}_V \end{bmatrix} = \begin{bmatrix} -0.9598 & -4.2724 & 0 & 0 & 0 & 0 & 0 \\ 0.9582 & -0.5712 & -0.0005 & 0 & 0 & 0 & 0 \\ -0.2583 & -1.2019 & -0.0122 & -9.81 & 0.0556 & 0 & 0 \\ 1 & 0 & 0 & 0 & 0 & 0 & 0 \\ 0 & 0 & 0 & 0 & -1 & 0 & 0 \\ 0 & 200 & 0 & -200 & 0 & 0 & 0 \\ 0 & 0 & -1 & 0 & 0 & 0 & 0 \end{bmatrix} \begin{bmatrix} q \\ \alpha \\ V \\ \theta \\ c_p \\ \epsilon_{\dot{h}} \\ \epsilon_V \end{bmatrix} + \begin{bmatrix} -0.1384 & 0 \\ -0.0012 & 0 \\ 0.0299 & 0 \\ 0 & 0 \\ 0 & 64.94 \\ 0 & 0 \\ 0 & 0 \end{bmatrix} \begin{bmatrix} \Delta\delta_e \\ \Delta\delta_t \end{bmatrix} + \begin{bmatrix} 0 & 0 \\ 0 & 0 \\ 0 & 0 \\ 0 & 0 \\ 0 & 0 \\ 1 & 0 \\ 0 & 1 \end{bmatrix} \begin{bmatrix} \dot{h}_d \\ V_d \end{bmatrix} \quad (3.21)$$

Assignment of LQR weightings

It is desirable to keep vertical and longitudinal motion tightly controlled for AAAR[1]. Using the aforementioned maximum-deviation method [152], $z_{\dot{h}_M}$ and z_{V_M} (representing maximum permissible deviations in a similar sense to those given in section 3.5.2) are selected as 0.3 and 0.5 m respectively. This gives:

$$\mathbf{Q}_{M\text{lon}} = \begin{bmatrix} 11.1111 & 0 \\ 0 & 4 \end{bmatrix} \quad (3.22)$$

[1]Values selected here would be relaxed for standard flight, only the AAAR capture mode is considered here.

from which

$$\mathbf{Q}_{\text{lon}} = \mathbf{H}_{\text{lon}}^{\top}\mathbf{Q}_{M\text{lon}}\mathbf{H}_{\text{lon}} = \begin{bmatrix} 0 & 0 & 0 & 0 & 0 & 0 & 0 \\ 0 & 444440 & 0 & -444440 & 0 & 0 & 0 \\ 0 & 0 & 4 & 0 & 0 & 0 & 0 \\ 0 & -444440 & 0 & 444440 & 0 & 0 & 0 \\ 0 & 0 & 0 & 0 & 0 & 0 & 0 \\ 0 & 0 & 0 & 0 & 0 & 0 & 0 \\ 0 & 0 & 0 & 0 & 0 & 0 & 0 \end{bmatrix} \tag{3.23a}$$

$$\mathbf{R}_{\text{lon}} = \begin{bmatrix} 1 & 0 \\ 0 & 1 \end{bmatrix} \tag{3.23b}$$

A stable solution is currently unable to be found, as the two unstable ($s = 0$) integrator states are currently unobservable (as would be x and h if they were retained in the model). This can be resolved by weighting them in the $\mathbf{Q}$ matrix:

$$\mathbf{Q}_{\text{lon}} = \begin{bmatrix} 0 & 0 & 0 & 0 & 0 & 0 & 0 \\ 0 & 444440 & 0 & -444440 & 0 & 0 & 0 \\ 0 & 0 & 4 & 0 & 0 & 0 & 0 \\ 0 & -444440 & 0 & 444440 & 0 & 0 & 0 \\ 0 & 0 & 0 & 0 & 0 & 0 & 0 \\ 0 & 0 & 0 & 0 & 0 & 1 & 0 \\ 0 & 0 & 0 & 0 & 0 & 0 & 1 \end{bmatrix} \tag{3.24}$$

producing a stable solution with gains[2]:

$$\mathbf{K}_{a\text{lon}} = \begin{bmatrix} -47.9 & 623.54 & 0.10 & -766.35 & -0.001 & 0.99 & -0.10 \\ 1.63 & -63.07 & 2.52 & 65.56 & 0.05 & -0.10 & -0.99 \end{bmatrix} \tag{3.25}$$

Closed-loop response of this system is shown in figure 3.8 (solid line). Climb rate demand is met in 15 s with negligible steady-state error, and airspeed demand in a similar time frame. Peak control inputs are 0.1 degree for elevator and 19% for throttle.

This response can be improved by relaxing the maximum permissible

[2]It should be noted that in this model the F-16's states are in radians but control inputs are in degrees, so relevant gains appear unusually large due to this $\frac{180}{\pi}$ scaling factor.

deviations on the performance measures, decreasing rise and settling time at the expense of overshoot. In the extreme, this will lead to control demand that exceeds the saturation limits of the nonlinear model, so an increased penalty on control effort is required.

The design process resulted in final weighting matrices:

$$\mathbf{Q}_{\text{lon}} = \mathbf{H}_{\text{lon}}^{\top}\mathbf{Q}_{M\text{lon}}\mathbf{H}_{\text{lon}} = \begin{bmatrix} 0 & 0 & 0 & 0 & 0 & 0 & 0 \\ 0 & 444440 & 0 & -444440 & 0 & 0 & 0 \\ 0 & 0 & 4 & 0 & 0 & 0 & 0 \\ 0 & -444440 & 0 & 444440 & 0 & 0 & 0 \\ 0 & 0 & 0 & 0 & 0 & 0 & 0 \\ 0 & 0 & 0 & 0 & 0 & 1 & 0 \\ 0 & 0 & 0 & 0 & 0 & 0 & 1 \end{bmatrix} \tag{3.26a}$$

$$\mathbf{R}_{\text{lon}} = \begin{bmatrix} 100 & 0 \\ 0 & 1000 \end{bmatrix} \tag{3.26b}$$

giving feedback gains:

$$\mathbf{K}_{b\text{lon}} = \begin{bmatrix} -10.633 & 76.698 & 0.023 & -90.728 & 0.001 & 0.099 & -0.018 \\ 0.028 & -2.997 & 0.161 & 2.843 & 0.007 & -0.006 & -0.031 \end{bmatrix} \tag{3.27}$$

Step response is shown in figure 3.8 (dotted line). Climb response is improved due to the higher weighting on throttle demand, but this is at the expense of airspeed response, which is slower.

Constraining feedback

In the optimal construction above, all demands and states are coupled. For a practical system some of these interactions are undesirable, e.g. compensation via the throttle against pitch rate. In fact, engine power demand gains are not typical in feedback controllers. Where gains are small and have little impact on performance, it is also convenient to zero them to reduce data processing and storage requirements and controller complexity.

These adjustments result in feedback gains:

$$\mathbf{K}_{c\text{lon}} = \begin{bmatrix} -10.633 & 76.698 & 0 & -90.728 & 0 & 0.099 & 0 \\ 0 & 0 & 0.161 & 0 & 0 & 0 & -0.031 \end{bmatrix} \tag{3.28}$$

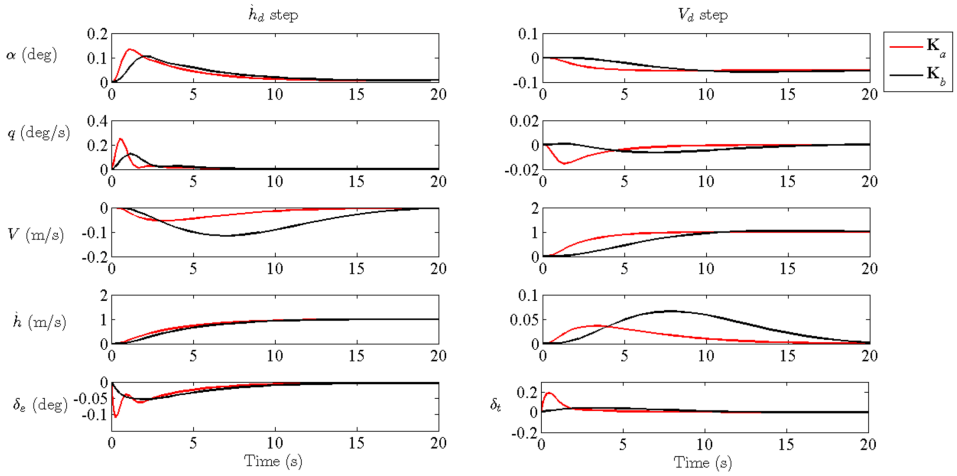

Figure 3.8: Step response of closed-loop longitudinal system

A comparison of closed-loop step response before and after feedback constraint is nearly identical, shown in figure 3.9. Airspeed response is similar despite the removal of the throttle term, because the control penalty on the throttle in weighting matrix $\mathbf{R}$ was already large.

This is no longer an optimal solution, as the algebraic Ricatti equation in the LQR formulation is no longer satisfied, but its performance is suitable for application to the AAAR problem and similar systems will be compared and contrasted for differing control architectures.

Closed-loop system

The final closed-loop longitudinal system is:

$$\mathbf{A}_{cl\text{lon}} = \mathbf{A}_{\text{lon}} - \mathbf{B}_{\text{lon}}\mathbf{K}_{c\text{lon}} =$$

$$\begin{bmatrix} -2.4311 & 6.3412 & 0 & -12.5552 & 0 & 0.0136 & 0 \\ 0.9453 & -0.4784 & -0.0005 & -0.1097 & 0 & 0.0001 & 0 \\ 0.0599 & -3.4972 & -0.0122 & -7.0940 & 0.0556 & -0.0029 & 0 \\ 1 & 0 & 0 & 0 & 0 & 0 & 0 \\ 0 & 0 & -10.4479 & 0 & -1 & 0 & 2.0219 \\ 0 & 200 & 0 & -200 & 0 & 0 & 0 \\ 0 & 0 & -1 & 0 & 0 & 0 & 0 \end{bmatrix} \tag{3.29}$$

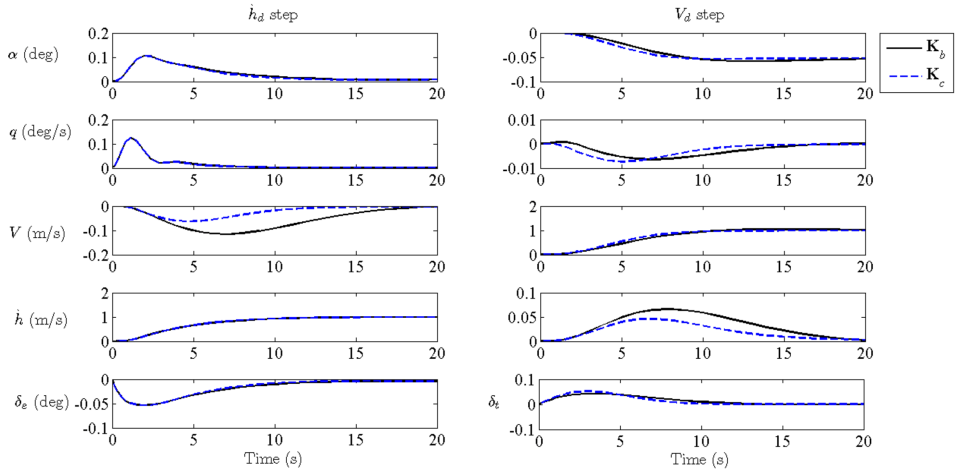

Figure 3.9: Comparison of longitudinal closed-loop step response without and with feedback constraint.

with eigenvalues compared with the open-loop system in figure 3.10. Most modes have shifted to the left, with only a minor decrease in damping for pole associated with engine power demand.

The states that were removed from the closed-loop system earlier (x and h can be replaced to give the full-state system:

$$\mathbf{A}_{cl\text{lon}} = \mathbf{A}_{\text{lon}} - \mathbf{B}_{\text{lon}}\mathbf{K}_{c\text{lon}} =$$

$$\begin{bmatrix} -2.4311 & 6.3412 & 0 & -12.5552 & 0 & 0 & 0 & 0.0136 & 0 \\ 0.9453 & -0.4784 & -0.0005 & -0.1097 & 0 & 0 & 0 & 0.0001 & 0 \\ 0.0599 & -3.4972 & -0.0122 & -7.0940 & 0 & 0 & 0.0556 & -0.0029 & 0 \\ 1 & 0 & 0 & 0 & 0 & 0 & 0 & 0 & 0 \\ 0 & 0 & 1 & 0 & 0 & 0 & 0 & 0 & 0 \\ 0 & -200 & 0 & 200 & 0 & 0 & 0 & 0 & 0 \\ 0 & 0 & -10.4479 & 0 & 0 & 0 & -1 & 0 & 2.0219 \\ 0 & 200 & 0 & -200 & 0 & 0 & 0 & 0 & 0 \\ 0 & 0 & -1 & 0 & 0 & 0 & 0 & 0 & 0 \end{bmatrix} \tag{3.30}$$

3.5.4 Lateral inner-loop

The lateral open-loop model is given in equation A.26b. Similarly to the longitudinal model, local dynamics are not influenced by lateral position y,

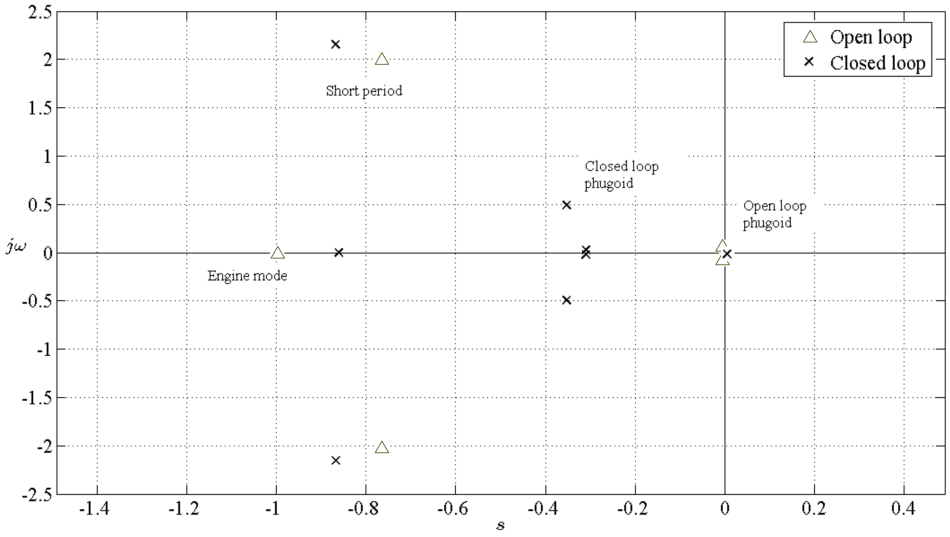

Figure 3.10: Comparison of longitudinal open-loop and final closed-loop eigenvalues.

so it is removed. Yaw angle cannot be removed as it is being controlled.

Tracking of ψ is required, so an additional state for its integral error is added. The augmented state vector is:

$$\mathbf{x}_{\text{lat}} = \begin{bmatrix} p \\ r \\ \beta \\ \phi \\ \psi \\ \hline \epsilon_\psi \end{bmatrix} \tag{3.31}$$

The derivative of this tracking state is:

$$\dot{\epsilon}_\psi = e_\psi = \psi_d - \psi \tag{3.32}$$

Performance vector and matrix are:

$$\mathbf{z}_{\text{lat}} = \psi, \qquad \mathbf{H}_{\text{lat}} = \begin{bmatrix} 0 & 0 & 0 & 0 & 1 & 0 \end{bmatrix} \tag{3.33}$$

with compensator matrix and demand vector:

$$\mathbf{G}_{\text{lat}} = 1, \qquad \mathbf{r}_{\text{lat}} = \psi_d \tag{3.34}$$

The augmented system becomes:

$$\begin{bmatrix} \dot{p} \\ \dot{r} \\ \dot{\beta} \\ \dot{\phi} \\ \dot{\psi} \\ \dot{\epsilon}_\psi \end{bmatrix} = \begin{bmatrix} -2.0260 & 0.4493 & -25.4971 & 0 & 0 & 0 \\ -0.0306 & -0.2930 & 7.6774 & 0 & 0 & 0 \\ 0.0664 & -0.9944 & -0.1805 & 0.0489 & 0 & 0 \\ 1 & 0.0664 & 0 & 0 & 0 & 0 \\ 0 & 1.0022 & 0 & 0 & 0 & 0 \\ 0 & 0 & 0 & 0 & -1 & 0 \end{bmatrix} \begin{bmatrix} p \\ r \\ \beta \\ \phi \\ \psi \\ \epsilon_\psi \end{bmatrix} + \begin{bmatrix} -0.5407 & 0.0936 \\ -0.0242 & -0.0488 \\ 0.0002 & 0.0005 \\ 0 & 0 \\ 0 & 0 \\ 0 & 0 \end{bmatrix} \begin{bmatrix} \Delta\delta_a \\ \Delta\delta_r \end{bmatrix} + \begin{bmatrix} 0 \\ 0 \\ 0 \\ 0 \\ 0 \\ 1 \end{bmatrix} \psi_d \quad (3.35)$$

Assignment of LQR weightings

Similarly to the longitudinal optimisation, lateral angular deviation is tightly controlled, with z_{ψ_M} therefore $\mathbf{Q}_M = 1$. The unstable integrator state is again weighed to permit a solution:

$$\mathbf{Q}_{\text{lat}} = \begin{bmatrix} 0 & 0 & 0 & 0 & 0 & 0 \\ 0 & 0 & 0 & 0 & 0 & 0 \\ 0 & 0 & 0 & 0 & 0 & 0 \\ 0 & 0 & 0 & 0 & 0 & 0 \\ 0 & 0 & 0 & 0 & 1 & 0 \\ 0 & 0 & 0 & 0 & 0 & 1 \end{bmatrix} \quad \text{and} \quad \mathbf{R}_{\text{lat}} = \begin{bmatrix} 1 & 0 \\ 0 & 1 \end{bmatrix} \quad (3.36)$$

Resulting feedback gains are:

$$\mathbf{K}_{a\text{lat}} = \begin{bmatrix} -0.736 & -2.716 & -6.843 & -1.295 & -7.762 & 0.986 \\ -0.096 & -0.367 & -0.994 & -0.166 & -1.130 & 0.168 \end{bmatrix} \quad (3.37)$$

Closed-loop step response is shown in figure 3.11. Damping ratio for heading response is around 0.6, and steady-state is achieved in around 30 s.

Again following a similar approach to the longitudinal system, response can be improved by modifying LQR weightings. Increasing z_{ψ_M} has little effect, but the integrator state weighting can be adjusted to affect time

response.

Final values are selected as:

$$\mathbf{Q}_{\text{lat}} = \begin{bmatrix} 0 & 0 & 0 & 0 & 0 & 0 \\ 0 & 0 & 0 & 0 & 0 & 0 \\ 0 & 0 & 1000 & 0 & 0 & 0 \\ 0 & 0 & 0 & 1 & 0 & 0 \\ 0 & 0 & 0 & 0 & 100 & 0 \\ 0 & 0 & 0 & 0 & 0 & 10 \end{bmatrix} \quad \text{and} \quad \mathbf{R}_{\text{lat}} = \begin{bmatrix} 0.01 & 0 \\ 0 & 0.01 \end{bmatrix} \tag{3.38}$$

resulting in gain matrix[3]:

$$\mathbf{K}_{b\text{lat}} = \begin{bmatrix} -4.609 & -8.530 & -127.550 & -7.617 & -129.210 & 28.173 \\ 3.696 & -78.457 & 145.983 & 3.188 & -55.546 & 14.363 \end{bmatrix} \tag{3.39}$$

The effects of these modifications are shown in figure 3.11. Tracking is improved, overshoot is eliminated, and rise time is faster. The small steady-state error in β is due to the steady-state rudder deflection, but this can be corrected by constraining feedback.

Constraining feedback

Again, undesirable couplings are removed by zeroing gains:

$$\mathbf{K}_{c\text{lat}} = \begin{bmatrix} -4.609 & 0 & 0 & -7.617 & -129.210 & 28.173 \\ 0 & -78.457 & 145.983 & 0 & 0 & 0 \end{bmatrix} \tag{3.40}$$

The constrained system is compared to the previous one in figure 3.12. There is little difference in response and sideslip error has been eliminated.

[3] Again angular states are in radians but control inputs are in degrees, so relevant gains appear large due to this $\frac{180}{\pi}$ scaling factor.

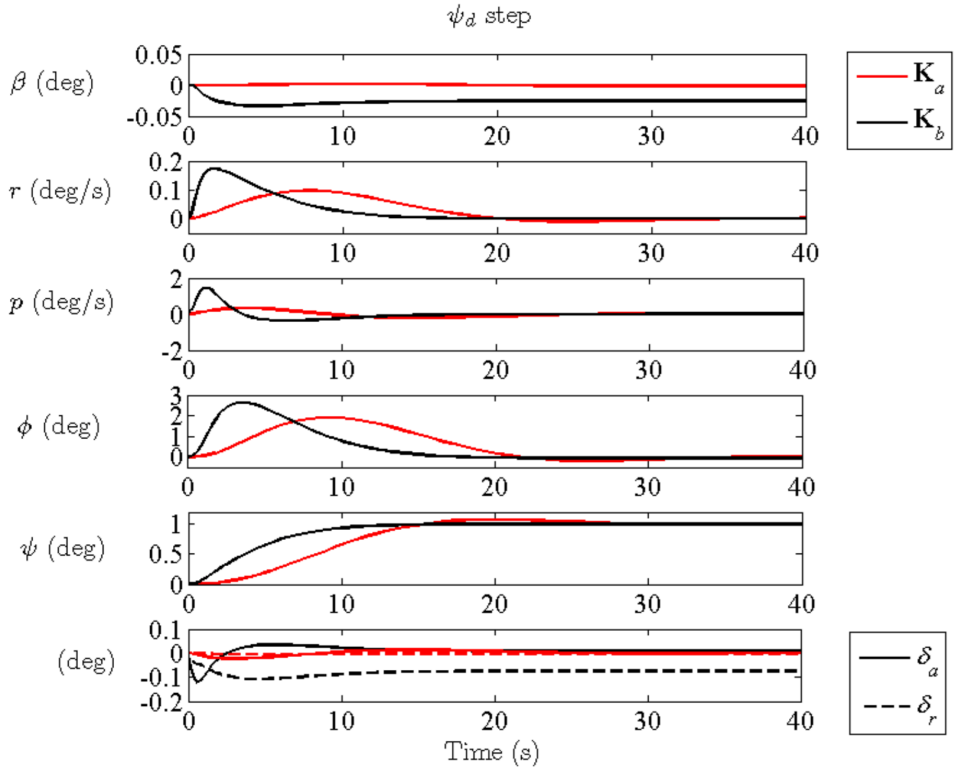

Figure 3.11: Step response of closed-loop lateral system

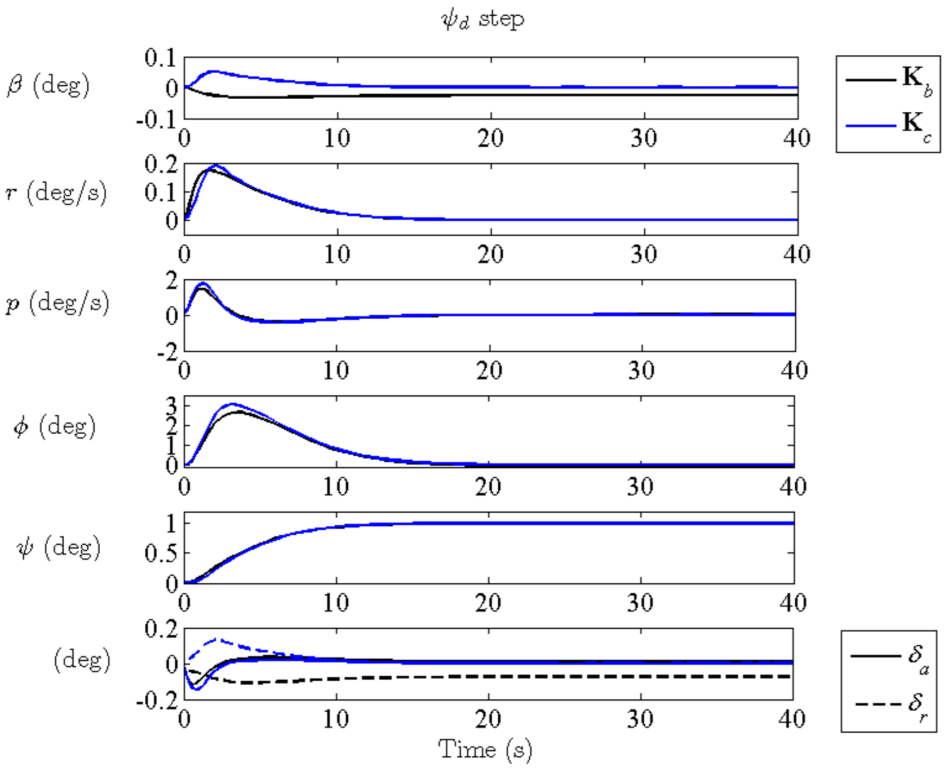

Figure 3.12: Comparison of lateral closed-loop step response without and with feedback constraint.

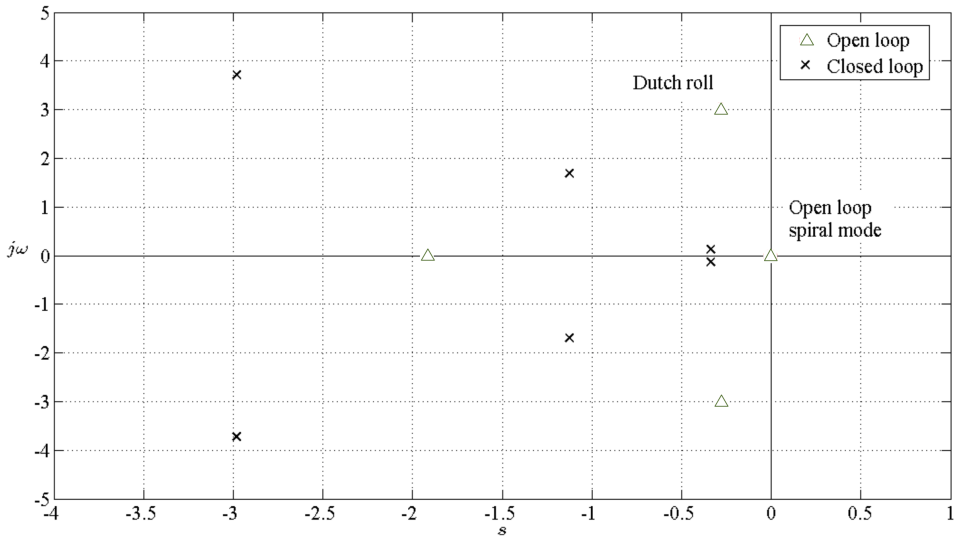

Figure 3.13: Comparison of lateral open- and final closed-loop eigenvalues.

Closed-loop system

The lateral closed-loop system is:

$$\mathbf{A}_{cl\text{lat}} = \mathbf{A}_{\text{lat}} - \mathbf{B}_{\text{lat}}\mathbf{K}_{c\text{lat}} = \begin{bmatrix} -4.5178 & 7.7908 & -39.1573 & -4.1184 & -69.8633 & 15.2329 \\ -0.1424 & -4.1254 & 14.8082 & -0.1847 & -3.1327 & 0.6831 \\ 0.0671 & -0.9590 & -0.2464 & 0.0502 & 0.0214 & -0.0047 \\ 1 & 0.0664 & 0 & 0 & 0 & 0 \\ 0 & 1.0022 & 0 & 0 & 0 & 0 \\ 0 & 0 & 0 & 0 & -1 & 0 \end{bmatrix} \tag{3.41}$$

with eigenvalues shown in figure 3.13. Poles have moved to the left, demonstrating that the closed-loop model has increased stability.

This is once again not an optimal solution, as the algebraic Ricatti equation is not satisfied, but characteristics are suitable for investigating AAAR techniques and similar systems will be compared.

3.5.5 Outer-loop control

For L/F AAAR, the outer-loop controller, shown in figure 3.14, acts only upon the receiver, and generates state demands V_d, $\dot{h}_d$, and ψ_d for the inner-

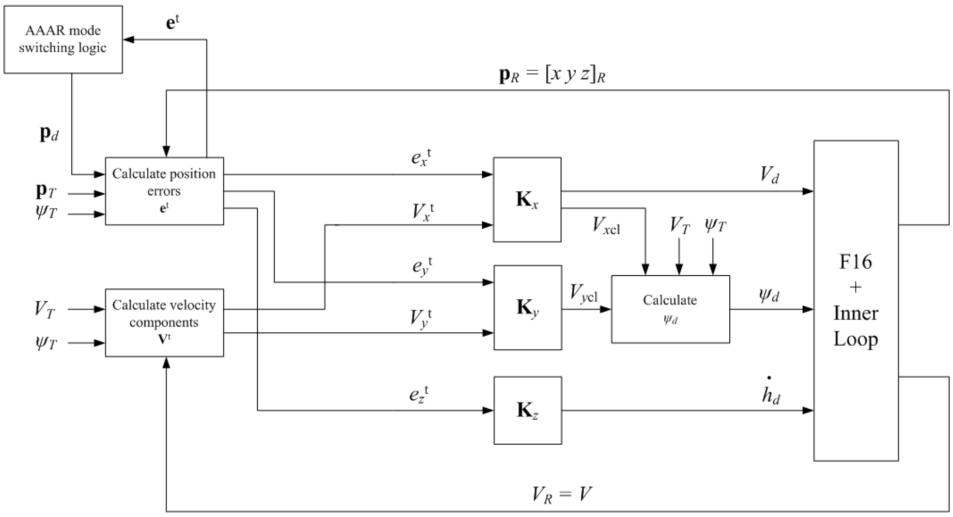

Figure 3.14: Outer loop control architecture for L/F AAAR.

Table 3.4: Tracking points for each refuelling stage.

Stage	$\mathbf{x}_1$	$\mathbf{x}_2$
Joining	Receiver CG	Tanker CG
Observation	Receiver CG	Tanker CG
Moving astern	Receiver CG	Tanker CG
Pre-contact	Probe tip	Drogue centre
Contact	Probe tip	Drogue centre
Disconnect	Receiver CG	Tanker CG
Reform	Receiver CG	Tanker CG

loop controller from positional error $\mathbf{e} = [e_x\, e_y\, e_z]^\top$, which is calculated between the receiver or probe tip, and the tanker or drogue, depending on refuelling stage and detailed in table 3.4.

To generate inner-loop demands from position error, the process is as follows[4]:

1. Transform errors and velocities from global to local tanker navigation frame.

2. Determine when to switch between refuelling stages by monitoring errors and capture criteria.

[4]Given that multiple reference frames are used in the AAR SE, we now use established reference frame notation [153], where subscript and superscript respectively denote 'from' and 'to' reference frames.

3. Evaluate demands V_d, $\dot{h}_d$ and closing speed components V_x^t, V_y^t.

4. Calculate heading demand ψ_d in global reference frame.

Error and velocity transformations

Position error is initially calculated in the global frame, and is then transformed to the tanker navigation frame. The tanker's heading ψ_t is the rotation between these two frames, so:

$$\mathbf{e}^n = \begin{bmatrix} e_x \\ e_y \\ e_z \end{bmatrix}^n = \begin{bmatrix} \cos\psi_t & \sin\psi_t & 0 \\ -\sin\psi_t & \cos\psi_t & 0 \\ 0 & 0 & 1 \end{bmatrix} \begin{bmatrix} e_x \\ e_y \\ e_z \end{bmatrix}^e \tag{3.42}$$

Velocities in the xy plane can be similarly transformed:

$$\mathbf{V}_r^n = \begin{bmatrix} V_{r_x} \\ V_{r_y} \end{bmatrix}^n = \begin{bmatrix} \cos\psi_t & \sin\psi_t \\ -\sin\psi_t & \cos\psi_t \end{bmatrix} \begin{bmatrix} V_r\cos\psi_t \\ V_r\sin\psi_t \end{bmatrix}^e \tag{3.43a}$$

$$\mathbf{V}_t^n = \begin{bmatrix} V_{t_x} \\ V_{t_y} \end{bmatrix}^n = \begin{bmatrix} \cos\psi_t & \sin\psi_t \\ -\sin\psi_t & \cos\psi_t \end{bmatrix} \begin{bmatrix} V_t\cos\psi_t \\ V_t\sin\psi_t \end{bmatrix}^e \tag{3.43b}$$

Generation of demands

The outer-loop system shown in figure 3.14 is effectively a proportional-derivative controller acting on position and velocity feedback. Gains are selected to feed appropriate magnitude demands to the inner-loop controller[5].

Outer loop gains $\mathbf{K}_x$ and $\mathbf{K}_y$ generate closing speed components V_x^t and V_y^t, which are summed with the tanker's velocity to produce speed demand V_d. Gain $\mathbf{K}_z$ produces closing speed component V_z^t, which is summed with the tanker's vertical velocity to give climb rate demand $\dot{h}_d$. Both of these demands are saturated to limits consistent with ATP-56(B) recommendations for each stage of the refuelling process.

Heading demand ψ_d is calculated from closing speeds. Since these are relative to the tanker's navigation frame, they need to be converted to the global frame in which the receiver is operating, via the inverse of equation

[5] An alternative approach to this could be via a 'total energy' approach, as detailed by Lambregts et al.[154]

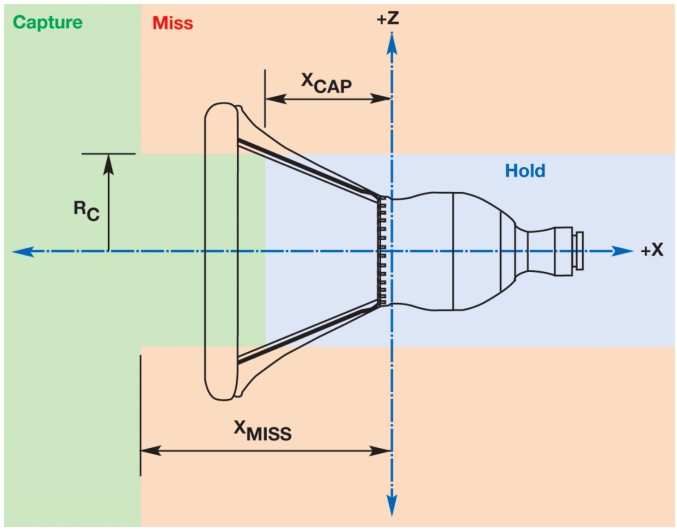

Figure 3.15: Drogue capture envelope [37].

3.43a:

$$\mathbf{V}_t^e = \begin{bmatrix} V_x^t \\ V_y^t \end{bmatrix}^e = \begin{bmatrix} \cos\psi_t & -\sin\psi_t \\ \sin\psi_t & \cos\psi_t \end{bmatrix} \begin{bmatrix} V_x^t \\ V_y^t \end{bmatrix}^n \tag{3.44}$$

and the velocity demand in the global reference frame can then be calculated as:

$$\mathbf{V}_d^e = \mathbf{V}_t^e + \mathbf{V}^{te} = \begin{bmatrix} V_t \cos\psi_t \\ V_t \sin\psi_t \end{bmatrix} \begin{bmatrix} V_x^t \\ V_y^t \end{bmatrix}^e \tag{3.45}$$

and heading demand as:

$$\psi_d = \tan^{-1}\left(\frac{V_t \sin\psi_t + V_y^t}{V_t \cos\psi_t + V_x^t}\right) \tag{3.46}$$

Switching logic and success criteria

The outer-loop controller bases its progression between refuelling stages on the position error and relative velocities between the tracked objects. When these are held within acceptable envelopes for a predetermined time, the refuelling stage is incremented.

Envelopes for most transitions are simple spheres, with near-zero relative velocity desired. Drogue capture is more involved, and based upon that used by NASA's AARD project [37], with an envelope shown in figure 3.15.

Based on flight hardware measurements and pilot recommendation, values shown in table 3.5 are selected. If the probe tip enters via the capture

Table 3.5: Drogue capture envelope dimensions (notation as in figure 3.15).

Parameter	Value	Unit
R_C	0.21	m
x_{CAP}	0.20	m
x_{MISS}	0.30	m

region and remains in the hold region, the capture is a success. If at any point the probe tip enters the miss region, the capture is a failure. Additionally, closing velocity must be between 1 and 2 m/s – this is achieved in a similar manner to the approach used by pilots, aiming 'behind' the drogue by shifting the target point several metres ahead. Once contact is made, the target point returns to the drogue centre.

Further failure criteria are implemented to reject attempts that would cause conflict between the receiver and refuelling equipment, and to detect failures of the model or of the receiver's control system caused by adverse conditions:

1. probe overshoots drogue by > 0.5 m.
2. aerodynamic range of the F-16 model is exceeded.
3. receiver loses > 500 m altitude.

Only one attempt is made for each simulated approach, and the simulation is terminated with successful or failed capture.

3.6 Atmosphere

3.6.1 General properties

The International Standard Atmosphere (ISA) detailed in ISO 2533 [155] is used to give atmospheric properties at flight conditions. This is implemented via MATLAB's `atmosisa()` function, which outputs ambient temperature, pressure, density, and speed of sound for a given altitude.

3.6.2 Turbulence

Instabilities in the atmosphere due to temperature, pressure and velocity gradients affect the forces and moments acting upon an aircraft, perturbing its translational and rotational motion. Measured data indicates that turbulence occurs in patches, and within these patches fluctuations are random, homogeneous and isotropic. Patches move with the atmosphere, but can be treated as static where the aircraft's ground speed is much larger than overall wind and turbulent velocities within the patch, as is the case here.

Turbulence can be modelled as continuous or discrete. For performance and control system analysis a continuous method is preferred. There are two commonly-used spectral forms for random continuous turbulence: von Kármán and Dryden [156], both detailed in MIL-HDBK-1797 [157].

The von Kármán approach models continuous gusts as spatially varying stochastic processes, and is the preferred model used by the US DoD and Federal Aviation Administration (FAA). It follows experimental and theoretical data more closely than the Dryden approach, particularly for higher frequency components [158], but has irrational Power Spectral Densities (PSDs) that make it more complex to model.

For the purposes of this study, rigid-body aircraft models are used and so the higher frequencies, which mostly affect structural vibration modes, are not of concern. Given that the AAAR SE is required to run in real-time on the RMR hardware, the Dryden form is selected as sufficient. MIL-HDBK-1797 states "when no comparable structural analysis is performed ... use of the Dryden form will be permissible".

The Dryden spectral form defines one-sided PSDs for linear velocity components:

$$\phi_u(\Omega) = \sigma_u^2 \frac{2L_u}{\pi} \frac{1}{1 + (L_u\Omega)^2} \tag{3.47a}$$

$$\phi_v(\Omega) = \sigma_v^2 \frac{2L_v}{\pi} \frac{1 + 12(L_v\Omega)^2}{(1 + 4(L_v\Omega)^2)^2} \tag{3.47b}$$

$$\phi_w(\Omega) = \sigma_w^2 \frac{2L_w}{\pi} \frac{1 + 12(L_w\Omega)^2}{(1 + 4(L_w\Omega)^2)^2} \tag{3.47c}$$

where $\sigma_{u,v,w}$ and $L_{u,v,w}$ are turbulence intensity and scale, and $\Omega = \frac{\omega}{V}$ is the spatial frequency of the gusts.

MIL-HDBK-1797 states that for medium/high altitude $L_u = 2L_v =$

$2L_w = 533.4$ m, and $\sigma_u^2 = \sigma_v^2 = \sigma_w^2$, which are looked up from the model given in figure 3.16 – these depend on the level of turbulence selected, categorised as light/moderate/severe.

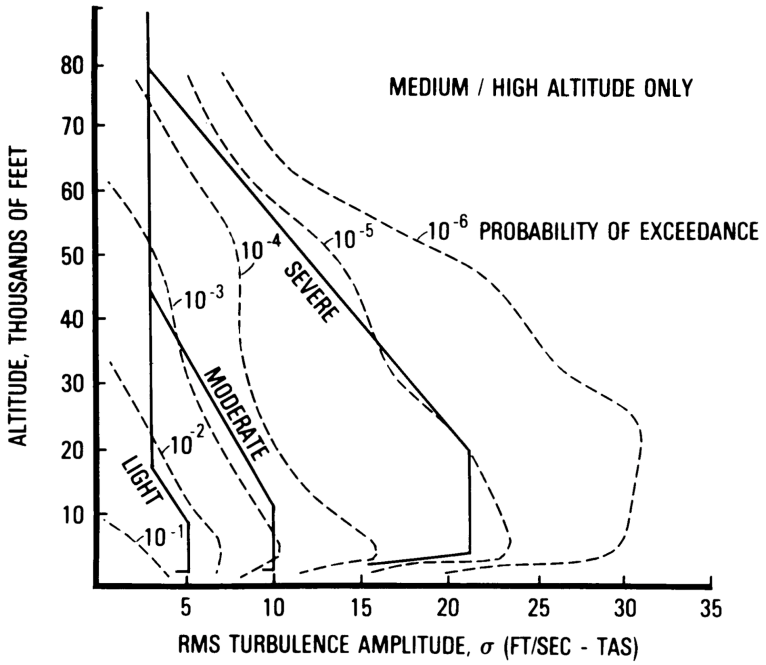

Figure 3.16: Dryden turbulence gust intensities [157].

Rotational components can be derived by assuming that the turbulence varies linearly over the surface of the aircraft. Vertical gradients have a much smaller effect than spanwise and lengthwise variations due to the relative dimensions of a typical aircraft. Once these PSDs are generated, time-domain signals are generated by passing white noise through a shaping filter. A detailed description of this process can be found in the text by Hoblit [156].

The turbulence process is implemented via Simulink's *Dryden Wind Turbulence Model (Continuous)* block, which outputs translational and rotational velocities to be added to the wind vector. The block permits easy customisation of noise generation seeds, which allows identical gusts to be applied to repeated simulations, which permits the repeated-capture comparison method in later chapters.

3.6.3 Aerodynamic interactions

Tanker wake

Tanker downwash and turbulent wake has significant impact as the receiver aircraft moves astern and towards the pre-contact position, but these effects decrease rapidly as the receiver approaches. A UoB-Cobham internal deliverable D2.3.39 [159] used wake vortex simulation data of the effect of a KC-135 tanker on an ICE receiver (figure 3.17, which shows that over the last 10 m of the capture (upon which this thesis is focused) the wake is not fully developed and its effect on the receiver was shown to be low compared to general atmospheric turbulence. Data for similar interactions between tanker and F-16 were unavailable.

For these reasons, and to minimise repeated-simulation runtime and ensure real-time simulation on RMR hardware, the effect of tanker wake on the receiver was neglected. This limits the applicability of this version of the SE to only the final 10 m of capture. It should be noted that the primary outcomes of this thesis are comparative between control architectures, which should minimise impact on absolute results.

Receiver bow wave

The bow wave effect, detailed in chapter 2, and methods by which to address it, was investigated in parallel to the work detailed in this thesis. It was found that without bow wave compensation, capture rates even at moderate turbulence were exceedingly low.

To permit comparative work on control systems in this thesis, the bow wave effect is omitted in this SE, with future work expected to merge these two strands of investigation.

3.7 Refuelling hardware

The most important factors in selecting models for this SE are fidelity and computational limitations – the model should be able to run in real-time as part of the RMR environment, and should accurately simulate drogue motion under turbulence, and permit the addition of wake and bow wave aerodynamics and drogue control forces.

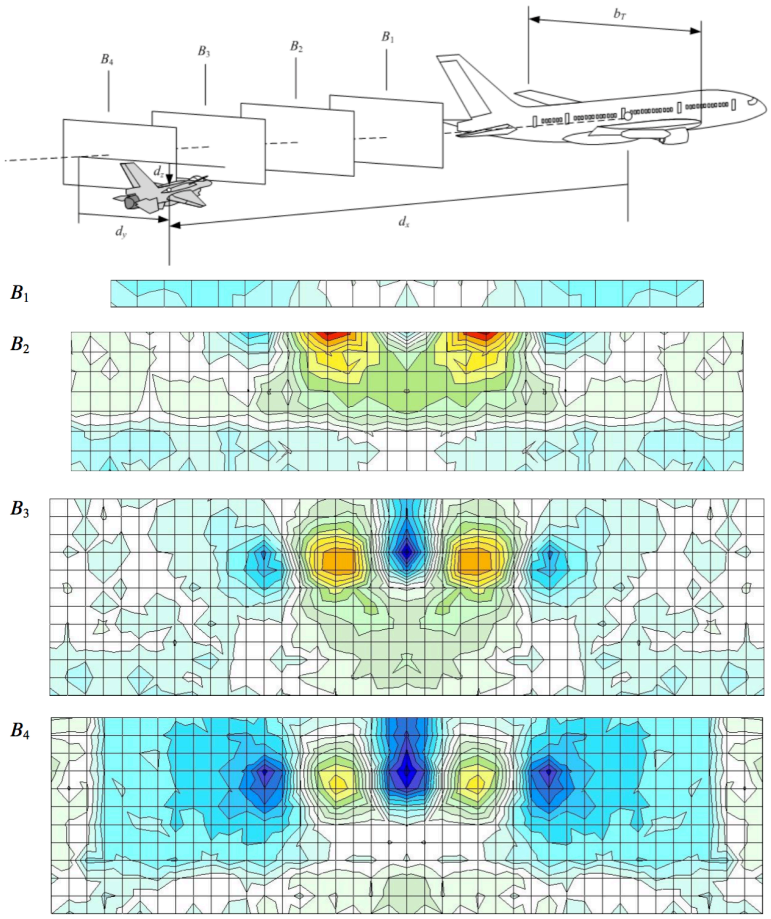

Figure 3.17: Wake vortex visualisation [159] (scale redacted – proprietary data).

Of the works detailed in section 2.3.3, the approach which is most attractive is that of Ro and Kamman [101]. Their model is verified against flight data, and they include information about solution fidelity and speed.

Notation in this section is based on that in the literature, and so differ from the terms introduced in section 3.3. Modifications to Ro and Kamman's model in this SE include the definition of the hose attachment point, and the aerodynamic method used for hose drag.

3.7.1 Hose construction

In Ro and Kamman's finite segment approach, the hose is modelled as a series of rigid cylindrical links connected by frictionless ball-and socket joints, shown in figure 3.18. Link masses, and gravitational and aerodynamic forces, are lumped at the joints, and drogue mass and forces are applied to the end of the final link. For optimal simulation, $n_{links} = 20$ is recommended as Ro and Kamman observed $< 1.85 \times 10^{-4}$ m drogue positional difference between this versus with $n_{links} = 40$ [101]. Simulation time step is fixed at 0.02 s to match the wider RMR and AAR SE.

3.7.2 Frames of reference

Ro & Kamman denote the inertial frame F_N, and the tanker's 'mean trajectory frame' F_W, within which they add perturbations to the hose tow point, representing disturbances such as those due to turbulence. Frame geometry is shown in figure 3.18. For a full AAR environment, attaching frame F_W to the instantaneous motion of the tow point removes the necessity for Ro and Kamman's turbulent additions to the tow point motion, as these are introduced by the aircraft model.

3.7.3 Link orientations

Hose link orientations are defined (for typical link K) as rotations $\theta_{K_{1,2,3}}$ about frame F_K, which is fixed to each link with x_K, y_K, z_K aligned with F_W when the link is pointing away from the attachment point, along $-X_W$. Order of rotation is about x_K, y_K, z_K. If link torsion is neglected then θ_{K_1} is always zero. Unit vectors along x_K, y_K, z_K are denoted $\boldsymbol{\lambda}_{K_{1,2,3}}$.

Figure 3.18: Reference frames and link geometry [101].

3.7.4 Tow point

The hose tow point $\mathbf{p}_0^N$ is described using the tanker aircraft's centre of gravity, $\mathbf{x}_t^N$ in F_N, and the offset of the tow point from the CG, $\mathbf{o}_t^B$ in tanker body axes F_B. Using transformation T_N^B (from F_N to F_B), where

$$T_N^B = \begin{bmatrix} \cos\theta\cos\psi & \cos\theta\sin\psi & -\sin\theta \\ \sin\phi\sin\theta\cos\psi - \cos\phi\sin\psi & \sin\phi\sin\theta\sin\psi + \cos\phi\cos\psi & \sin\phi\cos\theta \\ \cos\phi\sin\theta\cos\psi + \sin\phi\sin\psi & \cos\phi\sin\theta\sin\psi - \sin\phi\cos\psi & \cos\phi\cos\theta \end{bmatrix} \tag{3.48}$$

the location of the tow point is

$$\mathbf{p}_0^N = \mathbf{x}_t^N + \left[T_N^B\right]^{-1} \mathbf{o}_t^B \tag{3.49}$$

The direction of motion of the aircraft can be found in a similar manner, but angles of incidence and sideslip must be included, thus T_N^W, from inertial to wind axes, must use $\gamma = \theta + \alpha$ and $\chi = \psi + \beta$, in place of θ and ψ

respectively. Unit vectors $\hat{\mathbf{x}}_W^N$, $\hat{\mathbf{y}}_W^N$, $\hat{\mathbf{z}}_W^N$ along the wind axes, in F_N, can then be calculated by transforming from F_W, e.g.

$$\hat{\mathbf{x}}_W^N = \left[T_N^W\right]^{-1} \begin{bmatrix} 1 \\ 0 \\ 0 \end{bmatrix} \tag{3.50}$$

The angular velocity of the wind axes will be that of F_W:

$$\boldsymbol{\omega}_W = \frac{\mathbf{x}_t \times \mathbf{V}_t}{\|\mathbf{x}_t\|^2} \tag{3.51}$$

where $\|\|$ denotes a euclidian norm, and their angular acceleration $\boldsymbol{\alpha}_W$ will be the derivative of $\boldsymbol{\omega}_W$.

3.7.5 System motion

If the motion of F_W, the position of the hose attachment point $\mathbf{p}_0$, link angles θ and derivatives $\dot{\theta}$ are known, the system motion can be calculated.

Take $\mathbf{p}_K$ to be a vector along link K, which has link angles $\theta_{K_{1,2,3}}$ and derivatives $\dot{\theta}_{K_{1,2,3}}$ (the first of which will be zero if link torsion is ignored). Also take $\boldsymbol{\lambda}_{K_{1,2,3}}$ to be unit vectors along x_K, y_K, z_K. Link vector $\mathbf{p}_K$, from the start to the end of link K, will be

$$\mathbf{p}_K = -l_K(\cos\theta_{K_1}\cos\theta_{K_2}\boldsymbol{\lambda}_{K_1} + \sin\theta_{K_2}\boldsymbol{\lambda}_{K_2} - \sin\theta_{K_1}\cos\theta_{K_2}\boldsymbol{\lambda}_{K_3}). \tag{3.52}$$

If $\mathbf{r}_K$ is the position of lumped mass K in the inertial frame F_N, inertial positions of the whole system can be found by iterating down the hose. For the first link:

$$\mathbf{r}_A = \mathbf{p}_0 + \mathbf{p}_A \tag{3.53}$$

where $\mathbf{o}$ is the position in F_N of the hose attachment point. For subsequent links:

$$\mathbf{r}_K = \mathbf{r}_J + \mathbf{p}_K \tag{3.54}$$

Lumped mass velocities and accelerations may be found by differentiating in the inertial frame:

$$\mathbf{v}_K = \mathbf{v}_J + \dot{\mathbf{p}}_K \qquad \mathbf{a}_K = \mathbf{a}_J + \ddot{\mathbf{p}}_K \tag{3.55}$$

The derivatives of $\mathbf{p}_K$ are:

$$\dot{\mathbf{p}}_K = \sum_i (\mathbf{p}_{K,\theta_{K_i}} \dot{\theta}_{K_i}) + (\boldsymbol{\omega}_W \times \mathbf{p}_K) \tag{3.56}$$

$$\ddot{\mathbf{p}}_K = \sum_i (\mathbf{p}_{K,\theta_{K_i}} \ddot{\theta}_{K_i}) + \sum_i (\dot{\mathbf{p}}_{K,\theta_{K_i}} \dot{\theta}_{K_i}) + (\boldsymbol{\alpha}_W \times \mathbf{p}_K) + (\boldsymbol{\omega}_W \times \dot{\mathbf{p}}_K) \tag{3.57}$$

where $\mathbf{p}_{K,\theta_{K_i}} = \partial \mathbf{p}_K / \partial \theta_{K_i}$.

Link angle second derivatives can be found by taking the scalar product of equation 3.57 with $\mathbf{p}_{K,\theta_{K_i}}$. Since $\mathbf{p}_{K,\theta_{K_2}} \cdot \mathbf{p}_{K,\theta_{K_3}}$ is zero:

$$\ddot{\theta}_{K_j} = \mathbf{p}_{K,\theta_{K_j}} \cdot \left(\frac{\mathbf{a}_K - \mathbf{a}_J - \sum_i (\dot{\mathbf{p}}_{K,\theta_{K_j}} \dot{\theta}_{K_i}) - (\boldsymbol{\alpha}_W \times \mathbf{p}_K) - (\boldsymbol{\omega}_W \times \dot{\mathbf{p}}_K)}{\mathbf{p}_{K,\theta_{K_j}} \cdot \mathbf{p}_{K,\theta_{K_j}}} \right) \quad (j = 2, 3) \tag{3.58}$$

3.7.6 Equations of motion

The forces acting upon each lumped mass can be separated into external (i.e. gravity and aerodynamic forces), and internal (link tensions). For lumped mass K, with external forces $\mathbf{Q}_K$ and preceding and subsequent link tensions $\mathbf{t}_K$ and $\mathbf{t}_L$:

$$\mathbf{a}_K = \frac{\mathbf{Q}_K + \mathbf{t}_K + \mathbf{t}_L}{m_K} = \mu_K (\mathbf{Q}_K + \mathbf{t}_K + \mathbf{t}_L) \tag{3.59}$$

where, in Ro and Kamman's notation, μ_K denotes the reciprocal of mass m_K, i.e. $\mu_K = 1/m_K$.

3.7.7 Internal tensions

If all links are to have constant length l_K, internal hose tensions must constrain the links. Beginning with $(\mathbf{p}_K \cdot \mathbf{p}_K) = l_K^2$, and differentiating twice,

$$(\mathbf{a}_K - \mathbf{a}_J) \cdot \boldsymbol{\lambda}_{K_1} = l_K \boldsymbol{\lambda}_{K_1}^2. \tag{3.60}$$

Substituting equation 3.59 into 3.60,

$$-\mu_J (\boldsymbol{\lambda}_{J_1} \cdot \boldsymbol{\lambda}_{K_1}) t_J + (\mu_J + \mu_K) t_K - \mu_K (\boldsymbol{\lambda}_{L_1} \cdot \boldsymbol{\lambda}_{K_1}) t_L = l_K \dot{\boldsymbol{\lambda}}_{K_1}^2 + (\mu_J \mathbf{Q}_J - \mu_K \mathbf{Q}_K) \cdot \boldsymbol{\lambda}_{K_1} \tag{3.61}$$

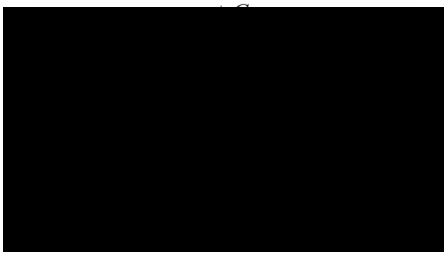

Figure 3.19: Hose drag geometry [118]

or,

$$[T]\{t\} = \{q\} \tag{3.62}$$

3.7.8 External forces

External force $\mathbf{Q}_K$ on lumped mass K is a combination of gravitational and aerodynamic forces:

$$\mathbf{Q}_K = m_K\mathbf{g} + \frac{1}{2}(\mathbf{D}_J + \mathbf{D}_K) \tag{3.63}$$

where $\mathbf{D}_K$ is the total aerodynamic force on link K.

Hose aerodynamics

For aerodynamic forces on hose links, Ro & Kamman use an empirical cylinder drag method from 1965 [117], however at typical refuelling conditions of 200 m/s at 4,000 m, $Re = 1.15 \times 10^6$ is supercritical. ESDU 80025 [118] provides detail on the influence of this, and a more modern method for calculating cylinder drag.

For these simulations, a fixed C_{D0} representing typical refuelling conditions was used. With an estimated effective roughness of 1×10^{-5} m (to be revisited) and a 7 cm diameter hose, ESDU 80025 gives $C_{D0} = 0.6$ (calculations are detailed in table 3.6). This is then converted to C_N, normal to the hose link, as shown in figure 3.19. ESDU 80025 states that for supercritical values of Re, tangential force C_T can be ignored.

The drag force on link K is then:

$$\mathbf{D}_K = \left(-\frac{1}{2}\rho_\infty \|\mathbf{v}_{Kn}\|^2 d_h l_K C_N\right) \frac{\mathbf{v}_{Kn}}{\|\mathbf{v}_{Kn}\|} \tag{3.64}$$

where $\mathbf{v}_{Kn} = \mathbf{v}_{K/air} - (\mathbf{v}_{K/air} \cdot \boldsymbol{\lambda}_{K_1})\boldsymbol{\lambda}_{K_1}$, the local normal velocity; d_h is

Table 3.6: Calculation of C_{D0} using ESDU 80025 method [118].

Parameter	Value	Note
Surface roughness ϵ	1×10^{-5} m	From table 10.1 in [118]
Hose diameter D	0.07 m	Used by Ro & Kamman [101]
ϵ/D	1.43×10^{-4}	
λ_R	1.1	From figure 2 in [118]
Free stream velocity V_∞	200 m/s	Typical refuelling condition
Altitude	4,000 m	Typical refuelling condition
Free stream densityρ	0.81913 kg/m^3	ISA
Dynamic viscosity μ	1.66×10^{-5} Pa s	ISA
Kinematic viscosity ν	2.03×10^{-5}	ISA
Re	6.9×10^5	
Turbulence intensity I_u	0.05	From table 10.2 in [118]
Turbulence scale ${}^rL_u$	140 m	From table 10.2 in [118]
$I_u(D/{}^rL_u)^{1/5}$	1.09×10^{-2}	
λ_{Tcrit}	2.3	From figure 3a in [118]
Re_{crit}	1.78×10^5	
Re/Re_{crit}	3.88	
$(\lambda_T - 1)/(\lambda_{Tcrit} - 1)$	0.4	From figure 3b in [118]
λ_T	1.52	
$Re_e = \lambda_T \lambda_R Re$	1.15×10^6	
C_{D0}	0.6	From figure 1c in [118]
C_N	$C_{D0} \cos^2 \phi$	From figure 4 in [118]

hose diameter; l_K is the link length; and $\mathbf{v}_{K/air} = \mathbf{v}_K - \mathbf{u}_K$, the velocity of lumped mass K relative to the local air velocity, including wake and turbulent effects.

Drogue aerodynamics

Ro & Kamman develop a parametric drag model based upon drogue geometry [101, 102]. In their model, parameters are normalised about median values. For initial simulations here, their median $C_{drogue} = 0.8$ is used, with drogue diameter $d_{drogue} = 0.6$ m. Drogue drag is then:

$$\mathbf{D}_{drogue} = -\frac{1}{2}\rho_\infty(\mathbf{v}_{N/air} \cdot \mathbf{v}_{N/air}) \left(\frac{\pi d_{drogue}^2}{4}\right) C_{drogue} \left(\frac{\mathbf{v}_{N/air}}{\|\mathbf{v}_{N/air}\|}\right) \quad (3.65)$$

The drogue drag is added to the final lumped mass, so the resultant external force for that node is

$$\mathbf{Q}_N = (m_n + m_{drogue})\mathbf{g} + \frac{1}{2}\mathbf{D}_N + \mathbf{D}_{drogue} \quad (3.66)$$

3.7.9 Validation

Simulations give qualitatively sensible results for free-swing and flight-condition scenarios. Figure 3.20 shows the hose released from a horizontal (towards the left) position, under gravitational and aerodynamic (still-air) forces. Figure 3.21 shows the hose profile at an airspeed of 120 m/s.

Ro and Kamman [101] compare their model against NASA Dryden flight test data [123]. To verify this implementation, a similar process can be followed.

The NASA Dryden measurements for steady state drogue position are given as DDVP, where

$$DDVP = \frac{V_D}{L_H} \quad (3.67)$$

with V_D the vertical distance from tow point to drogue coupling, and V_H the straight-line distance, as shown in figure 3.22.

NASA Dryden's data, shown in figure 3.23, does not vary appreciably with altitude, so a single set of simulations are conducted here at 4,000 m (13,000 ft). Using Ro and Kamman's dimensions for hose and drogue configuration (which are similar but not identical to those of the F/A-18's Aerial

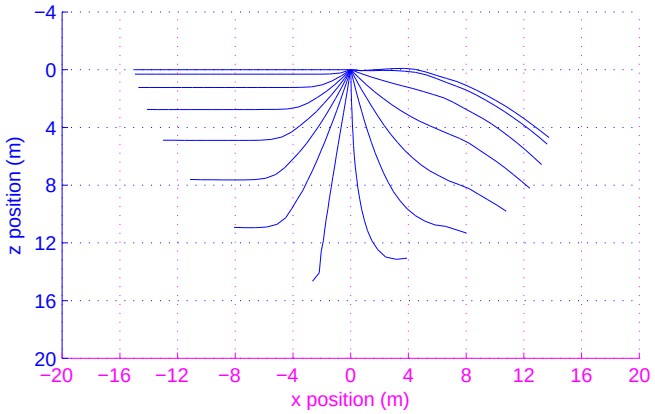

Figure 3.20: Hose free swing from horizontal left position, $\Delta t = 0.25$ s

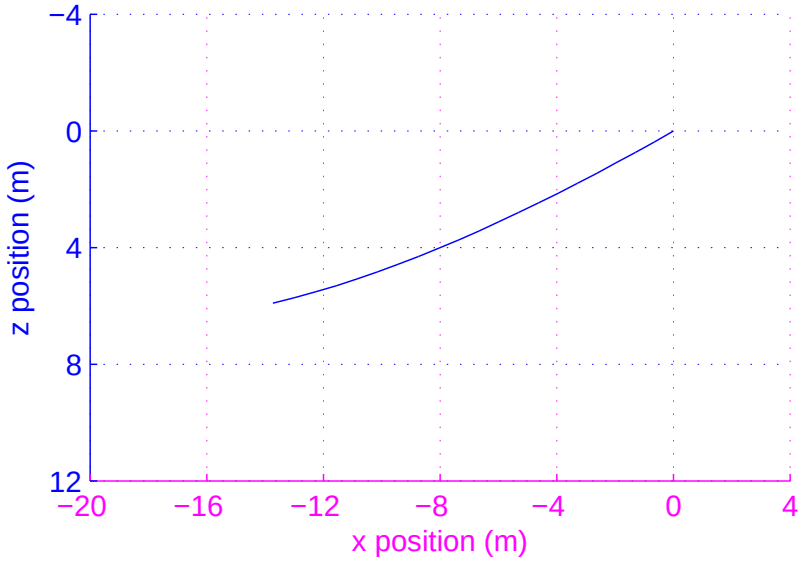

Figure 3.21: Hose static profile at 120 m/s

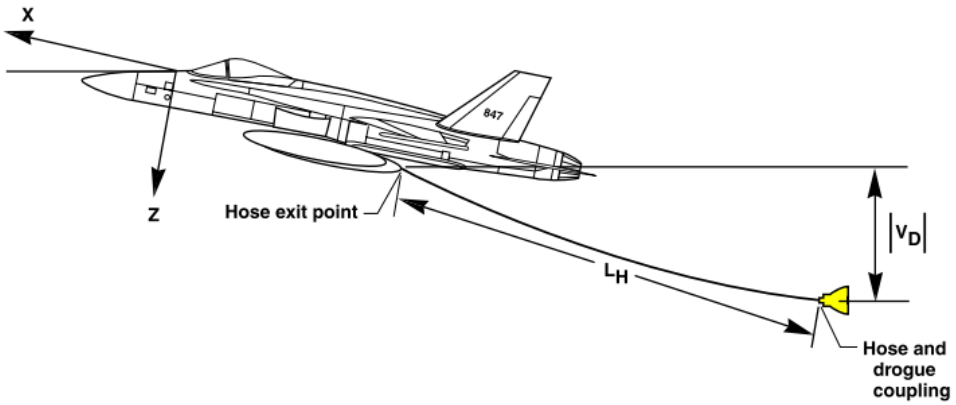

Figure 3.22: Dimensions for calculation of DDVP [123]

Refuelling Store (ARS) used by NASA Dryden), simulations with no turbulence, and no tanker wake or receiver upwash were run until the hose reached a steady state.

Figure 3.23 compares simulation results with flight data. Comparison is difficult without a scale on NASA Dryden's DDVP axis, but simulated data can be seen to qualitatively correlate. The increasing offset at lower airspeeds may be due to the lack of tanker downwash in the simulation, and other inconsistencies between simulated and measured conditions.

Hose-whip is a significant issue in AAR. By applying a horizontal force impulse to the drogue, the slackening of the hose caused by an over-speed drogue capture can be simulated. This results in the motion shown in figure 3.24: a pulse travels up the hose, is reflected at the tow point and returns, causing the drogue to whip violently.

3.8 Visualisation

SE position and pose data is output to a FlightGear-based 3D visualisation system, shown in figure 3.25, capable of displaying tanker, receiver, hose and drogue. This permits intuitive observation of simulations, and was also used in RMR demonstrations to industrial partners.

Visualisation output is disabled for repeated stochastic simulation runs, as faster than real-time simulation is desired in this case.

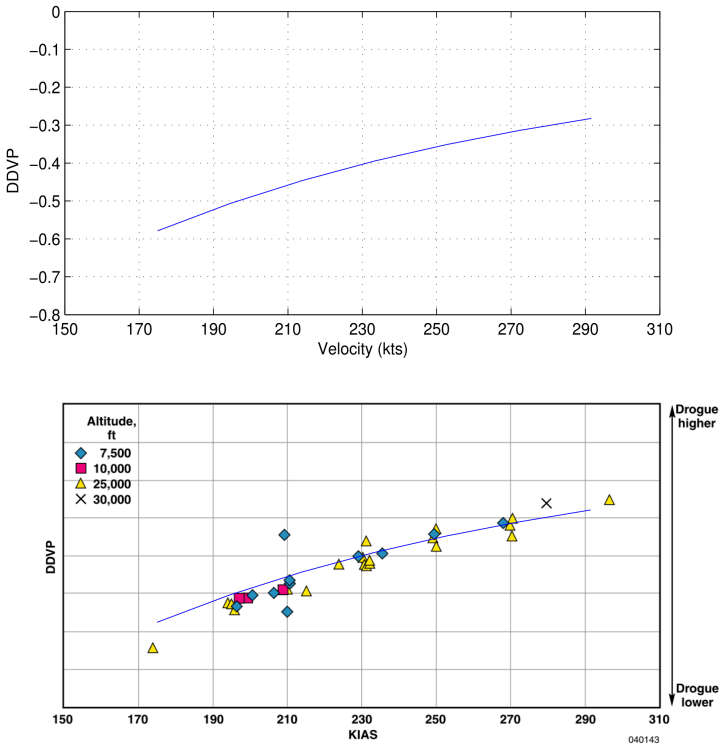

Figure 3.23: Simulated DDVP compared to NASA Dryden data [123] (simulated data superimposed in lower plot)

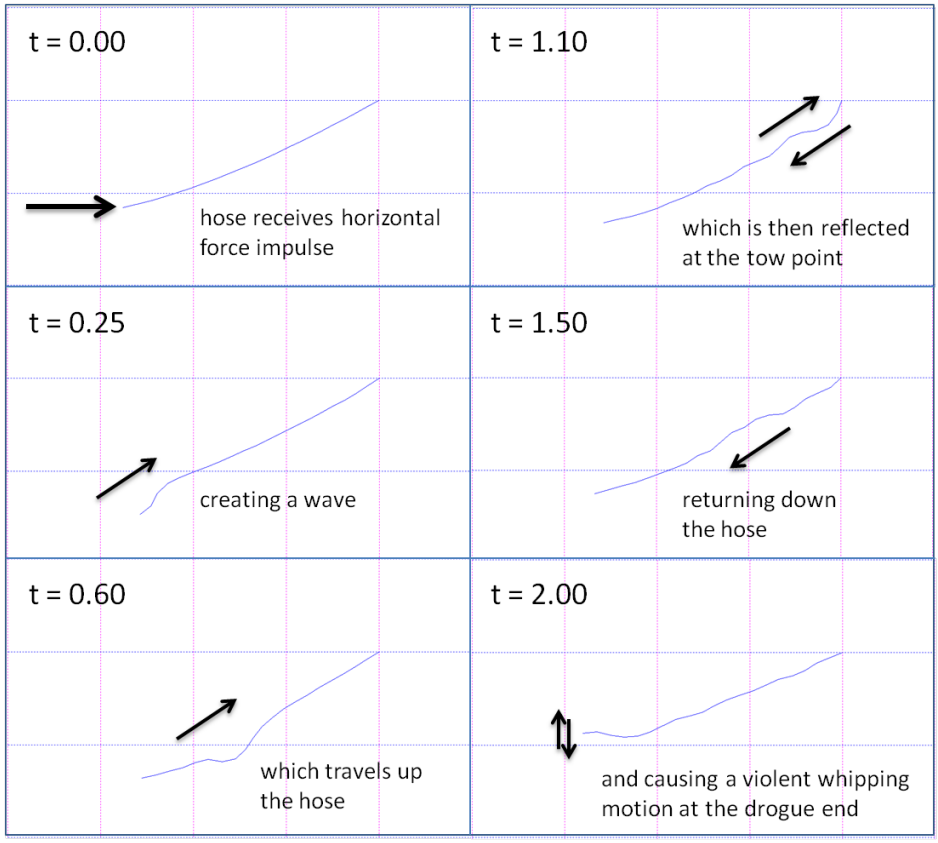

Figure 3.24: Simulation of hose whip

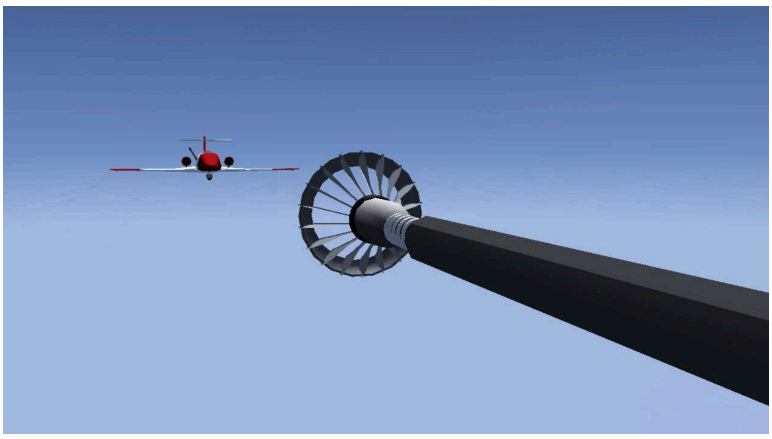

Figure 3.25: FlightGear visualisation

3.9 Simulation configuration

In order to compare the performance of different controller architectures and implementations, simulations were conducted for the final 10 m of approach and capture, with a reduced version of the full ASTRAEA SE. Modifications to the base version were made in order to increase the speed of iterative optimisation techniques and stochastic investigations, include:

- Tanker trimmed, straight and level at 8000 m altitude and 200 m/s airspeed.
- Receiver trimmed, straight and level, with probe tip 10 m astern and offset 1 m horizontally and vertically from drogue.
- Unused subsystems from wider ASTRAEA SE (alternative hose and wake vortex models) removed in order to improve simulation speed.
- Supervisory logic set to make a single capture attempt, and to abort if this fails drogue overrun, receiver flight envelope, and tanker safe-separation envelope criteria.
- Receiver initialised with its probe tip 10 m behind the drogue, with lateral and vertical offsets of 1 m, to simulate a fairly good, but not perfect, rendezvous and approach.
- For later simulations, drogue stabilisation, CC and IC receiver and drogue control systems added and configured as detailed in subsequent chapters.

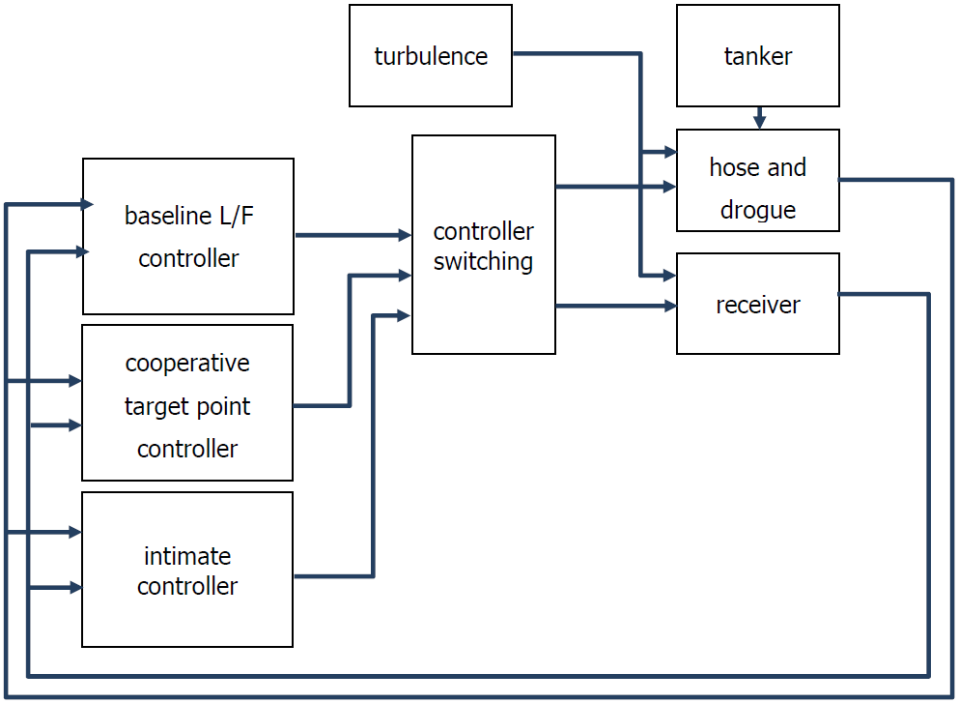

Figure 3.26: Simulation architecture

For simulations in subsequent chapters using alternative control architectures, cooperative and intimate controllers were added to the simulation, interfacing with receiver and hose/drogue states, outputs and demands. Figure 3.26 shows key components and interfaces of the complete simulation.

3.9.1 Turbulence

The drogue is subject to u, v, w turbulent gusts identical to those applied to the receiver, with a time delay between drogue and receiver gusts of $\Delta t = V_r/\Delta x_{pd}$ where V_r is receiver velocity and Δx_{pr} is the distance between receiver and drogue (figure 3.27).

3.9.2 Monte Carlo simulations

Capture simulations were run using the standard L/F controller detailed above in order to establish a baseline against which improvements can be measured. For a given set of initial conditions, i.e. relative tanker and receiver position, turbulence level, and turbulence probability seeds, the SE is deterministic.

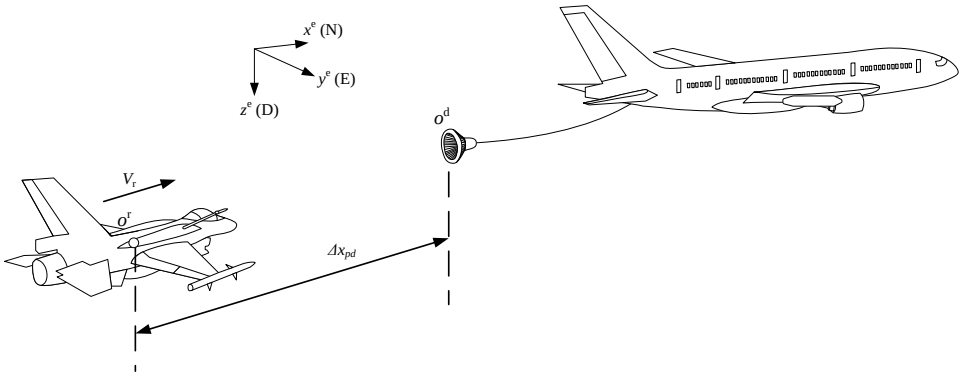

Figure 3.27: Gust delay between drogue and receiver

A Monte Carlo approach [160] was used, with one hundred capture attempts simulated at each level of turbulence in order to determine a success rate. A randomised set of turbulence seeds were generated and stored for use with each simulation configuration. The number of successful captures out of the hundred was taken to be the 'capture rate', effectively a probability of capture for a given level of turbulence.

This approach applies to all subsequent comparative simulations – all consist of 100 capture attempts for each level of turbulence. Increased confidence could be gained with a higher number of runs, but simulation time limited this. Future work could further optimise the simulation to enable this.

3.9.3 SE performance

The SE can simulate AAAR at faster than real-time rates, which permits later real-time simulation using the RMR. Without RMR or visualisation use, each capture simulation takes around 15 seconds of processing time to compute, using an office desktop running 32-bit Windows XP and MATLAB R2010a, on a 4-core 3.2GHz Intel Core i5 with 3GB of RAM. Simulink's 'Rapid Accelerator' mode was used, so that the model is compiled just once for repeated runs.

For each control architecture, the simulation was run 100 times for three levels of turbulence, plus once for zero turbulence (as all results would be identical), thus taking around 1h15m for a full set of results. For simulations investigating continuously-varying turbulence, 10 levels of turbulence were investigated, leading to 1,001 runs with a total time of just over 4h.

3.10 RMR simulation

The University of Bristol (UoB) has developed a RMR facility [27, 161] in conjunction with Cobham plc, based in the University's Advanced Composites Centre for Innovation in Science (ACCIS). The RMR facility has HIL simulation capabilities which provide a cost effective research and trials environment for evolving technology. The RMR facility employs two manipulators capable of supporting full-size refuelling apparatus with the capability to integrate pose estimation systems into a real-time control loop. In doing so the suitability of vision systems, tracking algorithms, control system designs, and refuelling hardware can be tested in a safe and repeatable environment.

The facility was principally devised for hardware-in-the-loop testing for cost-effective research trials for evolving aerial refuelling technology, however the RMR is also capable of investigating wider technology exploitation and utility to industry and academia for relative motion work [30]. Unlike the previous works [149, 162] which used reduced scale models, the RMR facility employs two manipulators capable of supporting full-size refuelling apparatus, along with the capability to integrate pose estimation systems into a real-time control loop. In doing so the suitability of vision systems, tracking algorithms, control system designs, and refuelling hardware that are mature in their development can be tested in a safe and repeatable environment.

Simulations are written in the Simulink environment and compiled with the Simulink Coder toolbox for use on a PXIe-8133RT platform using National Instruments' Veristand target language compiler. Simulations can cover the wider refuelling scenario in order to develop and investigate control strategies, with the RMR specifically providing the HIL capability for the more complex hookup space. The real-time operating system is capable of overseeing the deterministic execution of multiple models, or processes at defined rates. The primary control loop executes the simulation model and the supervisory process in turn, both at a 1 kHz rate. Compared to flight tests, the RMR facility has the important advantages of shorter lead time, reduced cost, safer operation, and guaranteed repeatability. A hardware summary is given in table 3.7.

Table 3.7: RMR software and hardware configuration

Component	Specification
Real-time hardware	PXIe-8133RT
Robotic arms	2 × ABB IRB6640
Track	ABB IRBT6004
Robot controller	ABB IRC5

3.11 Baseline L/F simulations

As a baseline for comparison with alternative control architectures, open-loop simulations with no drogue control are presented. Flight conditions were 200 m/s at 8,000 m, with the receiver starting 100 m behind the tanker. 100 capture simulations, with varying turbulent seeds, were conducted.

Plots in figure 3.28 show drogue and receiver vertical position and relative error for the last 10 seconds before capture under light turbulence[6]. Plots show the final 10 seconds of approach, and terminate when the longitudinal separation between probe and drogue is zero – success and failure criteria are as detailed in section 3.5.5. To be recorded as a success, lateral and vertical separation between probe and drogue must be within the drogue capture envelope, Each plot is for a single capture attempt, longitudinal separation reaching zero at the final plot point.

Figure 3.29 shows a failed capture under heavy turbulence (level 18). The drogue diverges by up to 1.5 m above and below its steady-state position, making capture by the receiver impossible.

To demonstrate the effect of turbulence on the relative magnitudes of receiver and drogue motion, successful capture under light and moderate turbulence is shown in figure 3.30. Drogue motion for these captures is shown in figure 3.31. The low-frequency vertical drogue motion is an artifact of tanker motion, and is present in all subsequent drogue capture plots – motion about the 'no turbulence' plot shows drogue offset from steady state position.

Turbulence levels can be varied continuously, to permit intermediate levels of turbulence between the light/moderate/severe categories. A 'better'

[6]For brevity, simulation plots show vertical response only, unless there are notable features in lateral or longitudinal directions. Simulations are all 6-DoF unless stated otherwise.

controller will be more tolerant to adverse atmospheric conditions, and will therefore maintain a higher capture rate under increased turbulence.

Figure 3.32 shows the capture rate across the turbulence spectrum for the baseline L/F simulation. For reference, on this scale light turbulence has a level of 3, and severe is level 18. It is clear that any disturbance beyond that of light turbulence reduces capture rate dramatically, and if AAAR is desired in any more adverse conditions then improvement to drogue-receiver convergence is required. This method will be used to compare control architectures in later chapters.

Capture rates in light/moderate/severe turbulence are given in table 3.8, for:

- static drogue (that is, static in the tanker reference frame): where the drogue is unaffected by turbulence – an unrealistic situation but useful to establish the performance of the receiver controller,
- open-loop drogue: where the drogue is affected by turbulence, as detailed in section 3.9.1.

Table 3.8: Baseline capture rates

	Turbulence			
	None	Low	Moderate	Severe
Static drogue	100 %	80 %	50 %	2 %
Open-loop drogue	100 %	59 %	17 %	0 %

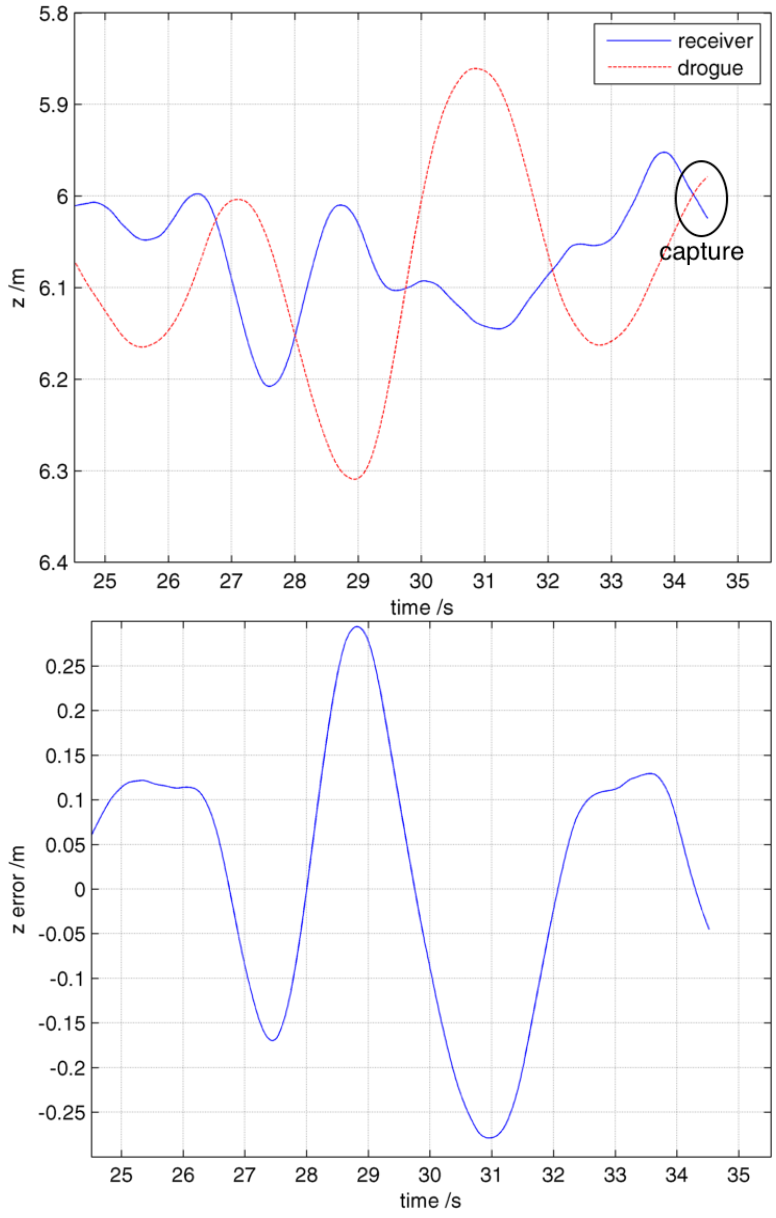

Figure 3.28: Vertical position and error of receiver and drogue with L/F control under light turbulence

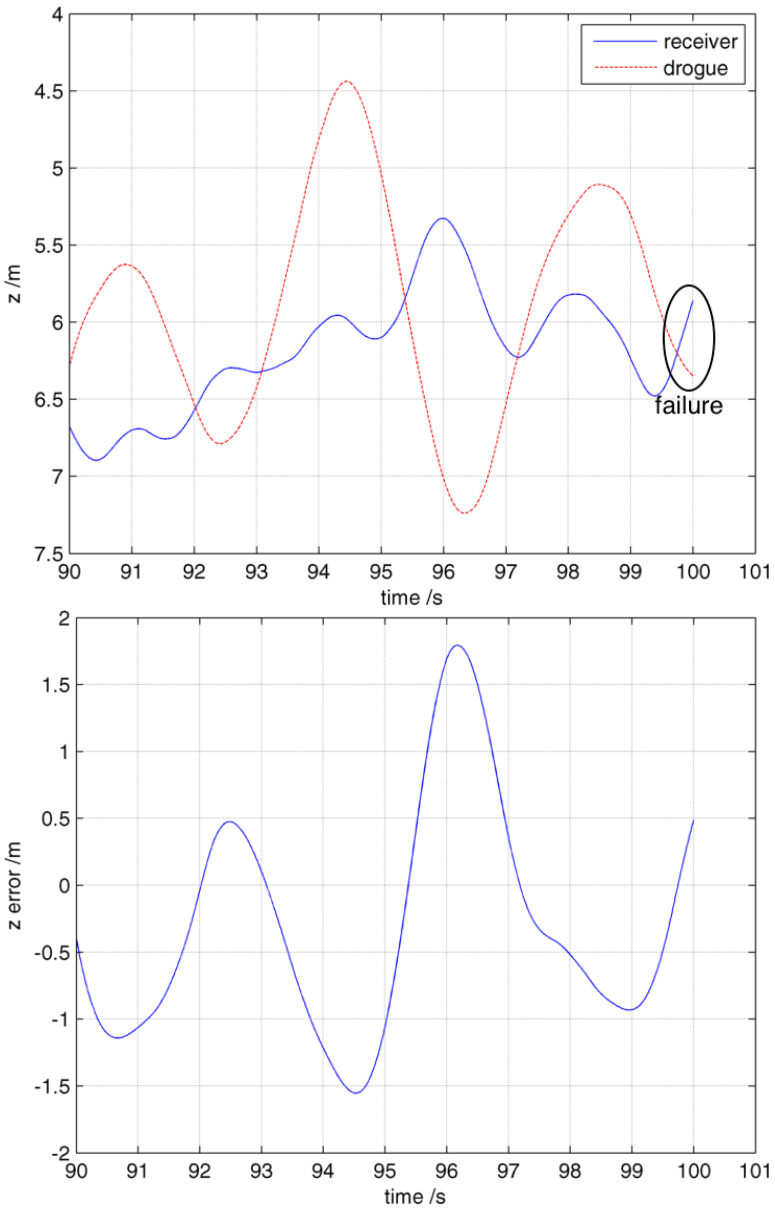

Figure 3.29: Vertical position and error of receiver and drogue with L/F control under severe turbulence

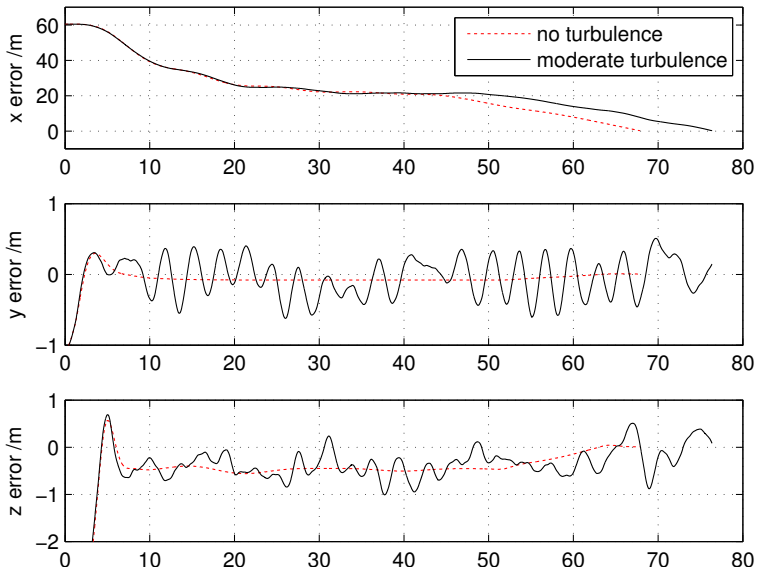

Figure 3.30: Drogue-receiver error with no and moderate turbulence

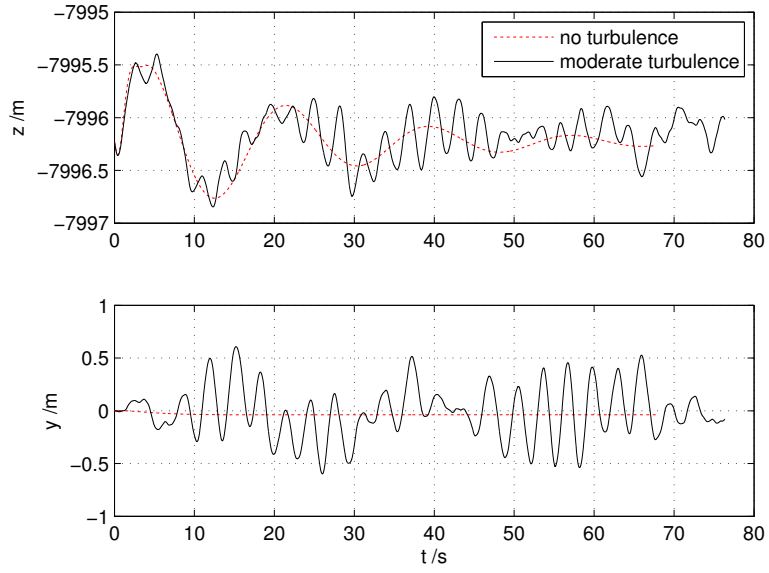

Figure 3.31: Open-loop drogue motion with no and moderate turbulence

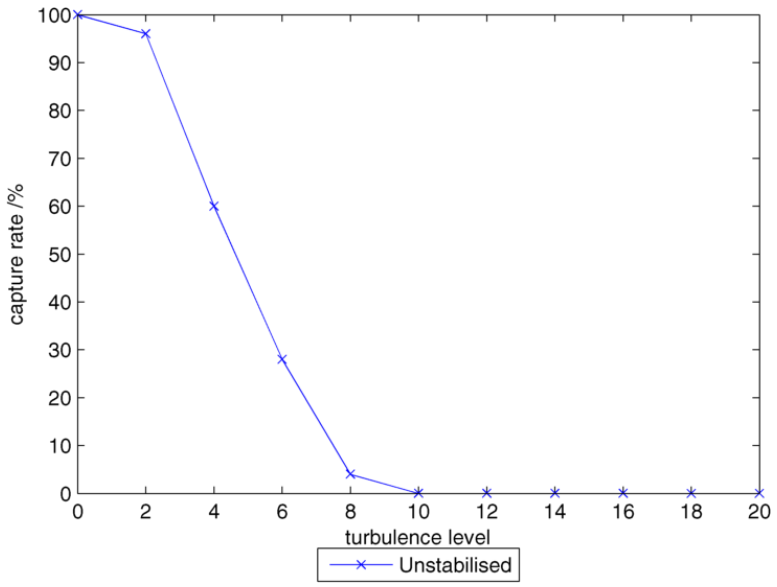

Figure 3.32: Capture rate for L/F controller under varying turbulence.

Chapter 4

Drogue control

AAR is a taxing process, whether manually controlled or automated. One issue is the effect of gusts on the refuelling drogue. The drogue has non-negligible side profile and gusts can cause significant motion. An active stabilisation method for the drogue may increase capture rates by minimising drogue motion under turbulence.

Section 3.7 of this thesis implemented and verified a hose and drogue model. This chapter surveys and characterises potential actuation methods, and an isolated model of the hose and drogue is augmented with a representative control force model. A PID control system is designed and several tuning approaches are trialled.

This controlled model is integrated into the wider SE and trials are conducted to determine capture success rates under varying turbulence, using the Monte Carlo method previously detailed in section 3.9.2.

4.1 Actuation methods

There is a range of existing work on drogue stabilisation. This section reviews published literature, with a view to establishing potential actuation methods and control approaches.

There are practical issues to consider when selecting a method of generating control forces. An ideal method would require minimal modification of existing systems.

4.1.1 Control surfaces

An obvious method of generating control forces on the drogue is the addition of aerodynamic control surfaces. Ro, Kamman and Kuk [92, 163] present simulations and wind tunnel tests of a cruciform arrangement of aerofoils (figure 4.1), controlled by acceleration feedback via a manually-tuned PID controller. They identify that the minimum actuation force required for bow-wave rejection is of the order of 45 N at their flight conditions. Their simulations indicate an almost complete reduction in turbulent drogue motion, whereas in wind-tunnel tests (with a 1/3-scale drogue on a 1 m rigid bar) they achieve a more modest level of stabilisation.

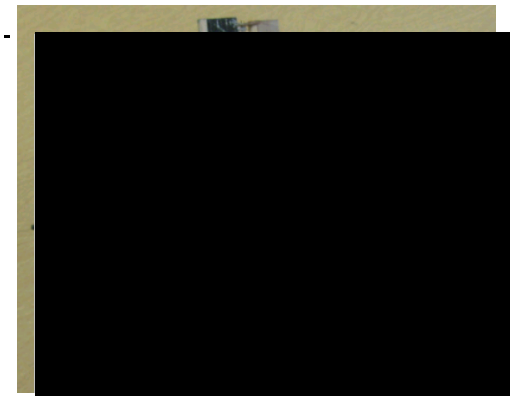

Figure 4.1: Drogue with control surfaces [163]

Thompson [164], presents wind tunnel data for a half-scale drogue (figure 4.2) comparing force generation via drogue incidence, control surfaces and spoilers. Data presented for aerodynamic control surfaces indicates an achievable force of around 300 N for a full-scale drogue. Thompson comments that his actuation method, with servos within the hose and drogue coupling, would need to be modified for an actual application to prevent obstruction of fuel flow. He also identifies that integration with existing systems could prove challenging if the drogue is required to collapse for stowage.

4.1.2 Canopy manipulation

Williamson et al [18] present a solution that uses manipulation of the drogue canopy to generate control forces, via an arrangement shown in figure 4.3. Varying the angle between leading and trailing edge strut arms changes

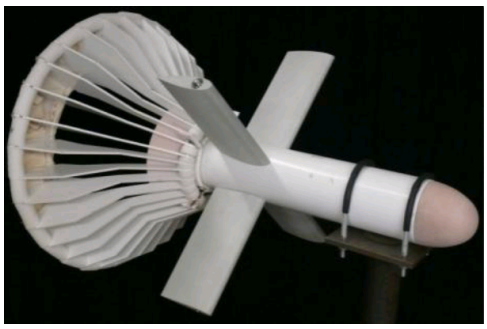

Figure 4.2: Drogue with control surfaces [164]

the local centre of pressure, generating side-forces of the order of 300 N at 130 m/s. They use wind tunnel testing of a drogue, with four actuators in a cruciform configuration, to generate an aerodynamic model, and then use a hose-drogue simulation to assess achievable lateral and vertical offsets from the steady-state uncontrolled position. They develop a control algorithm based on position feedback, for example via Differential GPS (DGPS), and acceleration via an Inertial Measurement Unit (IMU). This is optimised using a LQR approach, and stabilisation under the effects of wind, receiver forebody effects and disturbances is achieved.

Figure 4.3: Drogue with canopy manipulation [18]

The stated advantages of Williamson et al's approach include:

- builds upon existing drogue architectures,
- eliminates the need for additional control surfaces, which could detach and cause FOD damage,
- no requirement for tanker modification as all systems fit within refuelling coupling.

There is no mention of the issue of powering electronic systems at the drogue (but this will be an issue with almost any drogue control method), or of sensing methods.

4.1.3 Spoilers

Waghorn [165], Sims-Williams and Dominy [166], and Francis [167], of Durham University, use spoilers in a triangular configuration to create control forces. Their wind-tunnel tests and simulations indicate achievable forces of around 200 N for a full-scale drogue at 200 m/s and 8,000 m.

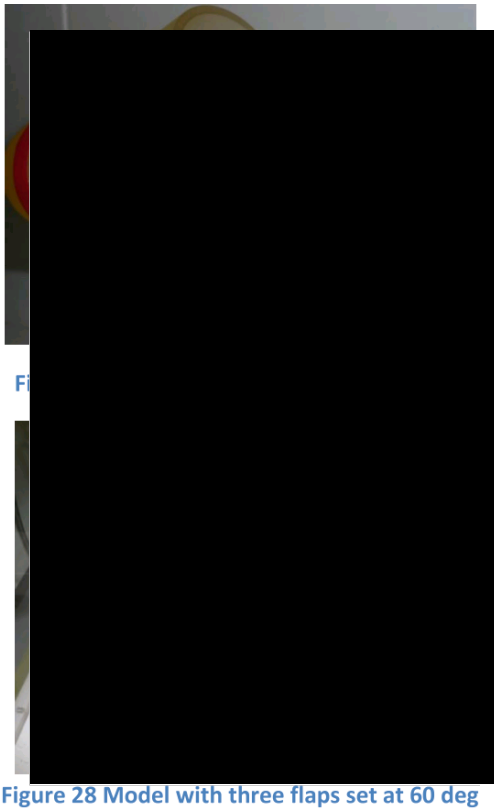

Figure 4.4: Drogue with spoilers [167]

Thompson's [164] wind tunnel data for a single spoiler (figure 4.5), indicate that a lateral control force of approximately 350 N is achievable via spoilers, with a correspondingly significant increase in drag.

A spoiler-based method as detailed here will likely be easier to stow than the other approaches above, due to the ability to collapse the control surfaces flush against the drogue.

Figure 4.5: Drogue with spoiler [164]

4.1.4 Other methods

Other methods of control force generation are feasible, such as pneumatic (via forced or ducted air), gyroscopic, and hose pressure manipulation. Given the consistency and success of the methods previously described in this section, the fact that these other methods are sparsely investigated in available literature, and their increased complexity compared to those methods presented, they are not reviewed here.

4.1.5 Method selection

A trade-off study was conducted, and was presented in an internal ASTRAEA/Cobham plc deliverable [168]. Recommendations were made for promising candidate architectures to pursue, but given the early development stages of all methods surveyed, keeping the effectors and actuators in the SE abstract is desirable at this stage – the indication from the literature is that force generation on the drogue is certainly feasible, but the method of implementation will be strongly driven by practical considerations that should be investigated in further more detailed design stages.

For interest, the trade-off ranking is shown in table 4.1. Full justification is given in the internal report [168].

4.2 Implementation in SE

For the AAAR SE a direct force demand method is implemented via lateral and vertical actuator models with a lag of $\frac{30}{s+30}$ and ± 150 N saturation

Table 4.1: Design scheme ranking (lower is better) – summary of internal report [168]

		Scheme			
		Fins	Spoilers	Canopy manip	Tri-flap
Integration	Stowage	4	1	3	2
	Power	1	2	3	4
Reliability	Comp count	3	1	4	1
	Maintenance	2	1	4	3
Robustness	Impact	3	1	2	4
	Wear	3	1	4	2
Aerodynamics	Coupling	1	2	3	4
	Effectiveness	1	4	2	3
Total		**18**	**13**	**25**	**23**

(6% of drogue drag at the selected operating point). This is conservative compared to all of the implementations referenced above.

The response of the non-linear model to a step input in lateral and vertical force demand is shown in figure 4.6 – lateral and vertical modes show slight coupling due to the fact that a lateral force will cause the drogue to move in an arc, as tension in the hose will pull it upwards. They are decoupled in the linearised model. For a force of 100 N, the displacement from initial steady-state conditions settles to around 0.75 m laterally and 1 m vertically (at a higher and faster operating point than many of the works referenced in section 4.1).

Linearisation

The 20-element finite-segment model is linearised about its steady-state conditions at 8,000 m and 200 m/s. This 80-state model can be reduced to simpler order state-space representations through balanced truncation model reduction methods (following Ro and Kamman's approach, implemented via MATLAB's `reduce` function) for control system design. Pole-zero maps and frequency responses for full-, 6th-, and 2nd-order models are shown in figures 4.7 and 4.8. The dominant response is at $0 \pm 2i$, and it is evident that the lower-order representations retain the gross action of the full-order linear model with good accuracy up to fairly high frequencies. For situations

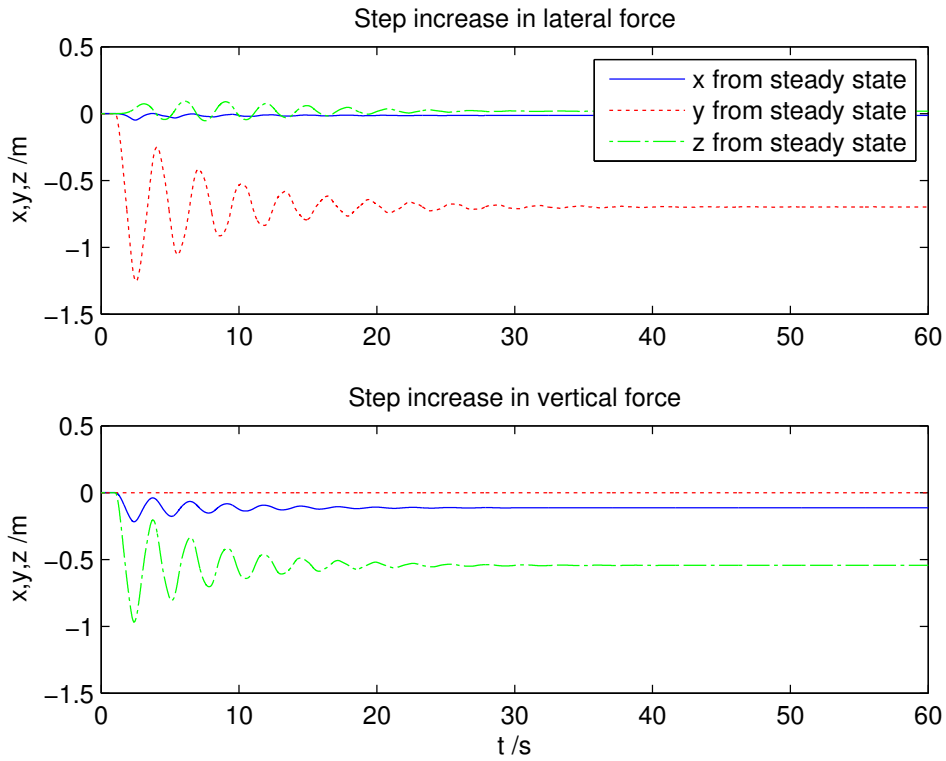

Figure 4.6: Non-linear hose-drogue model response to lateral and vertical force demands, $\Delta F = 100$ N @ $t = 1.00$ s

where the higher-frequency response needs to be represented, the full-order model is more appropriate.

Control system design

Control is against the error between demanded and actual drogue position in y and z, posed as an offset from the drogue tow point. Position could be obtained through optical and other methods, either by observing the drogue from the tanker (which will require data transmission from tanker to drogue) or observing the tanker from the drogue (perhaps against reference markers on the tanker). It could also be integrated from acceleration sensed via IMU, noting that drift must be corrected for somehow – if stabilisation time is short, it may be possible in still air to permit the drogue to return to its uncontrolled, steady-state position and reset its integrators.

A Proportional, Integral, Derivative (PID) controller is designed (figure 4.9) with separate lateral and vertical controllers. Initial gains are determined via the Ziegler-Nichols method [169]. According to this, the critical gain K_u is found by setting integral and derivative gains to zero and increasing proportional gain until the output oscillates with constant amplitude. Critical period T_u is the period of this oscillation. Values for lateral and vertical channels for the decoupled, second-order linear model are shown in table 4.2 – these appear relatively high due to unit conversions in the feeding back of position errors to force inputs, and the moderately damped response of the open-loop hose model. Position error in metres is being fed into a force demand in Newtons, and correction of errors in the order of 0.1 m requires forces in the order of 50-100 N.

For classic Ziegler-Nichols (ZN) tuning, gains are calculated using the formulae in the first row of table 4.3. The step response of the second-order linear model is shown in the first row of figure 4.10. The ZN gains produce good output tracking, but with a reasonably oscillatory response which is not ideal for drogue capture.

There exist a range of variations on the Ziegler-Nichols approach [170]. 'Some-Overshoot' (SO-OV) gains are shown in the second row of table 4.3. The response provided by these gains (second row of figure 4.10) is more suited to enabling drogue capture.

For non-cooperative control it is assumed that, within limits, steady-state error is not an issue as the receiver is aiming for the drogue whatever

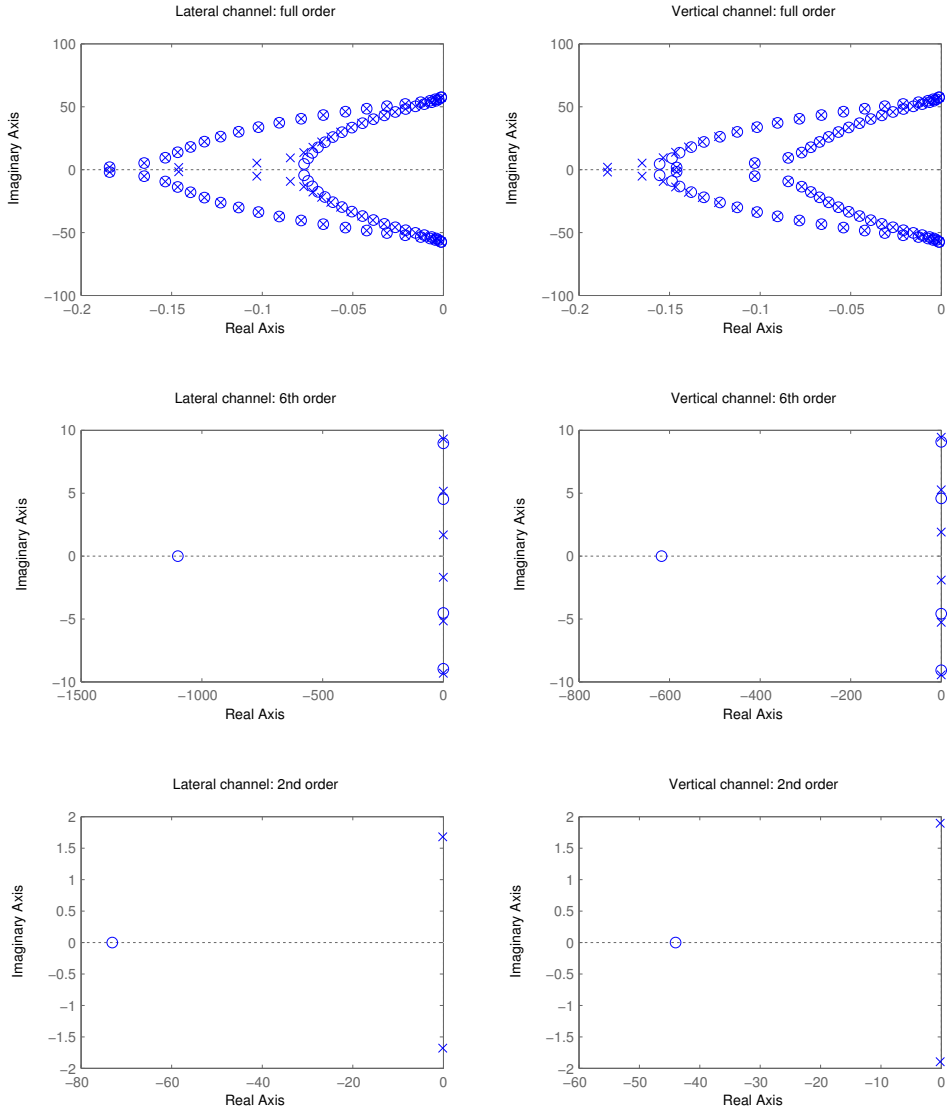

Figure 4.7: Pole-zero map of full, 6th and 2nd order linearised models

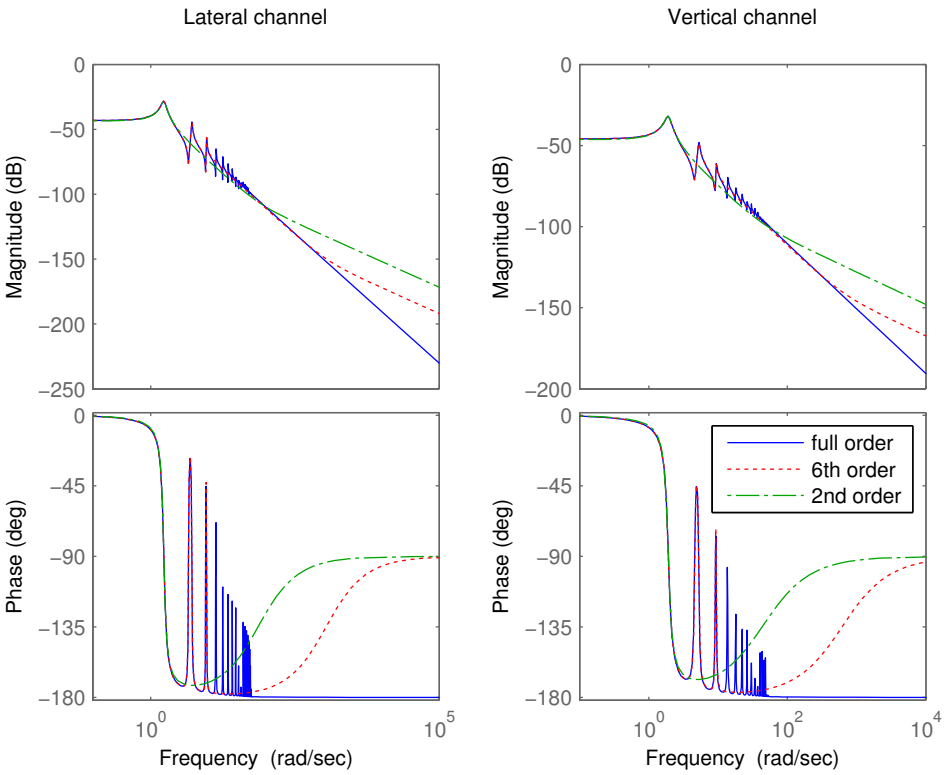

Figure 4.8: Frequency response of full, 6th and 2nd order linearised models

its absolute position. A controller with minimal integral gain and high derivative (HD) would provide a 'laggy' response with good disturbance rejection but poor steady-state error. For interest, arbitrary gains were selected, given in the third row of table 4.3 – although it should be noted that these would likely be unrealistic in a practical implementation. Step response for these is in the third row of figure 4.10.

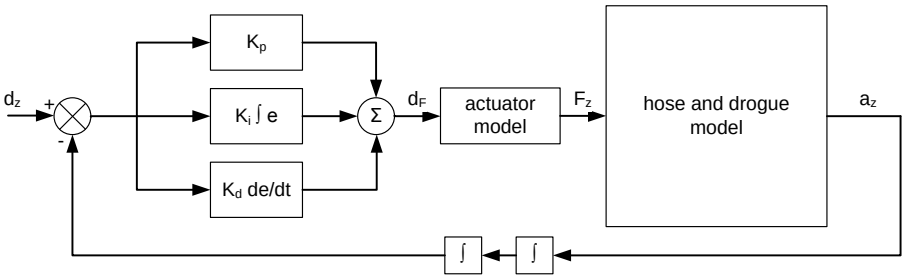

Figure 4.9: Drogue PID control (vertical channel)

Table 4.2: Critical gain and period for 2nd-order linear model

	K_u	T_u
Lateral channel	809	1.48 s
Vertical channel	2054	1.00 s

Table 4.3: Controller gains

	K_p	K_i	K_d
Ziegler-Nichols PID	$0.6K_u$	$2K_p/T_u$	$K_pT_u/8$
lateral =	485.40	695.95	89.80
vertical =	1232.4	2464.8	154.05
Some-Overshoot PID	$0.33K_u$	K_p/T_u	$K_pT_u/3$
lateral =	266.97	180.39	131.71
vertical =	677.82	266.97	88.99
High-Derivative PD	arbitrary	arbitrary	arbitrary
lateral =	100	0	500
vertical =	100	0	500

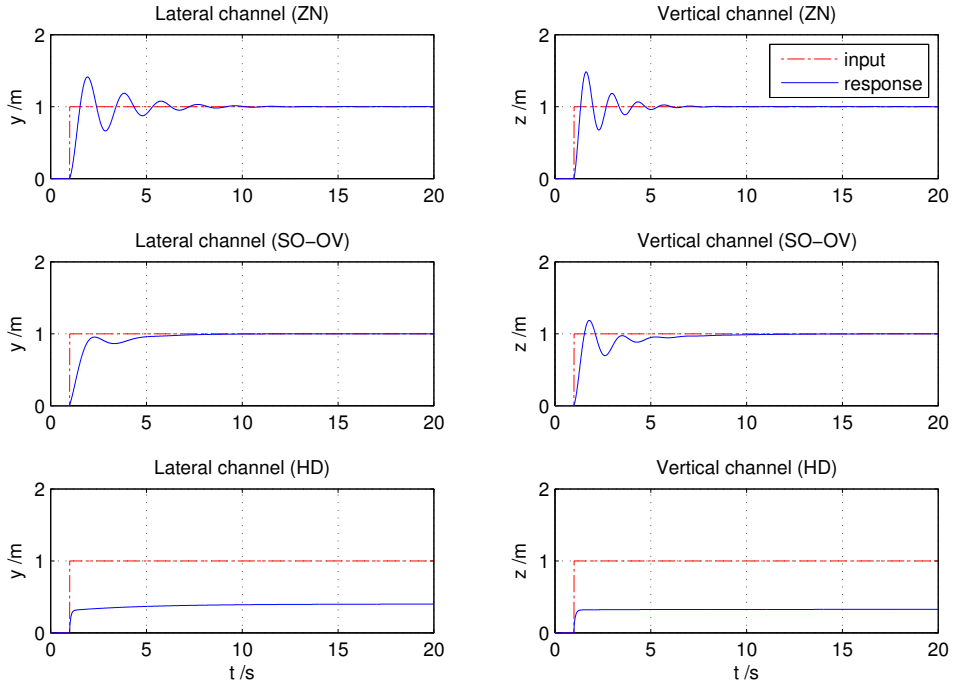

Figure 4.10: Step response of 2nd-order model, with PID controller using Ziegler-Nichols, Some-Overshoot and High-Derivative gains

Table 4.4: Closed-loop capture rates

	Turbulence			
	None	Low	Moderate	Severe
Finite-segment open-loop	100 %	59 %	17 %	0 %
Some-Overshoot PID	100 %	72 %	32 %	0 %
High-Derivative PD	100 %	87 %	40 %	0 %

4.3 Simulation results

Comparing stabilised drogue motion shown in figures 4.11-4.16 against the baseline open-loop captures previously shown in figures 3.30 and 3.31, the effect of the controller can be observed. Table 4.4 and figure 4.19 show that drogue stabilisation provides significant improvement in capture rate throughout the turbulence spectrum. Force demands for all three gain profiles trialled are given in figure 4.20.

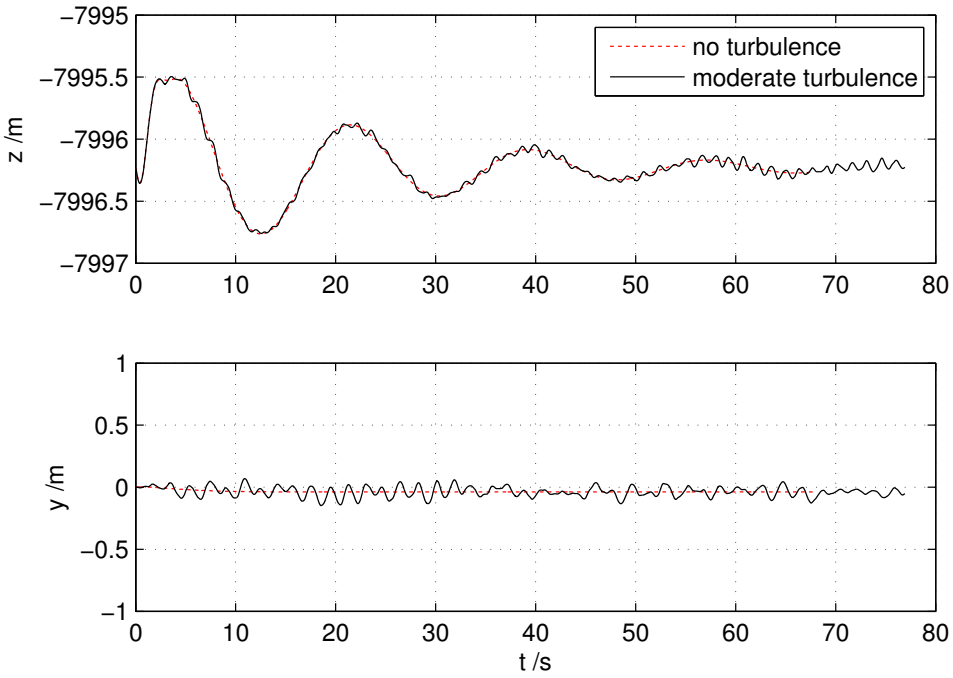

Figure 4.11: Closed-loop drogue motion under varying turbulence (ZN gains)

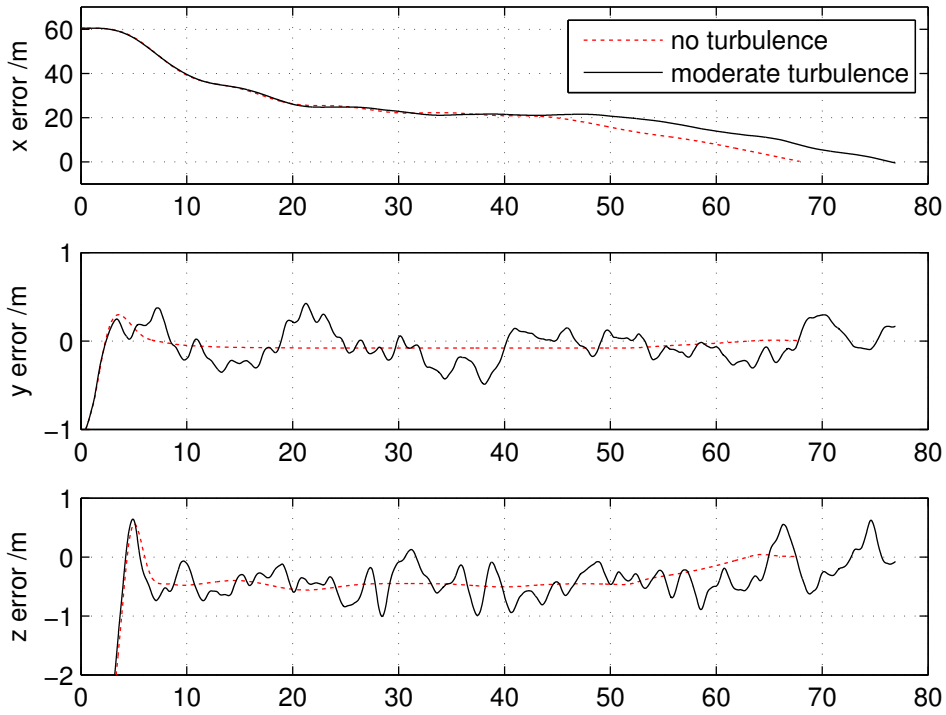

Figure 4.12: Closed-loop drogue-receiver error under varying turbulence (ZN gains)

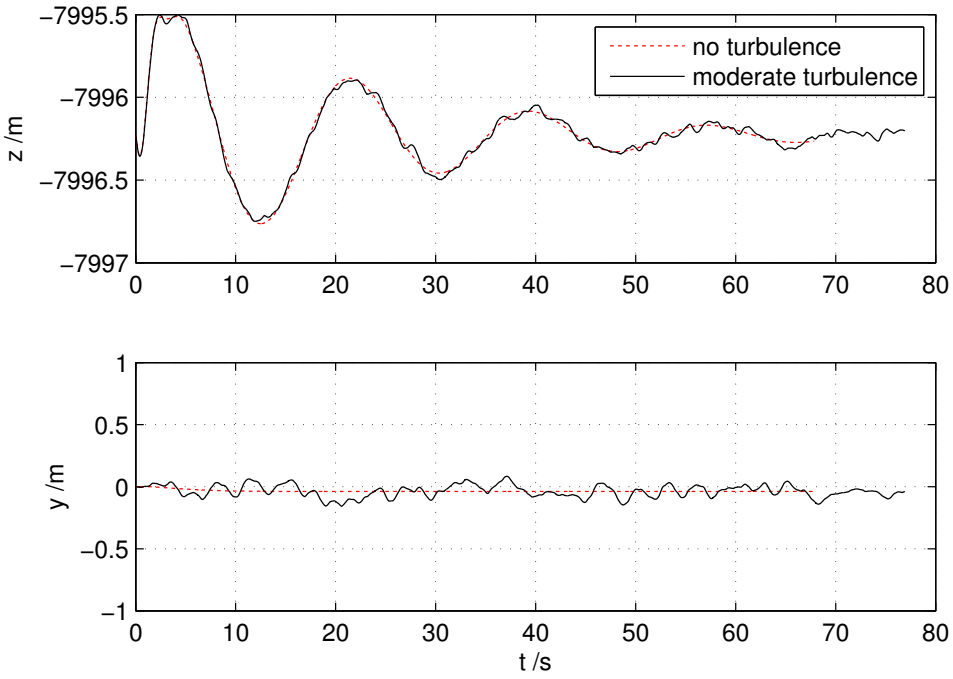

Figure 4.13: Closed-loop drogue motion under varying turbulence (SO-OV gains)

4.4 Dynamically matched drogue

It was noted whilst optimising the drogue stabilisation controller that gains which modify the drogue's gust response to cause it to behave more like the receiver appear to be beneficial – if the drogue responds in a similar way to the receiver then although position error from the refuelling envelope centre will be worse, the error over time between drogue and probe will decrease.

In order to briefly investigate this phenomenon further, linearised longitudinal models of receiver and drogue are used. The drogue is regulated by the same force-demand PID controller. The optimum gains to cause the drogue to respond in a manner similar to the receiver are found via an unconstrained nonlinear optimisation approach using the Nelder-Mead simplex algorithm [171] (via MATLAB's fminsearch function), minimising integrated position error over time. Drogue and receiver are passed identical demands to track the drogue's steady state position.

With the drogue controller gains set to those that bring its response closest to that of the receiver, the response is as shown in figure 4.21. The

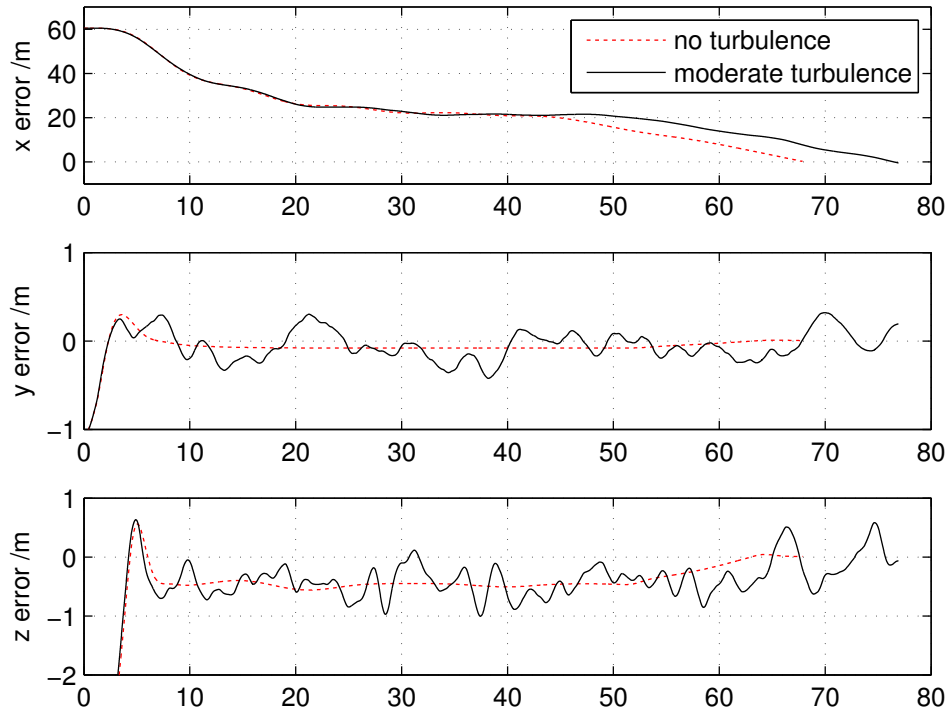

Figure 4.14: Closed-loop drogue-receiver error under varying turbulence (SO-OV gains)

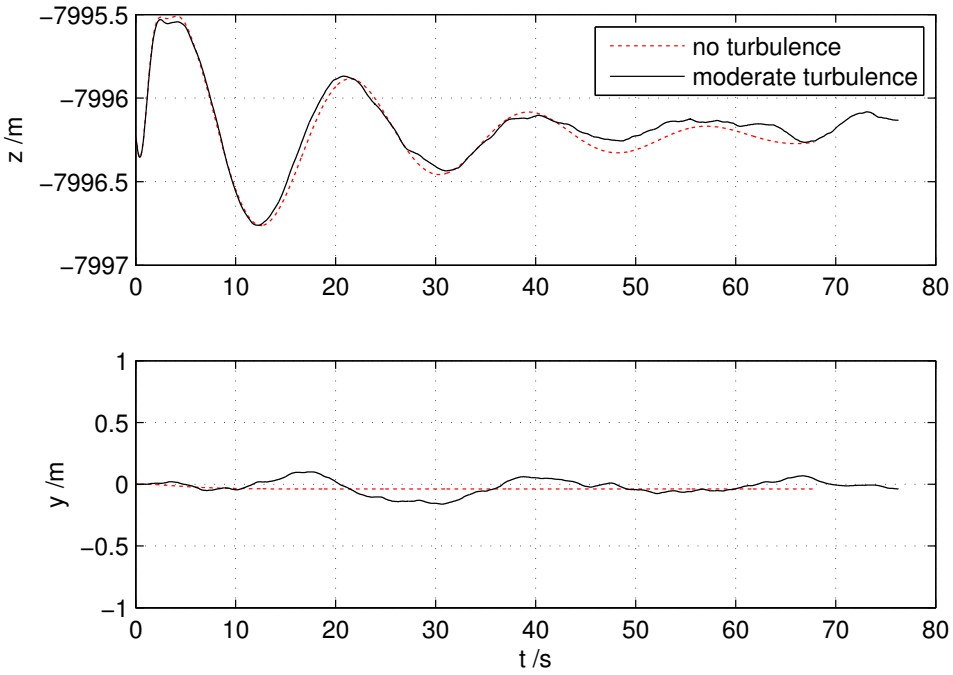

Figure 4.15: Closed-loop drogue motion under varying turbulence (HD gains)

drogue can be seen to behave similarly to the receiver in its response to gusts, and tracking error is greatly reduced. This does, however, demand significantly more force than stabilisation, shown in figure 4.22.

It should also be noted that the gusts will not impact receiver and drogue simultaneously, but will instead be subject to a time delay between drogue and receiver gusts of $\frac{\Delta t = V_r}{\Delta x_{rd}}$, where V_r is receiver velocity and Δx_{rd} is the distance between receiver and drogue.

This approach is not investigated further in this thesis, but should be considered for future work.

4.5 Summary of drogue control

A finite-segment drogue model has been constructed and validated against flight data. The model integrates with the RMR AAAR environment and runs in real-time. It has been linearised and characterised, and reduced-order representations have been shown to be valid and useful in system characterisation and control design.

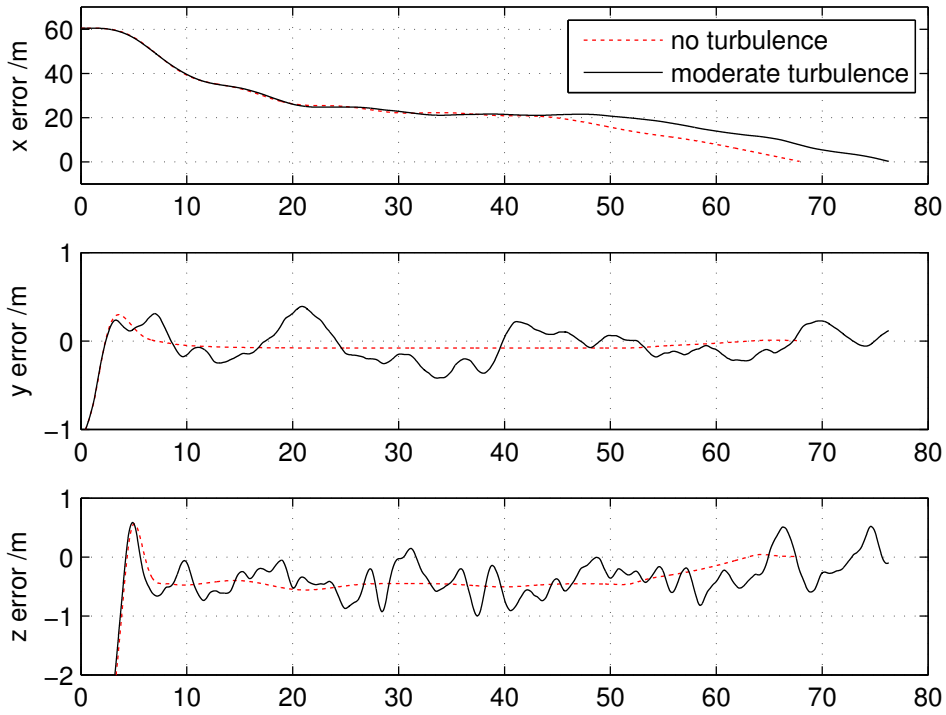

Figure 4.16: Closed-loop drogue-receiver error under varying turbulence (HD gains)

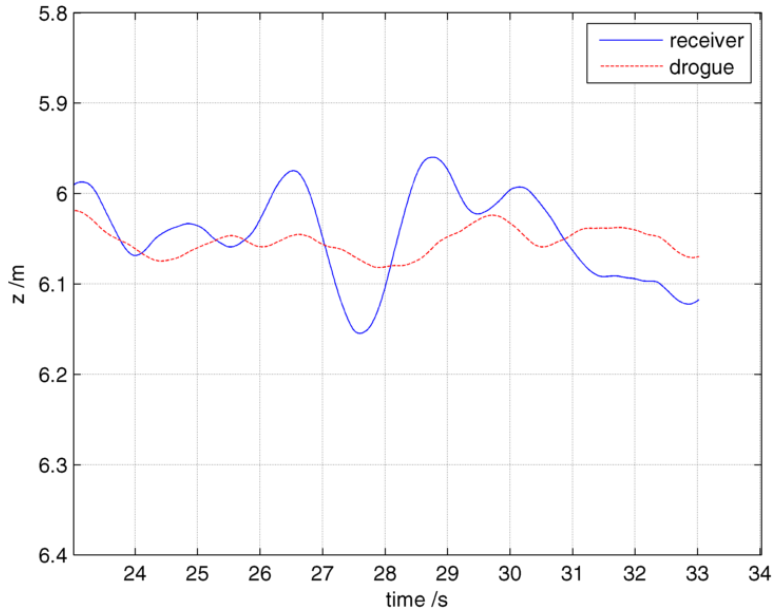

Figure 4.17: Vertical position of receiver and stabilised drogue under light turbulence – successful capture.

Drogue stabilisation using the reviewed actuation methods is certainly feasible – required force in all simulations was well within the available force suggested in the literature. Rejection of wake and bow wave effects will increase the force requirement but the conservative saturation limit of 150 N was never approached in these simulations, and achievable force is indicated to be up to double that in literature reviewed.

A significant improvement in simulated capture rate has been shown, from 59 % to 72 % for Some-Overshoot gains in low turbulence.

Comparing drogue position and drogue-receiver errors for Some-Overshoot against High-Derivative gains the latter is more successful, despite the fact that divergences are slightly greater and occur for longer, because of its slow response. The Some-Overshoot approach provides good position tracking but there is still significant overshoot and 'peaky' motion which makes capture more difficult than with the slow, laggy response with the High-Derivative gains. If close tracking of position demand is not essential (true in these simulations) then a High-Derivative controller is superior. Consideration must be made, however, to the effect of sensor noise on this controller.

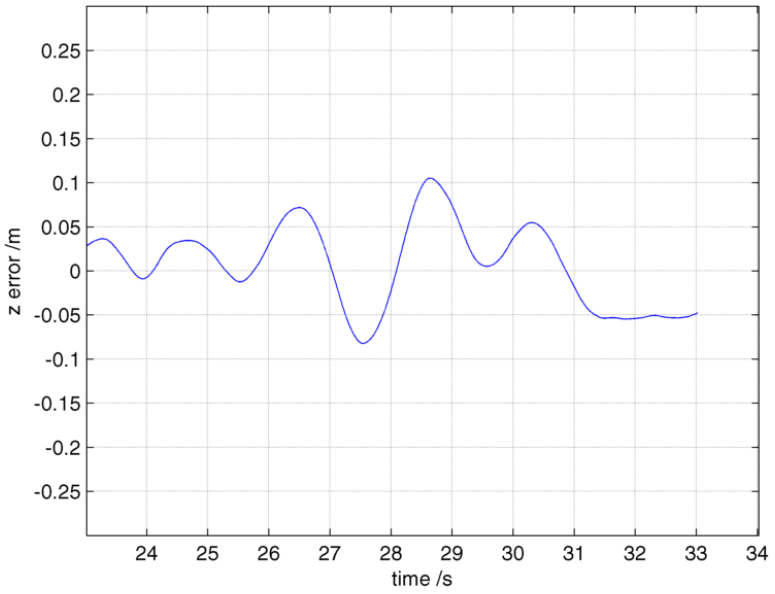

Figure 4.18: Vertical error between receiver and stabilised drogue under light turbulence – successful capture.

4.5.1 Frames of reference for drogue stabilisation

This implementation used drogue acceleration integrated to position, with error based on offset from steady-state as compared to the hose attachment point – a tanker-fixed reference frame. Alternatives include:

- Earth-fixed frame, which may be easier for the receiver to track depending upon tanker motion (although tanker manoeuvre would present a challenge here).
- Receiver-fixed frame, which leads towards intimate control methods that will be discussed in later chapters.

Issues with using the tanker frame include the fact that the drogue and receiver will both be subject to, and more susceptible to, similar gusts and tanker wake, which means that a drogue that is tracking the tanker will reject disturbances that may aid capture. Active modification of the drogue dynamics, to make it behave more similarly to the receiver, may prove beneficial as both bodies would respond similarly to gusts etc.

Drogue movement reduces significantly – to around ± 10 cm for moderate turbulence compared to non-turbulent values – when controlled (compare

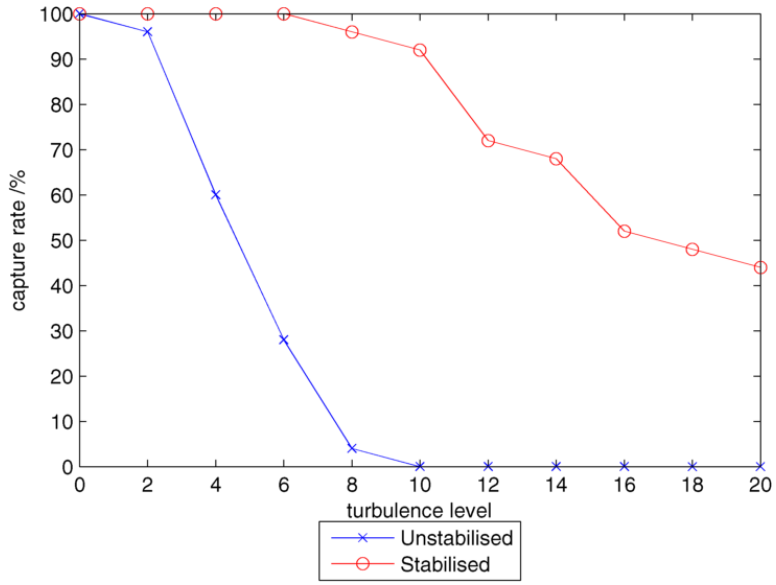

Figure 4.19: Capture rate for L/F and stabilised drogue controllers under varying turbulence.

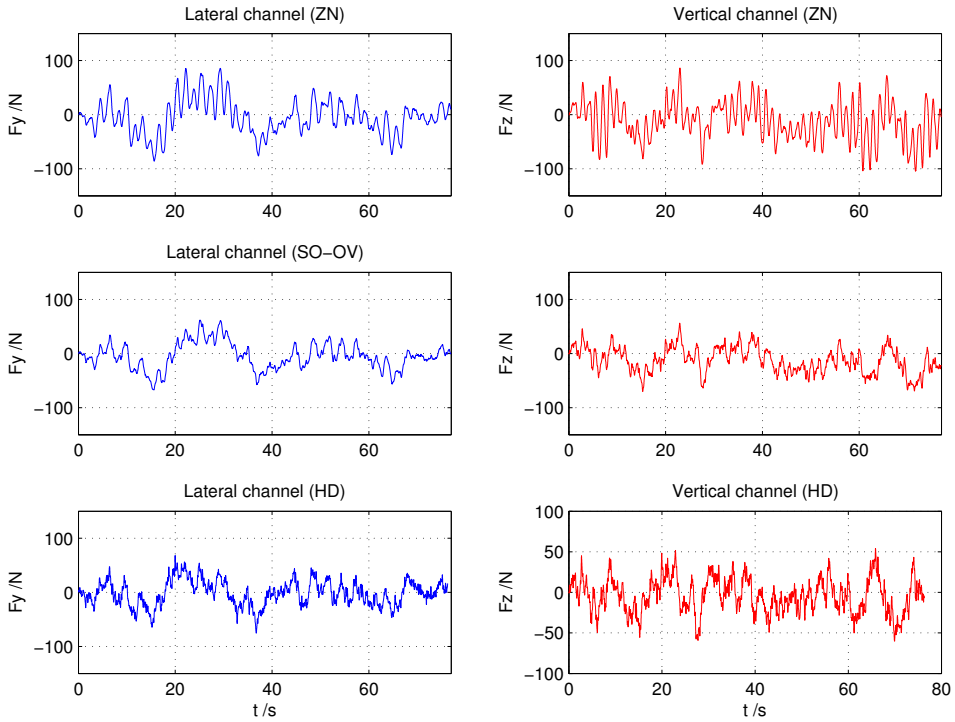

Figure 4.20: Actuation force for Zeigler-Nichols, Some-Overshoot and High-Derivative gains

figures 3.31, 4.11, 4.13 and 4.15). Looking in particular at the capture stage of the procedure, from around $t = 45$ s in figures 3.31-4.16 where x-error begins to reduce after a hold, drogue-receiver error does not decrease as noticeably. This suggests that much of this error is induced by receiver motion and having the drogue track the receiver rather than a steady-state position would be beneficial. The High-Derivative gains would not be suitable for this task, which would require low steady-state offset, but the Some-Overshoot values would be appropriate.

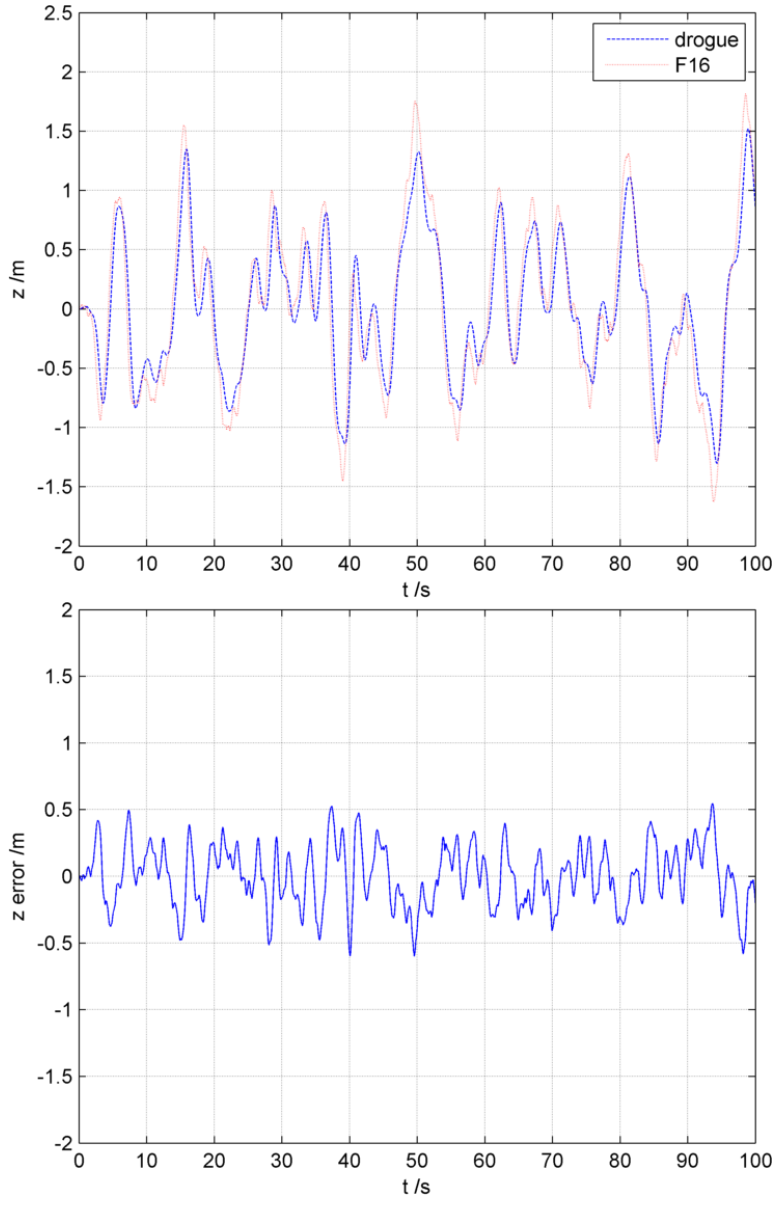

Figure 4.21: Vertical position and error of dynamically-matched linear drogue and L/F F16 under light turbulence.

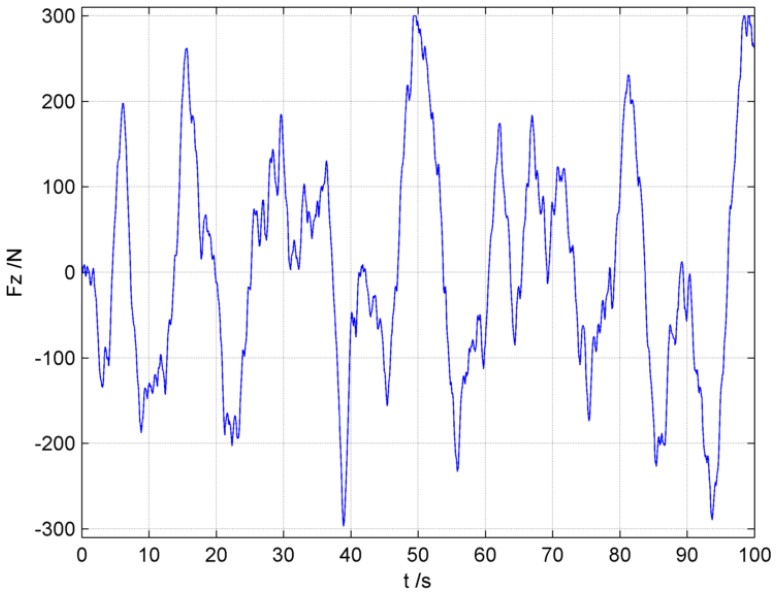

Figure 4.22: Force demand for dynamically matched drogue.

Chapter 5

Cooperative control methods

If drogue control is feasible, this creates a situation that can be posed as a multi-agent control problem. Multi-agent control has been investigated for general aircraft rendezvous and formation flight tasks extensively, including Chandler et al.'s work on cooperative UAV rendezvous [172] and How et al.'s 8-vehicle flight demonstrations [173].

5.1 Classification of architectures

In order to discuss and evaluate the 'novel architectures' mentioned in section 1.5, that may be enabled by a controllable drogue, it is convenient to have a framework by which to classify and describe them. This section reviews a small number of works that describe one approach to categorising them.

Scharf et al. [19] present a well-structured review of formation guidance and control with respect to spacecraft and satellites. They state that formation control architectur es fall within a number of classifications. These architectures can be identified by examining a system's control dependency directed graph.

Directed graphs, or digraphs, are a subset of graph theory, modelling pairwise relations between objects in a collection through the use of vertices (representing objects) and edges (representing relationships). Edges can have direction, representing a dependency e.g. a one-way transmission of information via datalink or sensors.

For the AAAR context, nodes represent aircraft or other controlled en-

tities, and edges represent control dependencies, i.e. if the control action of aircraft A depends on the state of aircraft B (or on a parameter in B's control system) then their digraph contains a directed edge from A to B.

A walk on a digraph is a series of directed edges that form a sequential chain. If there exists no chain of length greater than one, the digraph is single layer, else it contains a string or a mesh. A cycle on a digraph is a walk that can be repeated, i.e. the walk returns to the node at which it was started. If a digraph contains no cycles it is acyclic.

Figure 5.1 shows a range of simplified architectures which can be used to define categories of control systems – these are detailed in the following sections.

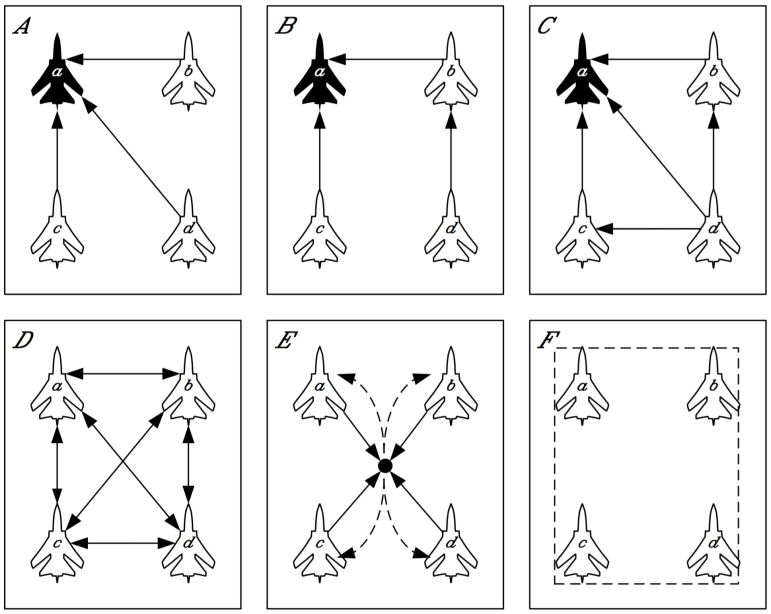

Figure 5.1: Control system architectures.

5.1.1 Leader/Follower

The Leader/Follower (L/F) architecture encompasses most existing work in AAAR. The subject of this thesis, CC and IC, does not include L/F architectures but the concepts and terminology used to define more complex architectures are built upon it and so it is included here for clarity and completeness.

A Leader/Follower (L/F) architecture (also referred to as target/chase

or master/slave) exists when the control dependency digraph is acyclic. Architectures A, B and C in figure 5.1 represent different L/F permutations where all states for aircraft b, c and d are defined (directly or indirectly) relative to the primary leader, aircraft a.

Architecture A is single-layer, where no walk has length greater than one. This architecture is simple and its stability and robustness depend only upon the controllers for each of the followers. Communication and sensing requirements are minimal – each following aircraft is aware only of the relevant states of a. One limitation of architecture A is that following aircraft are not aware of each other's positions and thus collision avoidance in the presence of disturbances is challenging.

Control systems for AAAR are generally single-layer, as there are only two aircraft involved, however if the system models tanker and boom/drogue as separate entities, or if the system encompasses multiple receiver aircraft (many tankers are capable of refuelling two or more receivers simultaneously) then the digraph is more complex. Multi-layer systems are examined here as they will likely prove useful in more complex development of IC systems.

Architecture B contains string $d \rightarrow b \rightarrow a$. In C, aircraft d has multiple leaders, creating a mesh. Architecture C is strongly connected, potentially producing a more stable and robust system with increased collision avoidance capability, but communication and sensing requirements are greater. Verification of the stability of these arrangements is more complex as errors and oscillations may propagate and be amplified along the strings. Significant work on string and mesh stability exists in literature concerning AHSs, for instance in the PATH project at UC Berkeley [20], and general stability criteria for these systems are reasonably well-defined.

5.1.2 Cyclic

Architecture D does not have a leader. Each aircraft attempts to position itself in relation to the others. Technically, digraph D should contain two directed edges between each aircraft, i.e. a senses or receives information from d and vice versa. These have been represented here as single undirected edges but this does not imply that communication or sensing is via the same method in each direction.

Digraph D is cyclic – the control of one aircraft depends upon the states of other aircraft, which in turn depend upon the state of the first aircraft.

Much work on cyclic formations relates to spacecraft and satellite control, e.g. for Multiple Spacecraft Interferometry (MSI), where formations of sensors must be accurately positioned relative to one another. The stability of decentralised control systems such as these are difficult to analyse because of their cyclic nature, but robustness can be greater than L/F systems as there is no critical single-point-of-failure. Communication and sensing requirements are significant in the arrangement shown, as each aircraft is aware of the state of every other aircraft, but other arrangements can be constructed where aircraft only require information about their nearest neighbours.

Architecture *E* shows a variation on the cyclic arrangement. A virtual reference point is constructed, for example from the centroid of the formation, and aircraft controllers hold position relative to this point. The reference point can be considered a virtual leader aircraft. This configuration requires similar stability, robustness and communication/sensing requirements to the cyclic architecture of *D* in order for each aircraft to construct the reference point independently, or a centralised controller is required which communicates reference point states to all aircraft.

5.1.3 Virtual structures

Another perspective on formation control is that nodes (aircraft) can be thought of as forming a pseudo-rigid polyhedron in 3-D space, a Virtual Structure (VS), with individual vehicles tracking their own reference nodes in the VS using their own L/F controllers.

Scharf et al. [19] state that, depending on implementation, the overall architecture of VS controllers are either L/F or cyclic: the structure can be attached to or offset from an individual aircraft, in which case the architecture is L/F, or a fitting algorithm can be used that references some or all of the nodes, making the architecture cyclic. The structure could also be made to travel without reference to vehicles in the formation, in which case the system would be L/F with reference to a virtual leader or the structure's origin.

The VS can undergo rigid body translation and rotation as well as scaling transformations to change the shape of the formation.

5.1.4 Potential fields

Yet another tool for tackling the formation control of multiple agents is the *potential field*, also referred to as a *potential function* or *virtual potential*. The dynamics of such controllers are sometimes modelled on the flocking behaviour of birds and fish [174] – it is suggested that three rules are required for flocking:

1. attraction to other members of the flock (potentially modelled as an attraction to the centroid of the formation),
2. repulsion from neighbours that are too close,
3. alignment or velocity matching with neighbours.

These are exemplified in Reynolds' distributed behavioural model of *boids* (bird-oids) [175]. Potential fields can be defined by a variety of methods, using distance- or location- based functions to determine magnitude and direction, with vehicles aiming to maximise or minimise their local potentials in order to structure the formation or avoid collisions. Potential fields can be applied to static obstacles in order to create avoidance. Multiple fields are usually superposed to create the desired flock dynamics, in a similar way to the superposition of demands in a behavioural controller. Since the construction of fields often depends on the location of other vehicles in the flock, controllers using potential fields are generally cyclic.

5.1.5 MIMO

In a MIMO controller, all elements of a formation are considered as one system, treated as a Multiple-Input Multiple-Output (MIMO) plant (architecture F). Errors based on vehicle states or outputs are defined and the full range of modern control methods are then available to design and optimise the system. There are surprisingly few current works which use a MIMO formation controller, possibly due to the increased communication requirements or single point of failure of such a system.

The MIMO approach is more a modelling method than an architecture, and systems from the other classifications identified in this chapter may also be analysed using MIMO methods. Since the construction of MIMO models allows significantly different analysis methods to be employed, literature which takes this approach is considered separately here.

5.2 Review of cooperative methods

McFarlane, Richardson and Jones [64] present a controller for boom-receptacle refuelling where boom and receiver aircraft share a common target point which is constructed from the positions of tanker, boom and refuelling window.

Their target point function produces a weighted average of the positions of the receiver and boom tip , relative to the centre of the refuelling envelope, then applies a gain to this average in order to attract the target point to the refuelling envelope.

Their controller is applied to an established F-16 model [63], with decoupled altitude-hold and horizontal-separation-hold controllers. The tanker is modelled as a point and the boom is based on a model from the US Air Force Research Laboratory [176]. Eigenstructure Assignment (EA) is used to tune the controllers to ensure close tracking of the receiver hold point.

The simulation is run subject to an isotropic Dryden turbulence model at light, moderate and severe intensities. In the first cooperative simulation, with the integral and derivative gains in the target point controller set to zero, the coupled boom and receiver show close tracking in the order of <10 cm, but their position drifts outside of the optimal refuelling envelope – this is successfully resolved by tuning the target point gain to increase its emphasis on station-keeping versus formation-keeping.

Anderson et al. [177] propose that a fully-decentralised formation can be kept through each agent preserving its distance from another in a directed fashion, i.e. the responsibility of keeping distance is assigned to only one of the agents along each graph edge. This is straightforward in acyclic formation, but problems arise when cycles are present.

Constraints are proposed to permit cyclic analysis: the formation graph must be balanced (although non balanced graphs are considered in other works by the authors), rigid and persistent. Agents are holonomic, massless points.

The control law directs agent i to move towards agent $i+1$ at speed $s_i = -(d_i - r_i)$, where d_i is the desired separation and r_i is the current measured separation (thus if $r_i < d_i$ the demand is negative and separates the agents).

It is shown that both separation and bearing of tracked agents is required

for formation control and a differential model is constructed. Based on analysis of error variables, which have exponential stability, and position variables, which generally will not converge, it is deduced that the formation will drift unless a further external input is required, either in the form of a whole-formation movement or 'dead zones' for individual agents which are larger than any errors or biases. The overall methodology is of interest but the abstract nature of the simulation here means that work is required in order to apply this to the AAAR context.

Zheng et al. [178] present a controller which uses a single gain to vary the weighting of relative and absolute positioning to drive either for formation-keeping or for path-following.

They present a review of networked vehicle system control which details several areas of work, including distributed hybrid systems and comment on formation topologies in a similar manner to this review. Significant consideration is given to string and mesh stability.

Their formation controller uses relative error with respect to neighbouring vehicles (up to three in the example used), and another sliding control law is used to drive this error to zero. The approach is proven mesh stable and simulations are conducted based upon ground robots, with next steps proposed to be transferring the controller to UAVs.

Zou et al. [65] construct simulated aircraft and inner-loop controller based upon Stevens and Lewis' work [63],and describe a formation controller presented as an undirected graph. For each edge they define a matrix which determines constraints on accelerations and velocities. These are translated into constraint forces through a virtual work principle. The constraint force on each aircraft is composed from states of all aircraft that directly communicate with it. The use of edge-based constraint matrices allows vehicles to be arbitrarily added or removed, creating a scalable controller.

Stability is shown through a composite Lyupanov function and simulations are run for a three-aircraft formation.

Li and Tan [179] enhance the performance of a VS controller by adding relative position tracking between aircraft. They detail their notation for a standard VS implementation, with no dynamics applied to the VS itself (unlike Ren and Beard's controller [180]), and PI formation controllers which present demands to each aircraft's autopilot.

The synchronisation aspect of their approach uses cross-coupling be-

tween different vehicles in the system, defined as combinations of position errors of different aircraft. Li and Tan comment on two cases to explain the improvement on formation keeping due to the use of coupled errors. They then demonstrate simulations of two UAVs performing a circular manoeuvre followed by straight and level flight.

Leonard and Fiorelli [174] develop a distributed controller which uses artificial potentials to define interaction control forces between vehicles, in order to enforce vehicle spacing. Their virtual leaders superimpose additional potentials to manipulate group geometry and direct the group's motion. Closed-loop stability is shown through a Lyapunov function using kinetic and artificial potential energy. Dissipative control terms are used to achieve this.

Leonard and Fiorelli analyse several formation patterns and motions. They identify ways in which the virtual leaders can shape the group and the influence of control parameters on performance. They describe the possibility of undesired equilibria being created by the interaction of vehicles' potential fields and conclude that further work is required to expand their model to three dimensions and to take account of nonholonomic and other possible dynamic constraints.

Do [181] develops a design methodology based on decentralised potential functions which enables formation keeping and collision avoidance. The design achieves near-global asymptotic convergence and guarantees collision avoidance.

Do poses the problem as relatively abstract, with agents represented as autonomous points. His construction includes the ability to rotate, expand and contract the formation using a parameter vector to specify changes whilst avoiding collisions.

The potential function used contains terms γ_i and β_i which are, respectively, a goal function representing the distances from an agent to its adjacent members, and a collision avoidance function which tends towards infinity as agents collide. The overall function attains a minimum when an agent is at its desired location with respect to other group members, and is infinity when agents collide.

Do proves the existence of solutions to the proposed controller such that collisions are avoided, and analyses critical points to show that desired equilibriua are asymptotically stable and undesired ones are unstable.

Chen and Tian [182] present a distributed formation controller with three agents, which only requires knowledge of neighbouring agents' velocities. Agents are represented by double integrators and the controller uses the integrator backstepping technique to create a triangle formation and ensure the agents' speeds converge to a common value. Later, inter-agent potential functions between agents are used to relax constraints but retain collision avoidance. Convergence of algorithms is proved through LaSalle's invariance principle.

Analysing a formation as a whole system seems like a logical proposal but, as stated earlier, the literature seems relatively sparse. There are, however, several direct applications of MIMO architectures to UAV-UGV docking procedures. These use realistic simulations and, in some cases, real-world trials and provide an excellent starting point to expand their application to AAAR. Although MIMO analysis is more a method than an architecture, modelling a system in this way permits use of alternative techniques, so such implementations are classified separately here.

Griffiths [17, 183] presents the first introduction of the term 'intimate control' with a MIMO controller for UAV-UGV docking. The UAV simulated is the XRAE developed by Cranfield and Imperial College, and the UGV is BAE Systems' ATC Wildcat. Both models are specific and realistic, representing relevant aerodynamic and mechanical aspects such as cross-coupling between the UAV's degrees of freedom and a model of the UGV's suspension. Wake effects are included using CFD models of the Unmanned Ground Vehicle (UGV).

Griffiths focuses on 2-vehicle docking, and splits the problem into two phases – a non-intimate Rendezvous Guidance (RG) phase, which brings the vehicles within 5 m and 2.5 m/s of one another, then an IC phase to achieve docking.

An LQG performance index is minimised to solve the control problem, with an arbitrary cost matrix used to weight control towards the UGV, which is more agile in yaw and acceleration.

Simplifications are made to the state space model with consideration to the vehicles' dynamics – the UAV dominates due to its slower response.

Simulations show a significant level of success even in the presence of vehicle wake turbulence. Proposed sensor requirements are specified: pitot, 3-axis gyro/accelerometer, altimeter and GPS on the UAV; 3-axis gyro/accelerometer

on the UGV, and communication bandwidth of 0.48 Mbs^{-1} anticipated for IC.

Griffiths later presents a refined analysis [183] examining the robustness of the controller. His simulation is enhanced with road roughness, wind shear and gusting, and torque induced by the docking process. Sensor and actuator models are also added.

Jones [184], citing Griffiths [17, 183], developed an intimate controller for UAV-UGV docking of a helicopter UAV. Trialling his controller on a Quanser 3-DOF platform, a 1-DOF UGV and vision-based tracking he shows that disturbances in one system can be rapidly compensated for by either system.

Jones develops a separate-systems RG process which is shown to be accurate but in this scheme neither vehicle is influenced by the state of the other. Limitations of this approach are stated and an intimate control proposal is formulated. The UAV and UGV are both represented in simulation by simple second-order models in order to identify the effect of the intimate architecture,and this is then applied to the 3-DoF Quanser in simulation and experiment.

After showing successful results with the second-order representation of vehicle dynamics, the controller is simulated with the more realistic dynamics of the Quanser UAV and a track-based UGV. As the dynamics of the UGV are vastly different to those of the UAV, the UGV is limited to a first order response. This is recognised as a limitation of intimate control – vehicle dynamics should be similar or forced to behave in a similar fashion. An improvement similar to the previous simulation is achieved, but it is identified that the tightly-controlled inner-loop dynamics of the Quanser UAV limits the influence of the IC controller.

Jones uses the feedback parameters from the previous simulation in his experimental trials. The simulated Quanser dynamics are replaced by the actual model, but the UGV is still limited to an artificial first-order response. Nonlinearities in the UGV model are identified as causing problems, particularly with low-velocity demands, and comparisons are made between intimate and non-intimate architectures in this case also.

Jones concludes that, given the assumptions made in his work, IC is simple to apply and is based on the assumed dynamic response of vehicles. He states that the problem formation allows an optimal tuning process to be

used which produces a clear improvement in tracking response. The primary limitation of the process is the assumption of similar vehicle dynamics – he suggests using an output feedback approach applied to a concatenated system representing the dynamics of both vehicles more accurately. The validity of these significant assumptions needs to be investigated further, and the application of techniques presented here are candidates for future work in AAAR.

5.3 Summary

A wide range of approaches to formation tracking and vehicle docking have been presented. The following are generalisations that can be made with regards to the applicability of many of these implementations to AAAR:

- Many works assume identical dynamics for all vehicles involved. This is unlikely to be the case for AAAR and selected architectures should be simulated with representative dynamic models.
- Many of the described controllers allow for scaling or other modification of formations – this could be used for control in the approach phase.
- Often a single approach is insufficient – additional behaviours must be imposed for collision avoidance etc.
- Most formation controllers are intended to be scaled to many vehicles, and simulations for formations of three or more vehicles are presented. The applicability of architectures to two-vehicle configurations must be analysed for AAAR.
- AAAR poses increased constraints for at least one agent in the formation – refuelling equipment is more limited in its motion than free aircraft.
- Those approaches targeted at spacecraft, and those with highly abstracted vehicle dynamics, must be adapted for the increased disturbances and nonholonomic limitations introduced by atmospheric flight.

Chapter 6

Cooperative control

There are many promising candidate architectures in the preceding review. In this chapter, one of these originally proposed for boom-receptacle refuelling is selected and replicated, applied to probe-drogue scenario and it then enhanced with a novel improvement. This technique is then applied to the probe-drogue AAAR environment.

The chosen implementation is McFarlane et al.'s cyclic controller [64]. It, along with Griffiths' UAV-UGV docking work [17, 183], is the closest to real-world applicability – the models used for receiver, boom and atmosphere are realistic and extensively used, and McFarlane et al.'s work is directly targeted at AAAR, making it a good candidate to pursue. Additionally, this work was conducted at the University of Bristol so in-depth reports and models are available.

6.1 Cyclic architecture with common target point

This section reproduces work by McFarlane, Richardson and Jones [64] in order to gain a full understanding of the design process and workings of their controller and to perform a wider range of simulations and analyses than were conducted in their original paper. Models and derivations are examined in order to gain understanding of approximations and applicability to probe-drogue refuelling.

6.1.1 Configuration

McFarlane et al.'s implementation of CC for boom refuelling consists of a cyclic controller which couples boom and receiver. It acts with respect to their positions, and that of the refuelling envelope within which the boom's tip position is constrained. A target point controller generates a common point upon which receiver and boom aim to converge and track. Further details of the models and control methods used are detailed in the following sections.

6.1.2 Boom model

The boom is based on data from the US Air Force Research Laboratory, by Smith and Kunz [176], for the KC-135 refuelling system.

The boom has two rigid parts: an anchored section, and an extension which translates along the boom centre line, with mass distributions as given in tables 6.1 and 6.2. The boom pitches and yaws about its attachment point. Control is via 'ruddervators' – aerodynamic surfaces towards the trailing end of the anchored section. Parameters are shown in figure 6.1.

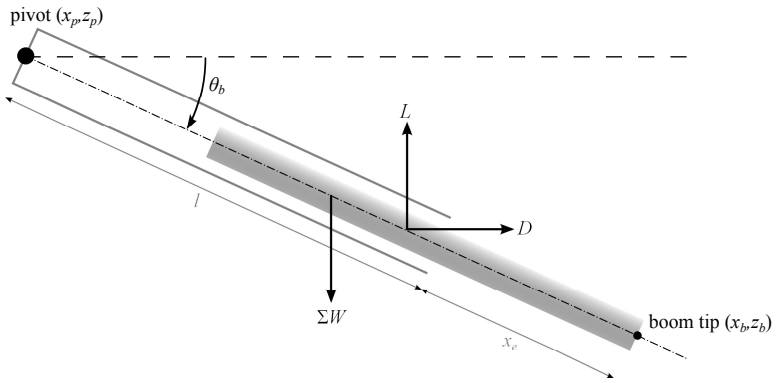

Figure 6.1: Boom mechanical configuration

The position of the boom tip (x_b, z_b) is given by:

$$x_b = x_p - (l + x_e)\cos\theta_b \tag{6.1}$$

$$z_b = z_p - (l + x_e)\sin\theta_b \tag{6.2}$$

with boom pitch angle θ_b from the horizontal, l the unextended length and

x_e the extension. Angular acceleration of the tip $\ddot{\theta}_b$ is

$$\ddot{\theta}_b = \frac{\tau}{I} - \frac{2}{3}\dot{\theta}_b \tag{6.3}$$

with τ the total torque about the pivot (from gravitational and aerodynamic forces) and I the boom's moment of inertia, which varies with extension. The $\dot{\theta}_b$ term represents the damping of the system's dynamics.

The refuelling envelope is 20-40° below tanker centreline, with 1.9-5.6 m extension range. In this model the boom is constrained such that it is unable to move outside this envelope, shown in figure 6.2.

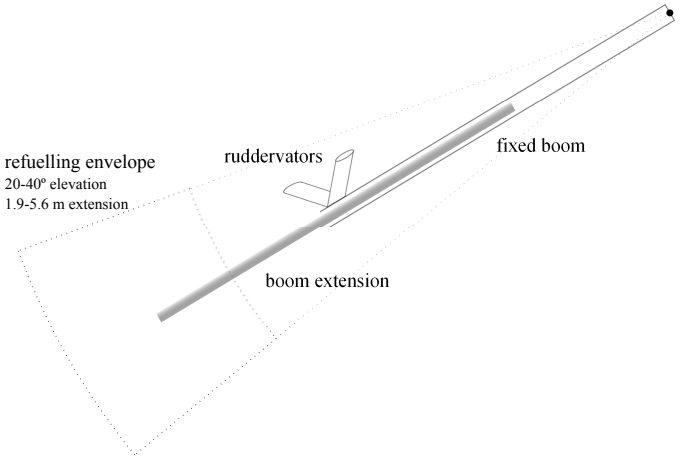

Figure 6.2: Boom and refuelling envelope

Aerodynamic forces

The ruddervators generate lift and drag forces L_v and D_v – it is assumed that these act at the ruddervators' CG. The weights of the boom components, whose positions vary depending upon extension, are summed to give weight and CG. Drag D is not included in this model.

In Smith and Kunz' work [176] lift and drag coefficients are interpolated from aerofoil tables as functions of angle of attack and Mach number – here ruddervator lift coefficient is approximated as a simple multiple of ruddervator incidence:

$$C_{L_v} = 0.1(\delta_v + \theta_b - 30) \tag{6.4}$$

where δ_v is ruddervator deflection away from their zero-incidence set-point at 30° from boom centerline. Ruddervator characteristics are given in table

Table 6.1: Anchored boom component masses [176].

Component	Mass /kg	CG from pivot /m
Snubber Hydraulic motor drive Stowage provisions Instrumentation Attaching provisions	55.6	0.00
Structure tube Fairing Hydraulics Fixed inner tube Electrical Fuel System	193.8	4.22 distributed
Ruddervators and supports Recoil assembly Ruddevator controls Ruddevator locking Dumping provisions	149.3	7.89

6.3.

Total torque acting about the pivot is

$$\begin{aligned}\tau &= \Sigma(m_i x_i) g \cos\theta_b - 7.89(L_v \cos\theta_b + D_v \sin\theta_b) \\ &= (28880 + 2049 x_e)\cos\theta_b - 7.89(L_v \cos\theta_b + D_v \sin\theta_b) \end{aligned} \tag{6.5}$$

with forces

Table 6.2: Boom extension component masses [176].

Component	Mass /kg	CG from pivot /m
Rollers and supports	10.6	x_e
Inner tube Tube lining Fuel	170.1	$4.19 + x_e$ distributed
Nozzle Shock absorber	28.12	$8.38 + x_e$

Table 6.3: Ruddervator characteristics [176].

Aerofoil	**NACA 65-012**
Chord	0.787 m
Span	1.549 m
Dihedral	42

$$L_v = \frac{1}{2}\rho V_T^2 S C_{L_v} \tag{6.6}$$

$$D_v = 0 \tag{6.7}$$

6.1.3 Cyclic controller

Boom and receiver aircraft share a common target point which is constructed from the positions of tanker, boom and refuelling window:

$$\begin{bmatrix} x'_t \\ z'_t \end{bmatrix} = \begin{bmatrix} x_b w + x_r(1-w) \\ z_b w + z_r(1-w) \end{bmatrix} \tag{6.8}$$

The target point equation 6.8 produces a weighted average (x'_t, z'_t) of the positions of the receiver (x_r, z_r) and boom tip (x_b, z_b), relative to the centre of the refuelling envelope (which is a constant offset from the tanker's position) with weighting factor w favouring the boom tip as $w \to 1$ and the probe tip when $w \to 0$, then applies a scaling factor $0 \leq K \leq 1$ to this average (whose coordinate origin is the centre of the refuelling envelope) in order to attract the target point (x_t, z_t) towards the envelope's centre, as demonstrated in figure 6.3.

Adjusting the gain in the target point controller varies the level of intimacy between the vehicles – a gain of zero ties the target point to the refuelling envelope centre; a gain of one puts it exactly between the receiver and boom tip, with no regard to envelope position. As the gain is reduced from $1 \to 0$ the target point moves closer to the envelope – further from a 'mutually beneficial' position but closer to the ideal refuelling location. Gains can be set independently for receiver and boom, so multiple levels of intimacy can be simulated, as described in table 6.4.

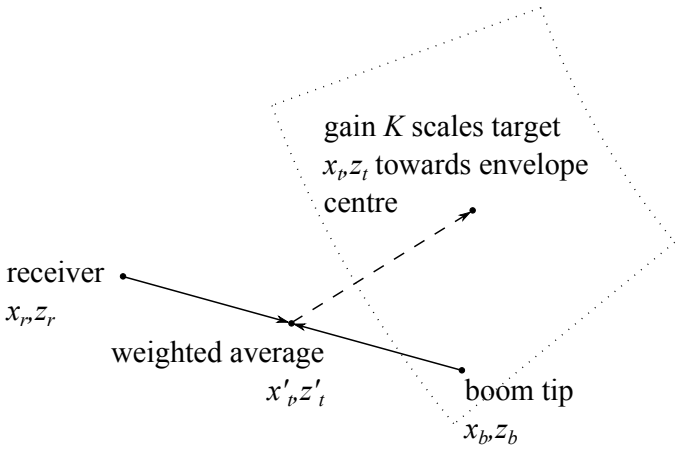

Figure 6.3: Target point construction

Table 6.4: Levels of intimacy defined by target point controller gains

Receiver and boom gains	Effect
$K = 0.00$	Non-cooperative control
$K_r = 0.00$, $K_b = 1.00$	L/F control
$0.00 < K < 1.00$	Cooperative control
$K = 1.00$	'Blindly' cooperative control

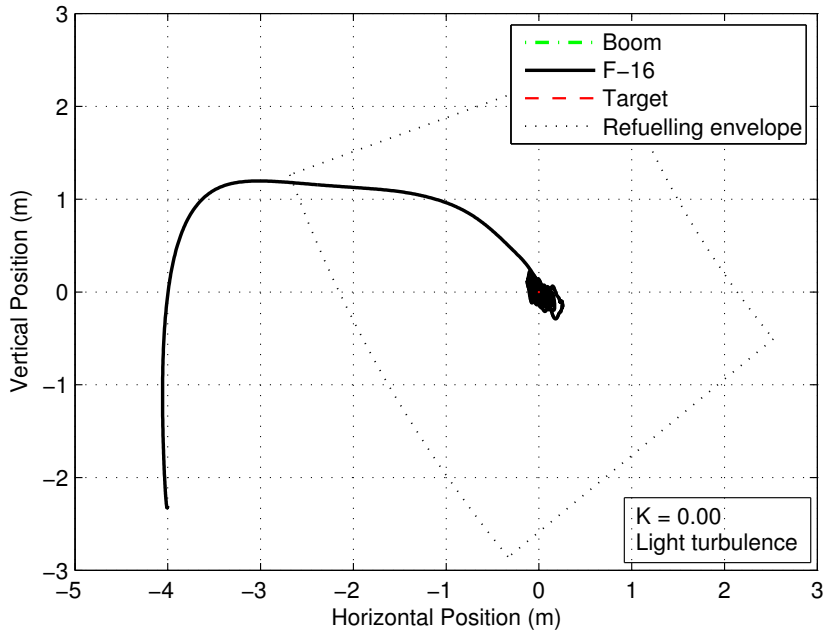

Figure 6.4: XZ displacement with target point gain $K = 0.00$

6.1.4 Simulation results

Effect of varying target point gains

Figures in this section show the effect of varying the gains in the target point function. At $K = 0$ the target point function continuously demands the centre of the refuelling envelope – control is non-cooperative: boom and receiver track the envelope without respect to one another's positions, shown in figure 6.4. As, in this model, the boom is unaffected by turbulence, it remains at the target point for the duration of the simulation. The F-16 is subject to turbulence but tracks the centre of the envelope – its absolute error, and thus the relative error (with non-turbulent boom) shown in figure 6.5 remains within 25 cm in this simulation, but if turbulence was also applied to the boom model it is anticipated that the relative error would be greater.

With $K = 1$ the target point is mid-way between boom and receiver, with no regard to envelope position. Figure 6.6 shows positional hold results, with receiver and boom starting at envelope centre, under light turbulence:

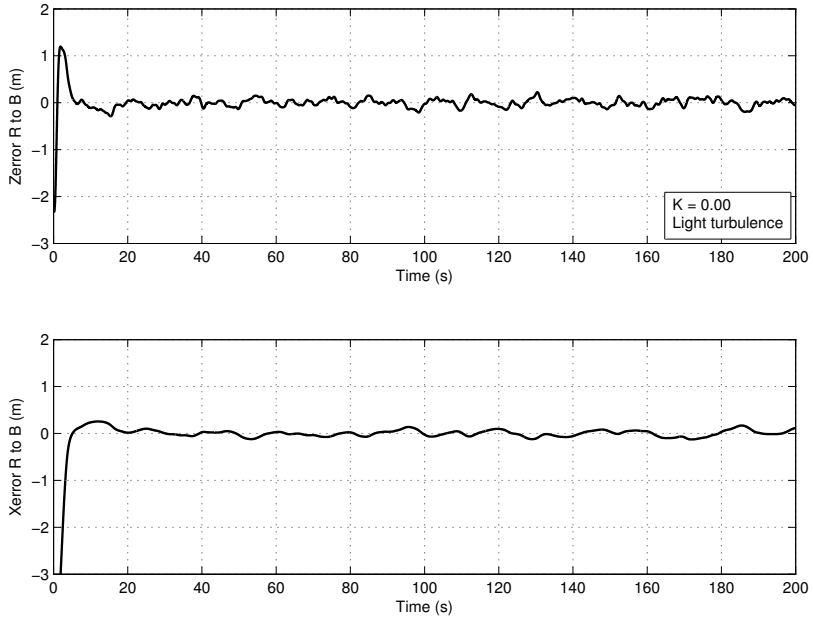

Figure 6.5: Relative error between receiver and boom for $K = 0.00$

boom and receiver show good tracking within the refuelling envelope, with relative error in the order of centimetres, but there is no attraction of the target point to the refuelling envelope so both bodies drift away from the centre point, the boom reaches position saturation at the envelope's edge but the F-16 continues, and relative error increases sharply. This is repeated several times over the whole 200 s simulation but only the first 90 s are shown here for clarity. Figure 6.7 shows relative displacement between boom and receiver – the effect of the receiver leaving the envelope is clear. If the start point for the receiver is outside the envelope, as in the other simulations in this section, the oscillations are even more pronounced, shown without turbulence in figures 6.8 and 6.9, resulting in a nonlinear periodic cycle.

Figures 6.10 and 6.11 show the effect of varying gain for $K = 0.25, 0.50, 0.75$. The trade-off between emphasis on the bodies tracking each other versus the centre of the envelope is clear – figure 6.11 shows how relative error is reduced by increasing gain but figure 6.10 shows how this reduces envelope tracking.

For comparison, figures 6.12 and 6.13 show results for a L/F approach,

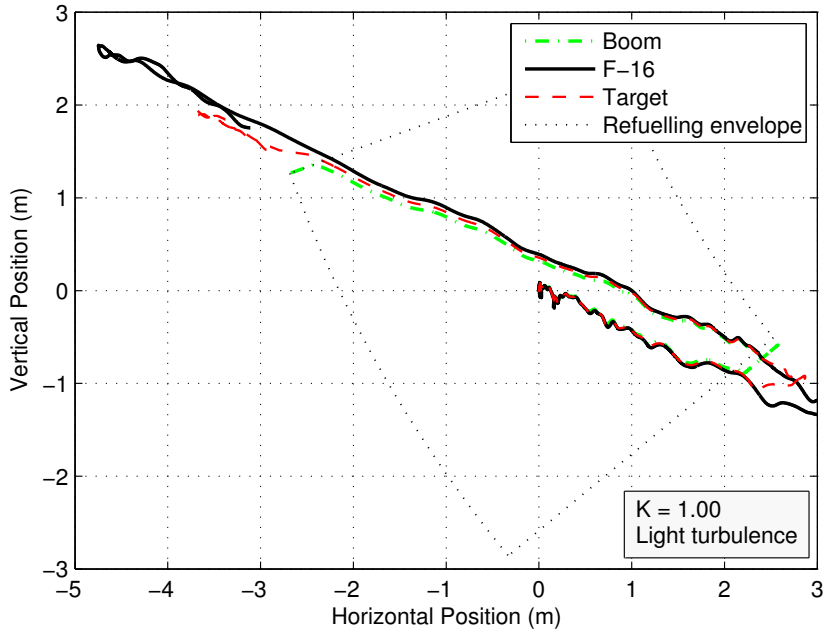

Figure 6.6: XZ displacement with target point gain $K = 1.00$, F-16 starting at centre of envelope

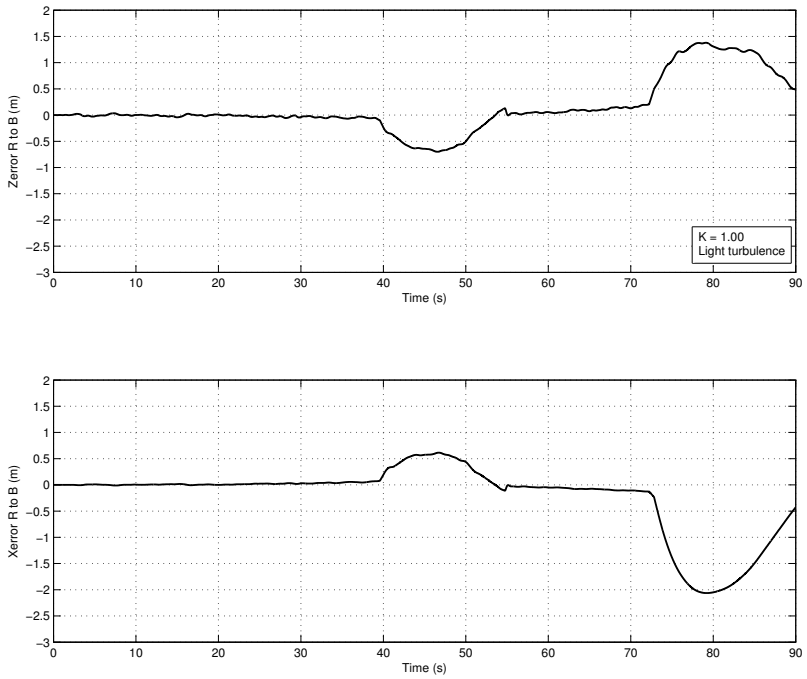

Figure 6.7: Relative error between receiver and boom for $K = 1.00$, F-16 starting at centre of envelope

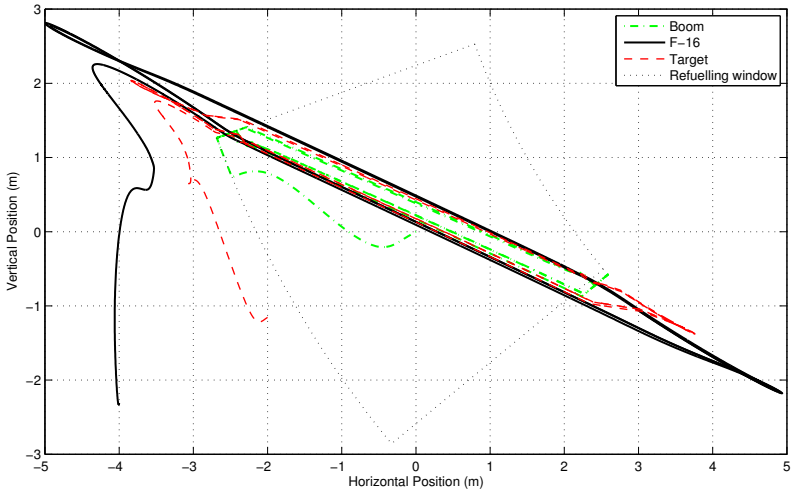

Figure 6.8: XZ displacement for $K = 1.00$, F-16 starting outside of envelope

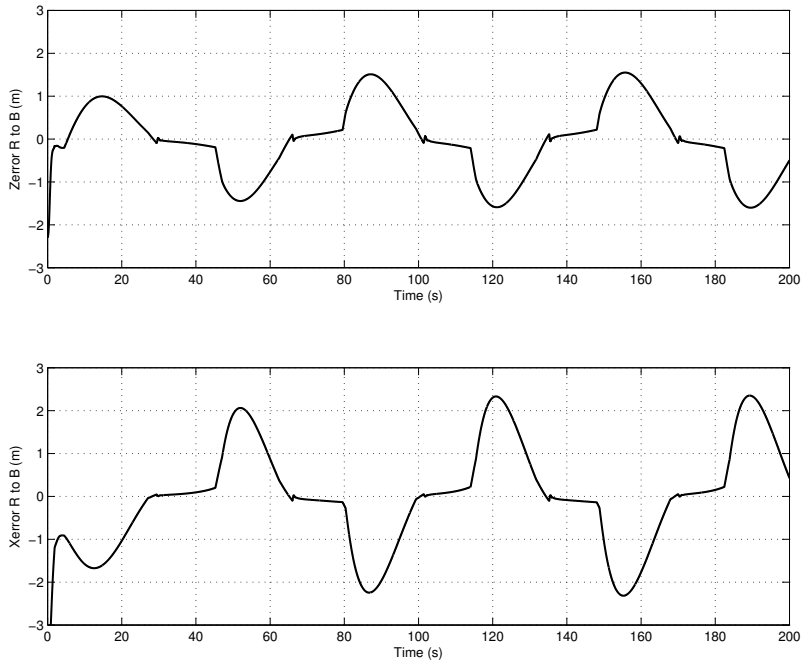

Figure 6.9: Relative error for $K = 1.00$, F-16 starting outside of envelope

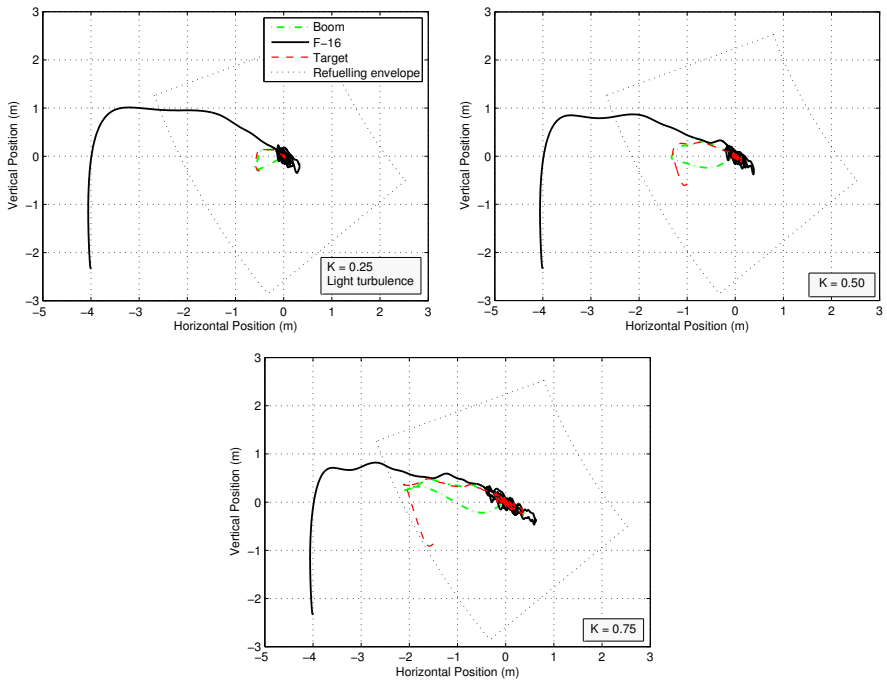

Figure 6.10: XZ displacement with target point gain $K = 0.25, 0.50, 0.75$, under light turbulence

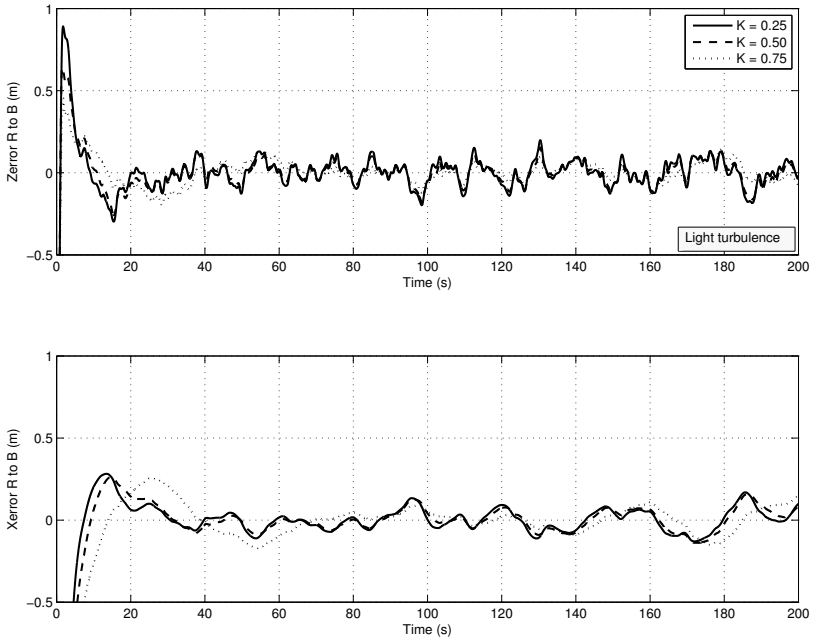

Figure 6.11: Relative error between receiver and boom for $K = 0.25, 0.50, 0.75$, under light turbulence

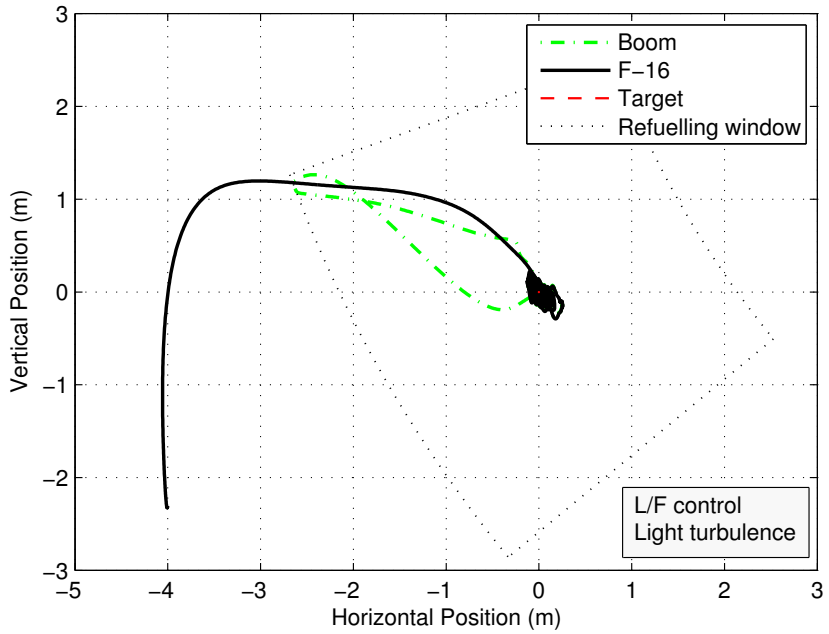

Figure 6.12: XZ displacement with L/F control

with receiver target point gain set to zero so that it tracks the refuelling envelope centre, and boom target point tracking the receiver. These results show relative error not exceeding 5 cm, but the lack of turbulent effects on the boom model may be misleading here too.

Impact of turbulence

Figures 6.14 and 6.15 show the effect of increasing turbulence upon displacement and relative error, at constant gain $K = 0.75$. The receiver remains within the envelope and relative error remains within 30 cm in all but severe turbulence. The larger relative errors under severe turbulence are due to the receiver exiting the envelope, so the limiting factor here is the closed-loop F-16 gust response.

6.1.5 Summary

The action of this cyclic implementation of CC has been replicated and analysed and it is certainly a feasible candidate for further investigation. Its

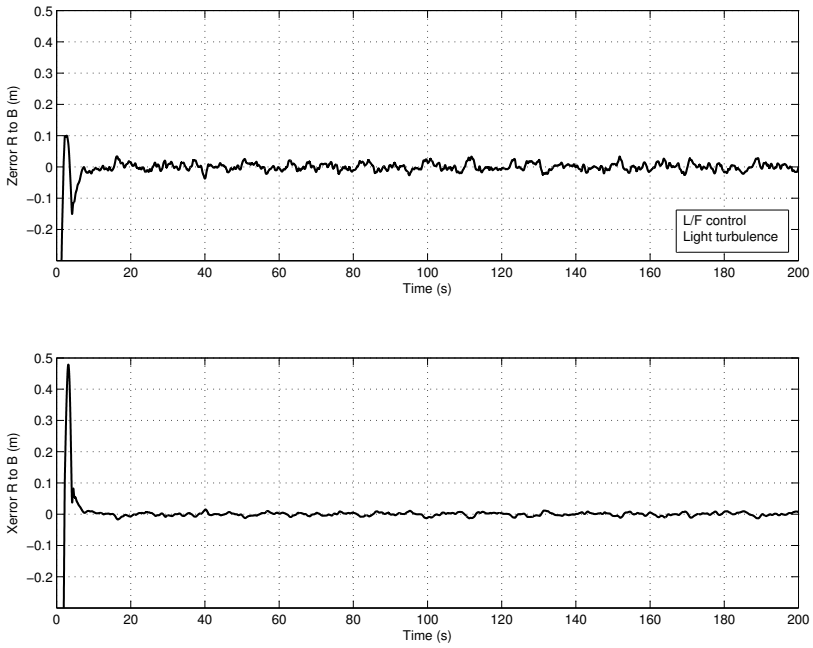

Figure 6.13: Relative error between receiver and boom with L/F control

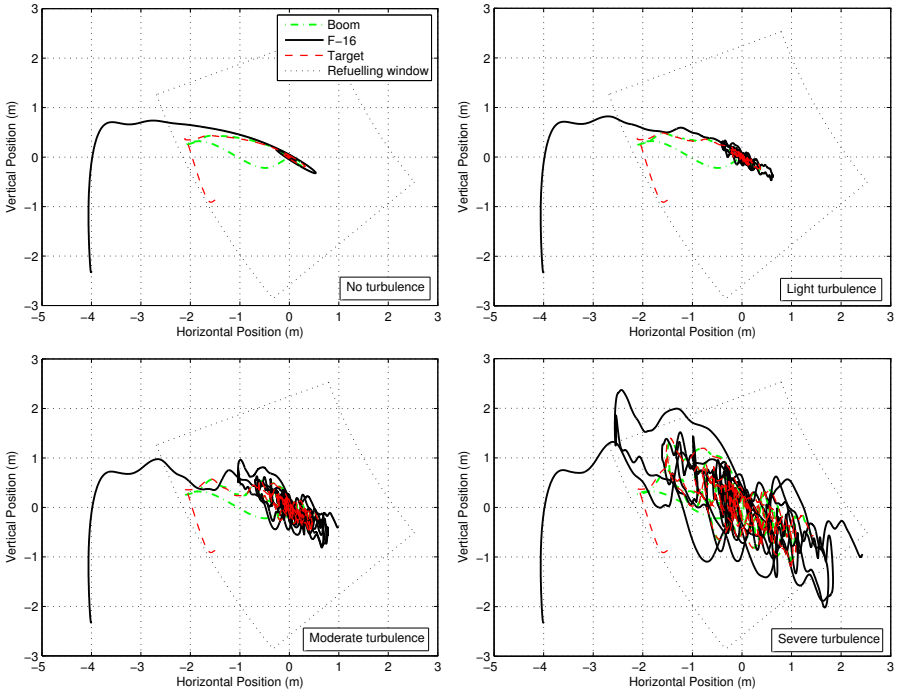

Figure 6.14: Effect of turbulence on XZ position with $K = 0.75$

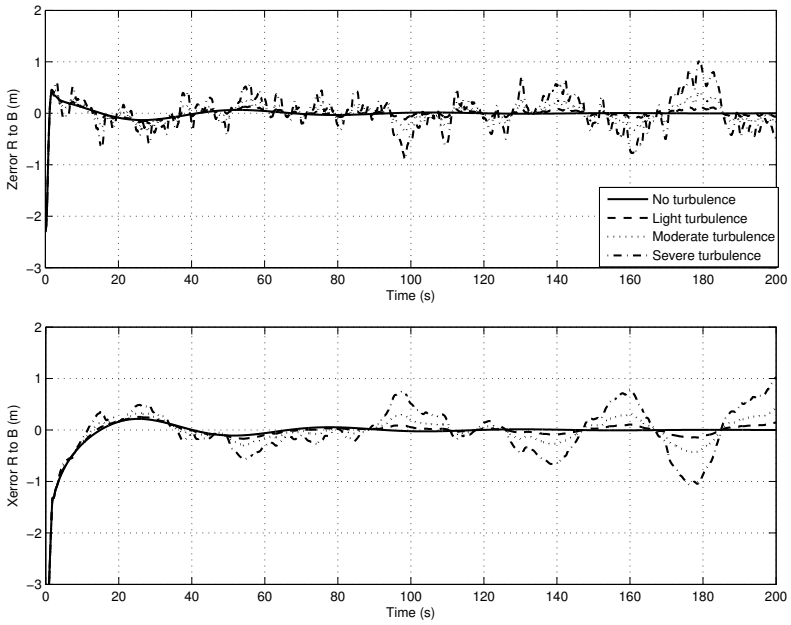

Figure 6.15: Effect of turbulence on relative error with $K = 0.75$

performance is promising under moderate levels of turbulence. The non-cooperative and L/F simulations currently produce similar results to the cooperatively controlled model but inclusion of boom gust response may produce significantly different results – this must be addressed in further work in order to fully evaluate this controller.

6.2 Cyclic common target with scheduled gain

One issue highlighted in the previous section was the trade-off between relative tracking of receiver/boom versus position hold within the refuelling envelope. At the extreme end of the scale of intimacy ($K = 1.00$) relative tracking was very tight but because there was no pull towards the centre of the envelope the bodies drifted outside it and the boom reached position saturation, causing a rapid divergence in relative error.

A scheduled gain on the target point controller may help to mitigate this trade-off. Setting the gain to a high value at envelope centre would direct receiver and boom to focus on one another; decreasing this as they diverge from the ideal refuelling point, to a low value at envelope edge, would increase their efforts to track the envelope.

This section extends the controller from the previous section via this novel method.

6.2.1 Scheduled gain implementation

This proposed improvement to McFarlane et al.'s controller uses the receiver's position relative to the envelope centre. In this extension the gain function is constructed as a product of the receiver's polar angle and radius errors about the boom root (the same coordinate frame in which the refuelling envelope is defined), scaling the function's value linearly from $K = 1.00$ at envelope centre to $K = 0.00$ at its edge as shown in figure 6.16.

The effect of this modification can be seen by comparing figures 6.17 and 6.18 (with scheduled gain) to figures 6.14 and 6.15 in the previous section. Convergence is much more rapid with scheduled gain implemented, the receiver remains within the refuelling envelope even under severe turbulence, and whilst the maximum magnitude of the boom-receiver error is similar, divergences are resolved much more quickly.

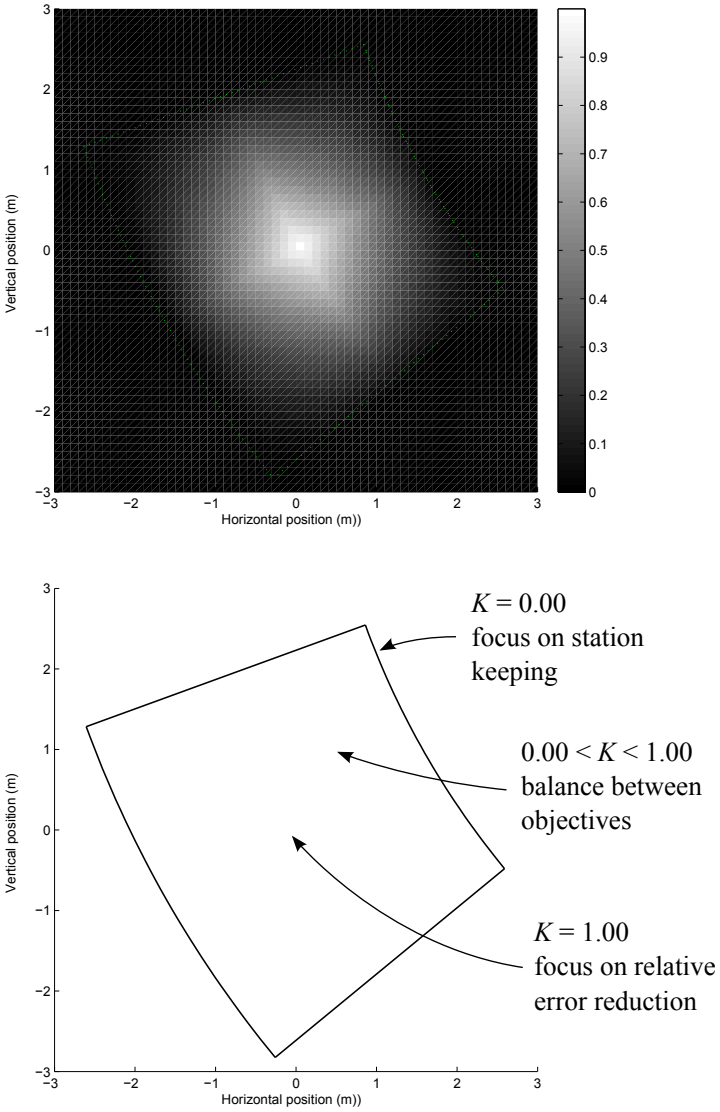

Figure 6.16: Potential function for target controller gain

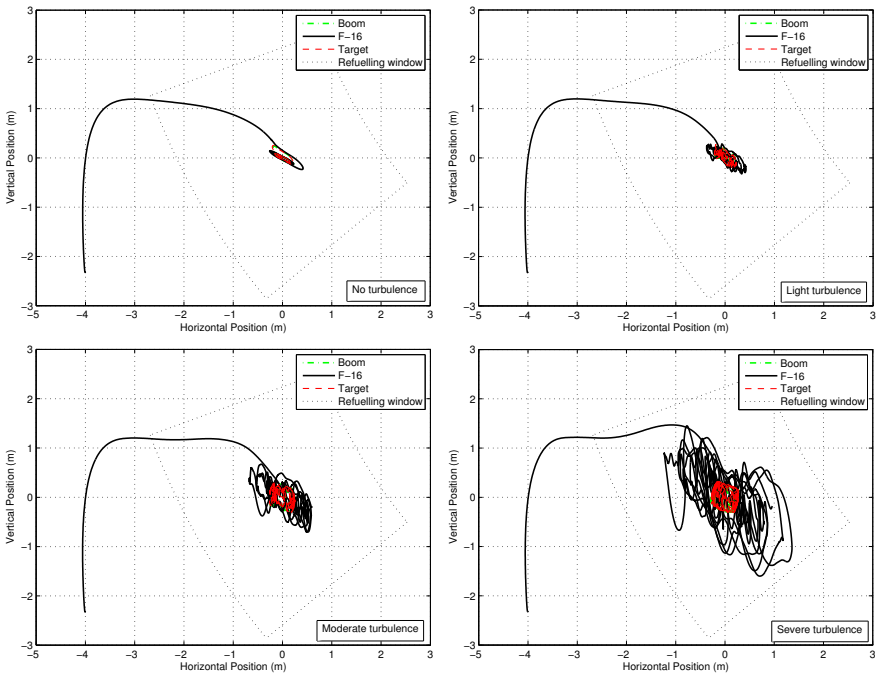

Figure 6.17: Effect of turbulence on XZ position with scheduled gain

An improvement in position hold (against constant gain $K = 0.75$) can be seen, particularly in the case of moderate and severe turbulence – the receiver does not leave the refuelling envelope at all. There is also a significant reduction in control effort by the boom – partly a product of the removal of demand when the receiver is outside the envelope.

The impact of the scheduled gain on the maximum relative error between boom and receiver does not seem significant, but convergence of the two is much faster. The rapid pitch response of the F-16 does increase the overshoot, but recovery is also quick and the horizontal and vertical errors stabilise in less than half the time of the static gain controller.

The action of the gain controller is shown in figure 6.19, with rapid variations evident at higher levels of turbulence.

6.2.2 Summary

Addition of a scheduled gain through a potential function acting upon receiver position is effective, preventing the receiver from leaving the refuelling envelope even under severe turbulence. Relative error remains within 0.5 m

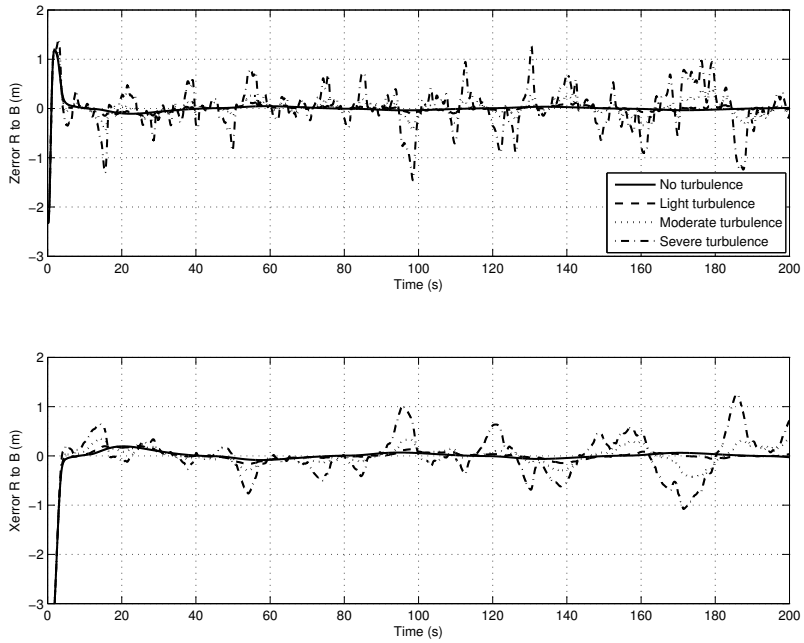

Figure 6.18: Effect of turbulence on relative error with scheduled gain

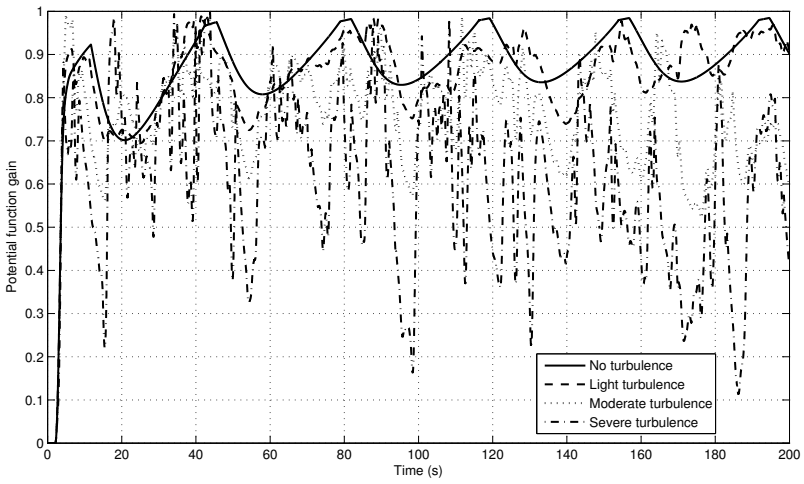

Figure 6.19: Magnitude of scheduled gain under varying turbulence

in all but severe turbulence, and convergence of receiver and boom positions is significantly quicker. The trade-off between position hold and relative error can be successfully addressed via this method.

6.3 Application to probe-drogue refuelling

The drogue stabilisation controller developed in chapter 4 (figure 4.9) works on the error between current drogue position and its steady-state position. This can be modified to permit active demand of drogue position.

In a similar manner to the cooperative controller presented by McFarlane et al., and extended in section 6.2, both receiver and drogue are passed a common target point generated from a weighted mean of current probe and drogue positions, scaled towards the drogue steady state position (figure 6.20, and equation 6.8).

The cooperative control architecture is based upon the generation of a target point towards which both receiver and drogue are aimed. Since the drogue possesses only transverse degrees of freedom (in a translational sense, neglecting hose pay-out/retraction), this target point is taken to be in a plane which lies across the drogue face, nominally in the tanker y-z plane for straight and level tanker flight. For drogue disturbances with fixed hose length the drogue moves along a curved surface, however even under severe turbulence the longitudinal motion is small compared to the length of the hose, therefore the level of curvature is considered negligible here. The target plane is assumed flat, but attached to the drogue, so it does move longitudinally with the drogue.

The target generation algorithm, shown in figure 6.20, takes into account the positions of probe, drogue, and envelope centre (drogue steady-state position). First, weighting factor w generates a point mid-way between the drogue and probe (as projected onto the drogue y-z plane), then scaling factor K draws the weighted point towards the refuelling envelope centre. In this manner, w can be adjusted to accommodate the differing dynamics of receiver and drogue, and K ensures that the target point does not drift out of the achievable drogue envelope.

Drogue controller gains are those used in the 'some-overshoot' controller in chapter 4.

The target point is constructed in two stages. An intermediate point

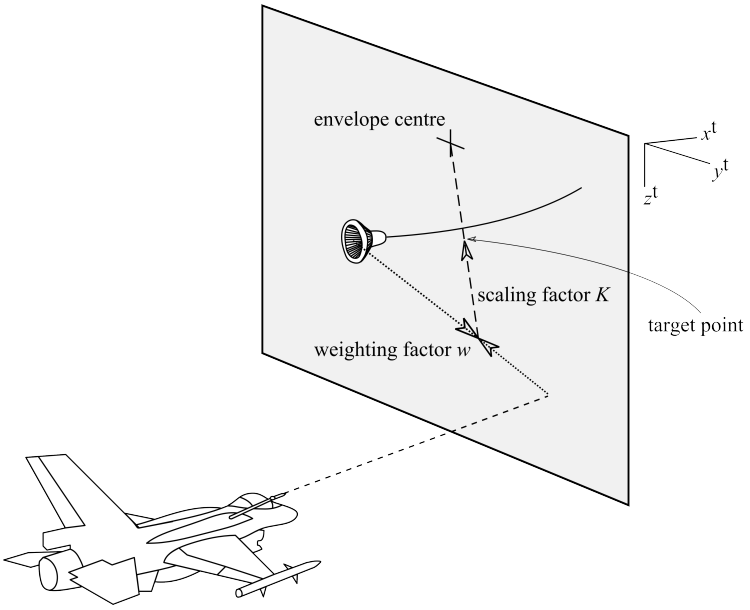

Figure 6.20: Cooperative target point construction

between the drogue and projected probe point (y'_t, z'_t) is calculated, where $w = 0$ places the point at the probe and $w = 1$ at the drogue:

$$\begin{bmatrix} y'_t \\ z'_t \end{bmatrix} = \begin{bmatrix} y_d & y_p \\ z_d & z_p \end{bmatrix} \begin{bmatrix} w \\ 1-w \end{bmatrix} \tag{6.9}$$

and then this is scaled towards the envelope centre (the drogue steady-state position) to create target point (y_t, z_t):

$$\begin{bmatrix} y_t \\ z_t \end{bmatrix} = \begin{bmatrix} y'_t & y_{\text{dss}} \\ z'_t & z_{\text{dss}} \end{bmatrix} \begin{bmatrix} K \\ 1-K \end{bmatrix} \tag{6.10}$$

The effect of the cooperative controller can be seen in figures 6.21 and 6.22, which show probe, drogue and target point z-position (relative to the tanker reference frame) and error with the cooperative controller active. Compared to the stabilised drogue plot in figures 4.17 and 4.18, the drogue can be seen tracking the target point and reducing the error between the systems. For this simulation, the target point weighting w and gain K are both set to 0.5 in the horizontal and vertical directions.

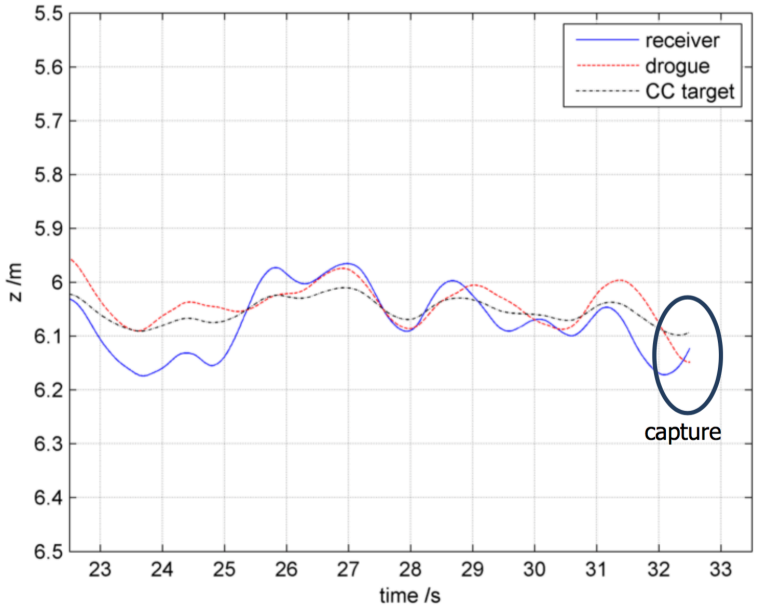

Figure 6.21: Vertical position of cooperatively controlled receiver and drogue (w = K = 0.5) under light turbulence – successful capture.

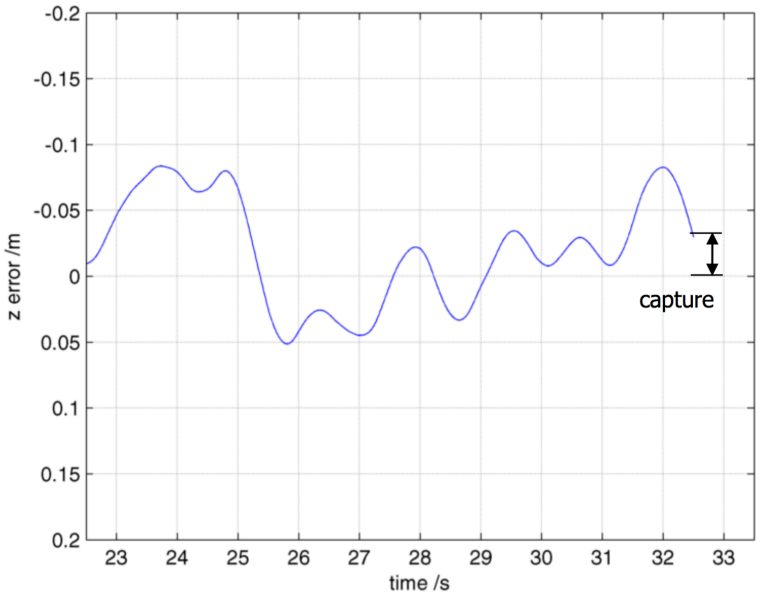

Figure 6.22: Vertical error between cooperatively controlled receiver and drogue (w = K = 0.5) under light turbulence – successful capture

6.3.1 Optimisation

The receiver and drogue dynamics are significantly different from one another. It is likely to be advantageous to position the target point closer to the receiver, as the drogue's more agile response will enable it to move more rapidly towards the target and cover a relatively larger distance than the receiver in the same time.

Optimisation was conducted on a simplified implementation of the AAAR SE, with a light-to-moderate turbulence level of 5 (out of 20, as in the baseline simulations). Given that the receiver and drogue both have differing, relatively uncoupled lateral and vertical dynamics, separate optimisations were conducted for lateral and vertical target point controllers. An unconstrained nonlinear optimisation approach using the Nelder-Mead simplex algorithm [171] (via MATLAB's `fminsearch` function) was used to minimise the absolute integral position error between the two systems in the final 5 seconds of approach and capture. Initialising the simplex algorithm with gains of $(w = 0.5, K = 0.5)$ performs an optimisation resulting in minimum absolute integral error and returning the optimum gains used to achieve this.

The nonlinear models are more computationally intensive, with each of the lateral and vertical optimisations taking around 65 minutes to complete on a desktop computer. Both converged to sensible values, given in table 6.5.

Table 6.5: Optimal cooperative controller gains for turbulence = 5

w_y	0.362
w_z	0.686
K_y	0.981
K_z	0.998

These values show an advantage, as expected, of weighting the target point towards the receiver in the lateral direction, and taking advantage of the drogue's faster response, however the weighting is towards the drogue in the vertical, likely because the receiver has very different dynamics in lateral and vertical directions, being much more agile vertically. The gains that scale the target point towards the envelope centre provide only a very light attraction – optimal values for this may be strongly dependent upon turbulence levels.

The target point generation method means that w and K are significantly coupled – an alternative method may be to use three gains that perform a triangular weighting between probe, drogue and envelope centre.

6.3.2 Simulations

Figure 6.23 shows capture with no turbulence, and figures 6.25 and 6.27 show a typical successful capture under low and moderate turbulence. Results presented begin around $t = 35$ s, just before the AAAR controller switches from tanker-based tracking to the cooperative, drogue-based, method. When the receiver is distant, the drogue is stabilised about its steady-state position, then as the receiver approaches the control system switches to common-target cooperative control (at $t \approx 38$ s in these figures). Convergence at $t = 35$-40 s is within the limits set out in chapter 3, indicating successful drogue capture.

Actuation demand for zero, low and moderate turbulence is shown in figures 6.24, 6.26 and 6.28. Drogue force demand does not exceed the conservative ±150 N limit under all but severe turbulence. Saturation does occur under severe turbulence, and raising the limit to ±300 N does not increase capture rate. It was identified that the zero capture rate under severe turbulence is due to limitations of the F-16 control system.

6.3.3 Results

Capture rates are shown in table 6.6. The cooperative controller produces significantly improved rates compared to the stabilised drogue.

Table 6.6: Drogue capture rates

	Turbulence			
	None	Low	Moderate	Severe
Open-loop	100 %	59 %	17 %	0 %
Stabilised	100 %	72 %	32 %	0 %
Cooperative	**100 %**	**90 %**	**46 %**	**0 %**

To assess the effect of the gust delay, similar simulations were run with gusts affecting drogue and receiver simultaneously. These produced capture rates of 91 %, 43 % and 0 % for low, moderate and severe turbulence, nearly

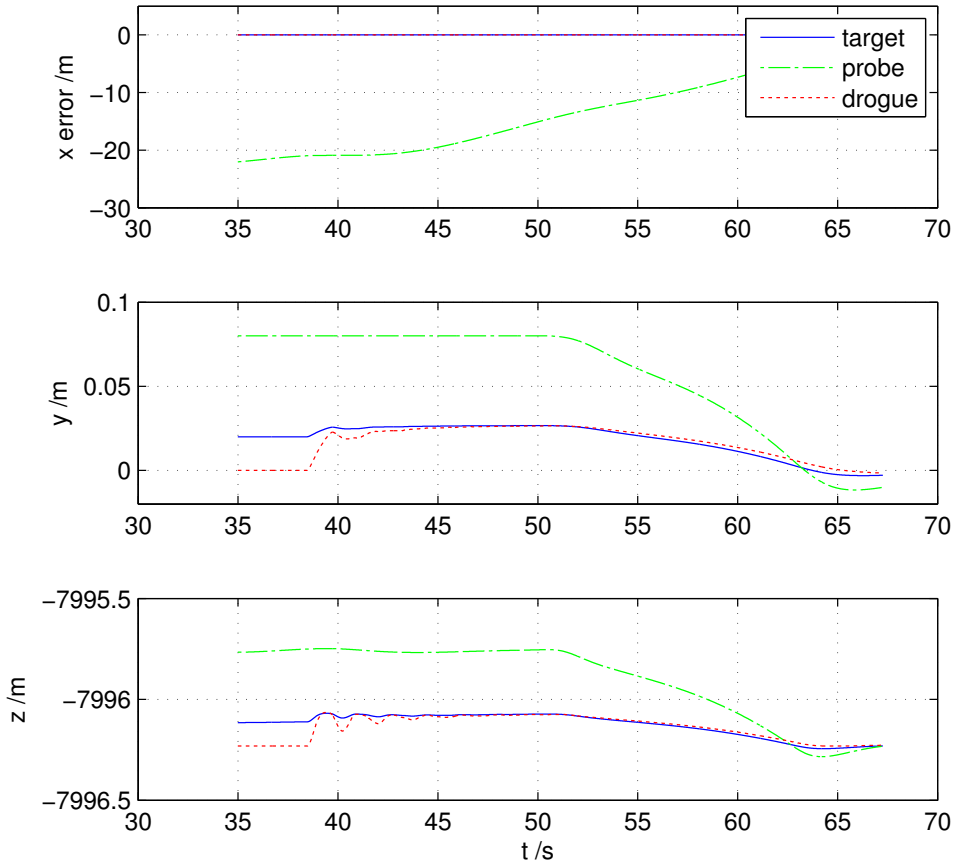

Figure 6.23: Probe, drogue and target point - cooperative controller, no turbulence

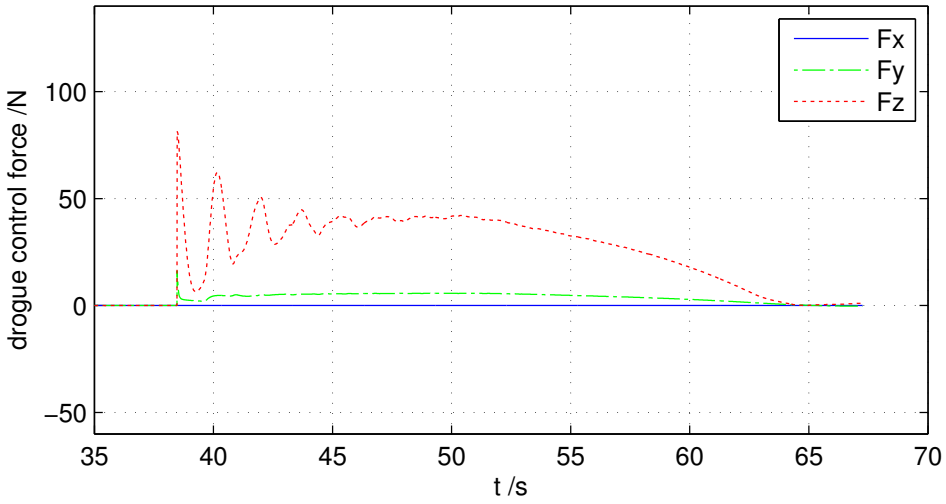

Figure 6.24: Drogue force - cooperative controller, no turbulence

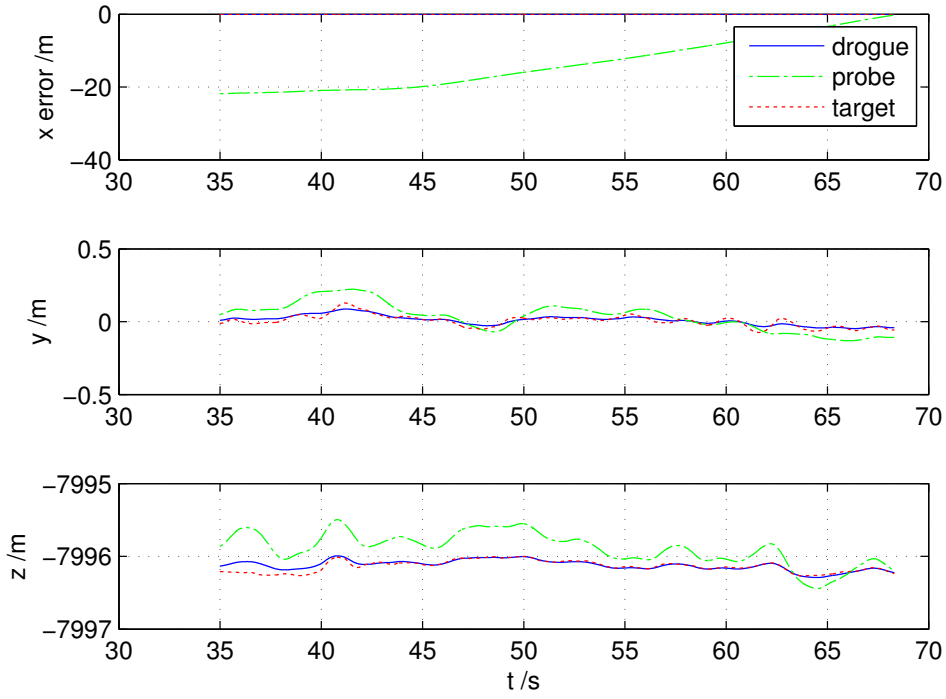

Figure 6.25: Probe, drogue and target point - cooperative controller, low turbulence

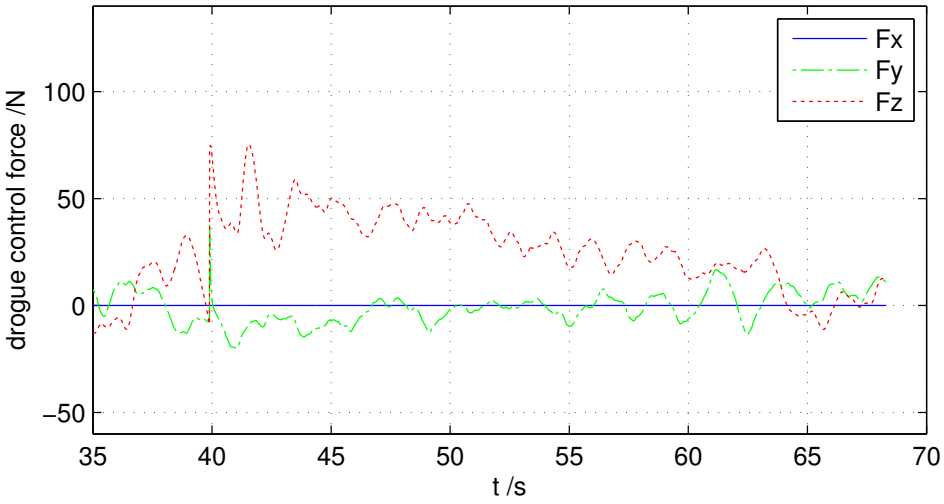

Figure 6.26: Drogue force - cooperative controller, low turbulence

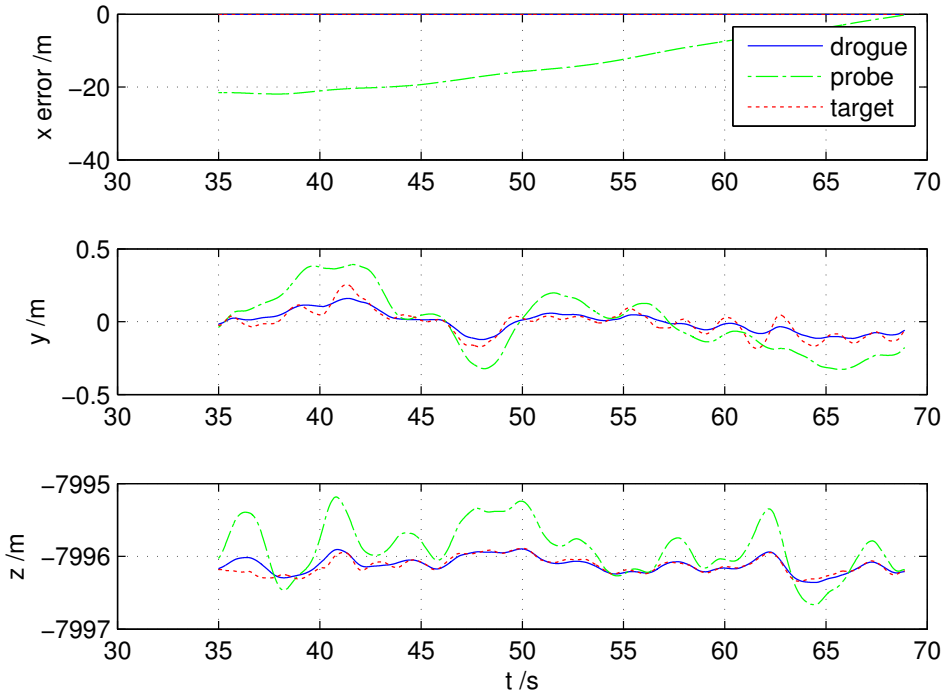

Figure 6.27: Probe, drogue and target point - cooperative controller, moderate turbulence

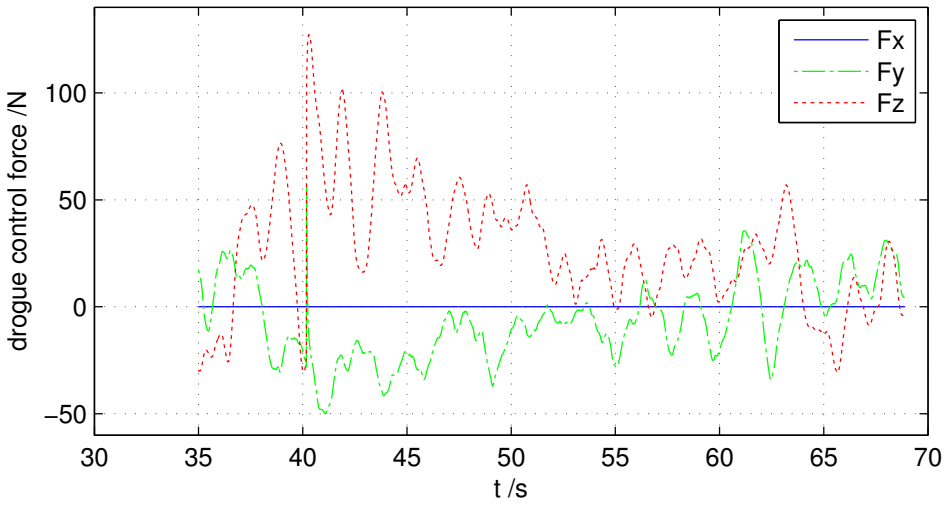

Figure 6.28: Drogue force - cooperative controller, moderate turbulence

identical to those with gust delay. Subsequent simulations will be conducted with gust delay enabled.

A series of simulations configured in the same way as in sections 3.11 and 4.3 were conducted to evaluate capture rate under varying turbulence. Results are shown in figure 6.29.

This controller produces an improved capture rate over drogue stabilisation up to high-moderate levels of turbulence, but at high turbulence its success drops rapidly. Figures 6.30 and 6.31 show that with this controller the target point moves away from the drogue steady-state position, at around 6 m below the tanker origin. The values of K, the envelope centre gain, do not pull the target point tightly enough towards the envelope centre at high turbulence, and drogue control authority is reduced.

6.3.4 Optimisation for severe turbulence

A second optimisation on the nonlinear models was conducted, this time with the turbulence level set at 18. As expected, the new optimal envelope centre gains, shown in table 6.7, draw the target point more tightly towards the drogue steady-state position, particularly in the lateral direction. The weightings between receiver and drogue, whose effect are already reduced due to the increased pull towards the envelope centre, are more balanced.

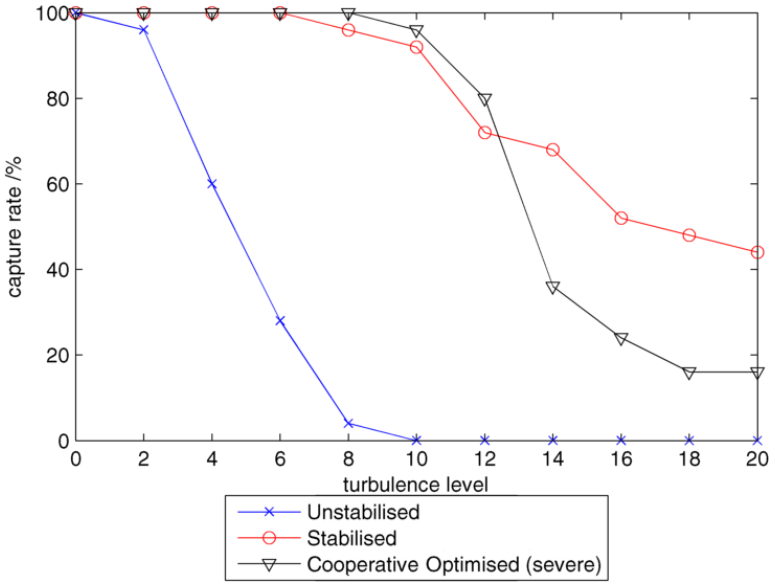

Figure 6.29: Capture rates for L/F, stabilised and cooperative controllers under varying turbulence (controller optimised at turbulence level 5).

Table 6.7: Optimal cooperative controller gains for turbulence = 18

w_y	0.592
w_z	0.405
K_y	0.094
K_z	0.564

Simulation results, with example cases shown in figure 6.32 and figure 6.33, show that the target point remains much closer to the envelope centre.

The performance of this heavy-turbulence optimised controller is shown in figure 6.34. At high levels of turbulence its performance is significantly better than the previous controller (although still less successful than the stabilised drogue), however at low turbulence its performance is worse, due to it restricting the freedom of the target point.

These results imply that an adaptive control system would provide the best solution for a cooperative controller across the turbulence spectrum, allowing the target point to drift in low turbulence, with high values of K, and pulling it tighter towards the envelope centre in higher turbulence via lower values of K.

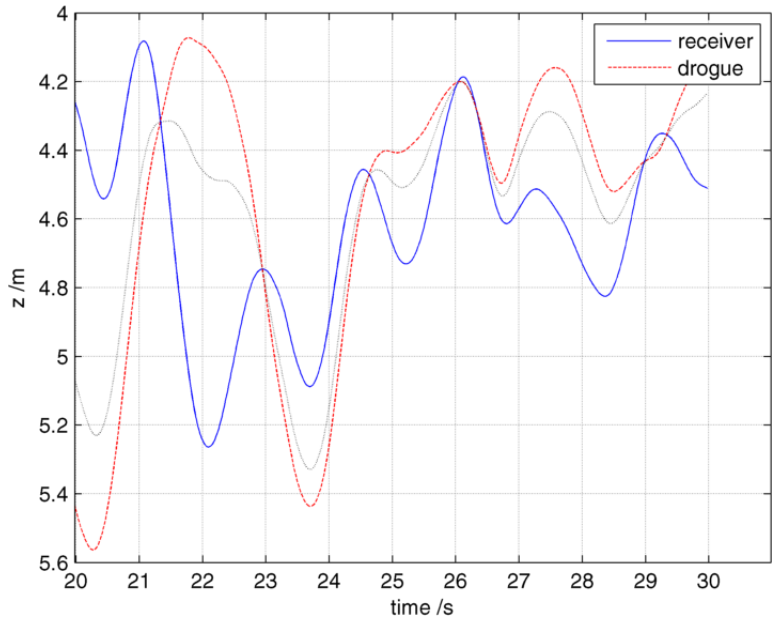

Figure 6.30: Vertical position of optimised cooperatively controlled receiver and drogue under severe turbulence – failed capture

Comparing this approach to the scheduled-gain implementation presented in section 6.2, it is evident that the AAAR optimisation problem is multivariable and the design and optimisation of a cooperative controller is complex. Combining the various methods of scheduling the target point generation may prove beneficial, but will also lead to complex interactions between the various weightings applied.

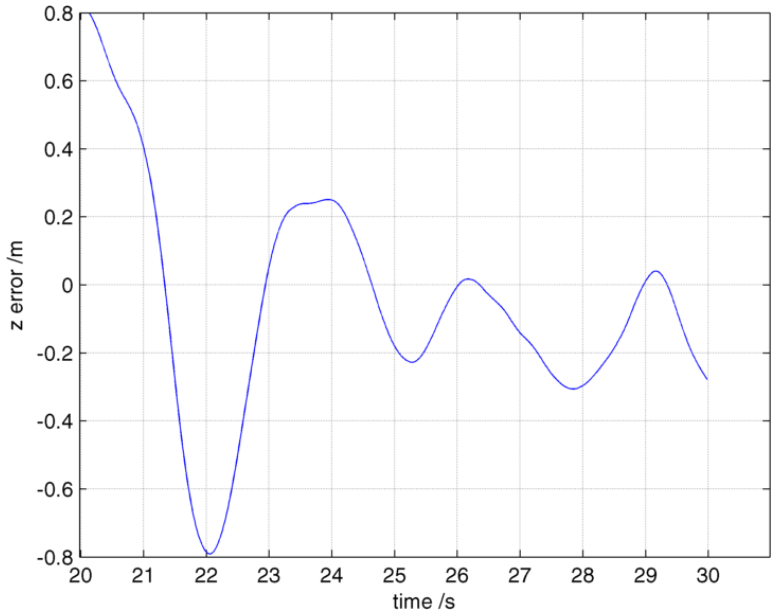

Figure 6.31: Vertical error between optimised cooperatively controlled receiver and drogue under severe turbulence – failed capture

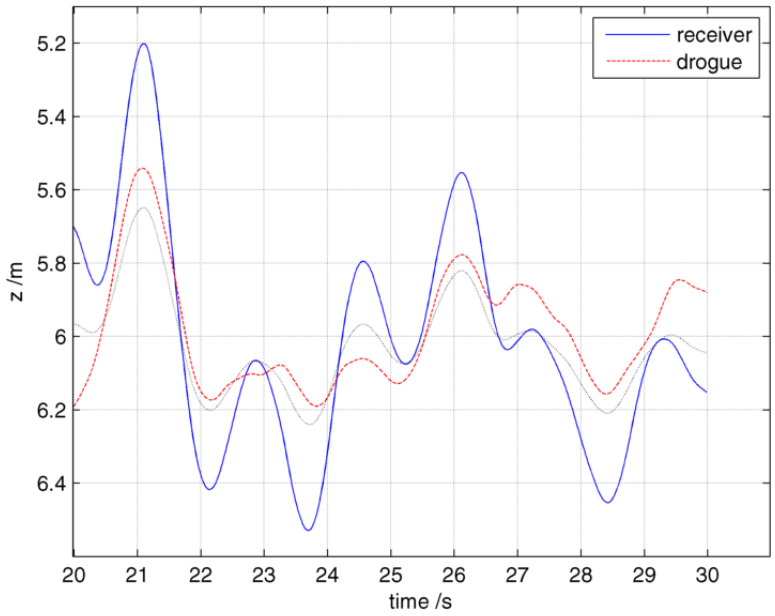

Figure 6.32: Vertical position of heavy-turbulence optimised cooperatively controlled receiver and drogue under heavy turbulence – failed capture

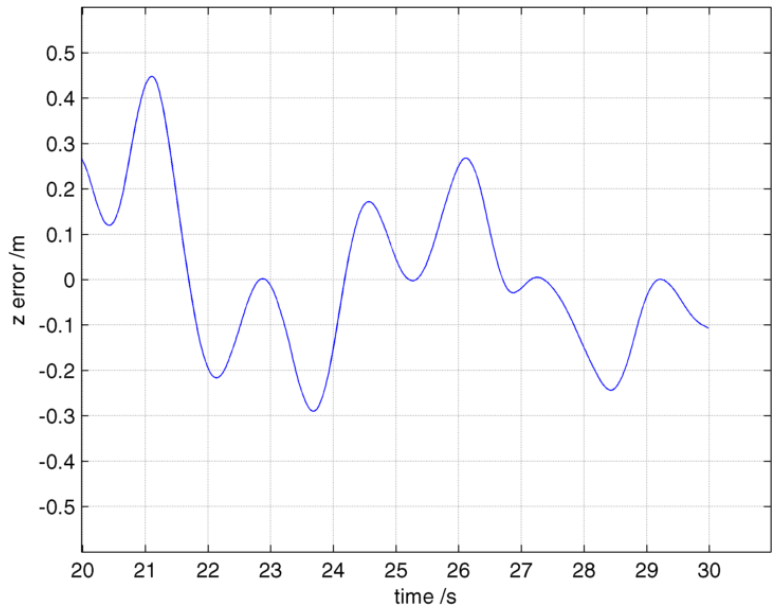

Figure 6.33: Vertical error between heavy-turbulence optimised cooperatively controlled receiver and drogue under heavy turbulence – failed capture

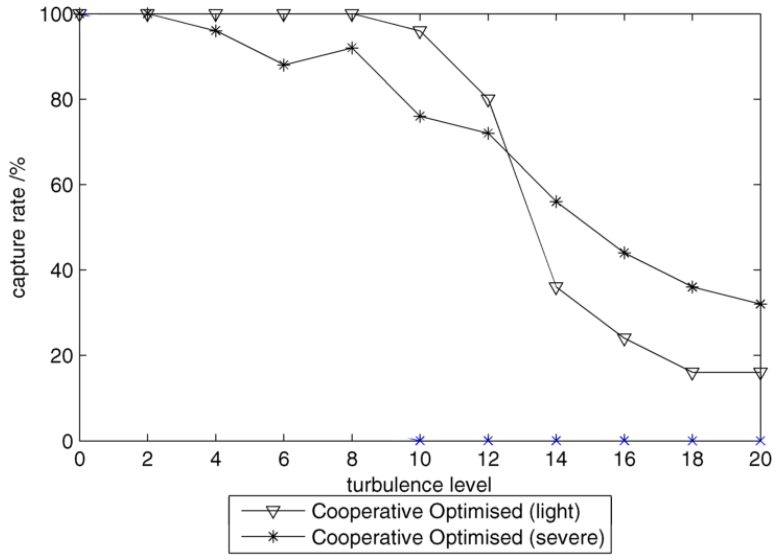

Figure 6.34: Capture rates for L/F, stabilised and cooperative controllers under varying turbulence (optimised at light turbulence = 5; and heavy turbulence = 18, showing a moderate improvement at higher turbulence levels.

6.3.5 Effect of noise and delay

Noise is almost always present in every signal and any real system is expected to cope with some degree of noise in the system. Increasing the level of noise degrades the quality of the signal and is expected to decrease performance of the associated system. The introduction of noise to the AAAR simulation is expected to degrade capture performance. Capture rate is expected to fall with increasing level of noise, reaching a level where it drops to zero meaning the simulation is incapable of drogue capture.

Randomly generated noise was introduced into the cooperative target signal to analyse the effect of sensor and processing noise on capture rate. Random noise was generated via MATLAB's `rand` function, generating a matrix of size $m \times n$ with random values with uniform distribution on the interval $[a, b]$, which were summed with the cooperative target point position. In order to simulate non-isotropic sensor noise in different axes, separate noise signal seeds are used for x, y and z values.

Different seeds are used for the target point signal transmitted to the receiver and drogue, to simulate differing sensor noise. A sample cooperative control target signal is shown in figure 6.35, for turbulence intensity of 3.

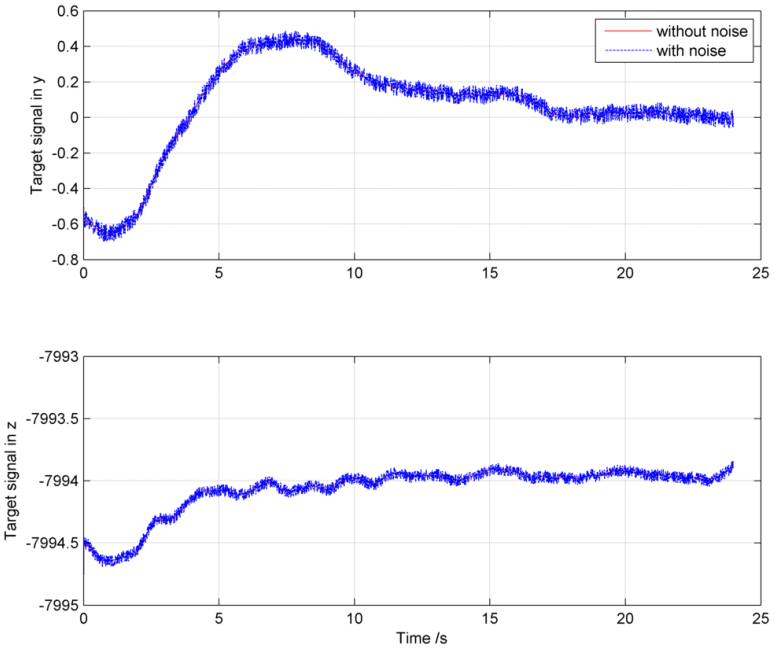

Figure 6.35: Cooperative target point signal with noise.

Multiple stochastic simulations were completed to investigate the effect of noise on capture rate. Once again the same set of turbulent seeds was used to keep results comparable. For the purposes of the simulation a turbulence intensity of 3 (corresponding to light turbulence) was chosen throughout the test cases. The peak-to-peak amplitude of the randomly generated noise signal was varied from 0 to 20 cm with an increment of 0.5 cm from 0 to 10 cm followed by an increment of 1 cm thereafter. Results are shown in figure 6.36. Beyond noise amplitude of 1-2 cm, capture rate falls rapidly.

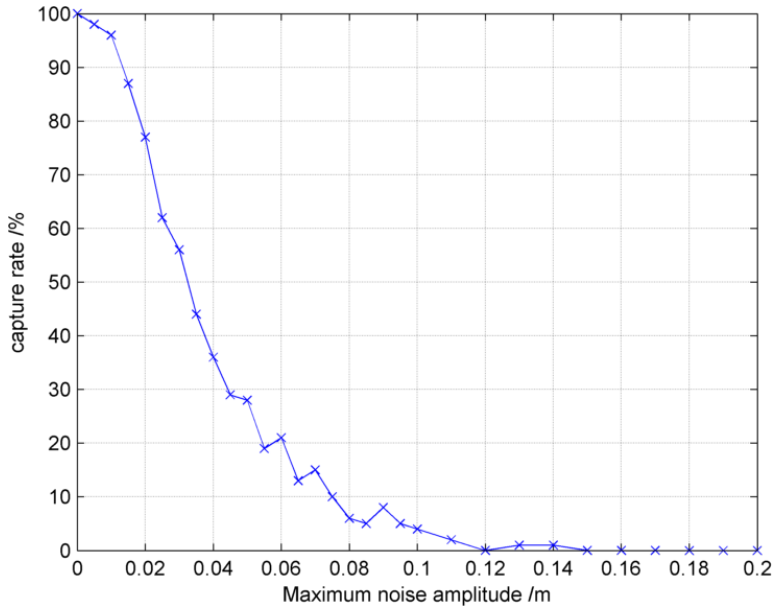

Figure 6.36: Capture rate with increasing noise amplitude at light turbulence.

Some degree of delay is also present in real systems. This delay is dependent on the time taken for sensors and systems to receive information, process it, and pass it to relevant subsystems.

Delay was introduced into the simulation by adding a transport delay to the cooperative control target point. This holds the input in a buffer for a specified amount of time before transmitting it. The capture performance of the AAAR simulation is expected to degrade with increasing delay in the cooperative control target point. Figure 6.37 shows the cooperative control target point signal for a simulation with 1 s delay.

Multiple simulations were again conducted to investigate the effect of the delay, with turbulence intensity of 3. Delay was varied from 0 to 2.5 s.

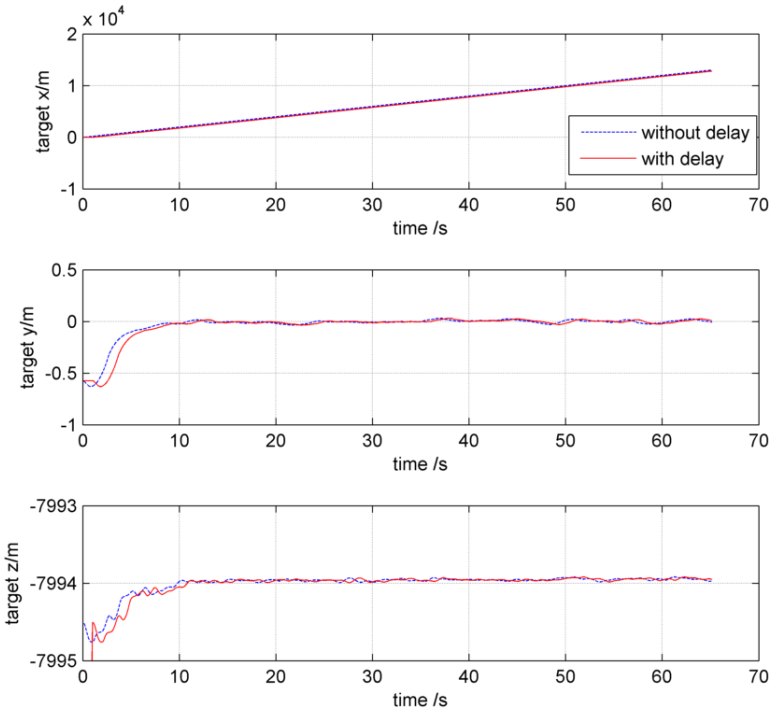

Figure 6.37: Cooperative target point signal with 1 s delay

Capture rates are plotted in figure 6.38

A high capture rate is maintained from 0.5 to 2.30 seconds after which it drops down to zero, failing to capture at all after this. The consistently high capture rate is due to the good position tracking of the controller in light turbulence. If the receiver and drogue remain within the drogue capture envelope, then it does not matter if they are tracking a time-offset signal. Performance is likely to be significantly worse for delay under increased turbulence.

Below 0.5 s there are several delay ranges which produce significant reductions in capture rate. These rapid and significant drops are likely due to interactions with modes of the combined drogue-receiver-controller system, and should be noted and avoided when designing a cooperative controller.

These results are for a single level of turbulence, with a uniform, single-frequency noise signal. In a real system noise will be multi-source and more complex in its nature, and performance is likely to be more variable.

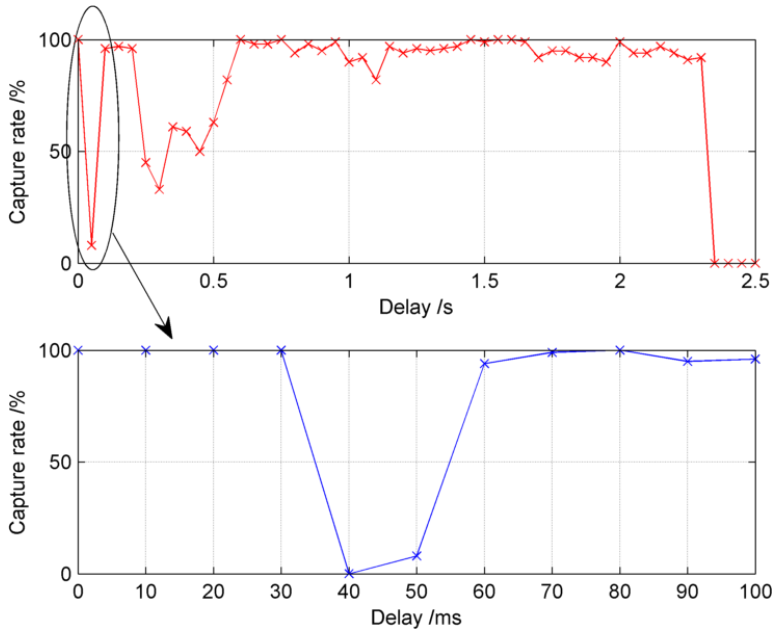

Figure 6.38: Capture rate vs target point signal delay (lower plot is magnification of upper plot).

6.3.6 HIL Verification

The RMR facility, developed by the University of Bristol ASTRAEA team in parallel to the work covered in this thesis, can be used to verify this control architecture at a higher TRL than via simulation alone, with real sensors in the loop. A proposed sensor configuration including INS, radar and optical sensors, is situated at the base of the refuelling probe, on the track-mounted robot ('Rob2'), and observes the position of the drogue which is attached to the floor-mounted robot ('Rob1')[1]. The simulation is compiled to run on the RMR PXIe controller, the robots are commanded to replicate probe and drogue motion at full-scale and in real-time, and the real-world sensors feed back to the virtual SE in a HIL configuration.

Figure 6.40 shows the relative position demanded of the robots, against the sensed relative position that is returned to the SE, for a small portion of one simulation run. It can be seen that the signal contains varying noise, delay and position offset.

Figures 6.41 and 6.42 show vertical motion for successful RMR captures

[1]These robots were informally known as 'Zippy', for the track-mounted arm, and 'Bungle' for the floor-mounted one.

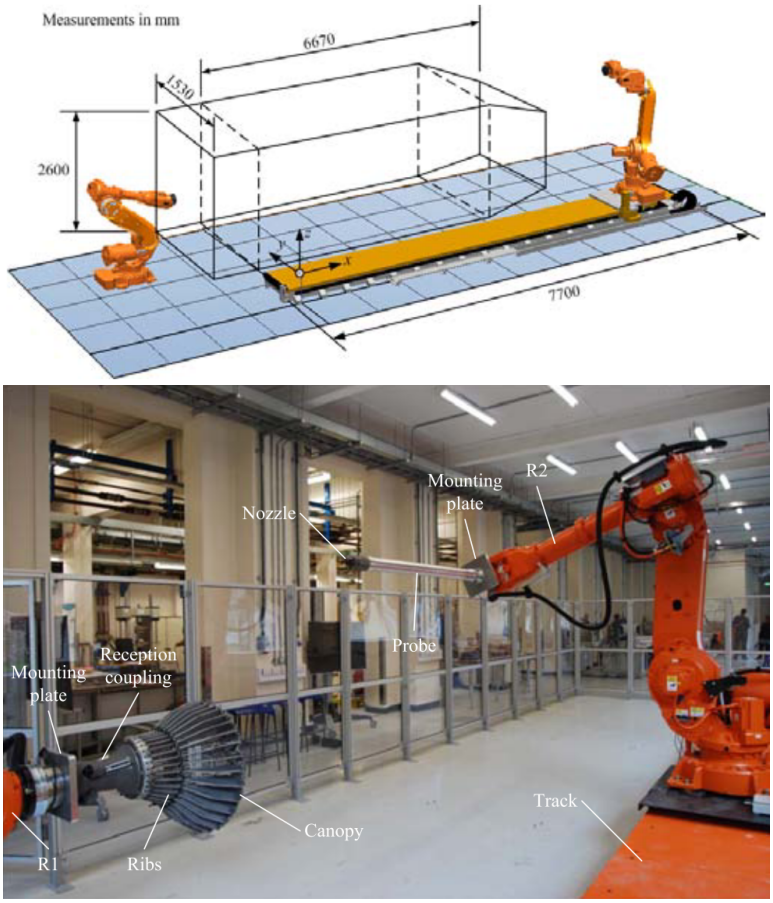

Figure 6.39: RMR facility layout and schematic.

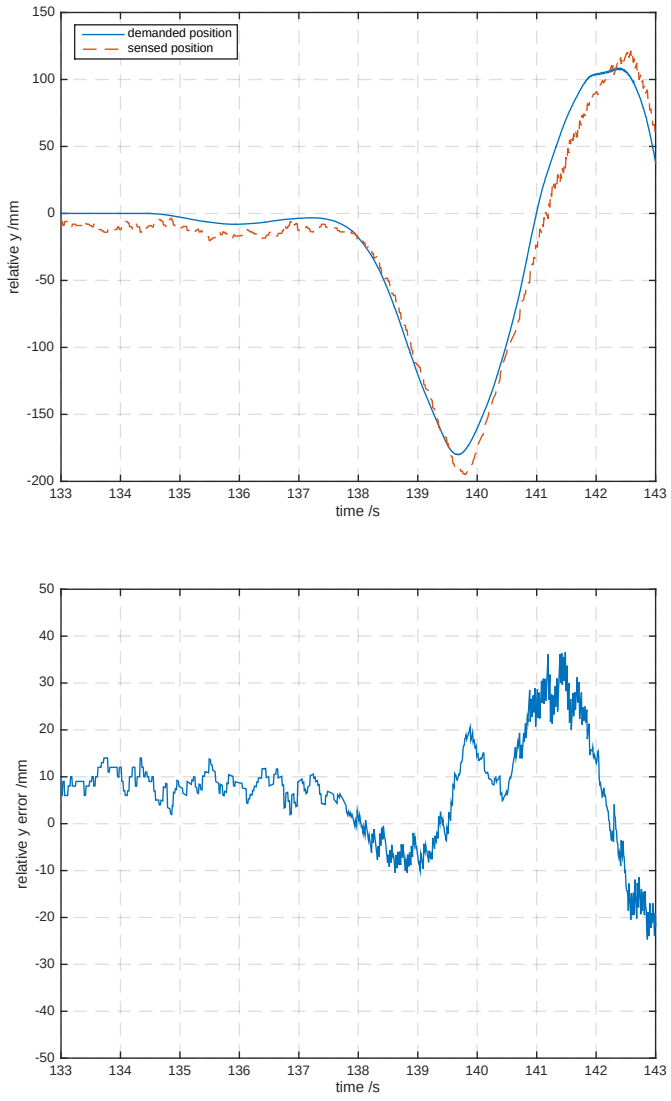

Figure 6.40: RMR relative probe-drogue position and error – demanded vs sensed.

with L/F and CC control respectively. Figure 6.43 shows the relative error between probe and drogue for these runs. It can be seen that as the receiver approaches the drogue, the CC controller significantly reduces probe-drogue error, with the controlled drogue tracking the receiver's motion and vice-versa. The offset between probe and drogue at the end of both simulations is within the capture envelope – different runs show varying capture offset, depending on controller and turbulence seeds.

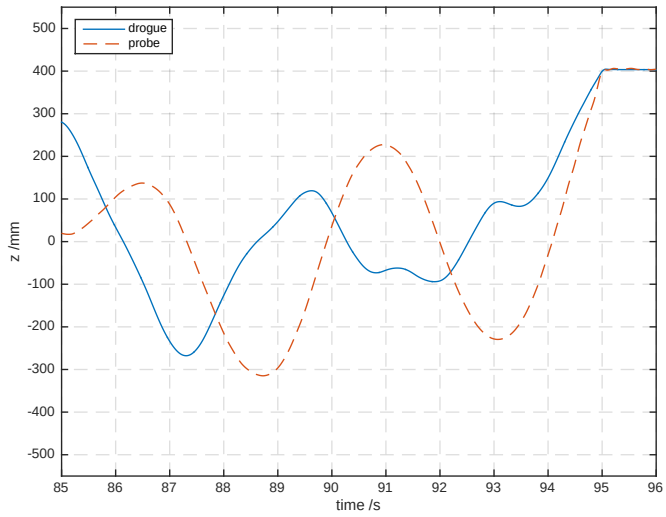

Figure 6.41: RMR HIL capture for L/F controller.

6.3.7 Practical considerations

The capture rate results above indicate a notable improvement over comparable open-loop and stabilised approaches. Actuation methods were considered in chapter 4 and consideration of physical robustness, safety and other issues are also detailed. The cooperative controller in this chapter requires multi-agent cooperation and the implications of this to sensing, processing and communications must be considered.

- **Information:** in the common-target architecture, the target point construction controller must be aware of the location of receiver, drogue and drogue steady-state locations. This could be implemented with separate sensors on tanker/drogue and receiver, which would permit

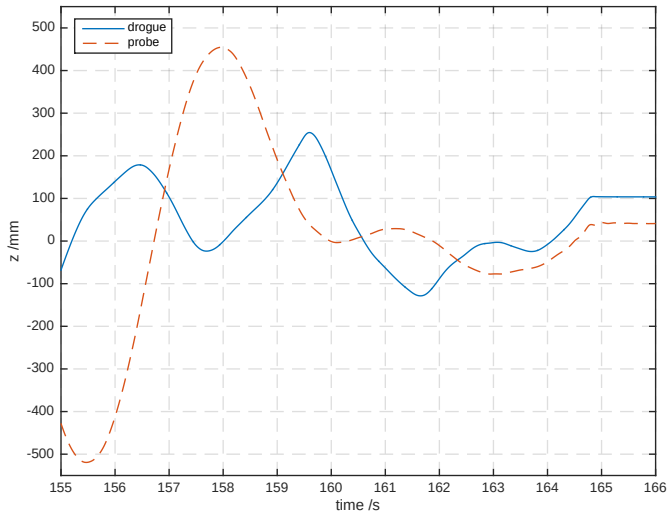

Figure 6.42: RMR HIL capture for CC controller.

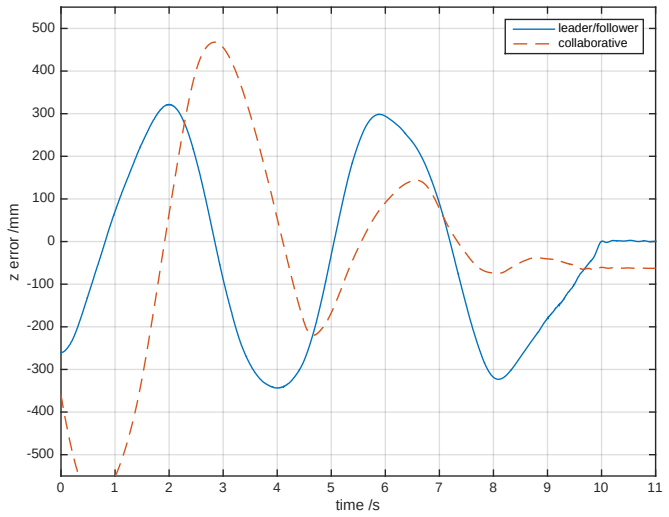

Figure 6.43: RMR HIL probe-drogue error for L/F and CC controllers.

local target point generation and limit the communications requirement, or with a centralised controller, probably on the tanker, which would require communication of the target point to the receiver.

- **Systems distribution:** Issues with a decentralised implementation include disagreement between sensors which would lead to discrepancies in target points. A centralised sensing and target point generation approach would be more desirable, but carries a communications burden.

- **Sensors:** for the simulations above, drogue acceleration was integrated twice to give position. In practice, this measurement would drift and requires a tanker-based reference measurement to give accurate drogue position. For drogue-probe convergence a relative position measurement is all that is required, but for station-keeping within the refuelling envelope this is not adequate. Further consideration to sensing methods will be given in subsequent deliverables.

- **Communication:** Depending on the distribution of sensors and systems, the communication of target point location and other parameters may be necessary. The requirement for drogue-receiver communication can be eliminated by duplication of sensors but at the possible expense of robustness as mentioned above.

Chapter 7

Intimate Control

In chapter 6 a Common-target-point Control architecture was demonstrated to improve capture rate over a range of turbulence in AAAR. The CC approach uses receiver and drogue position states to generate a target point that is passed to the separate receiver and drogue controllers.

If the receiver and drogue are modelled as one system rather than two, MIMO optimisation methods can be used. This will produce a more tightly-coupled solution, which will likely require data transmission between the two vehicles, but this may be an acceptable cost if capture rate is significantly improved.

7.1 Existing work

An IC approach was developed by Griffiths [17, 183], of MBDA, for UAV-UGV docking. His approach produces a combined system representing the error dynamics of the two bodies, and uses LQR optimisation to design a controller.

Griffiths' controller is for the XRAE UAV developed by Cranfield University and Imperial College, and the UGV is BAE Systems' ATC Wildcat. Both models are specific and realistic, representing relevant aerodynamic and mechanical aspects such as cross-coupling between the UAV's degrees of freedom and a model of the UGV's suspension. UGV wake effects are accounted for using CFD models of the Wildcat.

Griffiths reduces the vehicles' dynamics to first-order transfer functions of the form $\frac{1}{\tau s+1}$, and simplifies further by assuming similar dynamics for

both, as the UAV's slower dynamics will dominate.

He initially uses a finite-horizon Linear Quadratic Gaussian (LQG) optimisation method, with performance index

$$J_{LQG} = \left(\tilde{\mathbf{z}}^\top P \tilde{\mathbf{z}}\right)_{t=t_f} + \int_0^{t_r} (\mathbf{u}^\top R \mathbf{u})\ dt, \tag{7.1}$$

producing gains scheduled against time-to-go but determines this unnecessary and proposes a constant gain matrix via an infinite-horizon LQR approach, with performance index

$$J_{LQR} = \int_0^{\infty} (\tilde{\mathbf{z}}^\top Q \tilde{\mathbf{z}} + \mathbf{u}^\top R \mathbf{u})\ dt. \tag{7.2}$$

This produces simpler, constant gains as the drive is to minimise state errors $\tilde{\mathbf{z}}$ and inputs $\mathbf{u}$ at all times, rather than aim for a goal-state at a specific point in time.

Griffiths' 6-DoF simulations, including atmospheric turbulence and UGV wake effects, show that docking to a capture point 1 m above the roof of the UGV is possible.

Griffiths' methods were implemented by Jones [184] at the University of Bristol, using a Quanser 3-DoF rotorcraft and 1-DoF ground vehicle (figure 7.1). He showed that an IC approach improves convergence of those vehicles in simulation (figure 7.2) and practice.

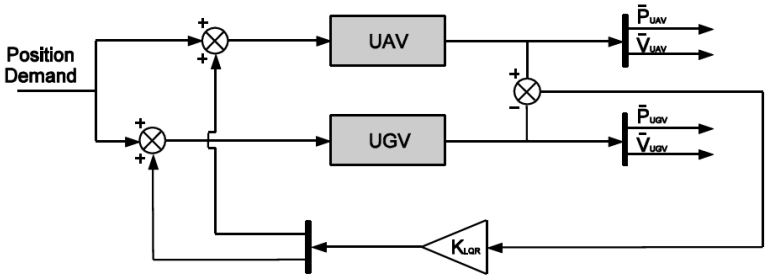

Figure 7.1: IC architecture [184]

Both Griffiths and Jones simplify their IC optimisation by assuming the dynamics of both systems to be identical. Chapter 6 showed that the refuelling hose and drogue display significantly different behaviour, and both models are of different order with different numbers of states. These are challenges which must be addressed for a full AAAR implementation.

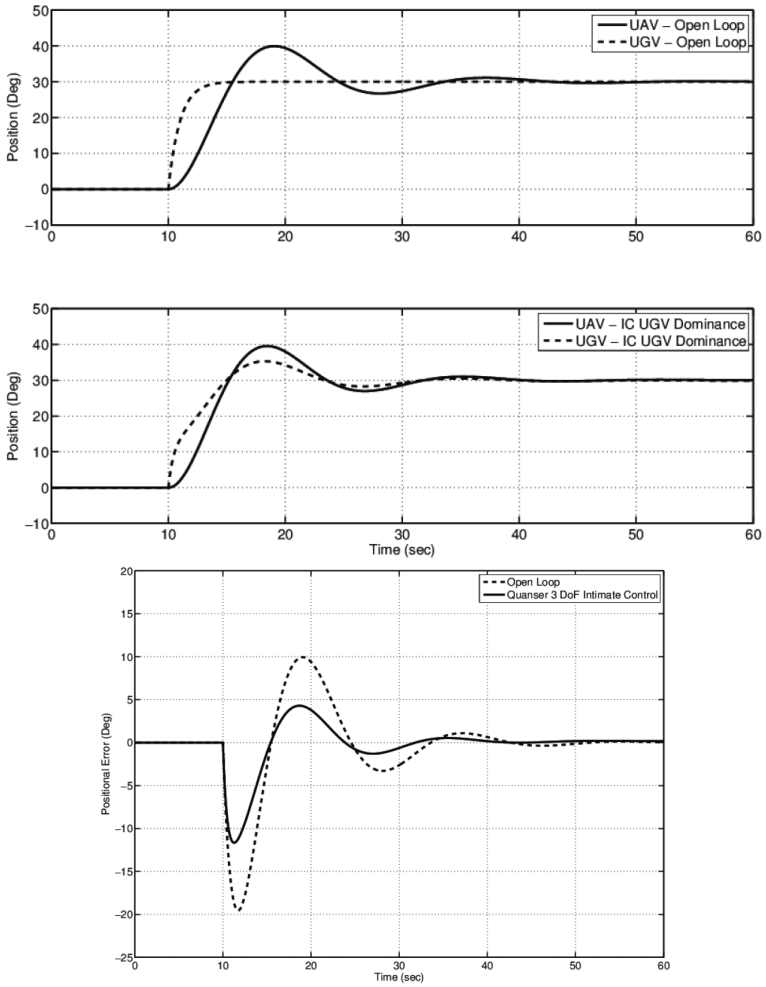

Figure 7.2: Quanser-UGV intimate control [184]

7.2 Intimate control methodology

7.2.1 Architecture construction

Understanding the existing similar-systems IC methodology is necessary in order to extend it towards the AAAR context. As an example, application of this method to two simple, identical, second order systems is conducted. Transfer function

$$\frac{y}{u} = \frac{1}{s^2 + s + 1} \tag{7.3}$$

has an open-loop step response shown in figure 7.3, with 2 % settling time $t_s = 8.08$ s, converging to steady state at $t = 12$ s.

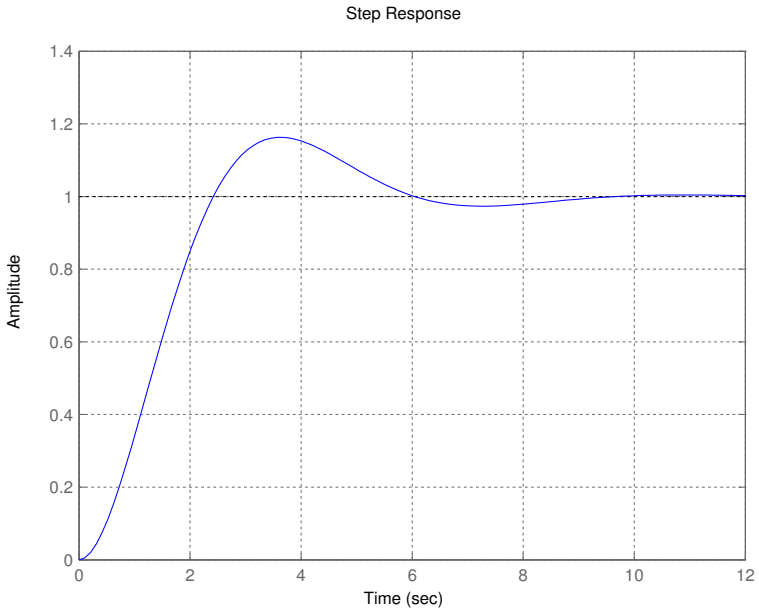

Figure 7.3: Step response for $\frac{y}{u} = \frac{1}{s^2+s+1}$

In state space form, this system can be represented as

$$\begin{aligned} \dot{\mathbf{x}} &= A\mathbf{x} + B\mathbf{u} \\ \mathbf{y} &= C\mathbf{x} + D\mathbf{u} \end{aligned} \tag{7.4}$$

where

$$\begin{aligned} A &= \begin{bmatrix} -1 & -1 \\ 1 & 0 \end{bmatrix} \qquad B = \begin{bmatrix} 1 \\ 0 \end{bmatrix} \\ C &= \begin{bmatrix} 0 & 1 \end{bmatrix} \qquad D = \begin{bmatrix} 0 \end{bmatrix}. \end{aligned} \tag{7.5}$$

Since these systems are linear, convergence of two decoupled open-loop systems

$$\{A_1, B_1, C_1, D_1\} = \{A_2, B_2, C_2, D_2\} = \{A, B, C, D\},$$

responding to identical position demands, occurs with identical settling time to that of the individual systems (figure 7.4). In this case, convergence occurs with respect to the demanded position only - no attention is paid to minimisation of the error between the systems.

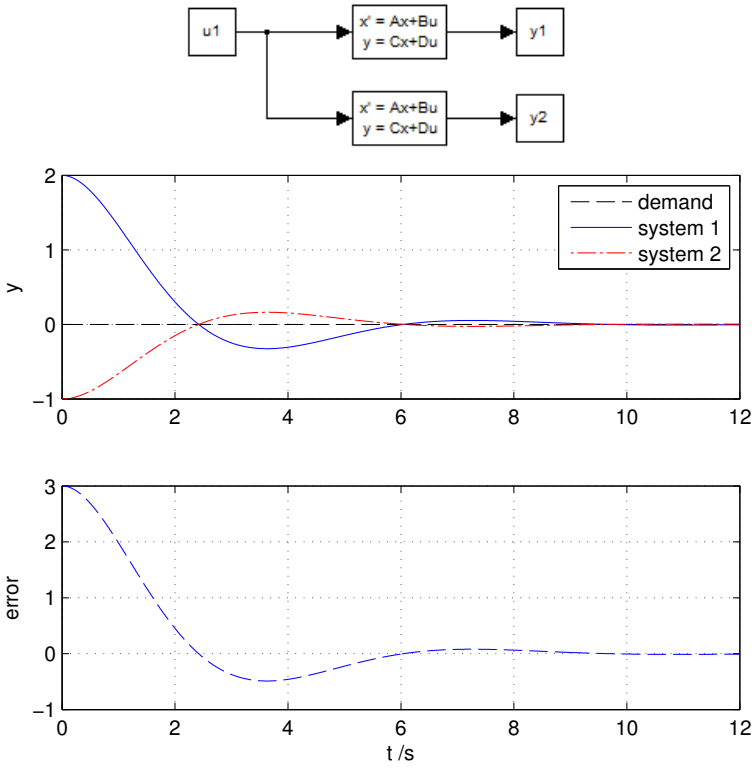

Figure 7.4: Response of decoupled, identical systems

In the open-loop example, the error between the systems was minimised by demanding identical position from both systems. Assuming either system

did not reach saturation of its control authority, and the goal is minimisation of the position error between the systems, the full capabilities of the systems would be underutilised even with separate feedback control on each system.

The two systems can be made to converge with respect to one another by passing a demand equal to the other's position to each, shown in figure 7.5. The systems converge faster but display higher overshoot. Settling time of the error is similar to the decoupled systems. The identical systems converge at a point half way between their initial positions.

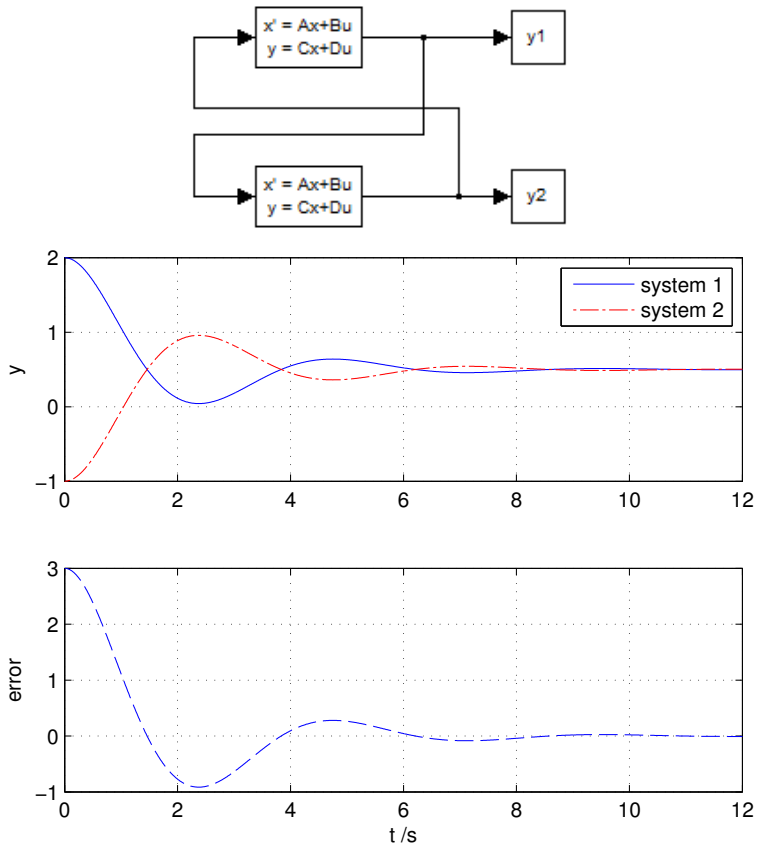

Figure 7.5: Convergence of identical systems with output cross-feedback

Given that station-keeping is required for AAAR, in addition to the convergence shown above, reintroduction of a position demand is necessary. Subtracting the position error of the vehicles from the demand drives the systems to the demanded position, shown in figure 7.6. The response, as with the previous architectures, is still suboptimal and the system requires

tuning to reduce overshoot, rise time and settling time.

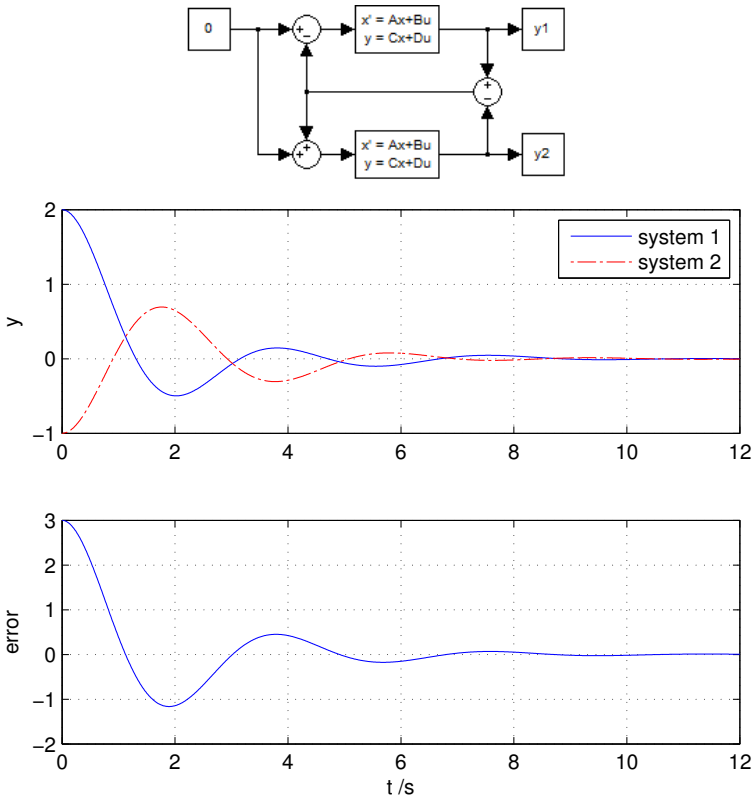

Figure 7.6: Convergence of identical systems with error feedback

7.2.2 Optimisation

Using the error feedback architecture in figure 7.6, Griffiths [17] identifies that optimisation can take place on the combined error dynamics of the two systems. Given systems of the form

$$\dot{\mathbf{x}}_1 = A_1\mathbf{x}_1 + B_1\mathbf{u}_1 \tag{7.6}$$

$$\dot{\mathbf{x}}_2 = A_2\mathbf{x}_2 + B_2\mathbf{u}_2, \tag{7.7}$$

the aim is to minimise the error vector

$$\tilde{\mathbf{z}} = \mathbf{x}_1 - \mathbf{x}_2. \tag{7.8}$$

Aiming to represent the error dynamics as state-space system

$$\dot{\tilde{\mathbf{z}}} = A\tilde{\mathbf{z}} + B\mathbf{u}, \tag{7.9}$$

the time derivative of equation 7.8 gives

$$\begin{array}{rcccc} \dot{\tilde{\mathbf{z}}} & = & \dot{\mathbf{x}}_1 & - & \dot{\mathbf{x}}_2 \\ & = & (A_1\mathbf{x}_1 + B_1\mathbf{u}_1) & - & (A_2\mathbf{x}_2 + B_2\mathbf{u}_2). \end{array} \tag{7.10}$$

Griffiths [17] assumes $A = A_1 \approx A_2$ (as for his systems the slower UAV dynamics dominate), so

$$\begin{array}{rcccc} \dot{\tilde{\mathbf{z}}} & = & A(\mathbf{x}_1 - \mathbf{x}_2) & + & B_1\mathbf{u}_1 - B_2\mathbf{u}_2 \\ & = & A\tilde{\mathbf{z}} & + & B_1\mathbf{u}_1 - B_2\mathbf{u}_2 \end{array} \tag{7.11}$$

If we now concatenate $\mathbf{u}$ and B, so $\mathbf{u} = [\mathbf{u}_1\ \mathbf{u}_2]^\top$, and $B = [(B_1)\ (-B_2)]$, the error dynamics can be represented in the form of equation 7.9.

Optimal feedback gain K is determined via an infinite-horizon LQR approach, minimising the performance index,

$$J_{LQR} = \int_0^\infty (\tilde{\mathbf{z}}^\top Q\tilde{\mathbf{z}} + \mathbf{u}^\top R\mathbf{u})\ dt. \tag{7.12}$$

The LQR methodology, as implemented in MATLAB, requires state feedback, so we are limited to systems where C outputs all states.

For the systems used in the example above, we have error dynamics:

$$\dot{\tilde{\mathbf{z}}} = A\tilde{\mathbf{z}} + B\mathbf{u} \tag{7.13}$$

where

$$\begin{array}{rclcrcl} A & = & \begin{bmatrix} -1 & -1 \\ 1 & 0 \end{bmatrix} & & B & = & \begin{bmatrix} 1 & -1 \\ 0 & 0 \end{bmatrix} \\ C & = & \begin{bmatrix} 0 & 1 \\ 1 & 0 \end{bmatrix} & & D & = & \begin{bmatrix} 0 & 0 \\ 0 & 0 \end{bmatrix}. \end{array} \tag{7.14}$$

Using MATLAB's `lqr` function, with Q and R as identity matrices, applying equal priority to minimisation of all errors and control effort, the

error feedback gain K is obtained:

$$K = \begin{bmatrix} 0.5564 & 0.3660 \\ -0.5564 & -0.3360 \end{bmatrix}. \tag{7.15}$$

Applying this to the previous error feedback architecture (where the systems are the original second-order models from equation 7.5, with the C and D matrices modified for full-state feedback), the response obtained is shown in figure 7.7.

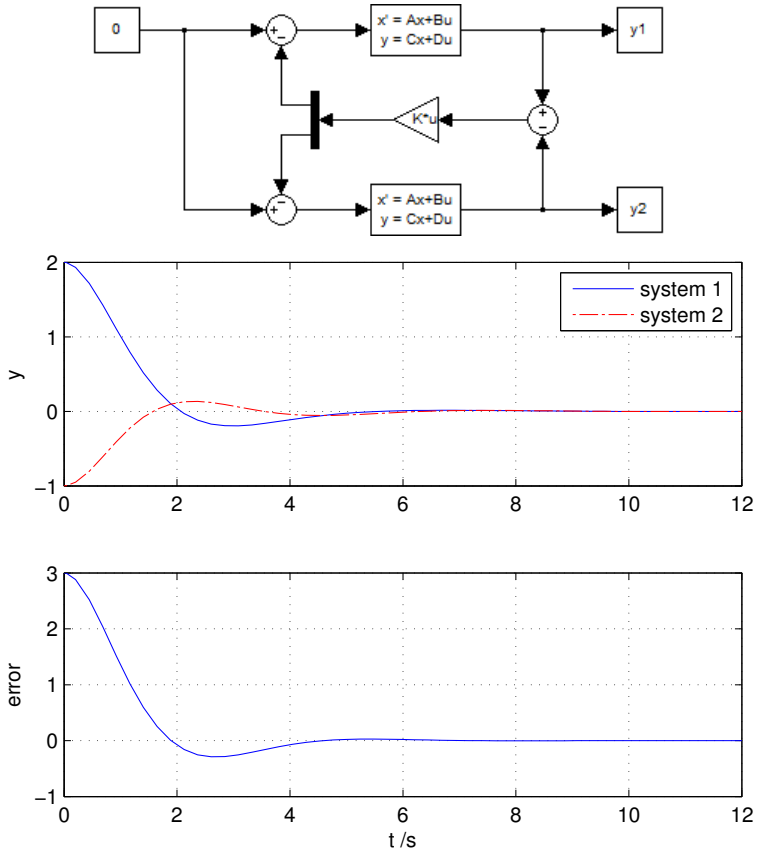

Figure 7.7: Convergence of identical systems with error feedback optimised via IC/LQR

Compared to figures 7.4, 7.5 and 7.6, significant improvement in convergence is evident. The effect of the intimate controller is more obvious if one vehicle has initial conditions equal to the demand, as in figure 7.8. The second vehicle can be seen to respond to the error demand by moving towards the first vehicle, leading to a faster convergence than for the open-

loop response. The first vehicle has a similarly increased demand towards the second, but this is harder to identify due to its initial offset.

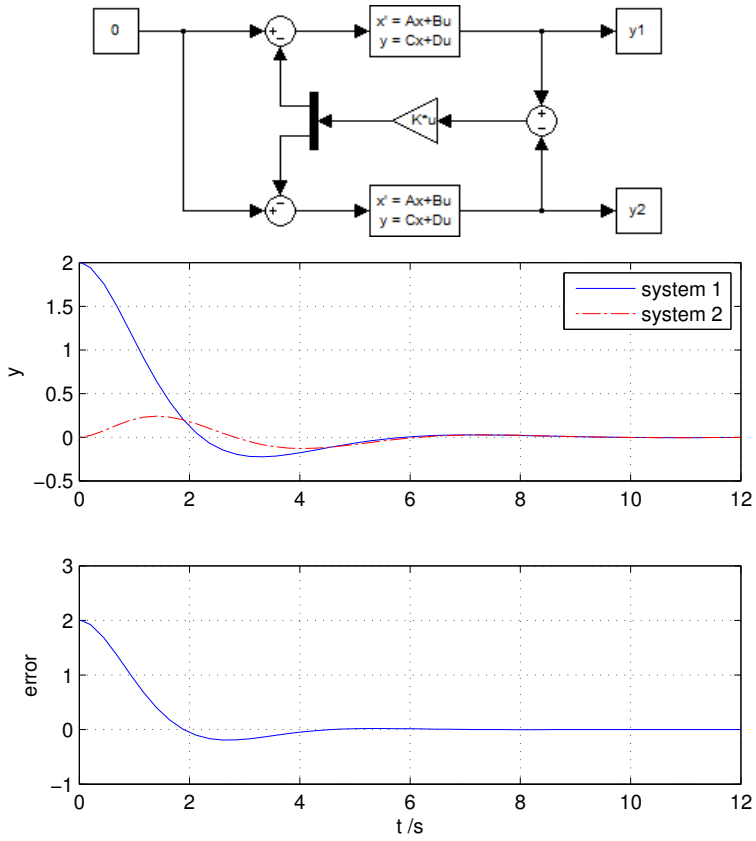

Figure 7.8: Convergence of identical systems with error feedback optimised via IC/LQR (one system with initial state equal to demand)

7.3 Application to similar aircraft systems

The IC optimisation above can be extended to higher order systems in a straightforward manner. The F-16 model used in UoB's AAAR simulation environment can be linearised and separated into longitudinal and lateral components, and an inner-loop controller developed and optimised via a LQR approach, as described in chapter 3.

The longitudinal, closed-loop model can then be linearised, producing a state-space system with 12 states.

A state-space model of the error dynamics for two aircraft, in the form of

equation 7.8 can now be produced, via the process detailed in section 7.2.2.

The convergence of these systems in x and z, with one at an initial position offset of 10 m, is shown in figure 7.9. Comparing the non-intimate (closed-loop aircraft, but with no error feedback) response, shown in the upper graphs, with the intimate response in the second row, the effect on aircraft 2 is again evident. The position error between the aircraft is reduced faster than without intimate control, moreso in the x direction due to the more responsive dynamics in z.

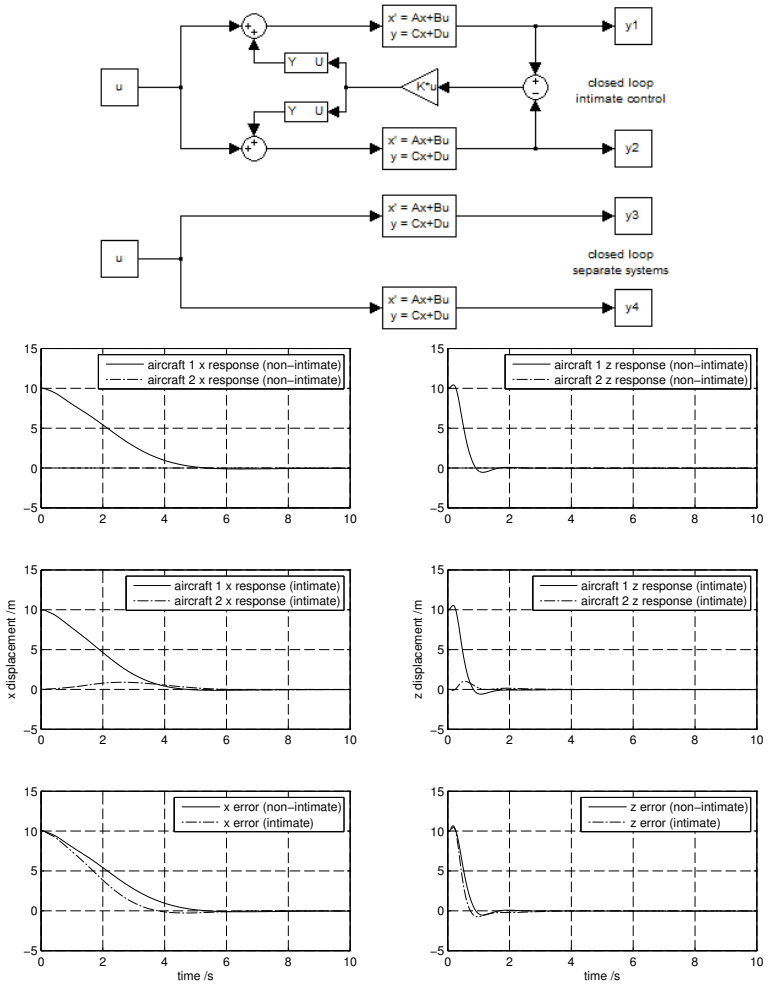

Figure 7.9: F16 longitudinal intimate control comparison

To evaluate the effect of this longitudinal controller under turbulence, the z demand of the nonlinear aircraft in the 6-DoF AAAR simulation environment was replaced with the z channel of the intimate controller above.

Two aircraft subject to turbulence were given identical initial conditions and trimmed to fly straight and level with identical velocities and headings.

Given that the two aircraft are identical, and will therefore respond identically to similar gusts, different seeds were used for the turbulence affecting each aircraft. The same random seed table from previous simulations was used, with the second aircraft being subject to turbulence from row $n + 1$ (looping back to row $n = 1$ for the 100th run).

Identical simulations were conducted for three controller configurations:

1. Basic position-demand controller (as used in previous simulations) to establish a baseline,

2. Intimate controller without position demand ('blindly' intimate),

3. Intimate controller with position demand, to demand station-keeping as well as convergence.

Example runs for each configuration (with moderate turbulence and identical turbulence seeds for these three iterations) are shown in figures 7.10, 7.11 and 7.12, with position errors compared in figure 7.13 (note the dissimilar vertical axis for figure 7.11). Mean values of the Root Mean Square (RMS) z error over all runs with and without the intimate controller are shown in table 7.1. For severe turbulence, as in previous simulations, the controller failed to maintain straight and level flight and so results are omitted.

Table 7.1: Mean RMS z error with and without intimate control.

Controller		Turbulence		
Position	Convergence (intimate)	None	Low	Moderate
On	Off	0.00 m	0.1774 m	0.4184 m
Off	On	0.00 m	0.1797 m	0.4157 m
On	On	0.00 m	0.1181 m	0.2901 m

It can be seen from the RMS errors that the IC controller alone maintains convergence between the aircraft but permits them to drift ('blindly' intimate). The IC and position controllers combined produce improved convergence, with station-keeping at the demanded position.

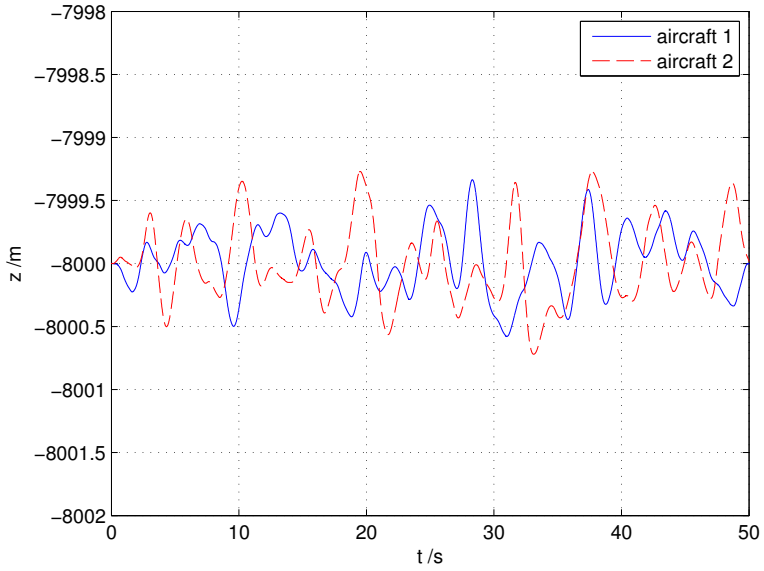

Figure 7.10: z position of two nonlinear F-16 aircraft, z controller only

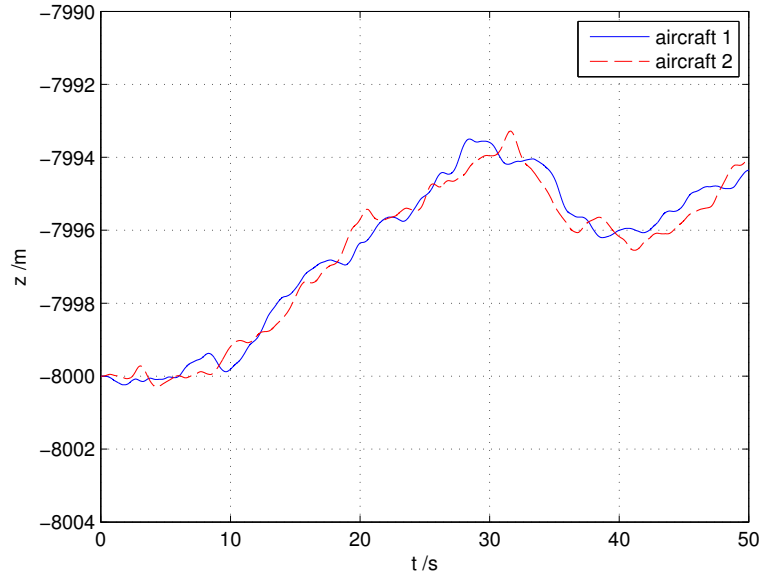

Figure 7.11: z position of two nonlinear F-16 aircraft, IC controller only

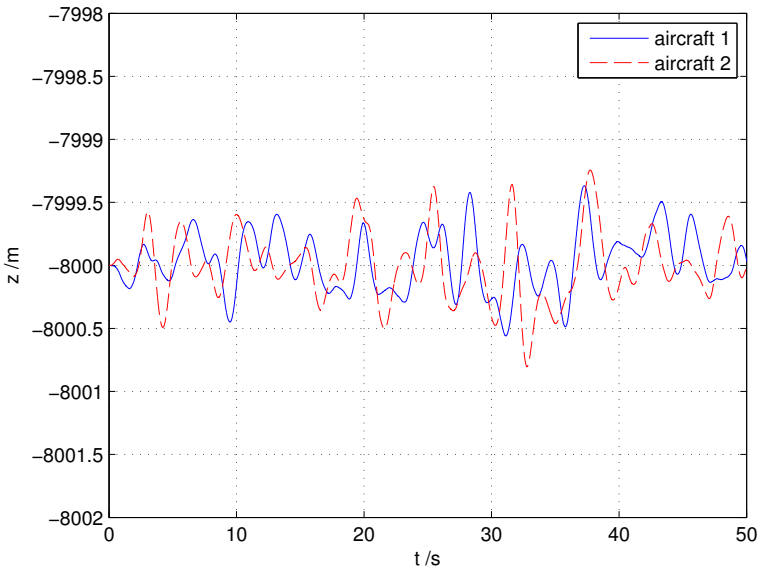

Figure 7.12: z position of two nonlinear F-16 aircraft, z+IC controller

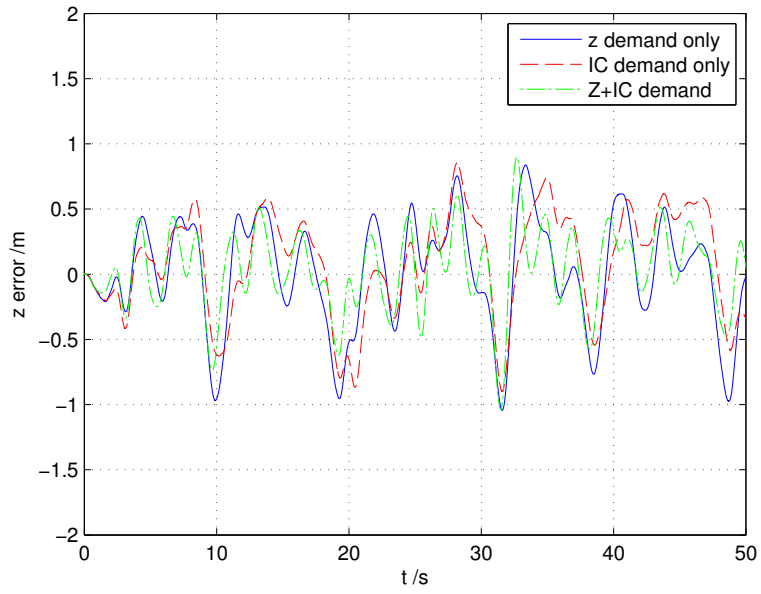

Figure 7.13: z error between two nonlinear F-16 aircraft, comparison of z, IC, and z+IC controllers

7.4 Extension to non-similar systems

Griffiths' and Jones' assumption of similar system dynamics permits a straightforward method of determining optimal gains for the error-state feedback above, but the system dynamics of drogue and receiver in AAAR are very different.

The aim is to create a system representing the combined error dynamics of two separate systems, upon which optimisation can be performed. Given, as above,

$$\dot{\mathbf{x}}_1 = A_1\mathbf{x}_1 + B_1\mathbf{u}_1 \tag{7.16}$$

$$\dot{\mathbf{x}}_2 = A_2\mathbf{x}_2 + B_2\mathbf{u}_2, \tag{7.17}$$

it is necessary to create a system containing the error vector

$$\tilde{\mathbf{z}} = \mathbf{x}_1 - \mathbf{x}_2. \tag{7.18}$$

It is not possible to concatenate the A_1, A_2 state matrices in the same way as the B_1, B_2 input matrices were previously, as this leads to the necessity to use state vector $[\mathbf{x}_1, \mathbf{x}_2]^\top$, which is not what is required. A simpler way of producing the error vector is to manipulate the C matrix to produce an output $\mathbf{y}$ which represents the errors between the systems. Output-weighted LQR, which minimises outputs rather than states, can be used, with performance index

$$J_{LQR} = \int_0^\infty (\tilde{\mathbf{y}}^\top Q\tilde{\mathbf{y}} + \mathbf{u}^\top R\mathbf{u})\ dt. \tag{7.19}$$

Concatenating state matrices such that

$$A = \begin{bmatrix} A_1 & 0 \\ 0 & A_2 \end{bmatrix} \tag{7.20}$$

and input matrices

$$B = \begin{bmatrix} B_1 & 0 \\ 0 & B_2 \end{bmatrix} \tag{7.21}$$

the decoupled systems can be combined. Using output matrix

$$C = \begin{bmatrix} I & -I \end{bmatrix} \tag{7.22}$$

where I is an identity matrix of the same order as the systems A_1 and A_2, the output vector $\mathbf{y} = \mathbf{x}_1 - \mathbf{x}_2 = \tilde{\mathbf{z}}$. MATLAB's `lqry` function takes state space system A, B, C, D and output and input weighting matrices Q and R, and produces optimal gain K for the minimisation of the error state $\tilde{\mathbf{z}}$.

To demonstrate this action, transfer functions is $\frac{y_1}{u_1} = \frac{1}{s^2+s+1}$, and $\frac{y_2}{u_2} = \frac{8}{s^2+4s+8}$ were chosen as simple second-order, dissimilar systems. These give state space systems

$$\begin{aligned} A_1 &= \begin{bmatrix} -1.0 & -1.0 \\ 1.0 & 0.0 \end{bmatrix} & B_1 &= \begin{bmatrix} 1.0 \\ 0.0 \end{bmatrix} \\ C_1 &= \begin{bmatrix} 0.0 & 1.0 \end{bmatrix} & D_1 &= \begin{bmatrix} 0.0 \end{bmatrix} \end{aligned} \tag{7.23}$$

and

$$\begin{aligned} A_2 &= \begin{bmatrix} -4.0 & -4.0 \\ 2.0 & 0.0 \end{bmatrix} & B_2 &= \begin{bmatrix} 2.0 \\ 0.0 \end{bmatrix} \\ C_2 &= \begin{bmatrix} 0.0 & 2.0 \end{bmatrix} & D_2 &= \begin{bmatrix} 0.0 \end{bmatrix} \end{aligned} \tag{7.24}$$

with step response as in figure 7.14.

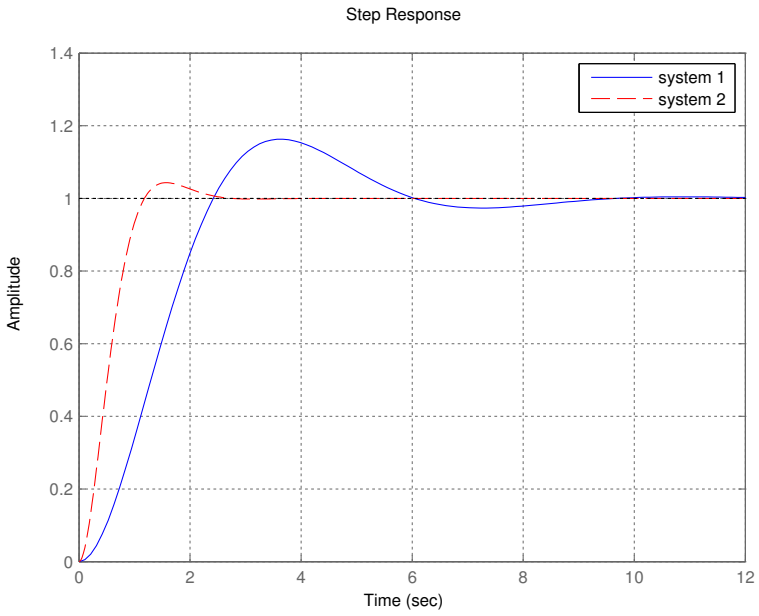

Figure 7.14: Step response for $\frac{y_1}{u_1} = \frac{1}{s^2+s+1}$ and $\frac{y_2}{u_2} = \frac{8}{s^2+4s+8}$

Conducting the optimisation on the error dynamic system as in equations 7.20, 7.21 and 7.22, against the output-weighted LQR performance index in equation 7.32, the gain produced is

$$K_{LQRy} = \begin{bmatrix} 0.3334 & 0.1890 & -0.0968 & 0.0686 \\ -0.7747 & -0.7657 & 0.6592 & 0.4125 \end{bmatrix} \tag{7.25}$$

This is applied to the non-similar systems, with the error states (which are of the same magnitude but with opposite sense for each system) producing the inputs to the two systems:

$$\begin{bmatrix} u_1 \\ u_2 \end{bmatrix} = K_{LQRy} \begin{bmatrix} x_{11} - x_{21} \\ x_{12} - x_{22} \\ x_{21} - x_{11} \\ x_{22} - x_{12} \end{bmatrix} \tag{7.26}$$

A system diagram, and convergence from initial offsets, is shown in figures 7.15 and 7.16. The response is similar to the previous similar-system convergence, with the second system rising to meet the first – this is more evident in figure 7.16 where the second system starts with zero offset from the demand.

7.5 F-16 and 2nd-order system

The process above was repeated for a linearised, 12-state longitudinal model of the F-16, as used with previous architectures. The step response of the F-16 and a second-order system with differing response, $\frac{y_2}{u_2} = \frac{8}{s^2+4s+8}$, is shown in figure 7.17. Intimate convergence of these two systems is successful – figure 7.20 shows the F16 rising to meet the other system, with faster convergence than the open-loop response.

In order to evaluate the effect upon systems with more differing dynamics, the F-16 model was scaled so that its response is around an order of magnitude different. The step response of the slow F-16 and a second-order system with faster response, $\frac{y_2}{u_2} = \frac{8}{s^2+4s+8}$, is shown in figure 7.19. Intimate convergence of these two systems is also successful – figure 7.20 shows the faster system rising to meet the slower F-16, with a rapid initial rate of convergence that is much more effective than the open-loop convergence shown

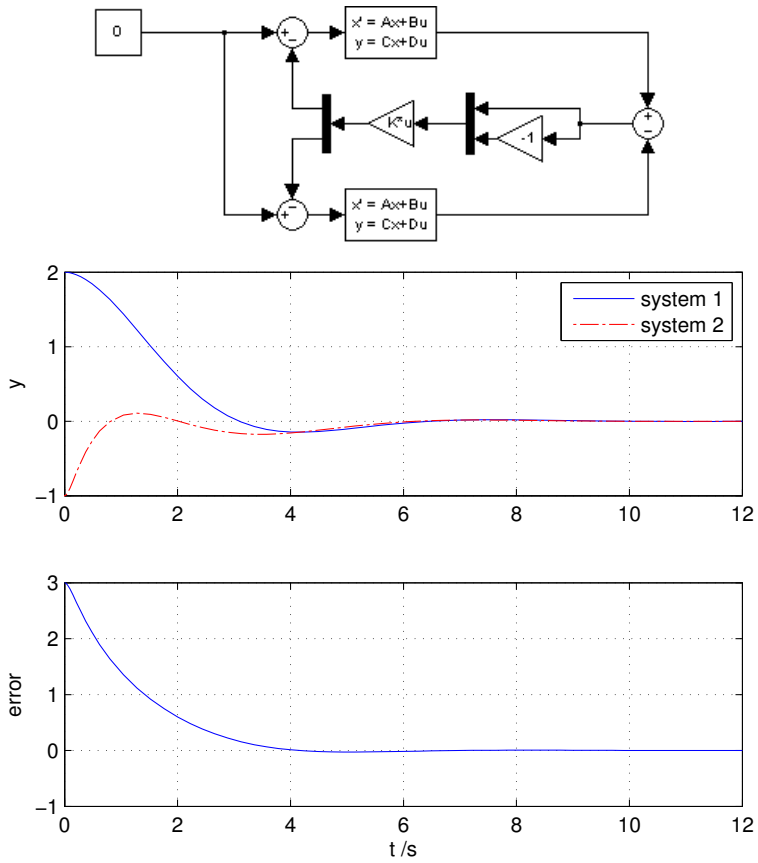

Figure 7.15: Convergence of nonidentical systems with error feedback optimised via IC/LQR (both start offset)

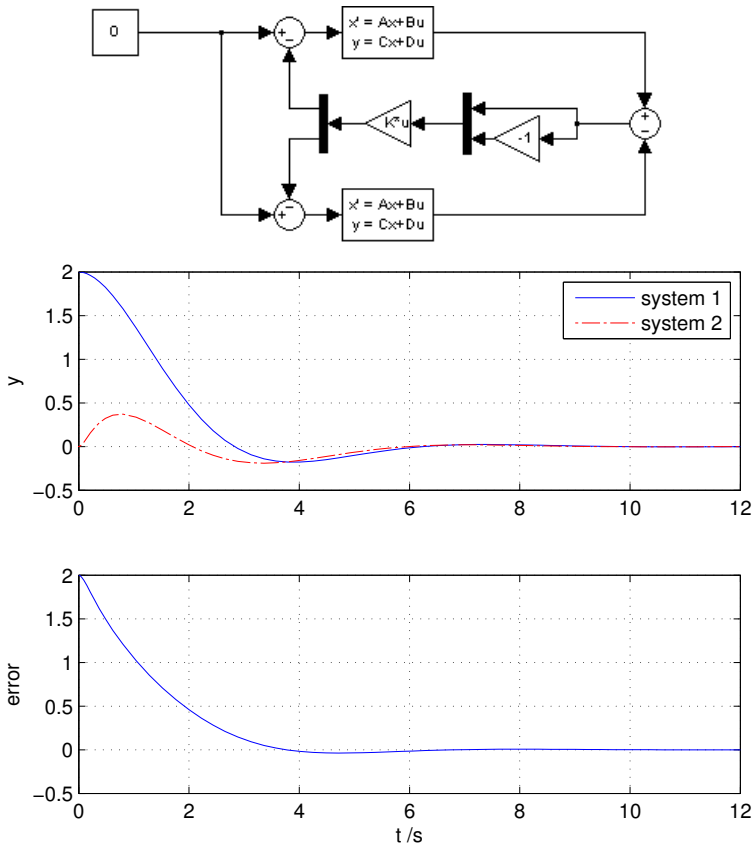

Figure 7.16: Convergence of nonidentical systems with error feedback optimised via IC/LQR (one starts offset)

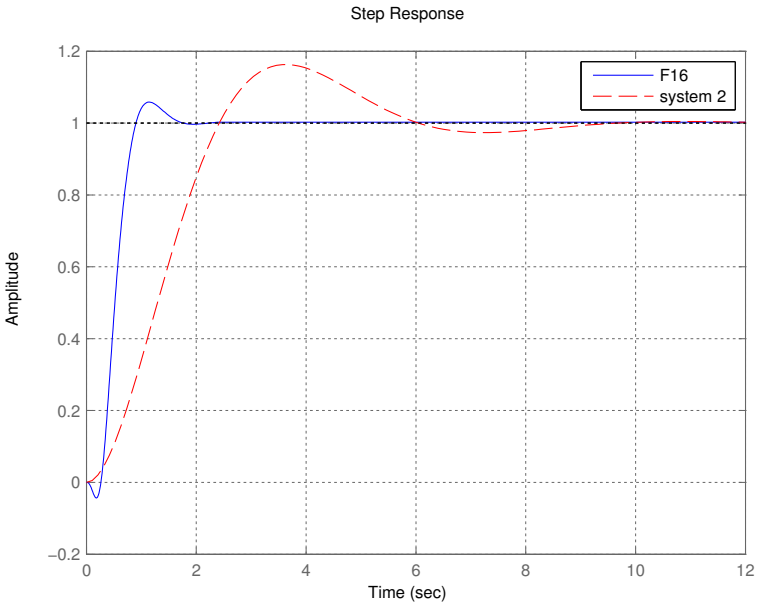

Figure 7.17: Step response of linear, longitudinal F-16 model and $\frac{y_2}{u_2} = \frac{8}{s^2+4s+8}$

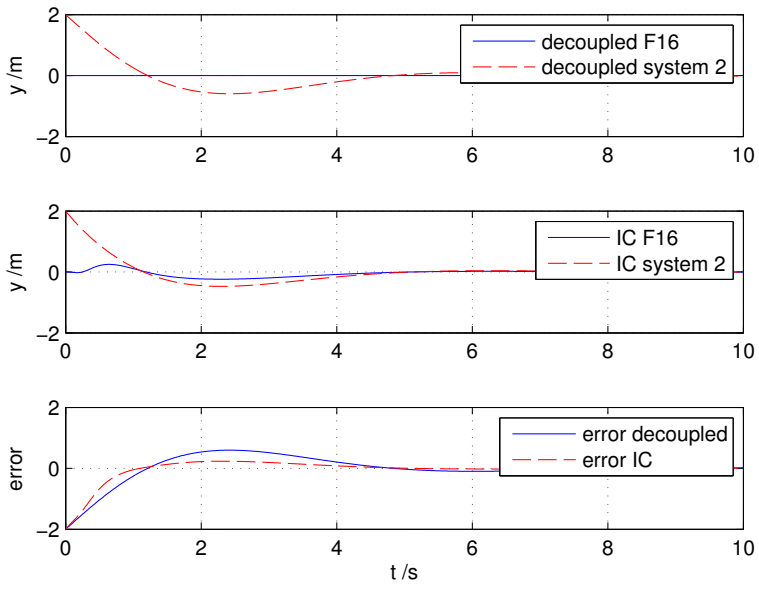

Figure 7.18: Convergence of F16 and $\frac{y_2}{u_2} = \frac{8}{s^2+4s+8}$ with error feedback optimised via IC/LQR

by the step response plot.

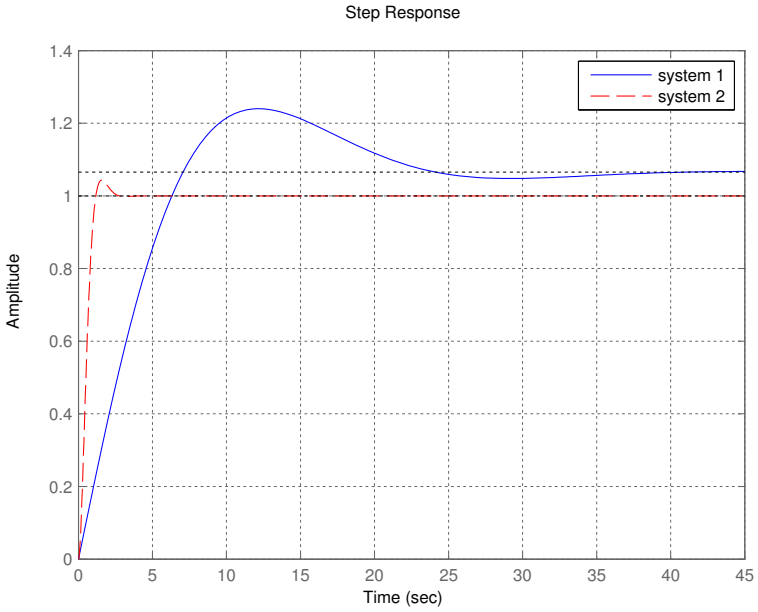

Figure 7.19: Step response of scaled F-16 model (system 1) and $\frac{y_2}{u_2} = \frac{8}{s^2+4s+8}$

7.6 F-16 and reduced-order hose

Now that the non-identical IC methodology detailed above has been shown to be effective on simple systems, and a simple system combined with a 12-state F-16 model, the problem of intimate control between F-16 and drogue can be approached.

7.6.1 Hose linearisation

The controlled hose model developed in chapter 4 is linearised in its closed-loop form, for z position demand input and z position and velocity output. This produces a 4-state model, due to the integrator and derivative in the PID controller, which is then converted to a canonical representation (where the only values in the C matrix are ones) through the following process,

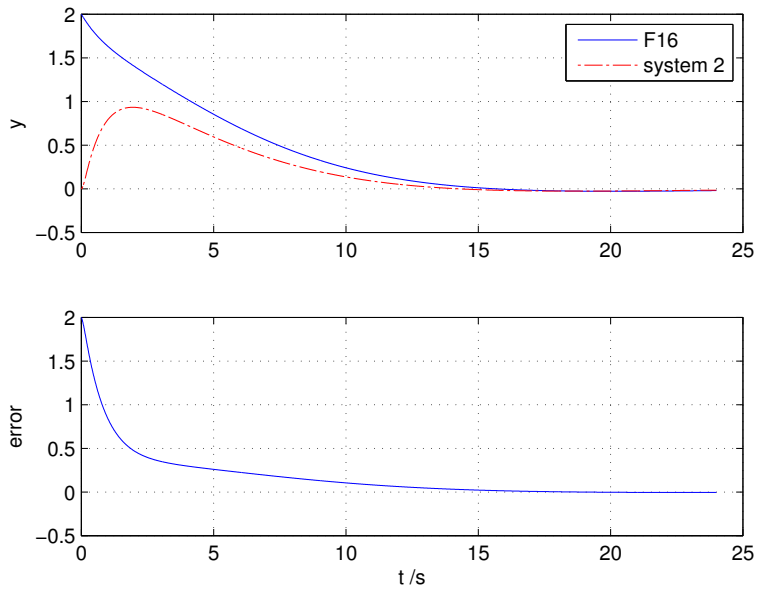

Figure 7.20: Convergence of scaled F16 and $\frac{y_2}{u_2} = \frac{8}{s^2+4s+8}$ with error feedback optimised via IC/LQR

where e.g. $\hat{\mathbf{A}}$ denotes the new value of each parameter:

$$\begin{aligned} \hat{\mathbf{A}} &= CAC^{-1} \\ \hat{\mathbf{B}} &= CB \\ \hat{\mathbf{C}} &= I \\ \hat{\mathbf{D}} &= 0 \\ \hat{\mathbf{x}} &= \mathbf{y}. \end{aligned} \tag{7.27}$$

The 4-state, closed loop, longitudinal hose with full state output, now takes the form:

$$A = \begin{bmatrix} -1.35 & 0.99 & -124.95 & 0.04 \\ -181.82 & -0.31 & -16425.48 & 4.93 \\ -1.00 & 0.00 & -100.00 & 0.00 \\ -1.00 & 0.00 & 0.00 & 0.00 \end{bmatrix} \quad B = \begin{bmatrix} 1.34 \\ 176.77 \\ 1.00 \\ 1.00 \end{bmatrix}$$

$$C = \begin{bmatrix} I_{4\times 4} \end{bmatrix} \quad D_1 = \begin{bmatrix} 0_{4\times 1} \end{bmatrix} \tag{7.28}$$

7.6.2 Model reduction

For the open-loop hose model, balanced truncation model reduction (via MATLAB's `reduce` function) can be used to produce a 2nd-order representation of the system dynamics. This matches closely with the full 80-state linear model, as shown in figure 7.21. Using the same method for the controlled hose z response is not as successful – figure 7.22 shows poor correlation, with peak overshoot, settling time and steady-state error being noticeably different. For this reason, the 4th order model is used.

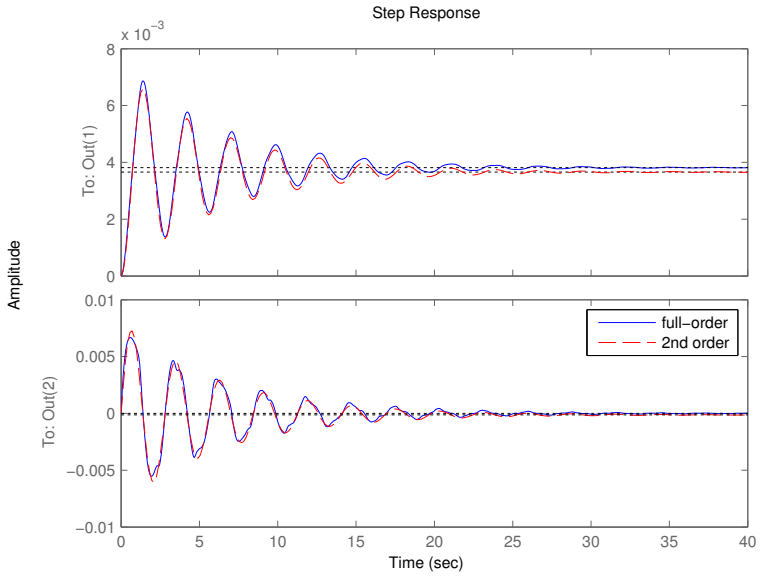

Figure 7.21: Open-loop hose z step response: full- vs 2nd-order linear models

Step response of the non-intimate, linear, longitudinal F-16 and drogue models are shown in figure 7.23.

7.6.3 Construction of error dynamic system

The differing number of states between drogue and F-16 models makes the construction of the error dynamic system $\dot{\tilde{\mathbf{z}}} = A\tilde{\mathbf{z}} + B\mathbf{u}$ problematic. To overcome this, the C matrix can be manipulated to select states to use in the output-weighted LQR methodology detailed in section 7.4. Given this, the 12-state longitudinal F-16 model is also used, rather than the reduced representation. To give the error between drogue and receiver z position,

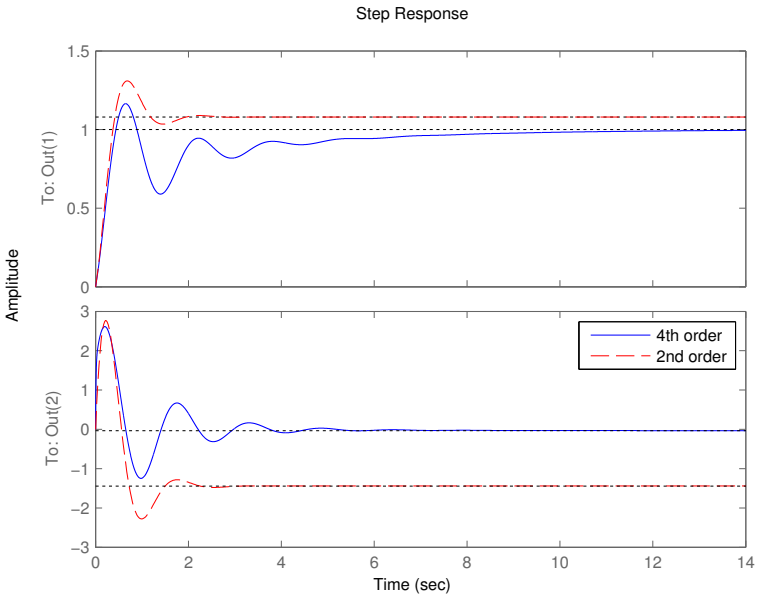

Figure 7.22: Closed-loop hose z step response: 4th order vs 2nd order linear models

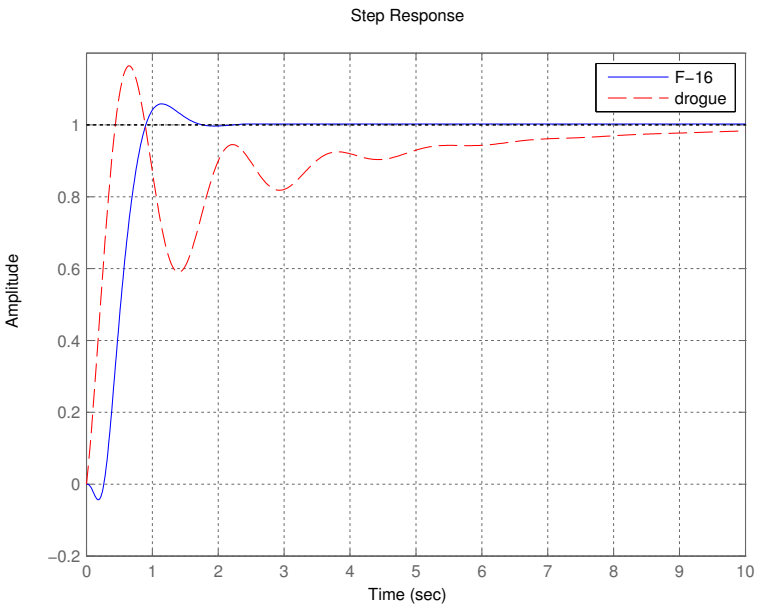

Figure 7.23: Step response of linear, longitudinal F-16 and drogue models

the matrix used is

$$C = \begin{bmatrix} 1.00 \\ 0.00 \\ 0.00 \\ 0.00 \\ 0.00 \\ 0.00 \\ 0.00 \\ 0.00 \\ 0.00 \\ 0.00 \\ 0.00 \\ 0.00 \\ 0.00 \\ -1.00 \\ 0.00 \\ 0.00 \end{bmatrix}^{\top} \tag{7.29}$$

which subtracts receiver position (state 14 in the concatenated system) from drogue position (state 1). Q and R in this case were set to $I_{1\times 1}$ and $I_{2\times 2}$ respectively, for the one output error state and the two input demands, one for each system.

7.6.4 Optimisation against error system

The output-weighted `LQRy` method produces a 2-by-16 gain matrix, which acts upon the four hose and twelve F-16 states:

$$K_{LQRy} = \begin{bmatrix} 0.3742 & 0.1597 \\ 0.1022 & -0.0436 \\ -16.6987 & 7.2497 \\ 0.0425 & -0.1311 \\ -25.9185 & 16.4818 \\ 0.3010 & -0.2560 \\ 27.6811 & -18.0461 \\ 0.0009 & -0.0025 \\ -0.0192 & 0.0426 \\ 0.0000 & -0.0001 \\ 0.0000 & 0.0000 \\ 0.0000 & 0.0000 \\ 0.0000 & 0.0006 \\ -0.7304 & 0.2110 \\ 0.0001 & 0.0013 \\ -0.0000 & -0.0000 \end{bmatrix}^{\top} \tag{7.30}$$

7.6.5 Simulation results

In this case, the error values are generated within the gain matrix and so all states are fed back directly, concatenated into one 16-element state vector. Convergence from initial offset (drogue starts -2 m offset and receiver +10 m) is shown in figure 7.24, compared with non-intimate response of the closed-loop systems.

Convergence with the intimate controller is slightly better, with the intimately controlled systems converging earlier than the non-intimate ones. The improvement is not as dramatic as for the previous non-identical simulations, perhaps due to the relatively fast response of both systems.

7.7 F-16 and full-order hose

The nonlinear receiver model (figure 7.25) is used, and the hose model (figure 7.26), as used in the SE with 9 links and y, z force demand on the

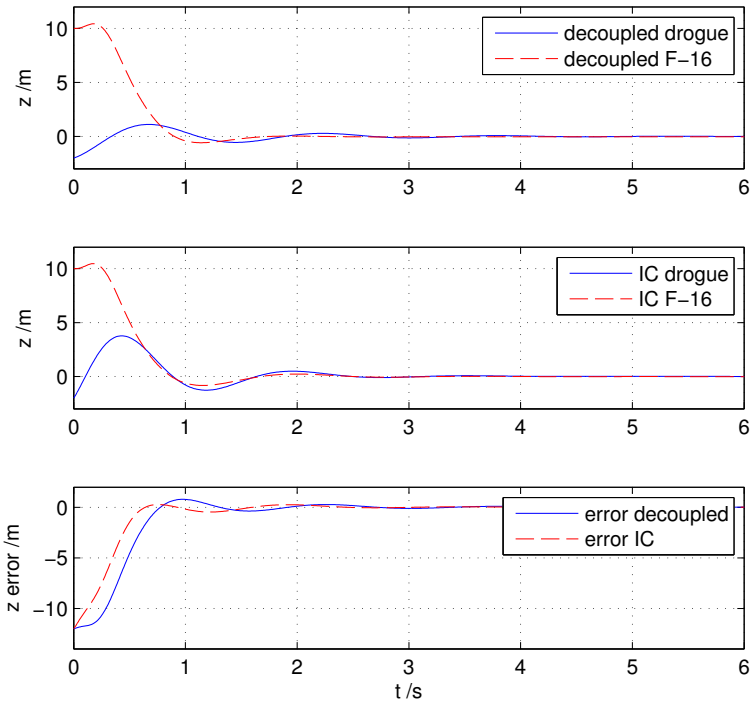

Figure 7.24: Effect of intimate controller on F-16 and hose convergence

drogue, are linearised and concatenated. The previously presented drogue PID controller is not included – the drogue is open-loop with force inputs.

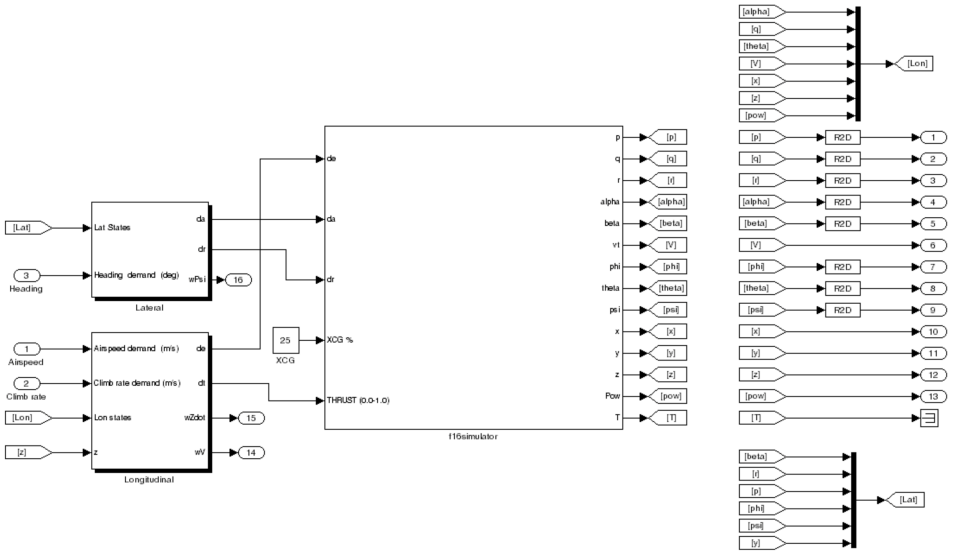

Figure 7.25: Closed-loop (inner stability controller) F16 model for linearisation (longitudinal and lateral)

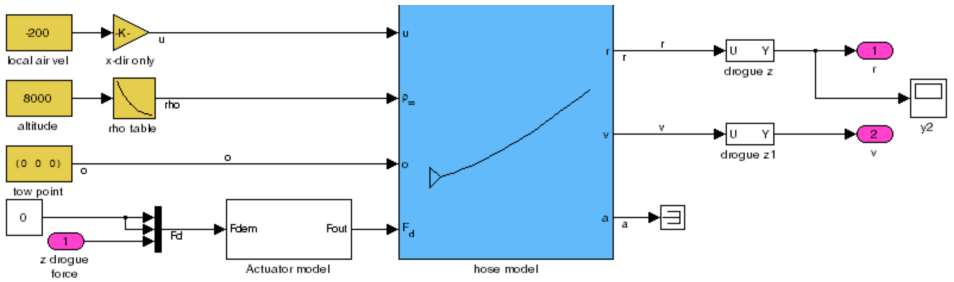

Figure 7.26: Hose model for linearisation (longitudinal)

The subsequent work in this section describes the concatenation and augmentation of the F-16 and hose models. Full values of state-space matrices are not printed here, not least because some are 48-by-48 elements in size. MATLAB code and Simulink models were submitted to project sponsor Cobham plc with project deliverable D2.3.37 part 2.

7.7.1 Longitudinal intimate control

Both models are trimmed at 200 m/s airspeed and 8,000 m altitude, and linearised into separate longitudinal and lateral state-space models. The

longitudinal models are approached first.

The longitudinal, closed-stability-loop, F-16 has states:

- α (rad) – angle of attack
- q (rad/s) – pitch rate
- θ (rad) – pitch angle
- V (m/s) - airspeed
- x (m) – horizontal position
- h (m) – vertical position (upwards positive)
- cp (%) – centre of gravity along wing chord
- $\int \dot{z}$ – height controller integrator
- $\int V$ – velocity controller integrator

Its inputs are:

- Airspeed demand (m/s)
- Altitude demand (m)

and all states are output via its C matrix, which converts radian values to degrees.

The longitudinal hose model, with force demand via the abstracted actuation model developed in chapter 4, has 39 states, with the last 36 corresponding to the horizontal and vertical angular positions and rates of each of its 9 links, and the first three being the states of the three actuator first-order lags. It is possible to reduce the number of states by eliminating lateral values but due to the construction of the finite-segment hose model using two polar angles for link orientations, anything more than small-angle deflections produces non-trivial coupling between longitudinal and lateral outputs and all 36 link states – thus these linearised models include all states, but only the relevant inputs and outputs.

State-space model concatenation and augmentation

The concatenation of the two longitudinal models is conducted as described above, producing a model with 48 states, 3 inputs and 11 outputs. The dynamics of both systems are represented in this concatenated model, but the systems are still entirely uncoupled within it.

The concatenated output matrix C is then augmented with an additional output, the vertical error between the receiver and drogue position, by subtracting the relevant rows of these outputs from one another.

The 6th output is receiver height, and the 10th is drogue vertical position. This error state is inserted as a new output (the 12th in this case) in the output matrix.

Output-weighted optimisation

Now that the concatenated and augmented model outputs a signal representing the error we wish to minimise, an optimisation method that takes this into account can be utilised.

In Griffiths' [17] and Jones' [184] work, an infinite-horizon LQR approach was used. This produces a state-feedback gain which minimises the cost function

$$J_{LQR} = \int_0^\infty \left(\tilde{\mathbf{z}}^\top Q \tilde{\mathbf{z}} + \mathbf{u}^\top R \mathbf{u} \right) \, dt. \tag{7.31}$$

where Q places emphasis on minimising system states (in this case the error between the systems), and R emphasises minimising control inputs. This requires error vector $\tilde{\mathbf{z}}$ to be constructed by direct subtraction of state vectors, necessitating systems with identical structure.

If instead an output-weighted LQR approach is used, minimising cost function

$$J_{LQR} = \int_0^\infty (\tilde{\mathbf{y}}^\top Q \tilde{\mathbf{y}} + \mathbf{u}^\top R \mathbf{u}) \, dt. \tag{7.32}$$

where now Q emphasises the minimisation of outputs, rather than states, we can use the concatenated and augmented system to design for minimisation of the new error state.

This approach still requires full state feedback, so application to a non-fully-observable system will require an alternative output feedback approach.

Application of output-weighted LQR, via MATLAB's lqry function, with weighting matrices

$$Q_{\text{lon}} = \text{diag}\left[\,0\;0\;0\;0\;0.1\;0\;0\;0\;0\;0\;0\;10^5\,\right] \tag{7.33}$$

$$R_{\text{lon}} = \mathbf{I} \tag{7.34}$$

which emphasises minimisation of the 12th output, the vertical position error (the 5th state is horizontal position, which if set to zero prevents the algorithm from stabilising the system or finding an optimal gain due to uncontrollability), and gives equal priority to demands on receiver airspeed and altitude, and drogue vertical force, produces a 3-by-48 element optimal feedback gain matrix.

7.7.2 Longitudinal response

The longitudinal response, as tested using the system in figure 7.27, is shown in figure 7.28. The systems, particularly the drogue, are obviously more complex than the second-order representations previously used – there are several modes observable in the oscillatory response.

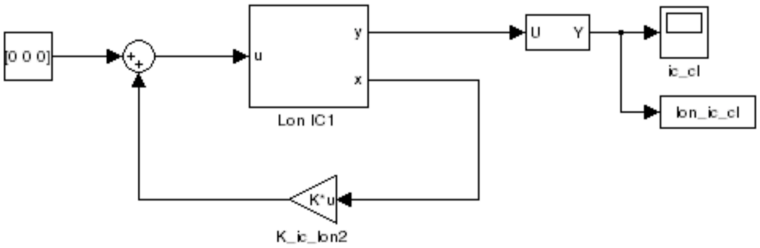

Figure 7.27: Linear concatenated systems for comparison

The action of the intimate controller can be observed in the fast convergence of receiver and drogue – they reach an error of less than 10 cm in around 1 second. Observing figure 7.28, however, the combined response is lightly damped – it would be desirable to improve station-keeping within the refuelling envelope. Additional damping can be created by optimising against velocity as well as position.

The linearised hose model includes a velocity output, but the receiver does not. An acceptable approximation can be created, for small angles of θ and low variation in airspeed, by simple trigonometry: for constant

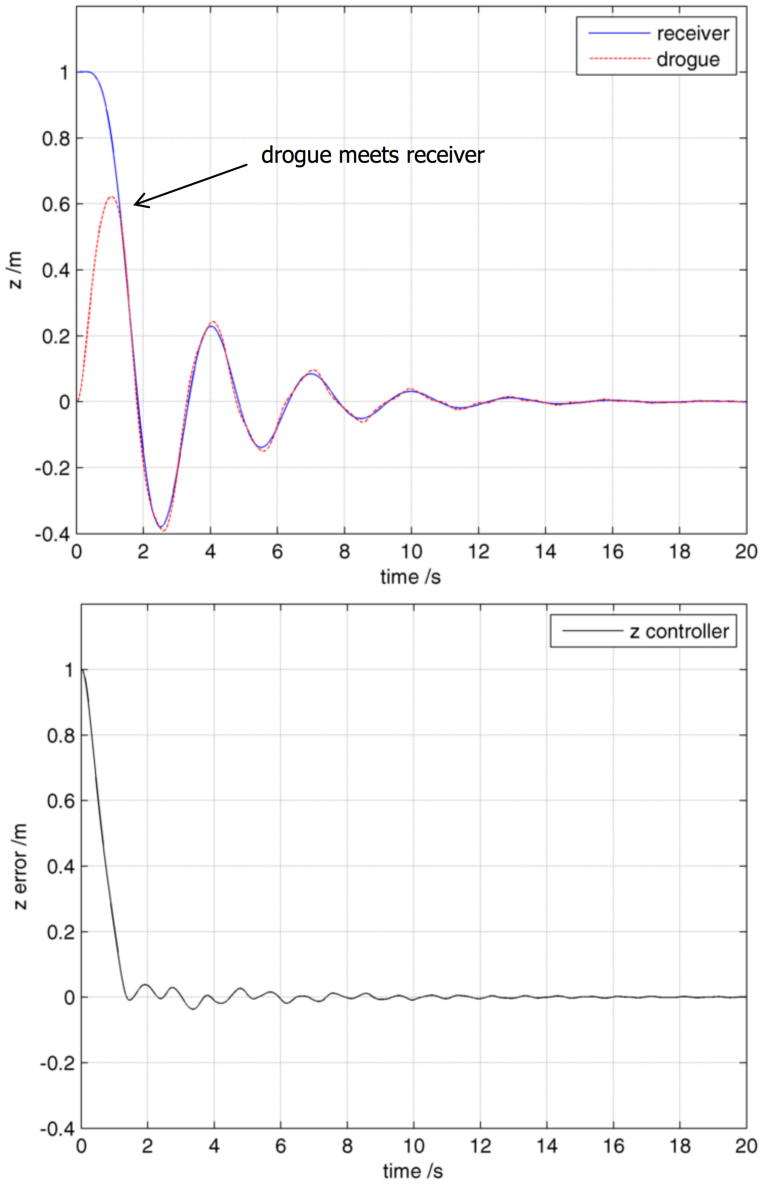

Figure 7.28: Closed loop longitudinal response with intimate controller on position error

V = 200 m/s, vertical velocity = $V\theta$, and this can be used in a further augmentation to the concatenated systems' output matrix – MATLAB command:

```
Clon_ic_aug(end+1,:)
= [0 0 200 0 0 0 0 0 0 zeros(1,39)]-Clon_ic(11,:)];
```

creates the error between vertical receiver velocity, via the second state which is receiver pitch angle, and the 11th output row which represents the drogue's vertical velocity.

The improvement in damping and thus station-keeping is evident in Figure 7.29, although this is at the expense of convergence rate.

7.7.3 Lateral intimate control

The lateral controller is constructed in a similar way, with models trimmed and linearised at 200 m/s at 8,000 m.

The lateral, closed-stability-loop, F-16 has states:

- β (rad) – sideslip angle
- r (rad/s) – yaw rate
- p (rad/s) – roll rate
- ϕ (rad) – roll angle
- ψ (rad) – yaw angle
- y (m) – lateral position
- $\int \psi$ – yaw controller integrator

input:

- heading (deg)

and outputs all states via its C matrix, which converts radian values to degrees.

The lateral hose model,again has 39 states, with the last 36 corresponding to the horizontal and vertical angular positions and rates of each of its 9 links, and the first three being the states of the three actuator first-order lags.

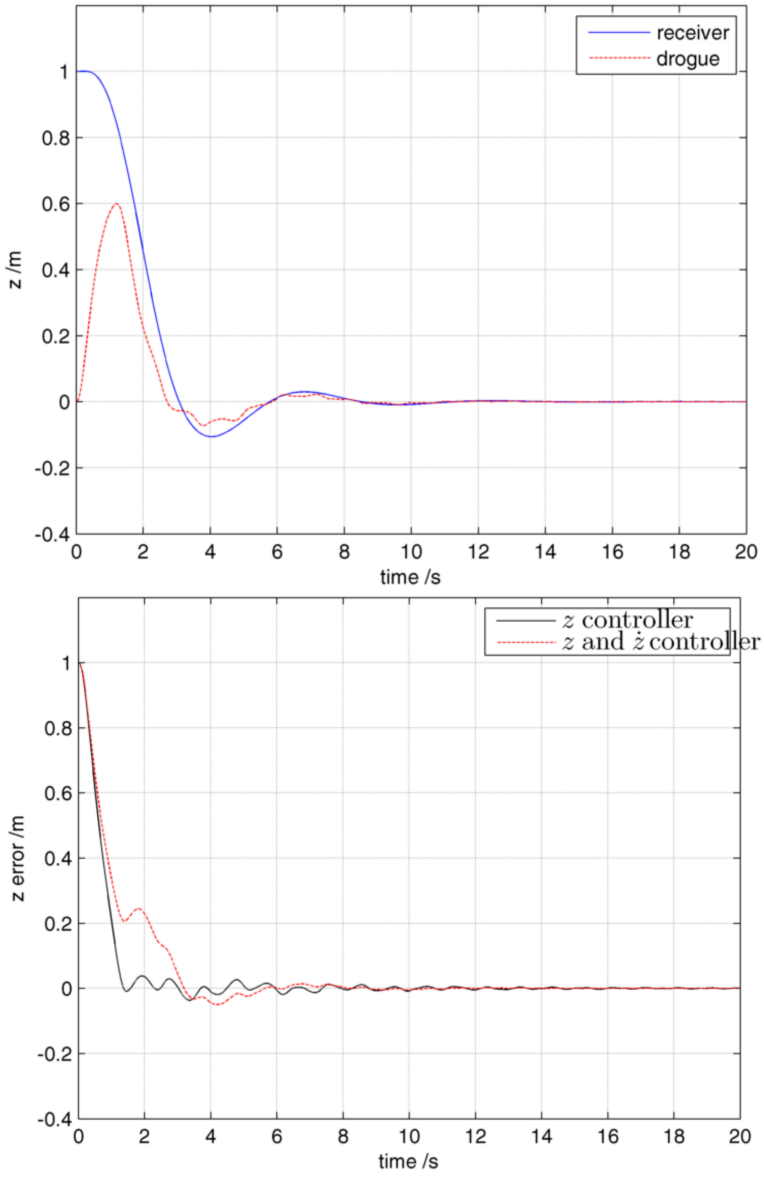

Figure 7.29: Closed loop longitudinal response with intimate controller on position and velocity errors

State-space model concatenation and augmentation

The concatenation of the lateral models is conducted as described above, producing a model with 46 states, 2 inputs and 9 outputs. The dynamics of both systems are represented in this concatenated model, but the systems are still entirely uncoupled within it.

The concatenated C matrix is then augmented to additionally output the lateral error between the receiver and drogue position, by subtracting the relevant rows of these outputs from one another:

```
Clat_ic_aug(end+1,:)  = Clat_ic(6,:)  - Clat_ic(8,:);
```

The 6th output is receiver height, and the 8th is drogue lateral position. This error state is inserted as a new output (the 10th in this case) in the output matrix.

Output-weighted optimisation

Again, application of output-weighted LQR, via MATLAB's `lqry` function, with weighting matrices

$$Q_{\text{lon}} = \text{diag}\left[\,0\;0\;0\;0\;0\;0\;0\;0\;0\;10^5\,\right] \tag{7.35}$$

$$R_{\text{lon}} = \mathbf{I} \tag{7.36}$$

which emphasises minimisation of the 10th output, the vertical position error, and gives equal priority to demands on receiver heading and drogue lateral force, produces a 2-by-46 element optimal feedback gain matrix.

7.7.4 Lateral response

The action of the intimate controller can be observed in figure 7.30. Again, the response is stable but oscillatory, and more complex than the second-order representations presented in previous deliverables. Receiver and drogue converge rapidly – they reach an error of lower than 10 cm in around 1 second. Observing figure 7.30, however, the combined response is again lightly damped – it would be desirable to improve station-keeping within the refuelling envelope. Adding optimisation against velocity is also desirable laterally.

Lateral velocity can be approximated in a similar way to longitudinal. For constant $V = 200$ m/s, lateral velocity is $V\phi$, and this can be used in a

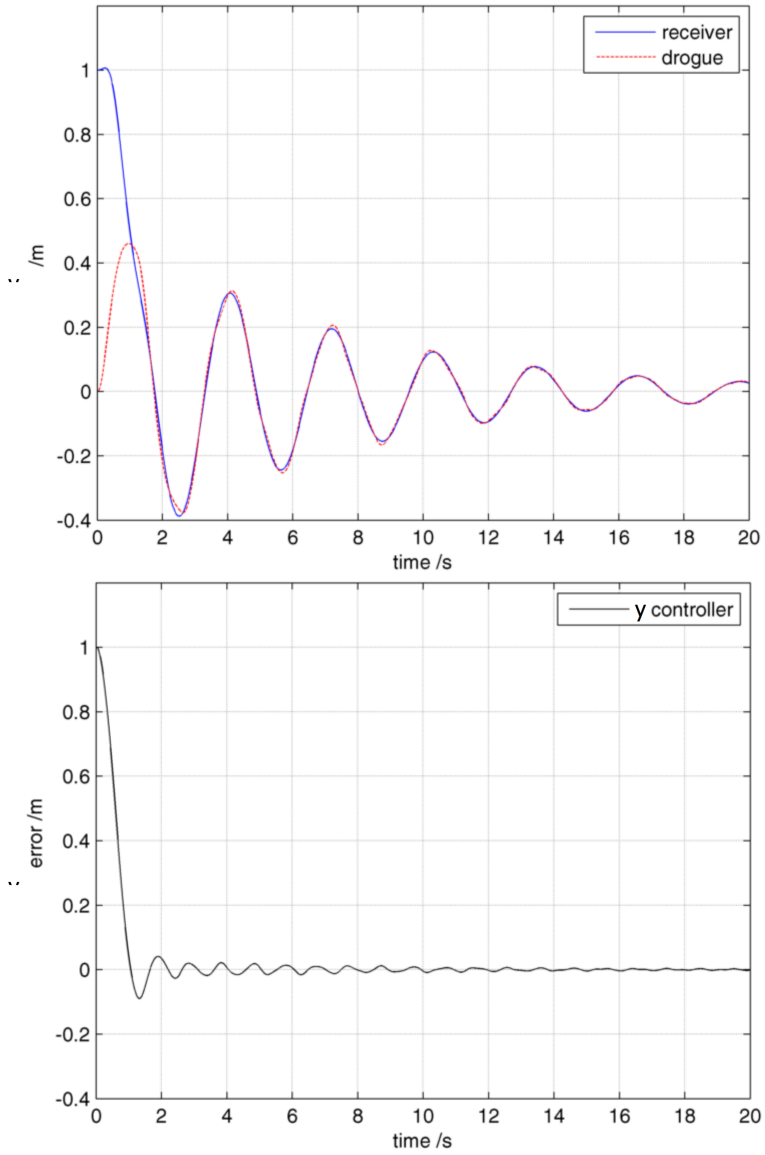

Figure 7.30: Closed loop lateral response with intimate controller on position error

further augmentation to the concatenated systems' output matrix:

```
Clat_ic_aug(end+1,:)
= [0 0 0 0 200 0 0 zeros(1,39)]-Clat_ic(9,:)];
```

creates the error between lateral receiver velocity, via the second state which is receiver yaw angle, and the 9th output row which represents the drogue's lateral velocity.

The improvement in damping and thus station-keeping is shown in figure 7.31, although again this is again at the slight expense of convergence rate.

7.8 Practical considerations

- **Communications and system distribution:** Given that this intimate approach synthesises demands based on states of both receiver and drogue, it is necessary for this controller to be centralised. This will require communication of relevant states between systems, likely requiring higher bandwidth than for the cooperative controller.
- **Observability of states:** the current controller acts upon position and velocity of the drogue, the states of the drogue PID controller, and all states of the F-16 model. Some of these will be problematic to observe, and consideration should be made in further work as to the implications of this and methods by which to address this.

7.9 Route to application within AAAR SE

The IC controller still presents barriers to implementation in the ASTRAEA SE. The gains produced by the output-weighted LQR optimisation act upon internal states of the 4th-order linear hose model which do not exist directly in the nonlinear hose.

One possible route to integration would be to develop estimators to produce the states required. A Linear Quadratic Estimator (LQE) such as a Kalman filter could be used in addition to the LQR approach to create a LQG controller, although this may still prove problematic given the large order of the full hose model, may not produce a unique and separable solution, and will not automatically ensure good robustness.

Non-classical approaches such as H_∞ methods are another potential

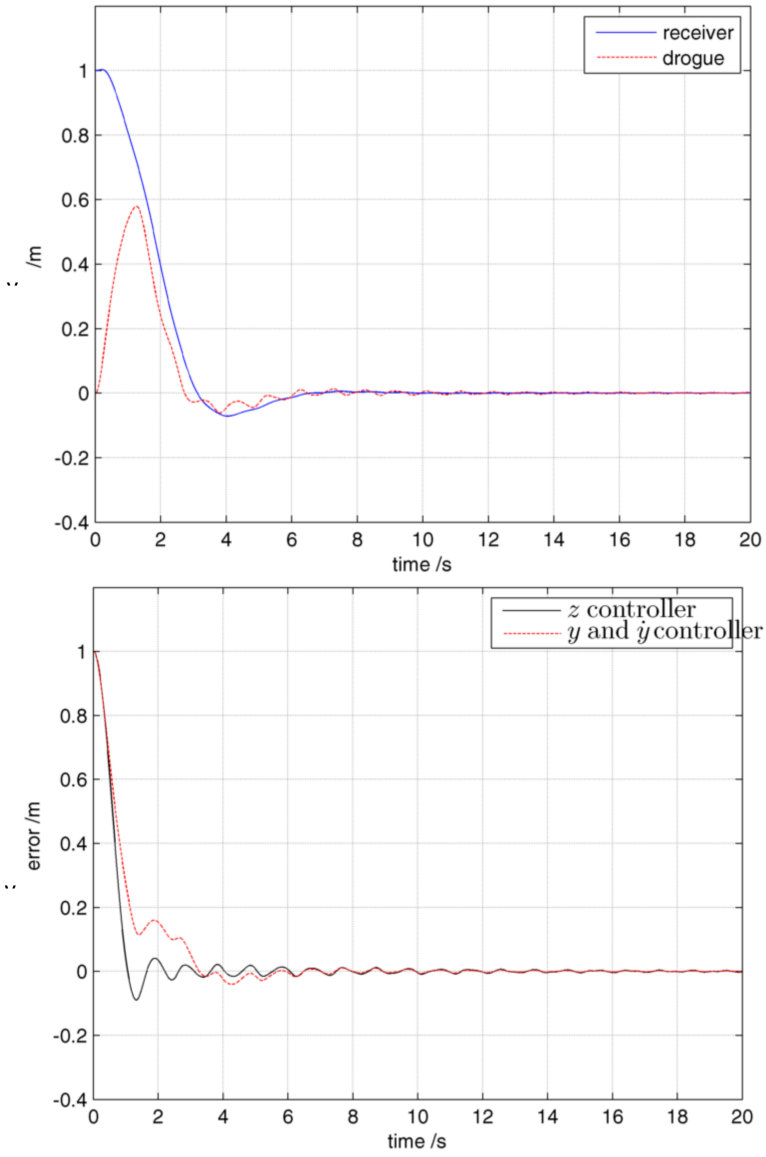

Figure 7.31: Closed loop lateral response with intimate controller on position and velocity errors

choice, producing stable controllers with guaranteed performance, but require a well-formed cost function and may struggle with nonlinearities.

7.10 Summary

In this chapter, intimate control has been extended beyond the similar-systems requirement originally present, and has now been applied to full-order linear models of F-16 (with 7 lateral and 9 longitudinal states) and hose and drogue (with 18 lateral and 18 longitudinal states), permitting full 6-DoF control.

The concatenation and augmentation method that has been proposed permits extension of intimate control optimisation methods to non-similar systems, and it has been shown that optimisation on position error produces good drogue-receiver tracking, but optimisation against position and velocity errors creates a controller with a more satisfactory convergence to the envelope centre, whilst retaining good tracking.

Chapter 8

Conclusions

Work in this thesis progressed through methods of coupling the receiver and drogue increasingly closely. Progressing down this spectrum, shown in figure 8.1, has been shown to improve capture rate via a range of methods – initially significantly, as seen in the difference in capture performance between L/F and stabilised-drogue systems in chapter 4. Dynamic matching of the drogue to receiver gust response was also briefly considered, but not pursued in depth.

The roadmap in figure 8.2 shows how chapters and sections of this thesis contribute to the overall aims.

Chapter 6 showed the Common-target-point Control approach to be successful when optimised for a particular turbulence level. It proved possible to reduce the effect of the gain-based trade-off between relative tracking and position hold via a scheduled gain method, which emphasises intimacy at the centre of the refuelling envelope but increases the significance of position hold, at the expense of relative tracking, as the edge of the envelope is approached. This has the added advantage of reducing unnecessary control effort when the receiver is outside the refuelling envelope, without a sharp transition between controllers.

Chapter 7 developed an intimate controller for hose-drogue refuelling, taking it from abstract second-order models to more realistic receiver and drogue models. It was not possible to apply the full-state-feedback optimisation method to the full nonlinear AAAR SE and this should be a priority for further work.

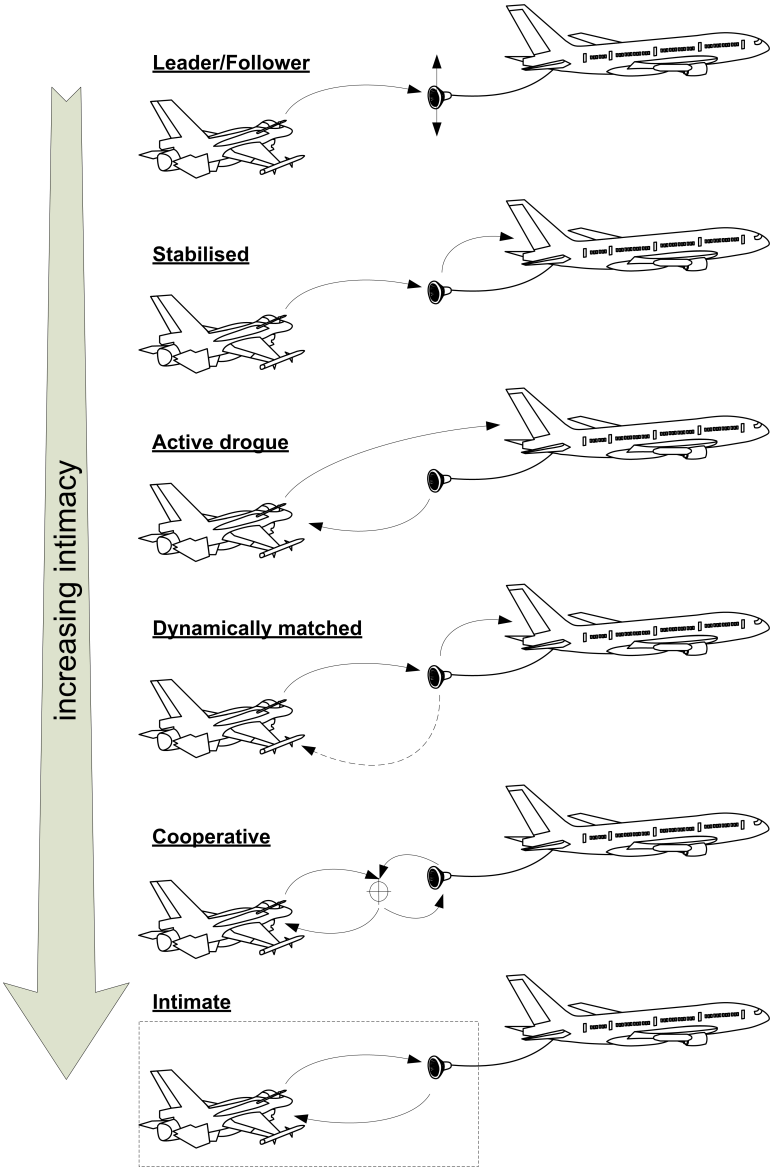

Figure 8.1: Levels of intimacy for AAAR demonstrated in this thesis. Solid line indicates active sensing and following, dotted line indicates 'matched' dynamics, without active sensing/following. L/F control was demonstrated in chapter 3; stabilised and dynamically matched in chapter 4; cooperative in chapter 6 and intimate control in chapter 7.

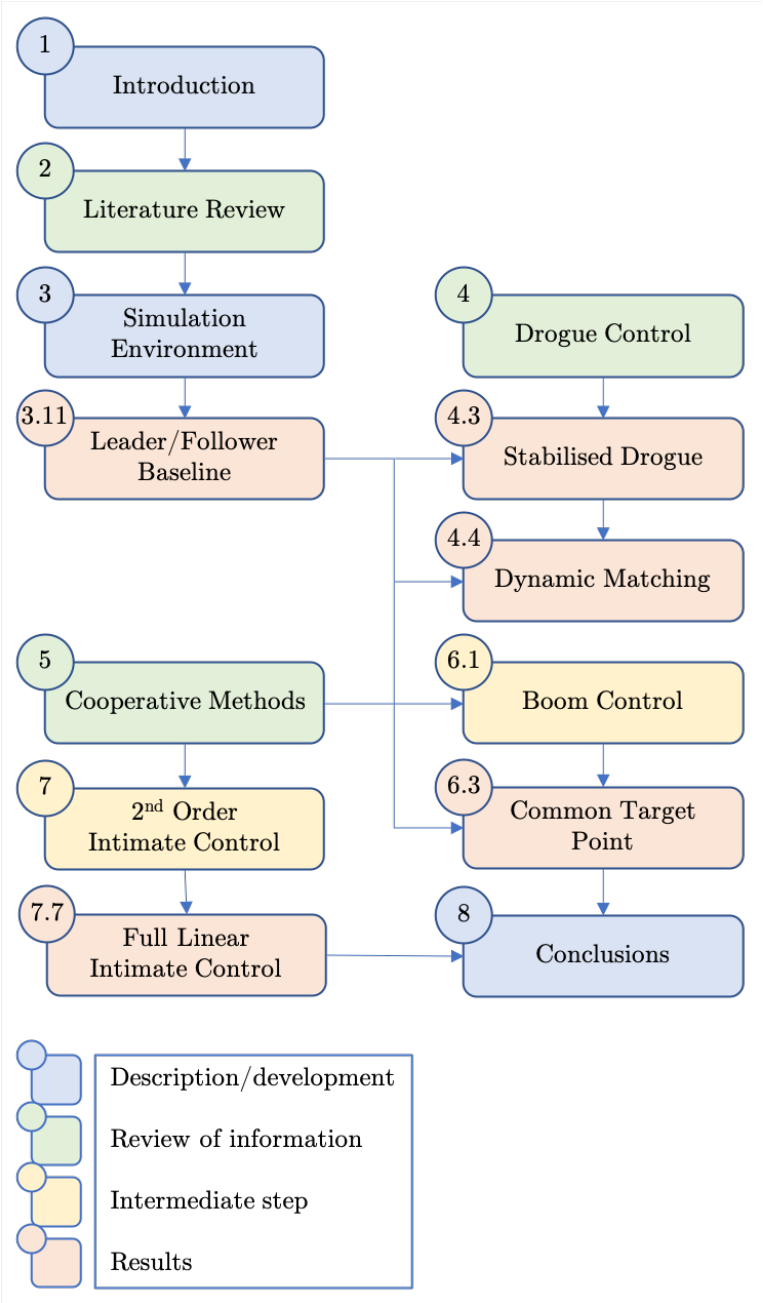

Figure 8.2: Thesis roadmap (numbers indicate chapters/ sections)

8.1 Thesis achievements

This thesis aimed to assess the scope for improvement in capture performance, against a baseline 'leader-follower' control architecture, in probe-drogue Autonomous Air-to-Air Refuelling, by harnessing additional degrees of freedom available in the tanker/ refuelling hardware/ receiver system.

There is still work required to bring control systems developed throughout this thesis to a flight-ready level, but it has met its aim in a variety of ways:

- Chapter 4 showed that drogue control is practically feasible by reviewing potential actuation methods, generating a representative force model, and constructing and optimising a drogue stabilisation controller that gave a significant improvement in capture rate over the baseline L/F controller.
- Chapter 6 applied a cooperative, common-target-point, architecture to the receiver-drogue system, optimising it for various turbulence levels and demonstrating an improvement in capture rate against the baseline L/F controller across the turbulence spectrum, and against a stabilised drogue at turbulence levels for which it was optimised. Performance of this controller was verified through full-scale real-time Hardware-in-the-Loop simulation in a Relative Motion Robotic environment.
- Chapter 6 also extended the common-target controller using a novel scheduled-gain approach, which improved capture rate for boom-receptacle refuelling.
- Chapter 7 investigated a MIMO intimate control method, applying it to increasingly-complex systems up to and including a full-order linear AAAR model, trialled several optimisation approaches, and showed improved response with the intimate controller.

8.2 Comparison of CC and IC architectures

At a high level, the intimate and cooperative controllers perform very similar functions. The flow of information in both architectures is nearly identical, as shown in figure 8.3.

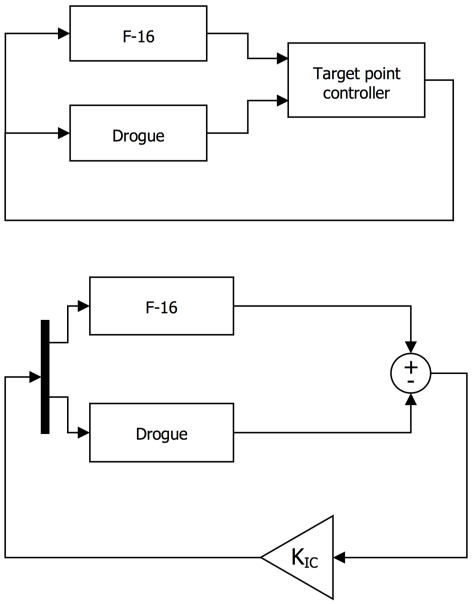

Figure 8.3: Simplified CC and IC architectures

Both controllers act upon the states, or a subset of the states, of both systems. The target point controller of the cooperative architecture performs a weighting function which produces a demand that converges the positions of the systems, and the intimate controller's gain performs a similar function on the states of receiver and drogue. For both:

$$\mathbf{u}_{\mathrm{F16}} = f\left(\mathbf{x}_{\mathrm{F16}}, \mathbf{x}_{\mathrm{drogue}}\right) \tag{8.1}$$

$$\mathbf{u}_{\mathrm{drogue}} = g\left(\mathbf{x}_{\mathrm{F16}}, \mathbf{x}_{\mathrm{drogue}}\right) \tag{8.2}$$

The intimate controller, having access to the states of both systems, has more information than the cooperative controller upon which to act. This should prove an advantage, but comes with the burden of higher bandwidth for information transfer.

The optimisation of both systems is via differing methods, but both take into account the different dynamics of the two systems – the cooperative

controller in its weighting of the target point, and the intimate controller in the magnitude of the drogue and F-16 parameters in its feedback gain.

Intimate control requires a data communication link between the two systems, as the controller action depends on states internal to each system. This may produce a better performing controller, but design, cost and reliability will be factors in determining an overall solution. Cooperative control requires less shared data than intimate control – given its requirement only for relative position, and possibly velocity, a vision system could be used to determine this information.

Noise and delays in sensing, processing and communication have been shown to have the expected effect of degrading capture performance. The cooperative controller is robust to noise and delay at low levels of turbulence but this degradation of performance is expected to increase at higher levels.

Selecting which method to use depends upon sensing and communications availability and limitations. Table 8.1 gives recommendations for various scenarios.

Table 8.1: Architecture recommendations for various configurations

Turbulence	Drogue control	Available states[1]		Recommended
		Receiver	Drogue	
Low	None	Drogue position	-	L/F
Varying	Available	Drogue/receiver position error	Drogue/tanker position error	Stabilised
Varying	Available	Drogue/receiver position error	Receiver/drogue position error	Cooperative
Varying	Available	Full drogue and receiver states	Full drogue and receiver states	Intimate

8.3 Further work

There are a number of suggested avenues through which this work could be further pursued:

- Drogue stabilisation, common-target control, and intimate control have all showed potential to improve drogue capture. Confidence in this can be increased by:

- – detailed design work and further practical testing of drogue control methods, including solutions to providing power and actuation to a drogue with minimal modification to existing systems.
  - wider testing of the CC controller in the RMR environment – trialling capture across a range of turbulence in a similar approach to the non-HIL SE trials.
- The extension of the CC controller via gain scheduling proved successful for boom-receptacle refuelling, and should be applied to the probe-drogue SE and verified through RMR simulation.
- A variety of methods by which the IC controller could be implemented and optimised for the nonlinear SE were identified in section 7.9 – these should be explored and trialled in a similar way to the CC controller.

Interesting points and questions that were noted throughout the design and optimisation process for each of the controllers include:

- Drogue stabilisation
- – Dynamic matching of drogue response to receiver was briefly investigated in section 4.4. This could be accomplished through active control, or potentially via customisation of passive drogues (using innovative manufacturing methods to tailor low-volume production?)
  - Alternative tuning/optimisation methods may provide improved response
- Common-target control
- – Alternative scheduling profiles (exponential, parabolic, more complex?) may provide improvement over the linear gain scheduling applied in this investigation.
  - Optimisation of the controller was numerical, rather than provably optimal. Alternative approaches may guarantee stability and robustness.
- Intimate control

- – Position and convergence are given even weighting in the optimisations trialled here. Applying a scheduling approach to the intimate controller may provide benefit in a similar way to the common-target controller enhancement.

References

[1] Dwayne A. Day. *Aerial Refueling*. 2003.

[2] Richard K Smith. *Seventy-five Years of Inflight Refueling*. Air Force History and Museums Program, 1998.

[3] Christopher Bolkcom and Jon D Klaus. *Air Force Aerial Refueling Methods: Flying Boom versus Hose-and-Drogue*. Tech. rep. Washington: Congressional Research Service, 2005.

[4] Office of the Secretary of Defense. *Unmanned Aircraft Systems Roadmap 2005-2030*. Tech. rep. Washington: Office of the Secretary of Defense, 2005.

[5] W. I. Glover. "Wings across the Atlantic". In: *Popular Mechanics* (Feb. 1931), pp. 186–191.

[6] Pedro Argelles et al. *European Aeronautics: A Vision for 2020*. Tech. rep. January. Luxembourg: European Commission, 2001.

[7] Marek Darecki et al. *Flightpath 2050: Europe's Vision for Aviation*. Tech. rep. Luxembourg: European Commission, 2011. DOI: 10.2777/50266.

[8] Matthew a. Bennington and Kenneth D. Visser. "Aerial Refueling Implications for Commercial Aviation". In: *Journal of Aircraft* 42.2 (Mar. 2005), pp. 366–375. DOI: 10.2514/1.4770.

[9] R K Nangia. "Operations and aircraft design towards greener civil aviation using air-to-air refuelling". In: *The Aeronautical Journal* 3088 (2006), pp. 705–721.

[10] R K Nangia. "Greener' civil aviation using air-to-air refuelling relating aircraft design efficiency and tanker offload efficiency". In: *The Aeronautical Journal* 111.1123 (2007), pp. 589–592.

[11] R K Nangia. "Air to Air Refuelling in Civil Aviation , An Opportunity & A Vision". In: *RAeS "Greener By Design" Conference*. London: RAeS, 2008.

[12] R K Nangia. "Achieving Highly Efficient Civil Aviation - Why & How with Air-to-Air Refuelling , Review & New Developments". In: *26th International Congress of the Aeronautical Sciences*. Vol. 3. Anchorage, USA: ICAS, 2008.

[13] Jia Xu et al. "Aircraft Route Optimization for Formation Flight". In: *Journal of Aircraft* 51.2 (Mar. 2014), pp. 490–501. DOI: 10.2514/1.C032154.

[14] Wendy Okolo, Atilla Dogan, and William Blake. "Benefits of Formation Flight of Extended Duration Considering Fuel Burn". In: *AIAA Atmospheric Flight Mechanics Conference*. June. Reston, Virginia: American Institute of Aeronautics and Astronautics, June 2015. DOI: 10.2514/6.2015-2234.

[15] Thomas E. Kent and Arthur G. Richards. "Analytic Approach to Optimal Routing for Commercial Formation Flight". In: *Journal of Guidance, Control, and Dynamics* 38.10 (Oct. 2015), pp. 1872–1884. DOI: 10.2514/1.G000806.

[16] Joseph P Nalepka and Jacob L Hinchman. "Automated Aerial Refueling: Extending the Effectiveness of Unmanned Air Vehicles". In: *AIAA Modeling and Simulation Technologies Conference and Exhibit*. San Francisco, California: AIAA, 2005.

[17] Tony Griffiths. "Intimate Control for UAV and UGV Rendezvous and Docking". In: *2nd SEAS DTC Technical Conference*. Edinburgh, 2007.

[18] Walton R Williamson et al. "Controllable Drogue for Automated Aerial Refueling". In: *Journal of Aircraft* 47.2 (2010). DOI: 10.2514/1.44758.

[19] D P Scharf, Fred Y Hadaegh, and S R Ploen. "A Survey of Spacecraft Formation Flying Guidance and Control (Part II): Control". In: *Proceeding of the 2004 American Control Conference*. Boston, Massachusetts: AACC, 2004, pp. 2976–2985.

[20] D. V. A. G. H. Swaroop. "String Stability Of Interconnected Systems: An Application To Platooning In Automated Highway Systems". PhD thesis. University of California at Berkeley, 1997.

[21] ASTRAEA Consortium. *http://astraea.aero*. 2014.

[22] The Economist. "This is your ground pilot speaking". In: *The Economist* (2012), pp. 76–77.

[23] BAE Systems. "Look no hands". In: *Innovation* (July 2013).

[24] Cobham plc. *About Cobham plc*.

[25] Department of Defense. *Technology Readiness Assessment Guidance*. Tech. rep. 13 May 2011. 2011.

[26] Jonathan Luke du Bois, Peter R. Thomas, and Thomas S. Richardson. "Development of a relative motion facility for simulations of autonomous air to air refuelling". In: *2012 IEEE Aerospace Conference*. IEEE, Mar. 2012, pp. 1–12. DOI: 10.1109/AERO.2012.6187309.

[27] Jonathan Luke J.L. du Bois et al. "Control Methodologies for Relative Motion Reproduction in a Robotic Hybrid Test Simulation of Aerial Refuelling". In: *AIAA Guidance, Navigation, and Control Conference*. Minneapolis, Minnesota: American Institute of Aeronautics and Astronautics, Aug. 2012. DOI: 10.2514/6.2012-4676.

[28] Ujjar Bhandari. "Control System Design for Autonomous Air-to-Air Refuelling". PhD thesis. University of Bristol, 2014.

[29] TS Richardson et al. "Implementation of a Relative Motion Robotic Rig for Hardware in the Loop Simulation of Automated Air-to-Air Refuelling". In: *26th Bristol International International UAV Systems Conference*. Bristol, UK: University of Bristol, 2011.

[30] Jonathan Luke du Bois et al. "Vision Based Closed-Loop Control System for Satellite Rendezvous With Model-in-the-Loop Validation and Testing". In: *23rd International Symposium on Space Flight Dynamics*. 2012, pp. 1–16.

[31] Ujjar Bhandari et al. "Bow Wave Effect in Probe and Drogue Aerial Refuelling". In: *AIAA Guidance, Navigation, and Control (GNC) Conference*. Reston, Virginia: American Institute of Aeronautics and Astronautics, Aug. 2013, pp. 1–21. DOI: 10.2514/6.2013-4695.

[32] Peter R. Thomas et al. "Advances in air to air refuelling". In: *Progress in Aerospace Sciences* 71 (Nov. 2014), pp. 14–35. DOI: 10.1016/j.paerosci.2014.07.001.

[33] Peter R. Thomas et al. "Collaborative Control in a Flying-Boom Aerial Refueling Simulation". In: *Journal of Guidance, Control, and Dynamics* 38.7 (July 2015), pp. 1274–1289. DOI: 10.2514/1.G000486.

[34] W Mao and F O Eke. "A Survey of the Dynamics and Control of Aircraft During Aerial Refueling". In: *Nonlinear Dynamics and Systems Theory* 8.4 (2008), pp. 375–388.

[35] Geoffrey Bower, Tristan Flanzer, and Ilan Kroo. "Formation Geometries and Route Optimization for Commercial Formation Flight". In: *27th AIAA Applied Aerodynamics Conference*. Reston, Virigina: American Institute of Aeronautics and Astronautics, June 2009. DOI: 10.2514/6.2009-3615.

[36] Jennifer L Hansen, James E Murray, and Norma V Campos. "The NASA Dryden AAR Project : A Flight Test Approach to an Aerial Refueling System". In: *AIAA Atmospheric Flight Mechanics Conference and Exhibit*. August. Providence, Rhode Island: American Automatic Control Council, 2004, pp. 1–19.

[37] Ryan P Dibley, Michael J Allen, and Nassib Nabaa. *Autonomous Airborne Refueling Demonstration , Phase I Flight-Test Results*. Tech. rep. December. Edwards, California: Dryden Flight Research Center, 2007.

[38] Sierra Nevada Corporation. *SNC System Performs First Ever Autonomous Airborne Refueling Engagement*. 2006.

[39] Keith Schweikhard. *Results of NASA/DARPA Automatic Probe and Drogue Refueling Flight Test*. Tech. rep. Edwards, CA: NASA Dryden Flight Research Facility, 2008.

[40] Nick Hague et al. *Limited Evaluation of Sensor Requirements for Autonomous Air Refueling Rendezvous (Project Medium Rare)*. Tech. rep. Edwards Air Force Base, CA: Air Force Flight Test Center, 2003.

[41] Steven M. Ross et al. *Demonstration of a Control Algorithm for Autonomous Aerial Refueling (Project "No Gyro")*. Tech. rep. Edwards AFB, CA: Air Force Flight Test Center, 2005.

[42] S M Ross et al. "Autonomous Aerial Refueling Based on the Tanker Reference Frame". In: *2006 IEEE Aerospace Conference* (2005), pp. 1–22. DOI: 10.1109/AERO.2006.1656016.

[43] S M Ross. "Formation Flight Control for Aerial Refueling". PhD thesis. Air Force Institute of Technology, 2006.

[44] Ryan McMahon and Paul Deppe. "State of the art in UAV Surrogacy for the 21st century". In: *2013 IEEE/AIAA 32nd Digital Avionics Systems Conference (DASC)*. IEEE, Oct. 2013, pp. 1–33. DOI: 10.1109/DASC.2013.6719656.

[45] R McMahon. "From in-flight simulators to UAV surrogates". In: *Annual international symposium of the society of flight test engineers*. Forth Worth, TX, USA, 2013.

[46] John Whittenbury. "Configuration Design Development of the Navy UCAS-D X-47B". In: *AIAA Centennial of Naval Aviation Forum "100 Years of Achievement and Progress"*. Reston, Virigina: American Institute of Aeronautics and Astronautics, Sept. 2011. DOI: 10.2514/6.2011-7041.

[47] Northrop Grumman Aerospace Systems. *Landmark Flight Brings Program One Step Closer to Demonstrating Autonomous Aerial Refueling Between Two Unmanned Aircraft*. 2011.

[48] Naval Air Systems Command. *Fueled in flight: X-47B first to complete autonomous aerial refueling*. 2015.

[49] Ben Sampson. *Autonomous refuelling passes key milestone - twice*. 2015.

[50] Daniel B Wilson and Ali Haydar Goktogan. "An Unmanned Aerial Vehicle Rendezvous and Formation Flight Demonstration". In: *International Conference on Unmanned Aircraft Systems*. 2012.

[51] Daniel B Wilson, Ali Haydar Goktogan, and Salah Sukkarieh. "UAV rendezvous: From concept to flight test". In: *Australasian Conference on Robotics and Automation, ACRA* (2012), pp. 3–5.

[52] Daniel B Wilson et al. "Real-time rendezvous point selection for a nonholonomic vehicle". In: *Proceedings - IEEE International Conference on Robotics and Automation* (2013), pp. 3941–3946. DOI: 10.1109/ICRA.2013.6631132.

[53] Daniel B Wilson, Ali Haydar Goktogan, and Salah Sukkarieh. "A Vision Based Relative Navigation Framework for Formation Flight". In: *IEEE International Conference on Robotics & Automation*. 2014, pp. 4988–4995.

[54] Daniel B Wilson, Ali Haydar Goktogan, and Salah Sukkarieh. "Drogue Motion Estimation Using Air-to-Air Observations". In: *Australasian Conference on Robotics and Automation*. 2014.

[55] NRJ Lawrance et al. "Long Endurance Autonomous Flight for Unmanned Aerial Vehicles". In: *Aerospace Lab Journal* 8 (2014), pp. 1–15.

[56] Richard Bourne. *ASTRAEA 2/MGT/006 AAR Pilot Control Techniques*. Tech. rep. Wimborne, UK: Cobham plc, 2010.

[57] MSgt Greg Conrad. "Aerodynamic Effects on the Air Refueling Platform". In: *Flying Safety* (Mar. 2001), pp. 12–15.

[58] Kenneth M. Dorsett and David R. Mehl. *Innovative Control Effectors (ICE)*. Tech. rep. Fort Worth, TX: Lockheed Martin Tactical Aircraft Systems, 1996.

[59] Kenneth M. Dorsett, Scott P. Fears, and Heather P. Houlden. *Innovative Control Effectors (ICE) Phase II*. Tech. rep. Fort Worth, TX: Lockheed Martin Tactical Aircraft Systems, 1997.

[60] Arthur Barfield and Jacob Hinchman. "An Equivalent Model for UAV Automated Aerial Refueling Research". In: *AIAA Modeling and Simulation Technologies Conference and Exhibit*. Reston, Virigina: American Institute of Aeronautics and Astronautics, Aug. 2005. DOI: 10.2514/6.2005-6006.

[61] Jay Farrell, Manu Sharma, and Marios Polycarpou. "Backstepping-Based Flight Control with Adaptive Function Approximation". In: *Journal of Guidance, Control, and Dynamics* 28.6 (Nov. 2005), pp. 1089–1102. DOI: 10.2514/1.13030.

[62] Scott P. Fears, Holly M. Ross, and Thomas M. Moul. *Low-speed wind-tunnel investigation of the stability and control characteristics of a series of flying wings with sweep angles of 50 deg.* Tech. rep. Hampton, VA, United States: NASA Langley Research Center, 1995.

[63] Brian L. Stevens and Frank L. Lewis. *Aircraft Control and Simulation.* John Wiley & Sons, 2003.

[64] Cormac McFarlane and Thomas S. Richardson. "Cooperative Control During Boom Air-to-Air Refueling". In: *AIAA Guidance Navigation and Control Conference and Exhibit.* Hilton Head, South Carolina: AIAA, 2007, pp. 1–17.

[65] Yunfei Zou, Prabhakar R. Pagilla, and Ryan T. Ratliff. "Distributed Formation Flight Control Using Constraint Forces". In: *Journal of Guidance, Control, and Dynamics* 32.1 (Jan. 2009), pp. 112–120. DOI: 10.2514/1.36826.

[66] Sriram Venkataramanan and Atilla Dogan. "Dynamic Effects of Trailing Vortex with Turbulence & Time-Varying Inertia Properties in Aerial Refueling". In: *AIAA Atmospheric Flight Mechanics Conference and Exhibit.* Reston, Virigina: American Institute of Aeronautics and Astronautics, Aug. 2004. DOI: 10.2514/6.2004-4945.

[67] Weixin Mao. "Effect of mass variation on the dynamics of receiver aircraft during aerial refueling". PhD thesis. University of California, Davis, 2008.

[68] W Jewell and R Stapleford. *Mathematical models used to simulate aircraft encounters with wake vortices.* Tech. rep. NASA Scientific and Technical Information Technical Report STI TR-1035-4 (DOT-FA73WA-3276-1), 1975.

[69] A W Bloy et al. "The lateral dynamic stability and control of a large receiver aircraft during air-to-air refuelling". In: *Aeronautical Journal* 90 (1986), pp. 237–243.

[70] A W Bloy, K A M Ali, and V Trochalidis. "The longitudinal dynamic stability and control of a large receiver aircraft during air-to-air refueling". In: *Aeronautical Journal* 91.902 (1987), pp. 64–71.

[71] A. W Bloy and V. Trochalidis. "The performance and longitudinal stability and control of large receiver aircraft during air to air refuelling". In: *The Aeronautical Journal* 93.930 (1989), pp. 367–378. DOI: 10.1017/S0001924000022193.

[72] A W Bloy and V Trochalidis. "The aerodynamic interference between tanker and receiver aircraft during air-to-air refuelling". In: *The Aeronautical Journal (1968)* 94.935 (1990), pp. 165–171.

[73] A W Bloy, V Trochalidis, and M G West. "The aerodynamic interference between a flapped tanker aircraft and a receiver aircraft during air-to-air refuelling". In: *The Aeronautical Journal (1968)* 95.948 (1991), pp. 274–282. DOI: 10.1017/S0001924000024106.

[74] A. W. BLOY et al. "Lateral aerodynamic interference between tanker and receiver in air-to-air refueling". In: *Journal of Aircraft* 30.5 (Sept. 1993), pp. 705–710. DOI: 10.2514/3.46401.

[75] A. W. Bloy and M. G. West. "Interference between tanker wing wake with roll-up and receiver aircraft". In: *Journal of Aircraft* 31.5 (Sept. 1994), pp. 1214–1216. DOI: 10.2514/3.46633.

[76] V. J. Rossow et al. *Velocity and rolling-moment measurements in the wake of a swept-wing model in the 40 by 80 foot wind tunnel.* Tech. rep. Moffett Field, CA: NASA Ames Research Center, 1975.

[77] V. J. Rossow. *Experimental investigation of wing fin configurations for alleviation of vortex wakes of aircraft.* Tech. rep. Moffett Field, CA, United States: NASA Ames Research Center, 1978.

[78] VERNON J. ROSSOW. "Estimate of loads during wing-vortex interactions by Munk's transverse-flow method". In: *Journal of Aircraft* 27.1 (Jan. 1990), pp. 66–74. DOI: 10.2514/3.45897.

[79] V. J. Rossow et al. "Wind-tunnel measurements of hazard posed by lift-generated wakes". In: *Journal of Aircraft* 32.2 (Mar. 1995), pp. 278–284. DOI: 10.2514/3.46713.

[80] Vernon J. Rossow. "Validation of vortex-lattice method for loads on wings in lift-generated wakes". In: *Journal of Aircraft* 32.6 (Nov. 1995), pp. 1254–1262. DOI: 10.2514/3.46872.

[81] Vernon J. Rossow. "Lift-generated vortex wakes of subsonic transport aircraft". In: *Progress in Aerospace Sciences* 35.6 (Aug. 1999), pp. 507–660. DOI: 10.1016/S0376-0421(99)00006-8.

[82] Vernon J. Rossow. "Effect of Wing Fins on Lift-Generated Wakes". In: *Journal of Aircraft* 15.3 (2012), pp. 160–167.

[83] A. W. Bloy and M. M. Khan. "Modeling of the Receiver Aircraft in Air-To-Air Refueling". In: *Journal of Aircraft* 38.2 (Mar. 2001), pp. 393–396. DOI: 10.2514/2.2775.

[84] Deborah Saban. "Wake Vortex Modelling and Simulation for Air Vehicles in Close Formation Flight". PhD thesis. Cranfield University, 2010.

[85] William Blake and David R Gingras. "Comparison of Predicted and Measured Formation Flight Interference Effects". In: *Journal of Aircraft* 41.2 (Mar. 2004), pp. 201–207. DOI: 10.2514/1.9278.

[86] William Blake, Edward G. Dickes, and David R. Gingras. "UAV Aerial Refueling - Wind Tunnel Results and Comparison with Analytical Predictions". In: *AIAA Atmospheric Flight Mechanics Conference and Exhibit*. August. A. Providence, Rhode Island: American Institute of Aeronautics and Astronautics, Aug. 2004, pp. 4820–4820. DOI: 10.2514/6.2004-4820.

[87] Dwayne Jackson, Charles Tyler, and William Blake. "Computational Analysis of Air-to-Air Refueling". In: *25th AIAA Applied Aerodynamics Conference*. Reston, Virigina: American Institute of Aeronautics and Astronautics, June 2007. DOI: 10.2514/6.2007-4289.

[88] Atilla Dogan, Shinya Sato, and William Blake. "Flight Control and Simulation for Aerial Refueling". In: *AIAA Guidance, Navigation, and Control Conference and Exhibit*. August. San Francisco, California: American Institute of Aeronautics and Astronautics, Aug. 2005. DOI: 10.2514/6.2005-6264.

[89] Obi Iloputaife, Gerald Svoboda, and T. Bailey. "Handling qualities design of the C-17A for receiver-refueling". In: *Guidance, Navigation, and Control Conference*. Reston, Virigina: American Institute of Aeronautics and Astronautics, July 1996. DOI: 10.2514/6.1996-3746.

[90] Atilla Dogan and William Blake. "Modeling of Bow Wave Effect in Aerial Refueling". In: *AIAA Atmospheric Flight Mechanics Conference*. Reston, Virigina: American Institute of Aeronautics and Astronautics, Aug. 2010. DOI: 10.2514/6.2010-7926.

[91] Christian Haag, Matthew Schwaab, and William Blake. "Computational Analysis of the Bow Wave Effect in Air-to-Air Refueling". In: *AIAA Atmospheric Flight Mechanics Conference*. Reston, Virigina: American Institute of Aeronautics and Astronautics, Aug. 2010. DOI: 10.2514/6.2010-7925.

[92] Kapseong Ro, Taeseung Kuk, and James W. Kamman. "Active Control of Aerial Refueling Hose-Drogue Systems". In: *AIAA Guidance, Navigation, and Control Conference*. August. Toronto, Ontario Canada: American Institute of Aeronautics and Astronautics, 2010, pp. 1–12.

[93] J.M. Winget and R.L. Huston. "Cable dynamics - a finite segment approach". In: *Computers & Structures* 6.6 (1976), pp. 475–480.

[94] Ronald L. Huston and Chris Passerello. "On multi-rigid-body system dynamics". In: *Computers & Structures* 10.3 (1978), pp. 439–446.

[95] Ronald L. Huston and James W. Kamman. "A representation of fluid forces in finite segment cable models". In: *Computers & Structures* 14.3-4 (1981), pp. 281–287.

[96] Ronald L. Huston and James W. Kamman. "Validation of finite segment cable models". In: *Computers & Structures* 15.6 (1982), pp. 653–660.

[97] James W. Kamman and Ronald L. Huston. "Modelling of submerged cable dynamics". In: *Computers & Structures* 20.1-3 (1985), pp. 623–629.

[98] James W. Kamman and Ronald L. Huston. "Multibody Dynamics Modeling of Variable Length Cable Systems". In: *Multibody System Dynamics* (2001), pp. 211–221.

[99] James W. Kamman and T.C. Nguyen. *Modeling Towed Cable System Dynamics*. Tech. rep. Panama City, Florida: Naval Coast Systems Center, 1990.

[100] Kapseong Ro, Husain Ahmad, and James W. Kamman. "Dynamic Modeling and Simulation of Hose-Paradrogue Assembly for Mid-Air Operations". In: *AIAA Infotech@Aerospace Conference and AIAA Unmanned...Unlimited Conference*. Seattle, Washington: AIAA, 2009, pp. 1–14.

[101] Kapseong Ro and James W. Kamman. "Modeling and Simulation of Hose-Paradrogue Aerial Refueling Systems". In: *Journal of Guidance, Control, and Dynamics* 33.1 (2010), pp. 53–62. DOI: 10.2514/1.45482.

[102] Kapseong Ro, Emre Basaran, and James W. Kamman. "Aerodynamic Characteristics of Paradrogue Assembly in an Aerial Refueling System". In: *Journal of Aircraft* 44.3 (May 2007), pp. 963–970. DOI: 10.2514/1.26489.

[103] Kapseong Ro, Taeseung Kuk, and James W. Kamman. "Dynamics and Control of Hose-Drogue Refueling Systems During Coupling". In: *Journal of Guidance, Control, and Dynamics* 34.6 (Nov. 2011), pp. 1694–1708. DOI: 10.2514/1.53205.

[104] Z Zhu and S Meguid. "Elastodynamic analysis of low tension cables using a new curved beam element". In: *International Journal of Solids and Structures* 43.6 (Mar. 2006), pp. 1490–1504. DOI: 10.1016/j.ijsolstr.2005.03.053.

[105] J. Eichler. "Dynamic Analysis of an In-Flight Refueling System". In: *Journal of Aircraft* 15.5 (May 1978), pp. 311–318. DOI: 10.2514/3.58361.

[106] Mario Fravolini et al. “Development of Modelling and Control Tools for Aerial Refueling for UAVs”. In: *AIAA Guidance, Navigation, and Control Conference and Exhibit*. August. Reston, Virigina: American Institute of Aeronautics and Astronautics, Aug. 2003, pp. 1–10. DOI: 10.2514/6.2003-5798.

[107] Mario Luca Fravolini et al. “Modeling and control issues for autonomous aerial refueling for UAVs using a probedrogue refueling system”. In: *Aerospace Science and Technology* 8.7 (Oct. 2004), pp. 611–618. DOI: 10.1016/j.ast.2004.06.006.

[108] M.L. Fravolini et al. “Feature Matching Algorithms for Machine Vision Based Autonomous Aerial Refueling”. In: *2006 14th Mediterranean Conference on Control and Automation*. IEEE, June 2006, pp. 1–8. DOI: 10.1109/MED.2006.328792.

[109] Soujanya Vendra et al. “Addressing corner detection issues for machine vision based UAV aerial refueling”. In: *Machine Vision and Applications* 18.5 (Oct. 2007), pp. 261–273. DOI: 10.1007/s00138-006-0056-9.

[110] G. Cantin and R. W. Clough. “A curved, cylindrical-shell, finite element.” In: *AIAA Journal* 6.6 (June 1968), pp. 1057–1062. DOI: 10.2514/3.4673.

[111] Z Zhu and S Meguid. “Elastodynamic Analysis of Aerial Refueling Hose Using Curved Beam Element”. In: *AIAA Journal* 44.6 (June 2006), pp. 1317–1324. DOI: 10.2514/1.17311.

[112] Z Zhu and S Meguid. “Modeling and simulation of aerial refueling by finite element method”. In: *International Journal of Solids and Structures* 44.24 (Dec. 2007), pp. 8057–8073. DOI: 10.1016/j.ijsolstr.2007.05.026.

[113] A. W. Bloy and M. M. Khan. “Modelling of the hose and drogue in air-to-air refuelling”. In: *Aeronautical Journal* 106.1055 (2002), pp. 17–26.

[114] John C Vassberg et al. “Numerical Simulations of KC-10 Wing-Mount Aerial Refueling Hose-Drogue Dynamics With A Reel Take-Up System”. In: *21st Applied Aerodynamics Conference*. June. Reston, Virigina: American Institute of Aeronautics and Astronautics, June 2003, pp. 1–22. DOI: 10.2514/6.2004-4719.

[115] John C Vassberg et al. “Numerical Simulations of KC-10 Centerline Aerial Refueling Hose-Drogue Dynamics With A Reel Take-Up System”. In: *22nd Applied Aerodynamics Conference*. August. Reston, Virigina: American Institute of Aeronautics and Astronautics, June 2004, pp. 1–19. DOI: 10.2514/6.2004-4719.

[116] John C Vassberg et al. "Numerical Simulations of KC-10 In-Flight Refueling Hose-Drogue Dynamics with An Approaching F/A-18D Receiver Aircraft". In: *23rd AIAA Applied Aerodynamics Conference*. June. Toronto, Ontario Canada: American Institute of Aeronautics and Astronautics, June 2005. DOI: 10.2514/6.2005-4605.

[117] S F Hoerner. *Fluid Dynamic Drag*. Published by the author, 1965.

[118] ESDU. *Mean forces , pressures and flow field velocities for circular cylindrical structures : single cylinder with two-dimensional flow*. Tech. rep. June. ESDU, 1986.

[119] William Ribbens et al. "Dynamic Modeling of an Aerial Refueling Hose & Drogue System". In: *25th AIAA Applied Aerodynamics Conference*. Reston, Virigina: American Institute of Aeronautics and Astronautics, June 2007. DOI: 10.2514/6.2007-3802.

[120] Andrey Styuart et al. "Numerical Simulation of Hose Whip Phenomenon in Aerial Refueling". In: *AIAA Atmospheric Flight Mechanics Conference*. Reston, Virigina: American Institute of Aeronautics and Astronautics, Aug. 2011. DOI: 10.2514/6.2011-6211.

[121] NATO. *ATP-56(B) Air-to-Air Refuelling*. 2010.

[122] Shigeo Hayashibara et al. "Simulation-Based Design (SBD) Applications for a Mid-Air Aerial Refueling Paradrogue System". In: *6th AIAA Aviation Technology, Integration and Operations Conference (ATIO)*. Reston, Virigina: American Institute of Aeronautics and Astronautics, Sept. 2006. DOI: 10.2514/6.2006-7770.

[123] Jennifer L Hansen, James E Murray, and Norma V Campos. *The NASA Dryden Flight Test Approach to an Aerial Refueling System*. Tech. rep. Edwards, California: NASA Dryden Flight Research Center, 2005.

[124] Michael Jacob Vachon, Ronald J Ray, and Carl Calianno. *Calculated Drag of an Aerial Refueling Assembly Through Airplane Performance Analysis*. Tech. rep. February. Edwards, California: NASA Dryden Flight Research Center, 2004.

[125] J. Hansen et al. "DARPA Autonomous Airborne Refueling Demonstration Program With Initial Results". In: Fort Worth, TX: Institute of Navigation, 2006, pp. 674–685.

[126] H.W. Ng and F.L. Tan. "Simulation of fuel behaviour during aircraft in-flight refueling". In: *Aircraft Engineering and Aerospace Technology* 81.2 (Jan. 2009), pp. 99–105. DOI: 10.1108/00022660910941785.

[127] Elliott D. Kaplan and C. (Christopher J.) Hegarty. *Understanding GPS : principles and applications*. Artech House, 2006, p. 703.

[128] Samer M. Khanafseh and Boris Pervan. "Autonomous Airborne Refueling of Unmanned Air Vehicles Using the Global Positioning System". In: *Journal of Aircraft* 44.5 (Sept. 2007), pp. 1670–1682. DOI: 10.2514/1.28195.

[129] Alison K Brown et al. "Precision Navigation for UAS Critical Operations". In: *ION GNSS*. Portland, Oregon: ION, 2011.

[130] OpenCV. *OpenCV*.

[131] Allen D. Wu, Eric N. Johnson, and Alison A. Proctor. "Vision-Aided Inertial Navigation for Flight Control". In: *Journal of Aerospace Computing, Information, and Communication* 2.9 (Sept. 2005), pp. 348–360. DOI: 10.2514/1.16038.

[132] Gianpaolo Conte and Patrick Doherty. "Vision-Based Unmanned Aerial Vehicle Navigation Using Geo-Referenced Information". In: *EURASIP Journal on Advances in Signal Processing* 2009 (2009), pp. 1–19. DOI: 10.1155/2009/387308.

[133] Pascual Campoy et al. "Computer Vision Onboard UAVs for Civilian Tasks". In: *Unmanned Aircraft Systems*. Dordrecht: Springer Netherlands, 2008, pp. 105–135. DOI: 10.1007/978-1-4020-9137-7_8.

[134] L Mejias et al. "Vision-based detection and tracking of aerial targets for UAV collision avoidance". In: *2010 IEEE/RSJ International Conference on Intelligent Robots and Systems*. IEEE, Oct. 2010, pp. 87–92. DOI: 10.1109/IROS.2010.5651028.

[135] Thomas S. Richardson et al. "Automated Vision-based Recovery of a Rotary Wing Unmanned Aerial Vehicle onto a Moving Platform". In: *Journal of Field Robotics* 30.5 (Sept. 2013), pp. 667–684. DOI: 10.1002/rob.21467.

[136] Meng Ding, Li Wei, and Bangfeng Wang. "Vision-based Estimation of Relative Pose in Autonomous Aerial Refueling". In: *Chinese Journal of Aeronautics* 24.6 (Dec. 2011), pp. 807–815. DOI: 10.1016/S1000-9361(11)60095-2.

[137] Rocco V Dell'Aquila et al. "Real-time machine-vision-based position sensing system for UAV aerial refueling". In: *Journal of Real-Time Image Processing* 1.3 (Mar. 2007), pp. 213–224. DOI: 10.1007/s11554-007-0023-3.

[138] Carol Martnez et al. "A vision-based strategy for autonomous aerial refueling tasks". In: *Robotics and Autonomous Systems* 61.8 (Aug. 2013), pp. 876–895. DOI: 10.1016/j.robot.2013.02.006.

[139] John Valasek et al. "Vision-Based Sensor and Navigation System for Autonomous Air Refueling". In: *Journal of Guidance, Control, and Dynamics* 28.5 (Sept. 2005), pp. 979–989. DOI: 10.2514/1.11934.

[140] Chris Harris and Mike Stephens. “A Combined Corner and Edge Detector”. In: *Fourth Alvey Vision Conference*. 1988, pp. 147–151. DOI: 10.1.1.231.1604.

[141] Stephen M. Smith and J. Michael Brady. “SUSAN - A New Approach to Low Level Image Processing”. In: *International Journal of Computer Vision* 23.1 (1997), pp. 45–78. DOI: 10.1023/A:1007963824710.

[142] II Curro and A Joseph. *Automated Aerial Refueling Position Estimation Using a Scanning LiDAR*. Tech. rep. Wright-Patterson Air Force Base, OH: Air Force Institute of Technology, 2012.

[143] Chao-I Ci Chen and Roger Stettner. “Drogue tracking using 3D flash lidar for autonomous aerial refueling”. In: *Laser Radar Technology and Applications XVI*. 3. International Society for Optics and Photonics, 2011. DOI: 10.1117/12.886572.

[144] *GE Aviation Performs Navigation System Flight Testing for Aerial Refueling Applications*. Grand Rapids, MI, 2009.

[145] *GE Aviation Completes Second GPS-Independent Navigation System Flight Test for Automated Aerial Refueling Applications*. Grand Rapids, MI, 2010.

[146] Giampiero Campa et al. “Autonomous Aerial Refueling for UAVs Using a Combined GPS-Machine Vision Guidance”. In: *AIAA Guidance, Navigation and Control Conference and Exhibit*. August. Providence, Rhode Island, 2004, pp. 1–11.

[147] Marco Mammarella et al. “GPS / MV based Aerial Refueling for UAVs”. In: *AIAA Guidance, Navigation and Control Conference and Exhibit*. August. Honolulu, Hawaii, 2008, pp. 1–16.

[148] Marco Mammarella et al. “Machine Vision/GPS Integration Using EKF for the UAV Aerial Refueling Problem”. In: *IEEE Transactions on Systems Man and Cybernetics Part C Applications and Reviews* 38.6 (2008), pp. 791–801. DOI: 10.1109/TSMCC.2008.2001693.

[149] Walton R Williamson et al. “Sensor Fusion Applied to Autonomous Aerial Refueling”. In: *Journal of Guidance Control and Dynamics* 32.1 (2009), pp. 262–275. DOI: 10.2514/1.34589.

[150] L. T. Nguyen et al. *Simulator study of stall/post-stall characteristics of a fighter airplane with relaxed longitudinal static stability*. Tech. rep. Hampton, VA: NASA Langley Research Center, 1979.

[151] R. Williams and D. Lawrence. *Linear State-Space Control Systems*. John Wiley and Sons, 2007.

[152] A. Bryson and Y. Ho. *Applied Optimal Control*. Ginn and Company, 1969.

[153] Aboelmagd Noureldin, Tashfeen B. Karamat, and Jacques Georgy. *Fundamentals of Inertial Navigation, Satellite-based Positioning and their Integration*. Berlin, Heidelberg: Springer Berlin Heidelberg, 2013, pp. 21–63. DOI: 10.1007/978-3-642-30466-8.

[154] L.F. Faleiro and A.A. Lambregts. "Analysis and tuning of a Total Energy Control System' control law using eigenstructure assignment". In: *Aerospace Science and Technology* 3.3 (Apr. 1999), pp. 127–140. DOI: 10.1016/S1270-9638(99)80037-6.

[155] International Organization for Standardization. *ISO 2533:1975 Standard Atmosphere*. Tech. rep. Geneva: International Organization for Standardization, 1975.

[156] Frederic M. Hoblit. *Gust Loads on Aircraft: Concepts and Applications*. Washington DC: American Institute of Aeronautics and Astronautics, Jan. 1988. DOI: 10.2514/4.861888.

[157] US Department of Defense. *MIL-HDBK-1797 Flying Qualities of Piloted Aircraft*. Tech. rep. US Department of Defense, 1997.

[158] S.T. Wang and W. Frost. *Atmospheric Turbulence Simulation Techniques with Application to Flight Analysis*. Tech. rep. NASA, 1980, Contractor Report 3309.

[159] Peter R. Thomas et al. *D2.3.39 AAAR Control Laws and Synthetic Environment*. Tech. rep. Bristol, UK: University of Bristol, 2011.

[160] Shlomo S. Sawilowsky and Gail C. Fahoome. *Statistics via Monte Carlo Simulation with Fortran*. Rochester Hills, MI: JMASM, 2003.

[161] Peter R. Thomas, T S Richardson, and J L Du Bois. "Robotic Relative Motion Reproduction for Air to Air Refuelling Simulation". In: *5th European Conference for Aerospace Sciences*. Munich: EUCASS, 2013.

[162] Lorenzo Pollini, Mario Innocenti, and Roberto Mati. "Vision Algorithms for Formation Flight and Aerial Refueling with Optimal Marker Labeling". In: *AIAA Modeling and Simulation Technologies Conference and Exhibit*. August. Reston, Virigina: American Institute of Aeronautics and Astronautics, Aug. 2005. DOI: 10.2514/6.2005-6010.

[163] Taeseung Kuk, Kapseong Ro, and James W. Kamman. "Design, Test and Evaluation of an Actively Stabilized Drogue Refueling System". In: *Infotech@Aerospace 2011*. St. Louis, Missouri: American Institute of Aeronautics and Astronautics, 2011, pp. 1–13.

[164] Edward V B Thompson. "Aerodynamic investigations of control surface configurations for an air-to-air refuelling drogue". Masters thesis. University of Bristol, 2012.

[165] E Waghorn. "Aerodynamic Evaluation of a Controllable Drogue Design for use in Air to Air Refuelling". Masters thesis. Durham University, 2011.

[166] David Sims-Williams and Rob Dominy. "Improved Air to Air Refuelling". In: *European Strategic Wind tunnels Improved Research Potential Workshop*. Bardonecchia, Italy: ESWIRP, 2011.

[167] Ben Francis. "Aerodynamic analysis of a controllable drogue for use in air to air refuelling". Masters thesis. Durham, 2010.

[168] Steve Bullock et al. *D2.3.34 Drogue stabilisation*. Tech. rep. Bristol: University of Bristol, 2012.

[169] J G Ziegler and N B Nichols. "Optimum Settings for Automatic Controllers". In: *Annual Meeting of the American Society of Mechanical Engineers*. 1941.

[170] A.S. McCormack and K.R. Godfrey. "Rule-based autotuning based on frequency domain identification". In: *IEEE Transactions on Control Systems Technology* 6.1 (1998), pp. 43–61. DOI: 10.1109/87.654876.

[171] Jeffrey C. Lagarias et al. "Convergence Properties of the Nelder–Mead Simplex Method in Low Dimensions". In: *SIAM Journal on Optimization* 9.1 (Jan. 1998), pp. 112–147. DOI: 10.1137/S1052623496303470.

[172] P.R. Chandler, M. Pachter, and S. Rasmussen. "UAV cooperative control". In: *Proceedings of the 2001 American Control Conference*. IEEE, 2001, 50–55 vol.1. DOI: 10.1109/ACC.2001.945512.

[173] Jonathan How, Yoshiaki Kuwata, and Ellis King. "Flight Demonstrations of Cooperative Control for UAV Teams". In: *AIAA 3rd "Unmanned Unlimited" Technical Conference, Workshop and Exhibit*. Reston, Virigina: American Institute of Aeronautics and Astronautics, Sept. 2004. DOI: 10.2514/6.2004-6490.

[174] N.E. Leonard and E. Fiorelli. "Virtual leaders, artificial potentials and coordinated control of groups". In: *Proceedings of the 40th IEEE Conference on Decision and Control (Cat. No.01CH37228)* December (2001), pp. 2968–2973. DOI: 10.1109/.2001.980728.

[175] Craig W. Reynolds. "Flocks, herds and schools: A distributed behavioral model". In: *ACM SIGGRAPH Computer Graphics* 21.4 (Aug. 1987), pp. 25–34. DOI: 10.1145/37402.37406.

[176] Austin L Smith and Donald L Kunz. *Dynamic Coupling of the KC-135 Tanker and Boom for Modeling and Simulation*. Tech. rep. Wright-Patterson Air Force Base, OH: Air Force Research Laboratory, 2006.

[177] B Anderson et al. “Control of a three-coleader formation in the plane”. In: *Systems & Control Letters* 56.9-10 (Sept. 2007), pp. 573–578. DOI: 10.1016/j.sysconle.2007.04.004.

[178] Zhibo Zheng, Stephen C Spry, and Anouck R Girard. “Leaderless Formation Control using Dynamic Extension and Sliding Control ”. In: *Proceedings of the 17th World Congress of The International Federation of Automatic Control*. Seoul: The International Federation of Automatic Control, 2008, pp. 16027–16032.

[179] Norman H. M. Li and Hugh H. T. Liu. “Formation UAV flight control using virtual structure and motion synchronization”. In: *2008 American Control Conference* (June 2008), pp. 1782–1787. DOI: 10.1109/ACC.2008.4586750.

[180] Wei Ren and Randal W Beard. “Formation feedback control for multiple spacecraft via virtual structures”. In: *IEE Proc.-Control Theory Appl.* 151.3 (2004), pp. 357–368. DOI: 10.1049/ip-cta.

[181] K.D. Do. “Formation control of mobile agents using local potential functions”. In: *2006 American Control Conference* (2006), pp. 2148–2153. DOI: 10.1109/ACC.2006.1656537.

[182] Yang-yang Chen and Yu-ping Tian. “A backstepping design for directed formation control of three-coleader agents in the plane”. In: *International Journal of Robust and Nonlinear Control* 19.7 (May 2009), pp. 729–745. DOI: 10.1002/rnc.1344.

[183] Tony Griffiths. “Intimate Control for UAV and UGV Rendezvous and Docking: Refined Analysis and Robustness”. In: *3rd SEAS DTC Technical Conference*. Edinburgh, 2008.

[184] Christopher G Jones. “Vision Based Recovery of Unmanned Rotary Wing Vehicles”. PhD thesis. University of Bristol, 2009.

[185] S.D. Ishmael and D.R. McMonagle. *AFTI/F-16 Flight Test Results and Lessons*. Edwards, California, 1983.

Appendix A

Aircraft model

A.1 Model structure

The F-16 model contains three primary elements, shown in figure A.1:

- **Aerodynamics:** computes aerodynamic coefficients for all six degrees of freedom, including dynamic stability.
- **Engine:** uses lookup tables and transfer functions to determine thrust from demand and aircraft states.
- **Equations of motion:** describing the time derivative of each aircraft state as a function of the current state values and applied forces.

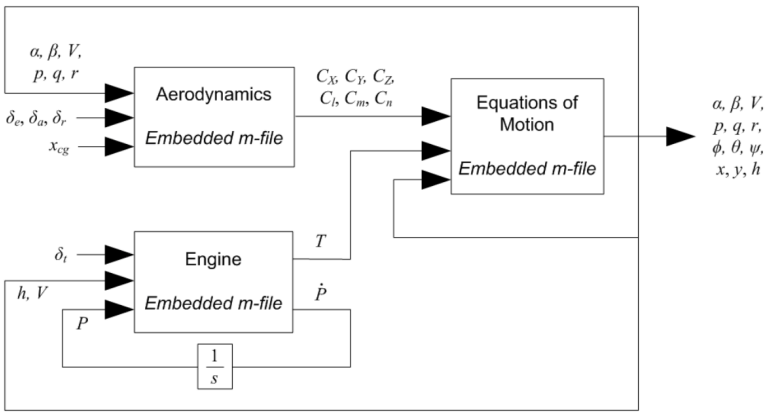

Figure A.1: F-16 model structure.

Each element is implemented in embedded MATLAB code, and integrated in a Simulink model that can be used as a block in the larger SE.

Inputs are control surface demands δ_e, δ_a, δ_r and δ_t, and the CG position as a percentage of Mean Aerodynamic Chord (MAC), x_{cg}.

Outputs are the twelve conventional aircraft states:

- 3 aerodynamic wind parameters α, β, V
- 3 angular rates p, q, r
- 3 angular orientations ϕ, θ, ψ
- 3 translational positions x, y, h

Note that altitude is given as $h = -z$.

The following sections summarise the elements of the F-16 model, the derivations of equations of motion, and the trim and linearisation process employed. The process is based on that specified by Stevens and Lewis, and more in-depth expansion of each section can be found in their text [63].

A.2 Aerodynamics

The aerodynamics routine calculates aerodynamic coefficients for the aircraft's six degrees of freedom from the previous timestep's states, using equations A.1. Static (subscript $_S$) and dynamic effects are linearly interpolated from lookup tables.

$$C_X = C_{X_S}(\alpha, \delta_e) + \frac{q\bar{c}}{2V}\left(\frac{\mathrm{d}C_X}{\mathrm{d}q}\right)\alpha \tag{A.1a}$$

$$C_Y = C_{Y_S}(\beta, \delta_a, \delta_r) + \frac{b}{2V}\left(p\frac{\mathrm{d}C_Y}{\mathrm{d}p} + r\frac{\mathrm{d}C_Y}{\mathrm{d}r}(\alpha)\right) \tag{A.1b}$$

$$C_Z = C_{Y_S}(\alpha, \beta_a, \delta_e) + \frac{q\bar{c}}{2V}\left(\frac{\mathrm{d}C_Z}{\mathrm{d}q}\right) \tag{A.1c}$$

$$C_l = C_{l_S}(\alpha, \beta) + \frac{q\bar{c}}{2V}\left(p\frac{\mathrm{d}C_l}{\mathrm{d}p} + r\frac{\mathrm{d}C_l}{\mathrm{d}r}\right) + \Delta\delta_a \tag{A.1d}$$

$$C_m = C_{m_S}(\alpha, \delta_e) + \frac{q\bar{c}}{2V}\left(\frac{\mathrm{d}C_m}{\mathrm{d}q}\right) + \left(\frac{35 - x_{cg}}{100}\right)C_Z \tag{A.1e}$$

$$C_n = C_{n_S}(\alpha, \beta) + \frac{b}{2V}\left(p\frac{\mathrm{d}C_n}{\mathrm{d}p}\right) + \Delta\delta_a\frac{\mathrm{d}C_n}{\mathrm{d}\delta_a}(\alpha, \beta) + \Delta\delta_r\frac{\mathrm{d}C_n}{\mathrm{d}\delta_r}(\alpha, \beta) - \frac{\bar{c}}{b}\left(\frac{35 - x_{cg}}{100}\right)C_Y \tag{A.1f}$$

where $\Delta\delta_a = \frac{\delta_a}{20}$ and $\Delta\delta_r = \frac{\delta_r}{30}$, 20°and 30°being the limits of the control surface deflections.

A.3 Engine

The transient response of the engine power output is modelled as a first order lag [63]:

$$\dot{P} = \frac{1}{\tau(c_p, r_p)} \left[r'_p(c_p, r_p) - r_p(\delta_t) \right] \tag{A.2}$$

where apparent demanded power r'_p is a function of current power c_p and demanded power r_p. All three are expressed as a percentage of maximum power. Engine time constant τ is also a function of c_p and r_p.

Demanded power r_p is modelled as [63]:

$$r_p = \begin{cases} 64.95\,\delta_t & \text{for } \delta_t \leq 0.77 \\ 217.38\,\delta_t - 117.38 & \text{for } \delta_t > 0.77 \end{cases} \tag{A.3}$$

Engine thrust T is linearly interpolated from a lookup table as a function of current power, altitude, and Mach number, and acts along the x^r body axis. Gyroscopically-induced pitching and yawing moments are neglected here, meaning:

$$\begin{aligned} X_{eng} &= T & L_{eng} &= 0 \\ Y_{eng} &= 0 & M_{eng} &= 0 \\ Z_{eng} &= 0 & N_{eng} &= 0 \end{aligned}$$

A.4 Equations of motion

The aircraft's equations of motion are defined by a set of state equations describing the time derivative of each state variable, as a function of the current state values and the applied aerodynamic and engine forces and moments.

The twelve states are:

- translational positions (x, y, z)
- translational velocities (u, v, w)
- Euler angles (ϕ, θ, ψ)[1]
- rotational velocities (p, q, r)

Assumptions made here for the AAAR capture scenario include:

- aircraft mass does not vary[2]

[1] Technically, the orientation parameters used in this thesis are Tait-Bryan angles, as three distinct rotational axes (z–y–x) are used rather than the two used by 'proper' or 'classic' Euler angles (e.g. z–x–z). In keeping with standard nomenclature in the field the Tait-Bryan angles in this thesis are referred to as Euler angles.

[2] This assumption and the following one are valid for the approach and capture phase, but will not be once fuel transfer commences.

- aircraft's CG does not change as % of $\bar{c}$
- aircraft is symmetric about the x–z plane
- aircraft is a rigid body
- aircraft has six unconstrained DoF
- effects of Earth's rotation are negligible
- changes in value of g are negligible
- for this initial work, the effect of tanker wake on the receiver is neglected (limits applicability to last 10 m of approach and capture)

Superscripts e and b denote Earth (inertial) and body reference frames. The generic equation for the translational velocities $\mathbf{v}^e$ is:

$$\mathbf{F} = \begin{bmatrix} X \\ Y \\ Z \end{bmatrix} = m\frac{\mathrm{d}}{\mathrm{d}t}\mathbf{v}^e = m\frac{\mathrm{d}}{\mathrm{d}t}\begin{bmatrix} u \\ v \\ w \end{bmatrix}^e \tag{A.4}$$

The derivative of the translational velocities relative to the Earth reference frame is expressed relative to the aircraft body reference frame as:

$$\frac{\mathrm{d}}{\mathrm{d}t}\mathbf{v}^e = \frac{\mathrm{d}}{\mathrm{d}t}\mathbf{v}^b + \boldsymbol{\omega} \times \mathbf{v} \tag{A.5a}$$

$$\therefore \mathbf{F} = m\left(\frac{\mathrm{d}}{\mathrm{d}t}\mathbf{v}^b + \boldsymbol{\omega} \times \mathbf{v}\right) \tag{A.5b}$$

where $\boldsymbol{\omega}$ is the angular velocity (p, q, r) of the aircraft with respect to the Earth reference frame. Equation A.5a can be expanded into individual axes as:

$$\begin{bmatrix} X \\ Y \\ Z \end{bmatrix} = m\left(\frac{\mathrm{d}}{\mathrm{d}t}\begin{bmatrix} u \\ v \\ w \end{bmatrix}^b + \begin{bmatrix} p \\ q \\ r \end{bmatrix} \times \begin{bmatrix} u \\ v \\ w \end{bmatrix}\right) \tag{A.6a}$$

$$\therefore \begin{bmatrix} X \\ Y \\ Z \end{bmatrix} = m\begin{bmatrix} \dot{u} \\ \dot{v} \\ \dot{w} \end{bmatrix}^b + m\begin{bmatrix} qw - rv \\ ru - pw \\ pv - qu \end{bmatrix} \tag{A.6b}$$

By substituting coefficient equations for the forces (X, Y, Z) in equation

A.6a, translational accelerations can be given as:

$$\dot{u} = rv - qw - g\sin\theta \qquad + \frac{1}{m}\left(\frac{1}{2}\rho V^2 S C_X + X_{eng}\right) \tag{A.7a}$$

$$\dot{v} = pw - ru + g\cos\theta\sin\phi + \frac{1}{m}\left(\frac{1}{2}\rho V^2 S C_Y + Y_{eng}\right) \tag{A.7b}$$

$$\dot{w} = qu - pv \ + g\cos\theta\cos\phi + \frac{1}{m}\left(\frac{1}{2}\rho V^2 S C_Z + Z_{eng}\right) \tag{A.7c}$$

where $(X, Y, Z)_{eng}$ are forces generated by the engine, given in section A.3.

Displacements x, y, z can be integrated from the translational velocities, and must be transformed into the Earth reference axes through, in this instance, ϕ–θ–ψ transformation $\mathbf{T}_b^e$:

$$\begin{bmatrix}\dot{x}\\ \dot{y}\\ \dot{z}\end{bmatrix}^e = \mathbf{T}_b^e \begin{bmatrix}\dot{u}\\ \dot{v}\\ \dot{w}\end{bmatrix}^b = \begin{bmatrix}\mathrm{c}\psi\mathrm{c}\theta & \mathrm{c}\psi\mathrm{s}\theta\mathrm{s}\phi - \mathrm{c}\phi\mathrm{s}\psi & \mathrm{s}\psi\mathrm{s}\phi + \mathrm{c}\psi\mathrm{c}\phi\mathrm{s}\theta\\ \mathrm{c}\theta\mathrm{s}\psi & \mathrm{c}\psi\mathrm{c}\phi + \mathrm{s}\psi\mathrm{s}\theta\mathrm{s}\phi & \mathrm{c}\phi\mathrm{s}\psi\mathrm{s}\theta - \mathrm{c}\psi\mathrm{s}\phi\\ -\mathrm{s}\theta & \mathrm{c}\theta\mathrm{s}\phi & \mathrm{c}\theta\mathrm{c}\phi\end{bmatrix} \begin{bmatrix}\dot{u}\\ \dot{v}\\ \dot{w}\end{bmatrix}^b \tag{A.8}$$

where, for clarity, cos is abbreviated as c, and sin as s.

Expanding:

$$\dot{x} = u(\mathrm{c}\psi\mathrm{c}\theta) + v(\mathrm{c}\psi\mathrm{s}\theta\mathrm{s}\phi - \mathrm{c}\phi\mathrm{s}\psi) + w(\mathrm{s}\psi\mathrm{s}\phi + \mathrm{c}\psi\mathrm{c}\phi\mathrm{s}\theta) \tag{A.9a}$$

$$\dot{y} = u(\mathrm{c}\theta\mathrm{s}\psi) + v(\mathrm{c}\psi\mathrm{c}\phi + \mathrm{s}\psi\mathrm{s}\theta\mathrm{s}\phi) + w(\mathrm{c}\phi\mathrm{s}\psi\mathrm{s}\theta - \mathrm{c}\psi\mathrm{s}\phi) \tag{A.9b}$$

$$\dot{z} = -u(\mathrm{s}\theta) \ + v(\mathrm{c}\theta\mathrm{s}\phi) \qquad\qquad + w(\mathrm{c}\theta\mathrm{c}\phi) \tag{A.9c}$$

Similarly to the translational motion, the generic equation for rotational motion is:

$$\mathbf{M} = \begin{bmatrix}L\\ M\\ N\end{bmatrix} = \frac{\mathrm{d}}{\mathrm{d}t}\mathbf{H}^e \tag{A.10}$$

where $\mathbf{M}$ is the vector of applied moments and $\mathbf{H}^e$ the angular momentum. $\mathbf{H}^e$ is the cross-product of inertial tensor $\mathbf{I}$ and angular velocity $\boldsymbol{\omega}$, so:

$$\mathbf{M} = \frac{\mathrm{d}}{\mathrm{d}t}(\mathbf{I}\boldsymbol{\omega}^e) \tag{A.11}$$

The inertial tensor is given as a positive-diagonal matrix:

$$\mathbf{I} = \begin{bmatrix}I_x & -I_{xy} & -I_{xz}\\ -I_{xy} & I_y & -I_{yz}\\ -I_{xz} & -I_{yz} & I_z\end{bmatrix} \tag{A.12}$$

Rotational velocities in the Earth reference frame in terms of the body

frame are:

$$\mathbf{M} = \mathbf{I}\frac{\mathrm{d}}{\mathrm{d}t}\boldsymbol{\omega}^b + \boldsymbol{\omega}^b \times \mathbf{I}\boldsymbol{\omega}^b \tag{A.13}$$

If we assume the aircraft to be symmetric about the x–z plane, $I_{xy} = Ixz = 0$. Therefore:

$$\begin{bmatrix} L \\ M \\ N \end{bmatrix} = \begin{bmatrix} I_x & 0 & -I_{xz} \\ 0 & I_y & 0 \\ -I_{xz} & 0 & I_z \end{bmatrix} \begin{bmatrix} \dot{p} \\ \dot{q} \\ \dot{r} \end{bmatrix} + \begin{bmatrix} p \\ q \\ r \end{bmatrix} \times \begin{bmatrix} I_x & 0 & -I_{xz} \\ 0 & I_y & 0 \\ -I_{xz} & 0 & I_z \end{bmatrix} \begin{bmatrix} p \\ q \\ r \end{bmatrix} \tag{A.14}$$

or

$$L = I_x\dot{p} - I_{xx}(\dot{r} + pq) + qr(I_z - I_y) \tag{A.15a}$$
$$M = I_y\dot{q} + pr(I_x - I_z) + I_{xz}(p^2 - r^2) \tag{A.15b}$$
$$N = I_z\dot{r} + I_{xz}(qr - \dot{p}) + pq(I_y - I_x) \tag{A.15c}$$

To rearrange for $\dot{p}$, $\dot{q}$, and $\dot{r}$, we first rearrange equation A.15b to give $\dot{q}$:

$$\dot{q} = \frac{1}{I_y}\left[M + pr(I_x - I_z) + I_{xz}(p^2 - r^2)\right] \tag{A.16}$$

Multiplying A.15a and A.15c by I_z and I_{xz} respectively, summing and rearranging for $\dot{p}$:

$$\dot{p} = \frac{pqI_{xz}(I_x - I_y + I_z) + qr[I_z(I_y - I_z) - I_{xz}^2] + I_zL + I_{xz}N}{(I_xI_z - I_{xz}^2)} \tag{A.17}$$

Similarly, multiplying A.15a and A.15c by by I_{xz} and I_x respectively, summing and rearranging for $\dot{r}$:

$$\dot{r} = \frac{pq[I_x(I_x - I_y) + I_{xz}^2] - qrI_{xz}(I_x - I_y + I_z) + I_{xz}L + I_xN}{(I_xI_z - I_{xz}^2)} \tag{A.18}$$

Applied moments L, M, N are the sum of aerodynamic and engine moments:

$$L = \frac{1}{2}\rho V^2 S\, b\, C_l \; + L_{eng} \tag{A.19a}$$
$$M = \frac{1}{2}\rho V^2 S\, \bar{c}\, C_m + M_{eng} \tag{A.19b}$$
$$N = \frac{1}{2}\rho V^2 S\, b\, C_n \; + L_{eng} \tag{A.19c}$$

where $(L, M, N)_{eng}$ are components generated by the engine model, from section A.3.

The rotational states ϕ, θ, ψ cannot be simply integrated from angular velocities, as they do not correspond to the summed rotations about orthog-

onal axes. Angular velocities are expressed in the body reference frame, so $\dot{\phi}$ does not need to be transformed. $\dot{\theta}$ requires a roll transformation, and $\dot{\psi}$ requires pitch then roll:

$$\begin{bmatrix} p \\ q \\ r \end{bmatrix} = \begin{bmatrix} \dot{\phi} \\ 0 \\ 0 \end{bmatrix} \begin{bmatrix} 1 & 0 & 0 \\ 0 & \cos\phi & \sin\phi \\ 0 & -\sin\phi & \cos\phi \end{bmatrix} \left(\begin{bmatrix} 0 \\ \dot{\theta} \\ 0 \end{bmatrix} + \begin{bmatrix} \cos\theta & 0 & -\sin\theta \\ 0 & 1 & 0 \\ \sin\theta & 0 & \cos\theta \end{bmatrix} \begin{bmatrix} 0 \\ 0 \\ \dot{\psi} \end{bmatrix} \right) \tag{A.20a}$$

$$\therefore \begin{bmatrix} p \\ q \\ r \end{bmatrix} = \begin{bmatrix} 1 & 0 & -\sin\theta \\ 0 & \cos\phi & \sin\phi\cos\theta \\ 0 & -\sin\theta & \cos\psi\cos\theta \end{bmatrix} \begin{bmatrix} \dot{\phi} \\ \dot{\theta} \\ \dot{\psi} \end{bmatrix} = \mathbf{R}_e^b \begin{bmatrix} \dot{\phi} \\ \dot{\theta} \\ \dot{\psi} \end{bmatrix} \tag{A.20b}$$

Transformation matrix $\mathbf{R}_e^b$ can be inverted to obtain expressions for Euler angle derivatives:

$$\dot{\phi} = p + \tan\theta(q\sin\phi + r\cos\phi) \tag{A.21a}$$

$$\dot{\theta} = q\cos\phi - r\sin\theta \tag{A.21b}$$

$$\dot{\psi} = \frac{q\sin\phi + r\cos\phi}{\cos\theta} \tag{A.21c}$$

We now have a complete set of 12 equations of motion, giving derivatives for:

- translational positions (x, y, z) in equations A.9a, A.9b, and A.9c
- translational velocities (u, v, w) in equations A.7a, A.7b, and A.7c
- Euler angles (ϕ, θ, ψ) in equations A.21a, A.21b and A.21c
- rotational velocities (p, q, r) in equations A.17, A.16 and A.18 respectively.

A.5 Flight conditions

Flight conditions representative of aerial refuelling are selected as:

- $V = 200$ ms^{-1}
- $h = 8000$ m

This airspeed is in the range recommended by ATP-56(B) [121] for high-speed drogue refuelling, typical of fighters such as the F-16, and by Cobham plc as Mach 0.65. The altitude is recommended as a flight level with reduced turbulence, however turbulence is varied in simulations detailed in

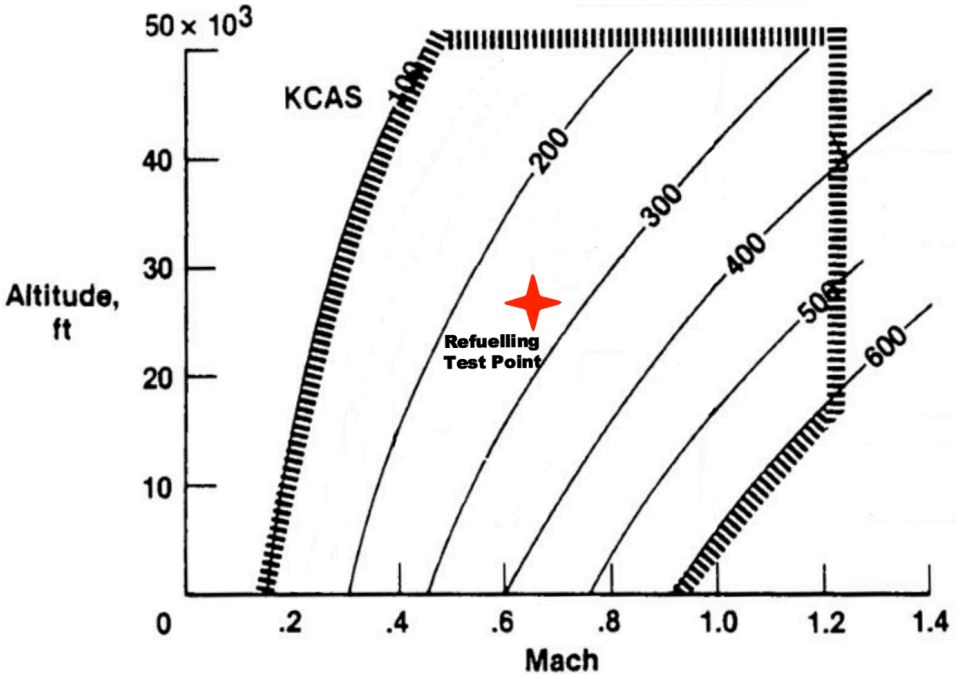

Figure A.2: F-16 flight envelope, with refuelling test point indicated. Adapted from [185].

later sections. The F-16's flight envelope is shown in figure A.2, with refuelling flight conditions marked—these conditions are central within that envelope. Again, the F-16 has been used as a baseline model because it is well characterised, taken as 'typical' of a refuelling-enabled UCAV, and likely a conservative surrogate.

A.6 Trim

State equations derived in section A.4 can be solved for state $\mathbf{x}$ and input $\mathbf{u}$ values producing a trimmed condition, where $\dot{\mathbf{x}} \to 0$. For straight and level flight:

$$\dot{u}, \dot{v}, \dot{w} \text{ (or similarly } \dot{V}, \dot{\alpha}, \dot{\beta}) = \dot{p}, \dot{q}, \dot{r} = 0 \tag{A.22}$$

Once trimmed conditions are established, a linear dynamic model about these equilibrium flight conditions can be obtained. This is taken as representative of the full nonlinear model in a region about the trim point, and will be used to formulate control laws based on linear systems theory.

Trimmed state and input values can be found for a given set of flight conditions defined by airspeed V and altitude h. A Sequential Quadratic Programming (SQP) algorithm is employed, via MATLAB's `trim` function. A least-squares cost function is used, with aircraft orientation initialised

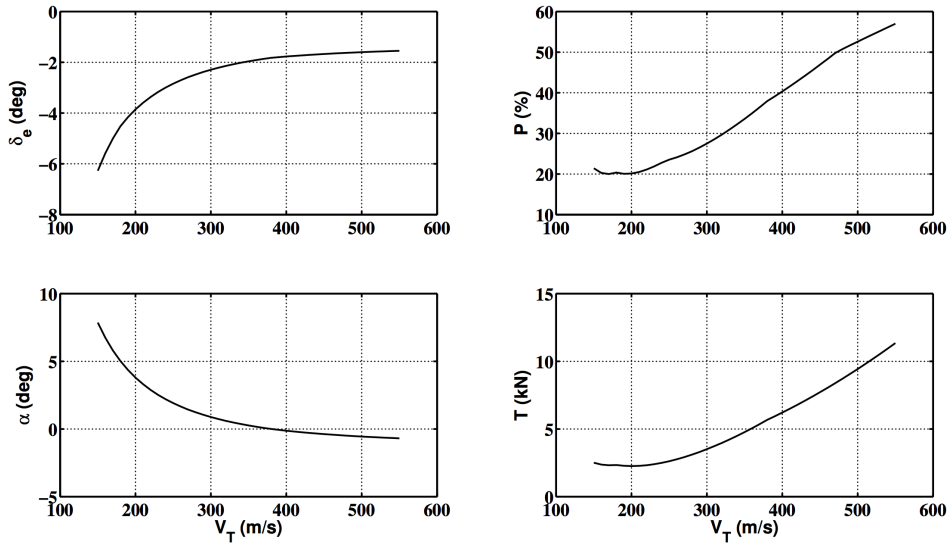

Figure A.3: Trimmed parameters at $h = 8000$ m

level with the LTP and control surfaces flat. The process minimises a cost function J that weights state variables as:

$$J = \dot{V}^2 + 100(\dot{\alpha}^2 + \dot{\beta}^2) + 10(\dot{p}^2 + \dot{q}^2 + \dot{r}^2) \tag{A.23}$$

and the minimisation is iterated until each derivative is less than 10^{-4}. Figure A.3 shows how trimmed elevator, incidence, engine power and thrust vary with airspeed at constant altitude, and figure A.4 shows how they vary with altitude at constant airspeed. For both figures, CG is constant at $0.25\bar{c}$. At refuelling flight conditions of $V = 200\text{m}\,\text{s}^{-1}, h = 8000\text{m}$, $J = 1.1303 \times 10^{-27}$.

Trimmed equilibrium values at the selected flight conditions, denoted with subscript $_\tau$ are given in table A.1.

A.7 Linearisation

Once trimmed states and inputs are established, a continuous-time state-space model is extracted about the trim point, taking the form:

$$\left.\begin{aligned}\dot{\mathbf{x}} &= \mathbf{A}\mathbf{x} + \mathbf{B}\mathbf{u}\\ \mathbf{y} &= \mathbf{C}\mathbf{x} + \mathbf{D}\mathbf{u}\end{aligned}\right\} \tag{A.24}$$

a standard state-space formulation, shown in figure A.5, where $\mathbf{A}$, $\mathbf{B}$, $\mathbf{C}$, and $\mathbf{D}$ are state, input, output and feed forward matrices ($\mathbf{C}$ is commonly unity and $\mathbf{D}$ is usually zero), and $\mathbf{x}$, $\mathbf{u}$, and $\mathbf{y}$ are state, input and output

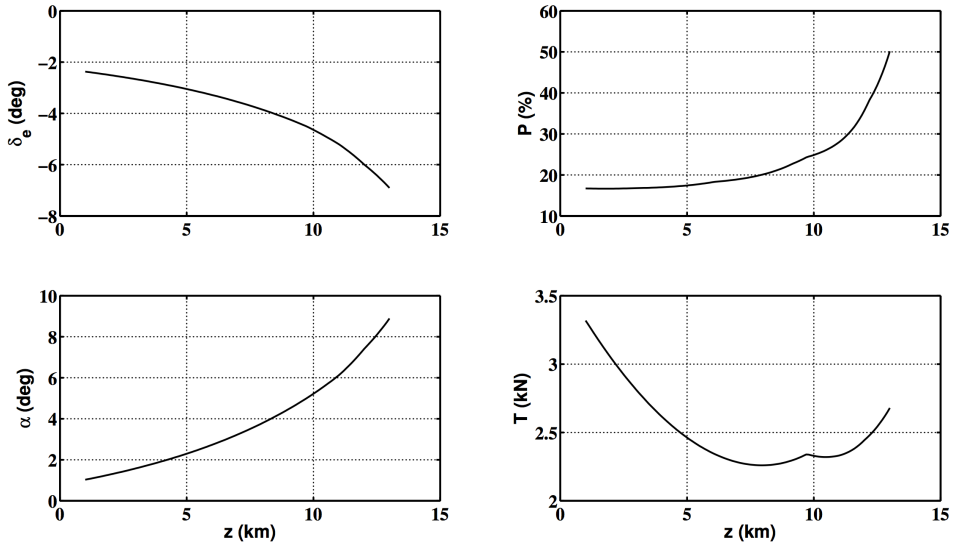

Figure A.4: Trimmed parameters at $V = 200$ ms^{-1}

Table A.1: F-16 trimmed states and inputs at refuelling flight condition.

Parameter	Value	Unit
p_τ	0	$^\circ\,\mathrm{s}^{-1}$
q_τ	0	$^\circ\,\mathrm{s}^{-1}$
r_τ	0	$^\circ\,\mathrm{s}^{-1}$
$\alpha_\tau = \theta_\tau$	3.79	$^\circ$
β_τ	0	$^\circ$
V_τ	200	$\mathrm{m\,s}^{-1}$
ϕ_τ	0	$^\circ$
ψ_τ	0	$^\circ$
y_τ	0	m
$z_\tau = -h_\tau$	8000	m
δ_{e_τ}	-3.86	$^\circ$
δ_{a_τ}	0	$^\circ$
δ_{r_τ}	0	$^\circ$
δ_{t_τ}	0.31	
c_{p_τ}	20.12	%

vectors, comprised of perturbed values about the trim point:

$$\mathbf{x} = \begin{bmatrix} \Delta p \\ \Delta q \\ \Delta r \\ \Delta \alpha \\ \Delta \beta \\ \Delta V \\ \Delta \phi \\ \Delta \theta \\ \Delta \psi \\ \Delta x \\ \Delta y \\ \Delta h \\ \Delta c_p \end{bmatrix} \qquad \mathbf{u} = \begin{bmatrix} \Delta \delta_e \\ \Delta \delta_a \\ \Delta \delta_r \\ \Delta \delta_t \end{bmatrix} \qquad \mathbf{y} = \begin{bmatrix} \Delta p \\ \Delta q \\ \Delta r \\ \Delta \alpha \\ \Delta \beta \\ \Delta V \\ \Delta \phi \\ \Delta \theta \\ \Delta \psi \\ \Delta x \\ \Delta y \\ \Delta h \end{bmatrix} \tag{A.25}$$

The resultant state-space model, presented as separate longitudinal- and lateral-directional components, is detailed in equations A.26. For this work, outputs $\mathbf{y}$ for both components are assumed identical to states $\mathbf{x}$, i.e. $\mathbf{C} = \mathbf{I}, \mathbf{D} = [0]$.

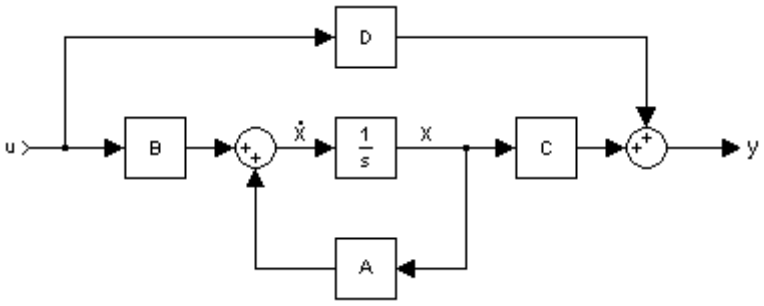

Figure A.5: Classical linear state-space model.

$$\begin{bmatrix} \Delta\dot{q} \\ \Delta\dot{\alpha} \\ \Delta\dot{V} \\ \Delta\dot{\theta} \\ \Delta\dot{x} \\ \Delta\dot{h} \\ \Delta\dot{c}_p \end{bmatrix} = \begin{bmatrix} -0.9598 & -4.2724 & 0 & 0 & 0 & 0 & 0 \\ 0.9582 & -0.5712 & -0.0005 & 0 & 0 & 0 & 0 \\ -0.2583 & -1.2019 & -0.0122 & -9.81 & 0 & 0 & 0.0556 \\ 1 & 0 & 0 & 0 & 0 & 0 & 0 \\ 0 & 0 & 1 & 0 & 0 & 0 & 0 \\ 0 & -200 & 0 & 200 & 0 & 0 & 0 \\ 0 & 0 & 0 & 0 & 0 & 0 & -1 \end{bmatrix} \begin{bmatrix} \Delta q \\ \Delta\alpha \\ \Delta V \\ \Delta\theta \\ \Delta x \\ \Delta h \\ \Delta c_p \end{bmatrix} + \begin{bmatrix} -0.1384 & 0 \\ -0.0012 & 0 \\ 0.0299 & 0 \\ 0 & 0 \\ 0 & 0 \\ 0 & 0 \\ 0 & 64.94 \end{bmatrix} \begin{bmatrix} \Delta\delta_e \\ \Delta\delta_t \end{bmatrix} \quad \text{(A.26a)}$$

$$\begin{bmatrix} \Delta\dot{p} \\ \Delta\dot{r} \\ \Delta\dot{\beta} \\ \Delta\dot{\phi} \\ \Delta\dot{\psi} \\ \Delta\dot{y} \end{bmatrix} = \begin{bmatrix} -2.0260 & 0.4493 & -25.4971 & 0 & 0 & 0 \\ -0.0306 & -0.2930 & 7.6774 & 0 & 0 & 0 \\ 0.0664 & -0.9944 & -0.1805 & 0.0489 & 0 & 0 \\ 1 & 0.0664 & 0 & 0 & 0 & 0 \\ 0 & 1.0022 & 0 & 0 & 0 & 0 \\ 0 & 0 & 200 & -13.2492 & 200 & 0 \end{bmatrix} \begin{bmatrix} \Delta p \\ \Delta r \\ \Delta\beta \\ \Delta\phi \\ \Delta\psi \\ \Delta y \end{bmatrix} + \begin{bmatrix} -0.5407 & 0.0936 \\ -0.0242 & -0.0488 \\ 0.0002 & 0.0005 \\ 0 & 0 \\ 0 & 0 \\ 0 & 0 \end{bmatrix} \begin{bmatrix} \Delta\delta_a \\ \Delta\delta_r \end{bmatrix} \quad \text{(A.26b)}$$

It should be noted that in this model the aerodynamic effects are isolated from the throttle and engine parameters, evident in the sparseness of the column corresponding to throttle input in equation A.26a. A throttle perturbation propagates via the 0.0556 gain ($\mathbf{A}[3,7]$), and then onwards via the induced change in airspeed V.

A.8 Characteristics

The five typical aircraft modes can be identified from the linearised model:

- Longitudinal
  - Short period

  - Phugoid

- Lateral
  - Dutch roll
  - Spiral
  - Roll subsidence

Eigenvalues and vectors corresponding to each of these are given in tables A.2 and A.3. Responses to excitation about the trim point are shown in figure A.6.

Table A.2: F-16 open loop longitudinal characteristics at refuelling flight condition.

Longitudinal		
λ	-0.7662 ± 2.0129i	-0.0045 ± 0.0736i
	Short period	Phugoid
α	-0.0332 ± 0.0213i	0
q	0.0514 ± 0.0656i	0
θ	-0.0370 ± 0.0115i	0
V	0.0041 ± 0.1949i	-0.0403 ± 0.0065i
x	-0.0852 ± 0.0304i	-0.0548 ± 0.5503i
h	0.9715	0.8321
c_p	0	0

Table A.3: F-16 open loop lateral characteristics at refuelling flight condition.

Lateral			
λ	-0.2845 ± 3.0262i	-0.0081	-1.9223
	Dutch roll	Spiral	Roll subsidence
β	0.0636 ± 0.0998i	0	-0.0020
r	0.2536 ± 0.1694i	0	0.0201
p	-0.8659	0	0.5724
ϕ	0.0225 ± 0.2784i	0	-0.2985
ψ	-0.0634 ± 0.0780i	0	-0.0105
y	0.2251 ± 0.0664i	-1	-0.7634

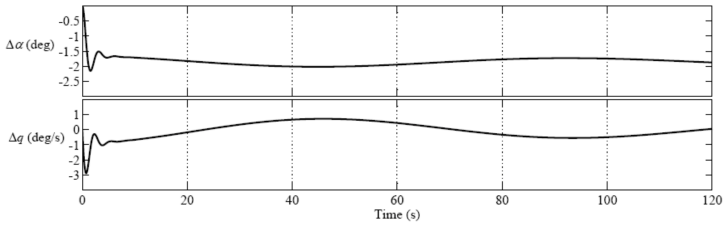

(a) Short period

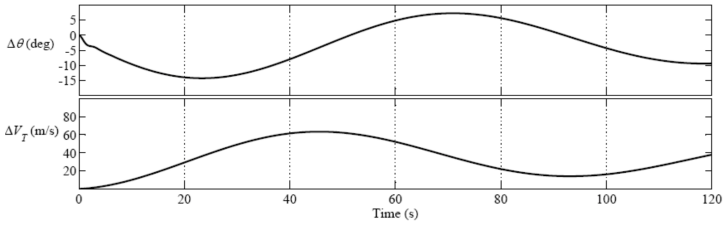

(b) Phugoid

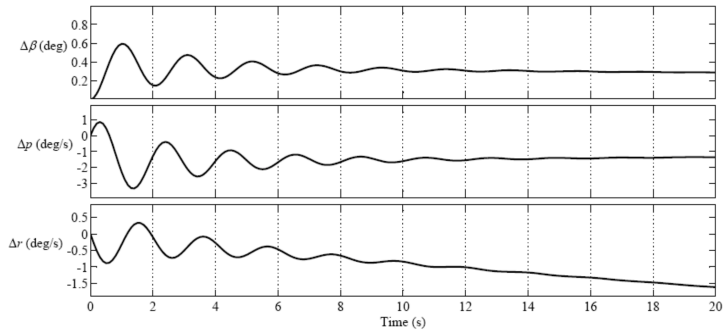

(c) Dutch roll

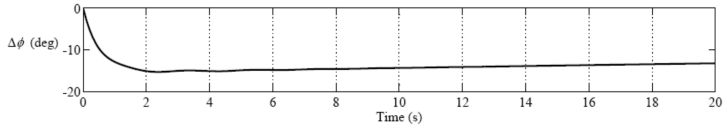

(d) Spiral

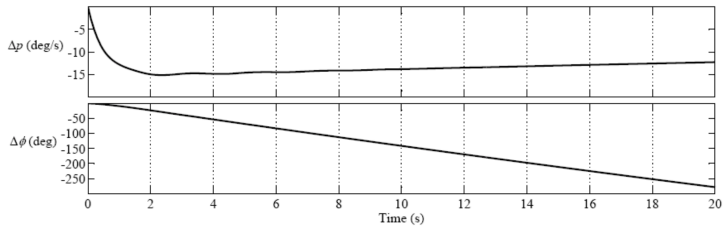

(e) Roll subsidence

Figure A.6: Modal characteristics of F-16 model